

SYNAPTIC MORPHOLOGY, FUNCTION, AND REGULATION IN A PAEDIATRIC-ONSET NEURODEGENERATIVE DISORDER

Andrew Peter Shoubridge B. Hlth. Sc. (Hons)

A Thesis submitted for the degree of Doctor of Philosophy in

The Discipline of Paediatrics, School of Medicine

Faculty of Health and Medical Sciences

March 2021

– TABLE OF CONTENTS –

THESIS ABSTRACT ..... **viii**

DECLARATION ..... **xi**

ACKNOWLEDGEMENTS ..... **xii**

CONFERENCES & COURSES ..... **xiii**

AWARDS ..... **xv**

ABBREVIATIONS ..... **xvi**

CHAPTER 1 – INTRODUCTION **1**

1.1 General Introduction 1

1.2 The Lysosome 3

1.2.1 The Endo-Lyso-Autophagosomal Pathways 3

1.2.2 Mannose-6-Phosphate Receptors 5

1.3 Lysosomal Storage Disorders 8

1.3.1 Diagnosis of Lysosomal Storage Disorders 11

1.4 The Mucopolysaccharidoses 13

1.5 Sanfilippo Syndrome (MPS III) 15

1.6 Mucopolysaccharidosis Animal Models 22

1.7 Therapeutic Approaches 27

1.7.1 Symptom Management 27

1.7.2 Hematopoietic Stem Cell (Bone Marrow) Transplantation 27

1.7.3 Enzyme Replacement Therapy (ERT) 30

1.7.4 Substrate Reduction Therapy (SRT) 32

1.7.5 Pharmacological Chaperone Therapy (PCT) 33

1.7.6 Gene Therapy 33

1.8 Neuronal Pathology 36

1.8.1 Neurodegeneration in MPS III 36
1.8.2 Synaptic Pathology of Neurons 36
1.8.3 Lysosomal Function at the Synapse 42
1.8.4 Morphological Changes of Neurons in Lysosomal Storage Disorders 44
1.8.5 Functional Changes of Neurons in Lysosomal Storage Disorders 46
1.8.6 Morphological and Functional Changes of Neurons in MPS III 50
1.9 Inflammation in the Central Nervous System 58
1.9.1 Adaptive Immunity 58
1.9.2 Innate Immunity 58
1.9.3 The Complement Cascade 60
1.9.4 Glial Cell Inflammatory Activation 62
1.9.5 Inflammation in MPS III 65
1.9.6 Inflammation in Lysosomal Storage Disorders 67
1.10 Research Significance and Outcomes 68
1.10.1 Hypothesis 68
1.10.2 Aims 69
CHAPTER 2 – MATERIALS AND METHODS 70
2.1 Materials 70
2.1.1 Animal Husbandry 70
2.1.2 Genotyping 70
2.1.3 Tissue Collection 71
2.1.4 Histology 72
2.1.5 Antibodies 72
2.1.6 Electrophysiology 73
2.1.7 Gene Therapy 73

2.1.8 Mass Spectrometry 74
2.2 Methods 75
2.2.1 YFP$^{+/-}$-MPS IIIA Mouse Colony Establishment and Maintenance 75
2.2.2 Mouse Ear-Notching 78
2.2.3 Genotyping YFP$^{+/-}$-MPS IIIA Mice 78
2.2.3.1 Genomic DNA Lysis from Mouse Tissue 78
2.2.3.2 Quantification of Genomic DNA 78
2.2.3.3 Genotyping Assay for Sulphamidase in YFP$^{+/-}$-MPS IIIA Mice 80
2.2.3.4 Genotyping Assay for *YFP* in YFP$^{+/-}$-MPS IIIA Mice 81
2.2.3.5 Genotyping Assay for *YFP* Copy Number in YFP$^{+/-}$-MPS IIIA Mice 83
2.2.4 Perfusion Fixation 84
2.2.5 Dendritic Spine Visualisation and Quantification 85
2.2.5.1 Brain Section Preparation 86
2.2.5.2 Dendritic Spine Imaging and Analysis 87
2.2.6 Immunofluorescence 89
2.2.6.1 Immunofluorescent Staining 89
2.2.6.2 Immunofluorescent Imaging 89
2.2.6.3 Immunofluorescent Analysis 91
2.2.7 Electrophysiology 92
2.2.7.1 Brain Slice Preparation 92
2.2.7.2 Whole-cell Patch-clamp Recording 94
2.2.8 Gene Therapy by Intraventricular Injection 97
2.2.8.1 Breeding for Day 0 Injection 97
2.2.8.2 Intraventricular Injection at Day 0 100

2.2.9 Behavioural Testing 103
2.2.9.1 Open Field Test 104
2.2.9.2 Pole Test 104
2.2.9.3 Negative Geotaxis Test 107
2.2.9.4 Grip Strength Test 107
2.2.10 Tissue Collection 108
2.2.11 Homogenisation of Brain Tissues 108
2.2.12 Bicinchoninic Acid Protein Assay 109
2.2.13 Mass Spectrometry 110
2.2.13.1 Heparan Sulphate Isolation from Brain Tissue 110
2.2.13.2 Liquid Chromatography/Mass Spectrometry of Heparan Sulphate 110
2.2.14 Statistical Analysis 114
CHAPTER 3 – TEMPORAL CHARACTERISATION OF DENDRITIC SPINES ON LAYER 5 PYRAMIDAL NEURONS IN THE MPS IIIA MOUSE MOTOR CORTEX 115
3.1 Introduction 115
3.2 Results 120
3.2.1 Visualisation of Dendritic Spines on YFP Neurons 120
3.2.2 Total Densities of Dendritic Spines are Reduced on MPS IIIA Neurons 120
3.2.3 Reduced Densities of Dendritic Spines Across Multiple Morphologies on MPS IIIA Neurons 124
3.3 Discussion 127
3.3.1 Potential Mechanistic Basis of Symptom 128
3.4 Conclusion 133

CHAPTER 4 – ELECTROPHYSIOLOGICAL PROPERTIES OF LAYER 5 PYRAMIDAL NEURONS IN THE MPS IIIA MOUSE MOTOR CORTEX 134

4.1 Introduction 134

4.2 Results 138

4.2.1 Electrophysiological Properties of Layer 5 Pyramidal Neurons in the MPS IIIA Mouse Motor Cortex 138

4.2.2 Sex May Have an Impact on Electrophysiological Properties 149

4.3 Discussion 154

4.4 Conclusion 165

CHAPTER 5 – NEUROIMMUNE PROPERTIES OF THE MPS IIIA MOUSE BRAIN AND THEIR RELATION TO DENDRITIC SPINE DEFECTS 166

5.1 Introduction 166

5.2 Results 170

5.2.1 Glial Cell Activation and Complement Component Levels are Higher in the MPS IIIA Motor Cortex 170

5.2.2 Activated Glia are Apposed to Sites of Synaptic Loss in the MPS IIIA Motor Cortex 178

5.3 Discussion 190

5.4 Conclusion 195

CHAPTER 6 – ASSESSING THE EFFECTS OF AAV9-*SGSH* GENE THERAPY ON THE MPS IIIA MOUSE MOTOR CORTEX 196

6.1 Introduction 196

6.2 Results 202

6.2.1 Open-Field Behavioural Testing 203

6.2.2 Motor Function Behavioural Testing 206

6.2.3 Lysosomal Dysfunction is Prevented Following AAV9-*SGSH* Administration to YFP$^{+/-}$-MPS IIIA Mice 210
6.2.4 Reduction of Dendritic Spine Loss Across Multiple Morphologies in YFP$^{+/-}$-MPS IIIA Mice Following AAV9-*SGSH* Treatment 214
6.2.5 Glial Cell Activation and Complement Component Levels are Reduced in the AAV9-*SGSH* Treated YFP$^{+/-}$-MPS IIIA Mice 217
6.2.6 Activated Glial Cell Apposition to Dendritic Spines is Reduced in YFP$^{+/-}$-MPS IIIA Mice Following AAV9-*SGSH* Treatment 225
6.3 Discussion 233
6.4 Conclusion 239
CHAPTER 7 – DISCUSSION AND FUTURE WORK 240
7.1 Project Significance 240
7.2 Outcomes, Limitations and Future Directions 241
7.3 Conclusion 255
APPENDICES 256
REFERENCES 265

– THESIS ABSTRACT –

The mucopolysaccharidoses are a group of inherited metabolic diseases wherein undegraded substrate accumulates within lysosomes as a result of dysfunctional lysosomal protein. The most common sub-group is mucopolysaccharidosis (MPS) III (collectively 1 in 70,000). In Australia, MPS IIIA is the most common sub-type and the focus of this study. MPS IIIA is caused by an autosomal recessive mutation in the sulphamidase gene, leading to accumulation of heparan sulphate. Progressive neurological symptoms are the primary manifestation, including impaired control of motor function. Despite the abnormal intracellular pathology, negligible neuronal cell loss occurs. This suggests that neurological dysfunction does not arise from cellular loss, but rather discrete structural or functional changes in the neurons themselves. Disease pathogenesis is presently not well understood, and the molecular basis of cognitive impairment is unknown. In this study, an MPS IIIA mouse model was utilised to:

1. Establish the time-course of changes in the morphology and number of dendritic spines on layer 5 pyramidal neurons in the cerebral motor cortex.
2. Elucidate the biological impact of synaptic dysfunction on neuronal activity by electrophysiology.
3. Determine the underlying mechanisms contributing to dendritic spine dysgenesis/loss.
4. Determine if synaptic degeneration can be prevented by administering AAV9-based gene therapy prior to symptom-onset.

The hypothesis was that changes in synaptic morphology and function underlie cognitive decline in MPS IIIA. The aim of the study was to increase understanding of neurological dysfunction in MPS IIIA, and potentially provide therapeutic targets for this presently untreatable disease.

Dendritic spine deficiencies were evident in the pre-symptomatic MPS IIIA mouse brain, with loss of immature and mature spine sub-types, and reductions in overall density. The deficits persisted with disease progression to at least 20-weeks of age. Whilst this did not alter electrophysiological action potential frequency/kinetics, reductions in excitatory post-synaptic current events and altered event kinetics were observed in these same neurons in the pre-symptomatic disease stage. Therefore, these structural and functional changes may be contributing to symptom onset and could help explain the neurological decline seen in MPS IIIA.

Immunofluorescence-based techniques demonstrated that pro-inflammatory glial cells were closely apposed to layer 5 pyramidal neurons in the MPS IIIA mouse motor cortex from a pre-symptomatic age when synaptic loss also occurs. Additionally, the recently identified A1-type reactive astrocyte was highly prevalent in the MPS IIIA mouse motor cortex. These cells have been linked to/associated with higher expression of inflammatory complement components which bind to and identify synapses for removal by microglia. This suggests over-active synaptic pruning could be contributing to the observed synaptic loss via pro-inflammatory marker expression.

Gene therapy delivered intraventricularly to MPS IIIA mice at birth resulted in prevention/delay of heparan sulphate accumulation and activation of astrocytes and

microglia and appeared to normalise dendritic spine density and maturation to 20-weeks of age. However, longer-term studies are needed to establish the longevity of this effect.

The findings, coupled with existing literature, indicate that synaptic dysfunction occurs in various neurons in the MPS III brain, and suggests that the evaluation of novel therapies should examine discrete changes to the brain architecture.

– DECLARATION –

I, Andrew Peter Shoubridge, certify that this work contains no material which has been accepted for the award of any other degree or diploma in my name in any university or other tertiary institution and, to the best of my knowledge and belief, contains no material previously published or written by another person, except where due reference has been made in the text. In addition, I certify that no part of this work will, in the future, be used in a submission in my name for any other degree or diploma in any university or other tertiary institution without the prior approval of the University of Adelaide and where applicable, any partner institution responsible for the joint award of this degree. I give permission for the digital version of my thesis to be made available on the web, via the University's digital research repository, the Library Search and also through web search engines, unless permission has been granted by the University to restrict access for a period of time.

I acknowledge the support I have received for my research through the provision of an Australian Government Research Training Program Scholarship, a Sanfilippo Children's Foundation Supplementary Scholarship, and Commonwealth Scholarships Program for South Australia Scholarship.

Andrew Peter Shoubridge

– ACKNOWLEDGEMENTS –

First and foremost, I wish to express my deepest gratitude to my supervisor, Associate Professor Kim Hemsley. Over the past several years, you have not only shaped and guided my PhD to its successful conclusion, but you have also developed and supported me towards an exciting career in research. I will be forever grateful for the opportunities and possibilities you provided me which led me to this point, and will carry me forward in the future. I also wish to thank my co-supervisor, Dr Emma Parkinson-Lawrence, for lending her expert knowledge and advice throughout my entire candidature.

My sincere gratitude also extends to Dr Cedric Bardy, for his invaluable expertise, advice, and infectious passion in the realm of electrophysiology.

I am indebted to the past and present members of the Childhood Dementia Research Group: Adeline, Barb, Daniel, Helen, Leanne, Meghan, Nazzmer, and Sarah. You were all willing and able to offer me assistance and support whenever the need arose, and wrested me free from difficult times. I also wish to express thanks to the members of the Hopwood Centre for Neurobiology, and in particular Julian and Sophie. You were both incredible sources of support and humour, and made the long days far more enjoyable. I will always cherish our times together.

Finally, and most importantly, I give my immeasurable gratitude and love for my family. To my parents, sister, and brother-in-law, you have been there to provide unconditional and unyielding support, encouragement and guidance from the very beginning. We rode this undulating journey together, and I would not have reached the end without you. And to my dearest fiancée, Zahra, and her parents. Words struggle to express the amount of joy you gave me throughout my PhD candidature, and our engagement was undoubtedly the glowing and unforgettable moment. Your unwavering love, support and patience illuminated the way right to the end. Thank you.

– CONFERENCES & COURSES –

Oral: Shoubridge AP, Bardy C, Parkinson-Lawrence EJ and Hemsley KM. Synaptic inflammation in a childhood-onset form of dementia. *Keystone Symposia: Neuro-Immune Interactions in the Central Nervous System 2020*, Keystone, CO, USA. *Cancelled (COVID-19).*

Invited Speaker: Shoubridge AP. Synaptic morphology, function, and regulation in Sanfilippo Syndrome. *Solving Sanfilippo Symposium 2020*, Adelaide, Australia.

Course: SAHMRI Communicate with Impact Masterclass. February – November 2019.

Poster: Shoubridge AP, Trim PJ, Douglass ML, Parkinson-Lawrence EJ, Snel MF and Hemsley KM. Complement plays a role in synapse loss in a paediatric-onset neurocognitive disorder. *Australian Neuroscience Society 2018*, Brisbane, Australia.

Course: Australian Course in Advanced Neuroscience (ACAN). 8-28 April 2018. Moreton Bay Research Station, North Stradbroke Island, Queensland, Australia.

Oral: Shoubridge AP, Lau AA, Parkinson-Lawrence EJ and Hemsley KM. A time-course study of dendritic spine morphology and density in a paediatric lysosomal storage disorder. *Australian Neuroscience Society 2017*, Sydney, Australia.

Poster: Shoubridge AP, Lau AA, Parkinson-Lawrence EJ and Hemsley KM (2017). A break in the neuronal circuit: mice with a paediatric-onset neurocognitive disorder have

pre-symptomatic synaptic abnormalities. *Australian Neuroscience Society 2017*, Sydney, Australia.

Poster: Shoubridge AP, Lau AA, Parkinson-Lawrence EJ and Hemsley KM. Synaptic abnormalities occur pre-symptomatically in mice with MPS IIIA, a paediatric-onset neurocognitive disorder. *Florey Postgraduate Research Conference 2017*, Adelaide, Australia.

Oral: Shoubridge AP, Trim PJ, Snel MF, Smith NJC, Hopwood JJ and Hemsley KM. Radio silence? Are symptoms in childhood-onset dementia linked to diminished neuronal communication? *South Australian Scientific Meeting, Australian Society for Medical Research 2017*, Adelaide, Australia.

– AWARDS –

Award: John Carew Eccles Prize for *in vivo* electrophysiological recordings. *Australian Course in Advanced Neuroscience 2018,* North Stradbroke Island, Queensland, Australia.

Award: Student Travel Grant to attend the *38th Annual Scientific Meeting, Australasian Neuroscience Society 2018,* Brisbane, Australia.

Award: Research Travel Award, The University of Adelaide Medical School to attend the *Australian Course in Advanced Neuroscience 2018*, North Stradbroke Island, Queensland, Australia.

Award: Student Travel Grant to attend the *37th Annual Scientific Meeting, Australasian Neuroscience Society 2017*, Sydney, Australia.

Scholarship: Commonwealth Scholarships Program for South Australia Scholarship, 2017-2020.

Scholarship: Sanfilippo Children's Foundation Supplementary Scholarship, 2017-2020.

Scholarship: Research Training Program Stipend, The University of Adelaide, 2017-2020.

– ABBREVIATIONS –

AAV	Adeno-associated virus
ACSF	Artificial cerebrospinal fluid
AMPA	α-Amino-3-hydroxy-5-methyl-4-soxazolepropionic acid
AMPAR(s)	AMPA receptor(s)
ANOVA	Analysis of variance
AP	Action potential
BORC	Biogenesis of lysosome-related organelles complex-1 related complex
C1q	Complement component 1 subcomponent q
C3	Complement component 3
CD	Cluster of differentiation
CDRG	Childhood Dementia Research Group
CNS	Central nervous system
CR3	Complement receptor 3
CSF	Cerebrospinal fluid
EPSC	Excitatory post-synaptic current
EPSP	Excitatory post-synaptic potential
GABA	Gamma-Aminobutyric acid
GFAP	Glial fibrillary acidic protein
HOPS	Homotypic fusion and vacuole protein sorting
HS	Heparan sulphate
HSCT	Haematopoietic stem cell transplantation
HSPG	Heparan sulphate proteoglycan
Iba1	Ionised calcium-binding adaptor molecule 1

IFN	Interferon
IL	Interleukin
IPSC**(s)**	Inhibitory post-synaptic current**(s)**
LAMP1	Lysosomal-associated membrane protein 1
LC-MS/MS	Liquid chromatography-tandem mass spectrometry
LIMP-II	Lysosomal integral membrane protein-2
LSD(s)	Lysosomal storage disorder(s)
M6P	Mannose-6-phosphate
mEPSC**(s)**	Miniature excitatory post-synaptic current(s)
MPR(s)	Mannose-6-phosphate receptor(s)
MPS	Mucopolysaccharidosis
MS/MS	Tandem mass spectrometry
NAGLU	N-acetyl-alpha-glucosaminidase
NMDA	N-methyl-D-aspartic acid
NPC1	Niemann-Pick type C1
PBS	Phosphate buffered saline
PCR	Polymerase chain reaction
PFA	Paraformaldehyde
PLEKHM1	Pleckstrin homology domain-containing protein family member 1
PSD	Post-synaptic density
RRP	Readily releasable pool
SAHMRI	South Australian Health and Medical Research Institute
SEM	Standard error of the mean
SGSH	Sulphamidase
SNARE	trans-Soluble N-ethylmaleimide-sensitive factor Attachment protein Receptor

SNP	Single nucleotide polymorphism
TNF	Tumour necrosis factor
VAMP	Vesicle-associated membrane protein
Vineland-II	Vineland adaptive behaviour scales II
VPS	Vacuolar protein sorting-associated protein
YFP	Yellow fluorescent protein

– CHAPTER 1 –

INTRODUCTION

1.1 General Introduction

Lysosomal storage disorders (LSDs) are a group of inherited metabolic disorders where undegraded substrate accumulates within the lysosomes of most cells due to lysosomal membrane protein or enzymatic abnormalities. The mucopolysaccharidoses comprise approximately one-quarter of the known LSDs (Neufeld and Muenzer, 2001), where the lysosomal abnormalities result in the dysfunctional transportation and degradation of sulphated components of connective tissue known as mucopolysaccharides (or glycosaminoglycans).

Mucopolysaccharidosis type III (MPS III; Sanfilippo syndrome) is the most prevalent of all the mucopolysaccharidoses, and MPS III type A (MPS-IIIA) is the most common sub-type (Meikle et al., 1999). The lysosomal enzyme deficiency in MPS IIIA (*N*-sulphoglucosamine sulphohydrolase; sulphamidase; SGSH) hinders the transport and degradation of its substrate, heparan sulphate (HS), leading to its cellular accumulation and the subsequent development of cellular, tissue, bone abnormalities, and eventual multisystem dysfunction (Neufeld, 1989).

Whilst enzyme deficiency is regarded as the primary cause of MPS IIIA, the molecular and cellular basis of symptoms remains unknown. Previous studies have reported negligible cellular loss during symptom onset in the brains of animal models affected by a mucopolysaccharide disorder, suggesting more discrete alterations are occurring to

neuronal structure and function (Li et al, 2002; Wilkinson et al, 2012; Beard et al., 2017). Progressive neurological dysfunction is associated with the majority of the mucopolysaccharidoses; clinically, this presents as delayed development, hyperactivity, aggressive behaviour, and reduced learning ability; death generally occurs in the second- to third decade of life (Bax and Colville, 1995; Meyer et al., 2007; Ruijter et al., 2008).

This literature review introduces lysosomes and the various disorders that result from lysosomal dysfunction, particularly the mucopolysaccharidoses. It discusses the neuropathology in LSDs, specifically at the synaptic level, in addition to the effects of neuroinflammation in the brain, and past and present therapeutic strategies for the mucopolysaccharidoses. Collectively, it highlights the established and emerging knowledge on potential mechanisms underlying symptom development in MPS IIIA, ultimately addressing the knowledge gap concerning altered neuronal structure and functionality in disease pathogenesis.

1.2 The Lysosome

The lysosome is an enzyme-filled organelle located in most animal cells that is responsible for degrading various biomolecules, including carbohydrates, proteins, and lipids. Lysosomes are involved in many processes, including cellular homeostasis, cellular metabolism, plasma membrane repair, tissue remodelling, pathogen defence, cell signalling, cell migration and adhesion, and cell death (reviewed in Ballabio and Bonifacino, 2020). The overall function of lysosomes hinges on the efficacy of soluble lysosomal enzymes (including acid hydrolases) and lysosomal membrane proteins. The degradation process within the lysosome occurs at an acidic pH of 4.6-5.0 due to proton-pumping vacuolar ATPases (Mellman et al., 1986). Substrates designated for degradation are transported to the lysosome via the endocytic, autophagic and phagocytic membrane-trafficking pathways. The mechanisms of these trafficking pathways that contribute to lysosomal formation are disputed and varied. They include maturation of vesicles into lysosomes, vesicular transport from endosomes to lysosomes, cycling and continual contact whilst transferring substrate (‘kiss-and-run’), and fusion of the lysosome with endosomes, phagosomes and autophagosomes (Fig 1.1; reviewed in Trivedi et al., 2020).

1.2.1 The Endo-Lyso-Autophagosomal Pathways

The degradative transport pathways are crucial for maintaining cellular homeostasis and removing unwanted cellular components. Engulfment of biomolecules via endocytosis necessitates transfer to the lysosome for removal and recycling. Late endosomes and lysosomes fuse via the recruitment of multiple proteins, including the GTPase Rab7, vacuolar protein sorting-associated protein (VPS) 18, VPS39, and pleckstrin homology domain-containing protein family member 1 (PLEKHM1) (Fig 1.2A; reviewed in Trivedi et al., 2020).

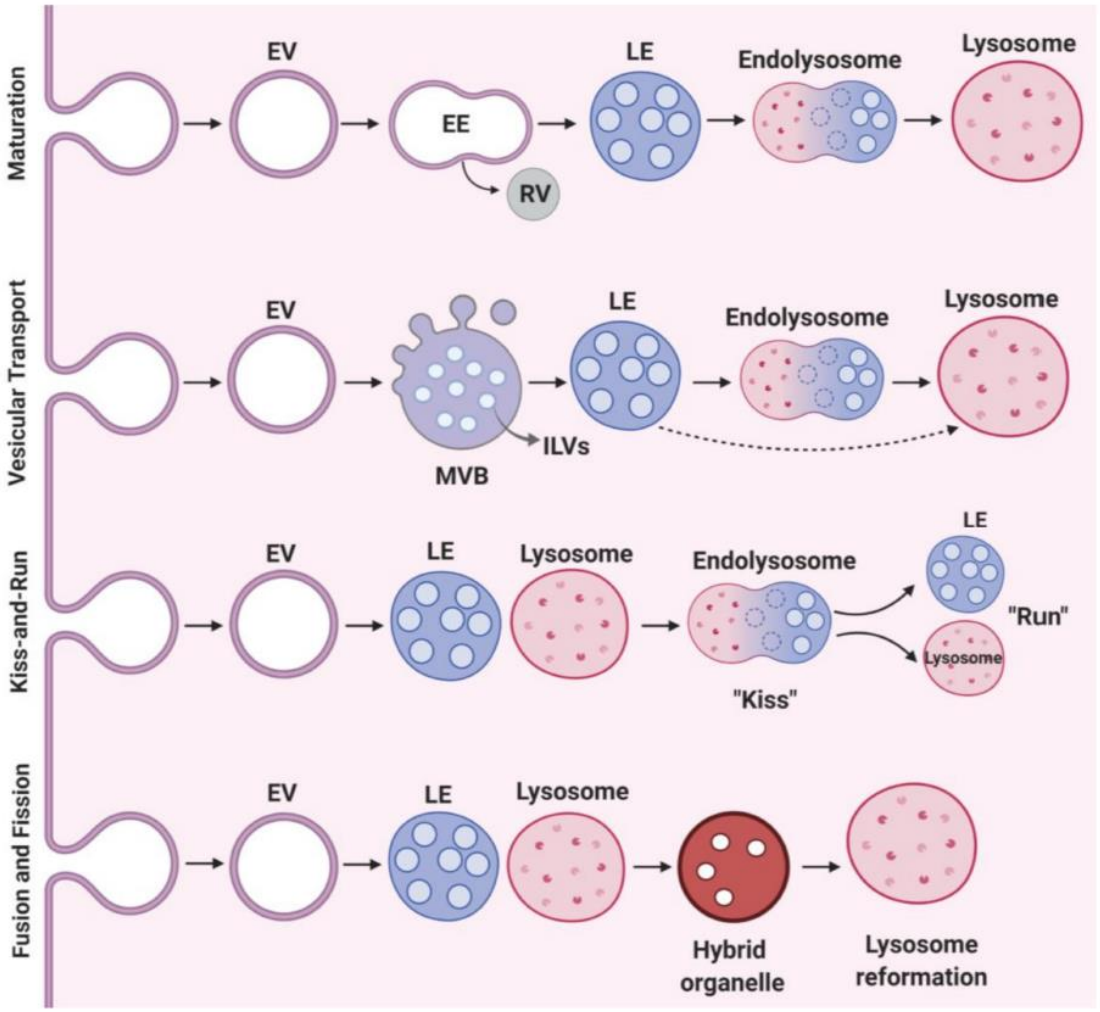


Figure 1.1 – Trafficking pathways to the formation of lysosomes. An illustration of the currently proposed mechanisms in which endocytic vesicles derived from the plasma membrane transport cargo to and from the lysosome. EE, early endosome; EV, endocytic vesicle; ILV, intraluminal vesicles; LE, late-endosome; MVB, multi-vesicular bodies; RV, recycling vesicles. Trivedi et al. (2020).

The fusion of lysosomes with autophagosomes also contributes to macromolecule degradation (primarily intracellular protein turnover) through the process of autophagy and formation of autophagosomes (Parzych and Klionsky, 2014). During periods of cellular starvation and stress, autophagy is initiated, particularly through the mechanistic target of rapamycin (mTOR), which facilitates engulfment of damaged cellular components, entailing turnover within the lysosome (Jung et al., 2020). The subsequent fusion process occurs effectively with successful transport of both lysosomes and autophagosomes to the perinuclear region within the cell (Morelli et al., 2004; Feng et al., 2010), which is triggered by an increase in intracellular pH during starvation (Johnson et al., 2016). As illustrated in Figure 1.2 (B), the autophagosome interacts through the homotypic fusion and vacuole protein sorting (HOPS) complex, Rab7, and PLEKHM1 (Trivedi et al., 2020). Inhibition of PLEKHM1 has been shown to fail to activate autophagy when halting mTOR activity (McEwan et al., 2015). Lastly, the trans-Soluble N-ethylmaleimide-sensitive factor Attachment protein REceptor (SNARE) complex also induces autophagosome-lysosome fusion through formation of STX17-VAMP8-SNAP29 (Jia et al., 2017).

1.2.2 Mannose-6-Phosphate Receptors

In addition to transporting degradative substrates, vesicular transport also facilitates lysosomal function. The lysosomal components of more than 50 soluble enzymes and 120 membrane proteins are synthesised within the endoplasmic reticulum (ER) and transported via vesicles to the Golgi apparatus (Braulke and Bonifacino, 2009). Upon arrival, the proteins are modified with the addition of sugar or mannose residues.

Additional phosphate groups to the mannose residues form mannose 6-phosphate (M6P) residues by the action of *N*-acetylglucosaminyl-1-phosphotransferase and *N*-acetylglucosamine-1-phosphodiester α *N*- acetylglucosaminidase (Lazzarino and Gabel, 1989). The M6P residues are then recognised in late Golgi compartments by type I transmembrane glycoprotein M6P-specific receptors (MPRs), which is the cation-

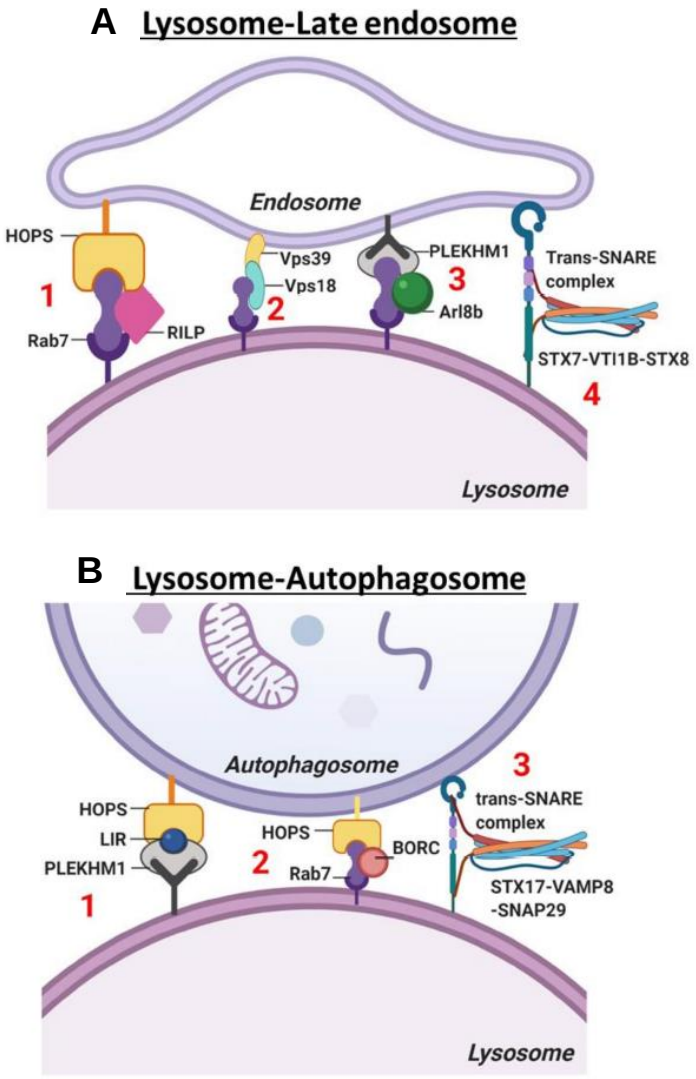


Figure 1.2 – Organelle fusion with lysosomes during endocytosis and autophagy. An illustration of endosomal and autophagosomal fusion with the lysosome to facilitate macromolecule degradation and maintenance of cellular homeostasis. Ar18b; Arf-like; BORC, BLOC-1 related complex; HOPS, homotypic fusion and vacuole protein sorting; LIR, LC3-interacting region; PLEKHM1, pleckstrin homology domain-containing protein family member 1; RILP, Rab7-interacting protein; SNAP, synaptosomal-associated protein; SNARE, soluble N-ethylmaleimide-sensitive factor attachment protein receptor; STX, syntaxin; VAMP, vesicle-associated membrane protein; VPS, vacuolar protein sorting-associated protein; VTI1B, VPS10 tail interactor-1B. (Trivedi et al., 2020).

dependent MPR46 and cation-independent MPR300 (Braulke and Bonifacino, 2009). Together, the MPRs target and mediate the transfer of newly synthesised lysosomal proteins containing M6P residues from the secretory pathway and the trans-Golgi network, to fuse with endosomal structures and then transport to the lysosome (van Meel and Klumperman, 2008). During transport, the enzymes are contained within vesicles and released into the late endosome when the pH falls to approximately 6.0. When the pH falls further to lysosomal-like levels of pH 5.0 during the final stages of maturation, the enzymes start to digest intracellular materials (Coutinho et al., 2012). Thus, whilst not directly involved with the sorting of lysosomal membrane proteins, MPRs are vital to the facilitation of functional lysosomal enzymes via transportation along the endo-lysosomal pathway. Changes to these trafficking and degradative pathways, and therefore to overall lysosomal function, have severe impacts on the health of the cell, and can manifest as a complete systemic disease.

1.3 Lysosomal Storage Disorders

LSDs were first defined pathologically by De Duve (1957), who discovered lysosomes as organelles involved in the digestion and recycling of waste. In 1963, Hers and others discovered the first LSD, Pompe disease, when a deficiency in the lysosomal enzyme α-glucosidase was found to be the cause of clinical symptoms in an infant who presented to Dr Joannes Pompe in 1932 (Hers, 1963). To the present, approximately 70 LSDs have been identified (Platt et al., 2018). Whilst they are individually defined as rare, LSDs have a collective incidence varying from one case in every 4,000 to 9,000 live births (Meikle et al., 1999; Giugliani et al., 2017; Platt et al., 2018). This number may vary further as diagnostic networks are increasingly developed and utilised (Giugliani et al., 2017). LSDs are monogenic diseases, with the majority being inherited through autosomal recessive mutations. LSDs often present as paediatric neurodegenerative diseases, with accompanying symptoms and effects to other organ systems (e.g. skeleton, soft tissues) depending on the specific genetic defect and substrate storage. When the genes encoding lysosomal function are mutated, there is a reduction in the efficacy of the degradative pathway. Substrate transported to the lysosome is only partially degraded, leading to accumulation of primary substrate within the lysosome, engorging the organelle and the cell (Neufeld, 1989). The LSDs are classified into major classes depending on the location of the genetic mutation and type of substrate accumulated or lysosomal defect (summarised in Table 1.1). Whilst basic classification of LSDs occurs by accumulation of a single primary substrate, the continual presentation of patients and the study of various disease models has revealed the heterogenous nature of substrate storage, and increased pathological complexity with multi-organ and -tissue deterioration (Sharma et al., 2018).

Table 1.1 – **Lysosomal storage disorders (continued).** Disorders of the lysosome, and lysosome-related organelles (Platt et al., 2018).

Lysosomal Storage Disorder	Mutated Lysosomal Enzyme	Primary Substrate/Defect
Mucopolysaccharidoses (MPS)		
MPS I (Hurler's syndrome) (infantile-onset)	α-L-iduronidase	heparan/dermatan sulphate
MPS IS (Scheie syndrome) (juvenile-onset)	α-L-iduronidase	heparan/dermatan sulphate
MPS II (Hunter's syndrome)	iduronate-sulphatase	heparan/dermatan sulphate
MPS IIIA (Sanfilippo syndrome A)	heparan N-sulphamidase	heparan sulphate
MPS IIIB (Sanfilippo syndrome B)	α-N-acetylglucosaminide	heparan sulphate
MPS IIIC (Sanfilippo syndrome C)	heparan-α-glucosaminide N-acetyltransferase	heparan sulphate
MPS IIID (Sanfilippo syndrome D)	N-acetylglucosamine 6-sulphatase	heparan sulphate
MPS IIIE (Sanfilippo syndrome E)	Arylsulphatase G	heparan sulphate
MPS IVA (Morquio A)	galactosamine-6-sulphate sulphatise	keratan/chondroitin 6-sulphate
MPS IVB (Morquio B)	β-galactosidase	keratan sulphate
MPS VI (Maroteaux-Lamy syndrome)	arylsulphatase B	dermatan sulphate
MPS VII (Sly disease)	β-glucuronidase	heparan/dermatan/chondroitin 4,6-sulphate
MPS IX (Natowicz syndrome)	hyaluronidase	hyaluronic acid
Mucolipidoses (ML)		
ML I (Sialidosis): Type I	Neuraminidase-1	sialyloligosaccharides
ML I (Sialidosis): Type II	Neuraminidase-1	Sialyloligosaccharides, LAMP1, and APP
ML II α/β (I-cell disease) (infantile)	N-acetylglucosamine-1-phosphotransferase	oligosaccharides and lipids
ML II α/β (Pseudo-Hurler polydystrophy) (juvenile)	N-acetylglucosamine-1-phosphotransferase	oligosaccharides and lipids
ML III γ (Pseudo-Hurler polydystrophy) (late-juvenile)	N-acetylglucosamine-1-phosphotransferase	oligosaccharides and lipids
ML IV (Sialolipidosis)	mucolipin I	lipids
Sphingolipidoses		
GM1 gangliosidosis	β-galactosidase	GM1 gangliosides
GM2 gangliosidosis Type I (Tay-Sachs disease)	β-hexosaminidase A	GM2 gangliosides
GM2 gangliosidosis Type 2 (Sandhoff disease)	β-hexosaminidase B	GM2 gangliosides
GM2 gangliosidosis (GM2 activator deficiency)	GM2 ganglioside activator protein	GM2 gangliosides
Niemann-Pick Type A and B	sphingomyelinase	sphingomyelin
Niemann-Pick Types C1 and C2	NPC1/NPC2	cholesterol/glycolipids
Gaucher's disease: Type I, Type II, Type III	glucocerebrosidase	glucocerebrosides
Farber's disease	ceramidase	lipids
Fabry's disease	trihexosylceramide α-galactosidase	glycolipids
Metachromatic leukodystrophy	arylsulphatase A	sulphatides
Mucosulphatidosis	sulphatase-modifying factor-1	sulphatises
Krabbe's disease	galactocerebrosidase	galactocerebroside

Table 1.1 – Lysosomal storage disorders (continued).

Lysosomal Storage Disorder	Mutated Lysosomal Enzyme	Primary Substrate/Defect
Oligosaccharidoses		
Galactosialidosis	cathepsin A	Sialyloligosaccharides and LAMP2
α-Mannosidosis	α-mannosidase	mannose and oligosaccharides
β-Mannosidosis	β-mannosidase	mannose and oligosaccharides
Fucosidosis	α-fucosidase	fucose
Aspartylglucosaminuria	aspartoglucosaminidase	glycoasparagine
Schindler disease Type I (infantile-onset)	α-N-acetylgalactosaminidase	oligosaccharides
Schindler disease Type II (Kanzaki disease)	α-N-acetylgalactosaminidase	oligosaccharides
Schindler disease Type III (intermediate severity)	α-N-acetylgalactosaminidase	oligosaccharides
Neuronal Ceroid Lipofuscinoses		
CLN1 (Haltia-Santavuori disease)	palmitoyl-protein thioesterase 1	lipidated thioesters and saposins A and D
CLN2 (Jansky-Bielschowsky disease)	tripeptidyl peptidase 1	subunit C of mitochondrial ATP synthase
CLN3 (Batten-Spielmeyer-Sjogren disease)	battenin	subunit C of mitochondrial ATP synthase
CLN4 (Parry disease; Kufs Type A and B)	cysteine string protein	subunit C of mitochondrial ATP synthase
CLN5 (Finnish variant)	ceroid-lipofuscinosis neuronal protein 5	subunit C of mitochondrial ATP synthase
CLN6 (Lake-Cavanagh or Indian variant)	transmembrane ER protein	subunit C of mitochondrial ATP synthase
CLN7 (Turkish variant)	major facilitator superfamily domain containing 8	subunit C of mitochondrial ATP synthase
CLN8 (northern epilepsy)	CLN8	subunit C of mitochondrial ATP synthase
CLN9 (rapid course)	battenin	subunit C of mitochondrial ATP synthase
CLN10	Cathepsin D	Saposins A and D
CLN11	granulin	Unknown
CLN12 (Kufor-Rakeb syndrome)	Cation-transporting ATPase 13A2	Inorganic cations
CLN13	Cathepsin F	Unknown
CLN14	Potassium channel tetramerization domain containing 7	Unknown
Others		
Glycogen storage disease type II (Pompe disease)	α-glycosidase	glycogen
Salla disease	sialin	sialic acid
Wolman disease	lysosomal acid lipidase	cholesterol esters
Cystinosis	cystinosin	cystine
Danon disease	LAMP-2	cytoplasmic debris and glycogen
Action myoclonus-renal failure syndrome	LIMP-2	unknown

1.3.1 Diagnosis of Lysosomal Storage Disorders

To assist with screening and diagnosis of LSDs, elevations in substrate levels have generally been measured in various biological samples such as urine, blood, skin, and cerebrospinal fluid (CSF), with dried blood spots becoming the primary sample type more recently (Suzuki, 1978; Gelb, 2018). If low enzyme activity is detected in combination with elevated substrate, genetic testing using DNA sequencing can confirm the specific mutation (Platt et al., 2018). However, genetic variability may present difficulty in diagnosis if the specific mutation has not been previously recorded, particularly when attempting to correlate with a phenotype (Schielen et al., 2017). Presentations of disease phenotype later in life help to correlate results with a definitive diagnosis. However, to ensure any feasible treatment is at its maximum effectiveness, diagnosis must still occur as early as possible (Donati et al., 2018). This is particularly relevant for LSDs which affect neurological function.

Whilst clinical presentations are not generally evident in infants, the earliest screening can possibly occur for maximum treatment impact is prenatally or in newborns. Prenatal screening is sought after by families with existing affected children and can include *in vitro* fertilisation with pre-implantation genetic diagnosis. However, it is expensive, is not available world-wide, and is not always successful (Platt et al., 2018). The process of newborn screening is becoming more prevalent and encompassing a wider range of disorders. This is increasingly and initially facilitated by analysing proteins and substrates in dried blood spots through tandem mass spectrometry (MS/MS) and fluorometric assays (Millington et al., 1990; Chamoles et al., 2001; Gelb, 2018). The multiplex MS/MS technique presents a high-throughput method of quantifying multiple markers simultaneously (Li et al., 2004). More recently, it has been noted that false positives are

often reported through newborn screening for LSDs. Therefore, a new approach has been developed utilising pattern matching statistical analysis incorporated with assays of enzyme activity and biomarker levels (Gelb, 2018). The new method has also been shown to be more powerful than genotype analysis. Thus, with these recent advances, these methods are assisting in the diagnosis of LSDs early in life with greater accuracy, which is particularly important when considering treatment for the early-onset and rapidly progressing disorders, including the mucopolysaccharidoses.

1.4 The Mucopolysaccharidoses

The mucopolysaccharidoses comprise approximately 30% of all LSDs (Muenzer, 2011). There are eleven currently identified variants of lysosomal enzyme deficiency which contribute to the seven different disorders classified as the mucopolysaccharidoses (mucopolysaccharidosis (MPS) types I, II, III, IV, VI, VII, and IX). The mucopolysaccharide disorders were identified with the case description by Hunter (1917) of two brothers who presented with symptoms including coarse facial features, large abdomen, and bone dysplasia, which later became known as Hunter syndrome (MPS II). Several years later, two unrelated males were identified by Dr Gertrude Hurler (Hurler, 1920; Hurler syndrome, MPS I) with a similar clinical presentation; Scheie syndrome is the more attenuated form of MPS I and was identified in a patient with the same lysosomal enzyme deficiency who presented differently with clouding of the cornea (Gifford et al, 1962).

Sanfilippo syndrome (MPS III) was first described by paediatrician Sylvester Sanfilippo in eight children who exhibited mental impairment and hepatosplenomegaly (Sanfilippo et al., 1963). Morquio syndrome (MPS IV) was identified from case reports by Morquio (1929) and Brailsford (1929), who described a condition of skeletal dystrophy without organomegaly or cognitive impairment. A similar skeletal condition was separately identified with excessive excretion of urinary chondroitin sulphate without cognitive impairment (MPS VI, Maroteaux-Lamy syndrome) (Maroteaux et al, 1963). Sly et al (1973) reported the first case of MPS VII in a patient with coarse facial features, hernias, skeletal abnormalities, organomegaly, and mental impairment. The first case of MPS IX was identified by Natowicz et al (1996) in a patient with short stature, and skeletal and joint abnormalities.

The accumulating substrates in the mucopolysaccharidoses (Table 1.1) are components of connective tissue known as mucopolysaccharides or glycosaminoglycans (Neufeld and Muenzer, 2001). The enzymes involved in the mucopolysaccharidoses are involved in the step-wise degradation of HS, either individually or together (MPS-I, -II, -III, -VII), dermatan sulphate (MPS-I, -II, -VI, -VII), keratan sulphate (MPS IVB), chondroitin sulphate (MPS-IVA, -VI) and hyaluronic acid (MPS IX).

1.5 Sanfilippo Syndrome (MPS III)

Sanfilippo syndrome (MPS III) comprises a group of five neurodegenerative LSDs (MPS-IIIA, -IIIB, -IIIC, -IIID, -IIIE) which result from the deficiency in one of five lysosomal enzymes responsible for the step-wise degradation of HS (Figure 1.3) (Scott et al, 1995; Weber et al., 1996; Kowalewski et al., 2012). Any of these enzyme deficiencies result in the primary accumulation of HS in affected patients (Table 1.1). MPS IIIE has been identified in animal models but has yet to be reported in a human patient (Kowalewski et al., 2012). Within Australia, MPS IIIA has the highest incidence at 1 in 128,000 live births, followed by MPS IIIB (1 in 235,000), MPS IIIC (1 in 1.4 million), and MPS IIID (1 in 1.1 million) (Meikle et al., 1999). Collectively, MPS III is the most prevalent of the MPS disorders in Australia, with an incidence of approximately 1 in 66,000 live births (Meikle et al., 1999).

MPS IIIA is the primary focus of this study and is caused by an autosomal, recessively inherited mutation in the N-sulphoglucosamine sulphohydrolase gene located on chromosome 17q25.3 encoding lysosomal SGSH (EC 3.10.1.1) (Kresse and Neufeld, 1972; Scott et al, 1995; Lee and Kamitani, 2001; Muenzer, 2011). SGSH functions by cleaving N-sulphate groups from the non-reducing ends of HS (Fig 1.3; Schmidt et al., 1977). As a result of this mutation, zero or dysfunctional protein is produced, leading to a deficiency of enzyme activity and subsequent storage of HS (Neufeld and Muenzer, 2001; Valstar et al., 2008).

Whilst enzyme deficiency occurs in the majority of cells the brain is the primary site of pathology and MPS IIIA patients primarily present with progressive neurological

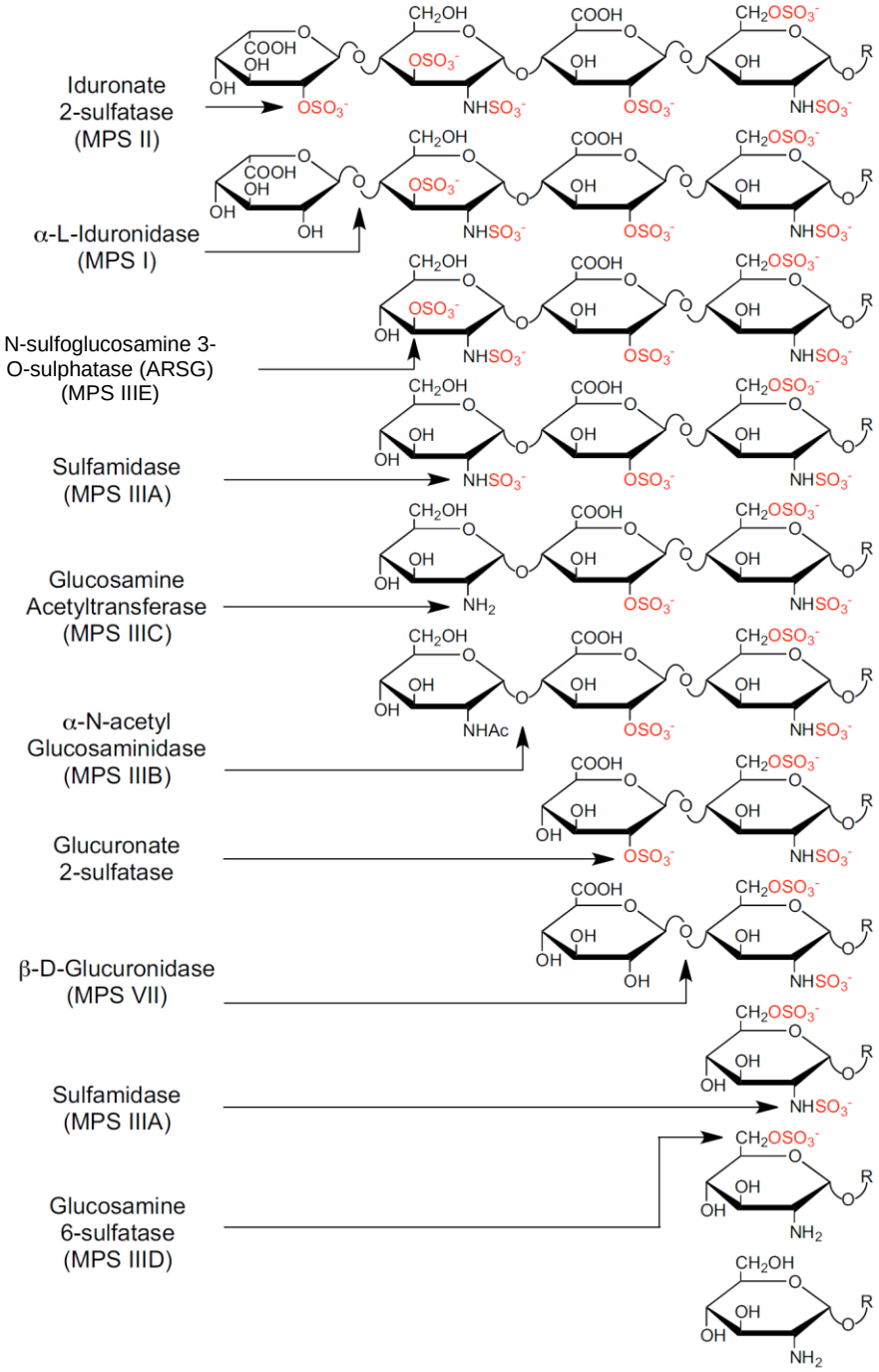


Figure 1.3 – The process of heparan sulphate (HS) degradation. The step-wise degradation of (HS). Each MPS disorder is indicated by its respective enzyme deficiency at its required location in the process. (Kowalewski et al., 2012).

symptoms. Initially, this manifests as delays in cognitive development, generally between one- and four-years of age; behavioural difficulties (such as aggression and hyperactivity), sleep disturbance and progressive cognitive decline develop with loss of motor function from three- to four-years of age. The final symptomatic stage varies with age, but includes feeding and aspiration problems, and usually eventuates in death due to inanition during the teenage years (Cleary and Wraith, 1993; Neufeld and Muenzer, 2001; Valstar et al., 2011; Shapiro et al., 2018). The median age of death is 18 years (Valstar et al., 2011).

To document the physical development of MPS III patients over the disease course, a natural history study was conducted on a cohort of 182 German patients (Muschol et al., 2019). It was discovered that while individual body height, weight, and head circumference were within the normal physiological ranges at birth, by two-years of age MPS III patients were significantly taller. By four-years of age, only male patients remained taller, and growth velocity decreased after the ages of 4.5- to five-years for all patients. By the age of 17.5-years, both males and females were significantly shorter than the reference group. Head circumference was larger by two-years of age in MPS III patients, and remained larger into physical maturity (Muschol et al., 2019).

Cardiac abnormalities are reported to contribute to early mortality in MPS I and II patients, so a one-year natural history study of MPS III patients was conducted to assess cardiac function (Wilhelm et al., 2018). Twenty-five patients were enrolled (15 MPS IIIA and 10 MPS IIIB), and underwent 45 echocardiograms to assess anatomic, valvular, and functional abnormalities. Sixty-percent of all patients presented with an initial abnormal echocardiographic result at an age of 6.8 ± 2.8 years. Throughout the study, left-sided valve abnormalities were commonly reported over time, including: seven patients with mitral valve thickenings; two with mitral valve prolapses; eight with mild mitral

regurgitation and eight with trivial mitral regurgitation; three with aortic valve thickenings, seven with mild aortic regurgitation; and two with trivial aortic regurgitation. Despite this array of noted abnormalities, the patients presented with only mild progression of abnormalities during a follow-up, and none required intervention (Wilhelm et al., 2018).

Evidence of central nervous system (CNS) pathology in MPS III has brought about characterisation of cognitive changes and brain size over the course of disease. In a study of MPS IIIB, nearly all 19 patients showed a decline in cognition, adaptive behaviour, and cortical grey matter volume, even with the wide age range of 1.6- to 31.7-years (Whitley et al., 2018). Patients diagnosed at younger ages exhibited a stronger decline in measurements. Additional assessments into cognitive function showed that MPS IIIA and MPS IIIB patients recorded similar outcomes on the Autism Diagnostic Observation Schedule (Shapiro et al., 2016). The similar outcomes recorded were social communication, playfulness, excessively intense interests and repetitive behaviours. MPS IIIA patients, however, expressed lower levels of fear and attention when compared with MPS IIIB patients (Shapiro et al., 2016).

Natural history studies have also been conducted in Taiwan where clinical information was lacking (Lin et al., 2018). A study of three MPS IIIA, 23 MPS IIIB, and two MPS IIIC patients with a median age of 8.2-years (range of 2.7- to 26.5-years) was conducted. Records for this study were collected between 1996-2017 from patient visits to medical centres across Taiwan. The median age of diagnosis was 4.6-years, and initial symptoms were most commonly speech delay (75% of patients), excess body hair (hirsutism; 64% of patients), and hyperactivity (54% of patients). The most common clinical manifestations were speech delay (100%), intellectual disability (100%), hirsutism (93%), hyperactivity (79%), coarse facial features (68%), sleep disorders (61%), and hepatosplenomegaly (61%)

(Lin et al., 2018). By the conclusion of the study, seven of the 28 patients had died, with a median age of death of 13-years. MPS IIIB was determined to be the most common MPS III sub-type in the Taiwanese population (Lin et al., 2018).

A one-year prospective natural history of 15 North American MPS IIIA children (aged 5 ± 1.9 years) found cognitive function peaked at the developmental age of 2.5- to three-years, and then deteriorated significantly over a six-month period (Truxal et al., 2016). Adaptive behaviour was reported by parents of the children in the form of an interview using the Vineland Adaptive Behaviour Scales II (Vineland-II) which accounts for communication, daily living skills, socialisation, and motor skills. Cognitive function was found to inversely correlate with age of the children, and significantly declined over six-month intervals (Truxal et al., 2016). Magnetic Resonance Imaging (MRI) of the liver and spleen found significantly enlarged volumes when compared to controls but these parameters did not change significantly during the six-month-long study. MRI of the brain revealed enlargement of the ventricles and loss of cortical volume in all reported patients.

A separate prospective natural history study of North American MPS IIIA patients aimed to characterise the clinical course of the disease in children over a span of two-years (Shapiro et al., 2016a). Of the 24 children enrolled in the study (ranging from approximately one- to 18-years of age), 19 presented a “rapidly-progressing” form, and five with a more “slowly-progressing” form. Categorisation was based on diagnosis occurring before (rapidly-progressing) or after (slowly-progressing) the age of six-years, and was found to be a suitable indicator of disease severity (Shapiro et al., 2016a). Children with the rapidly-progressing form plateaued in cognitive development by 30-months of age, then declined rapidly after 40- to 50-months. Cognitive development was measured by the Bayley Scales of Infant and Toddler Development (Third Edition) or the

Kaufman Assessment Battery for Children (Second Edition). A development quotient was derived and compared with age-equivalent scores from normative data and is shown in Figure 1.4. These same children also presented cortical grey matter atrophy associated with the decline. Slowly-progressing MPS IIIA children presented a similar yet more prolonged disease course. All patients showed enlarged liver and spleen to approximately double the normal size, and HS levels remained consistently elevated in the CSF and urine over time (Shapiro et al., 2016a).

A follow-up study on these 24 children occurred in 2018 to assess disease progress (Shapiro et al., 2018). The patients reported a low incidence of surgeries and hospitalisations, and showed behavioural difficulties subsiding towards the end stages of the disease. However, adaptive levels were very low, with children functioning below a two-year-old level when scored with the Vineland-II. One slowly-progressing patient was the only individual functioning above a three-year-old level, and parental burden had moved from behavioural to physical management for all patients (Shapiro et al., 2018). By the conclusion of the study, five rapidly-progressing patients had died (between the ages of eight- to 12-years), and one slowly-progressing patient also died (at age 21-years).

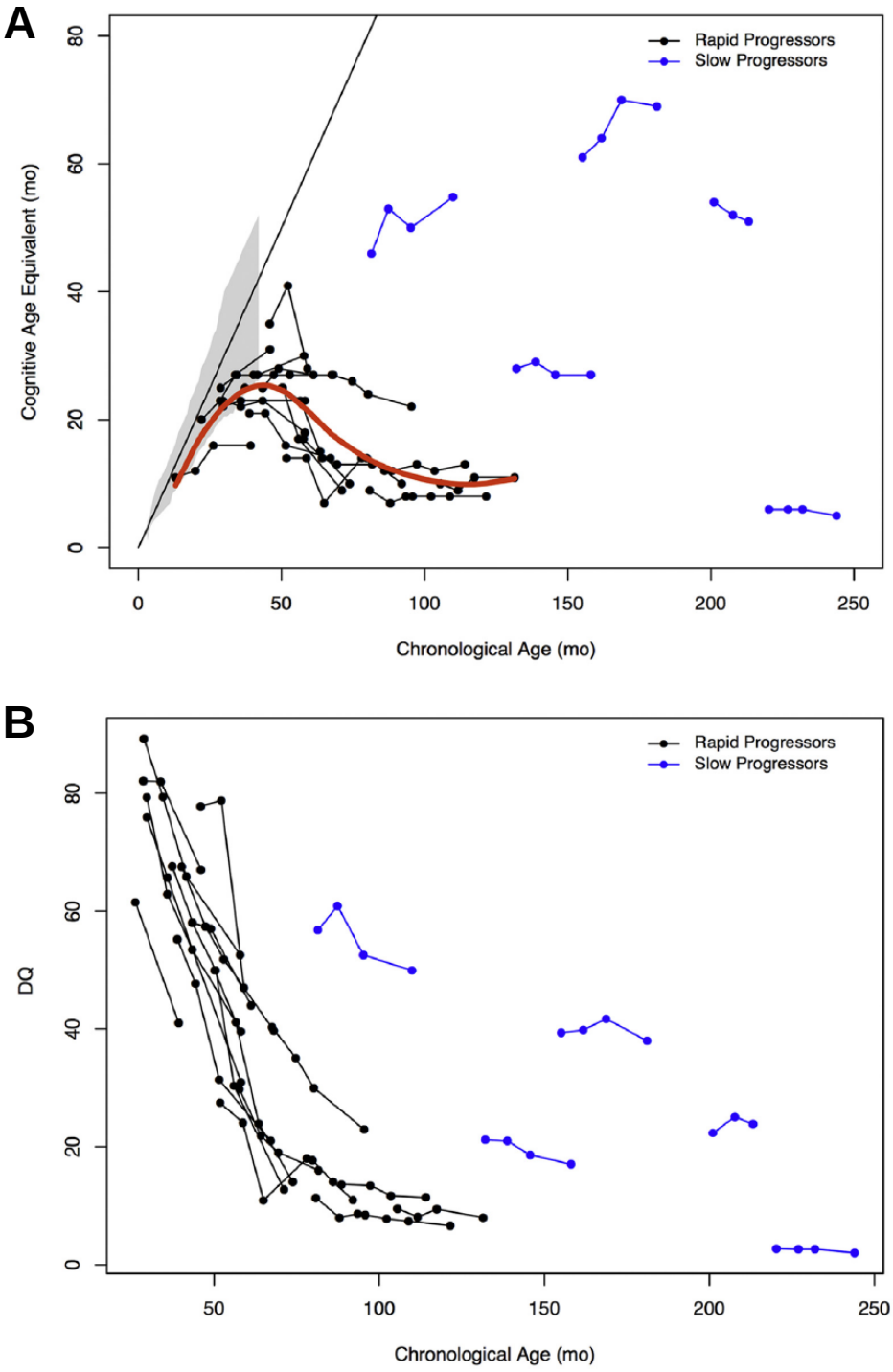


Figure 1.4 – Cognitive development in a natural history study of MPS IIIA. Trajectory of cognitive growth by age for rapid and slow progressors of MPS IIIA (A). Change in developmental quotient derived by comparison of age equivalent with chronological age (B). (Shapiro et al., 2016a).

1.6 Mucopolysaccharidosis Animal Models

MPS III has been described in a variety of large animal models where the disease is naturally occurring, including MPS IIIA in a Huntaway dog (Jolly et al, 2000) and a Dachshund dog (Fischer et al, 1998); MPS IIIB has been identified in a cow (Karageorgos et al, 2007), a pig (Yang et al, 2018), a Schipperke dog (Ellinwood et al, 2003), and an emu (Giger et al, 1997); and MPS IIID has been identified in a goat (Thompson et al, 1992). Smaller animal models that have been generated include the knockout MPS IIIA mouse (Lau et al., 2017); MPS IIIB knock-out mouse (Li et al, 1999); multiple MPS IIIC mouse models (Martins et al., 2015; Marco et al., 2016), and a recently generated MPS IIID mouse model (Roca et al, 2017).

In addition to these MPS IIIA models is the naturally occurring MPS IIIA mouse model, which has been extensively characterised and was the model utilised for this study. It was originally identified in a collaborative study between the Albert Einstein College of Medicine in New York, USA and the Lysosomal Diseases Research Unit at the Women's and Children's Hospital in Adelaide, Australia. It was first reported following the identification of a spontaneous (hence naturally occurring) mutation during attempts to produce a targeted mutation in the *Mgat3* gene by injecting blastocysts of CD1 mice (Bhaumik et al, 1999). An aged mouse was identified to have abnormal behaviour, and subsequent histological analysis revealed abnormal lysosomal pathology. Subsequent characterisation of the gene revealed the mutation as a single point mutation (G to A) at nucleotide position 91 (G91A), resulting in a change in amino acids from aspartic acid to asparagine (D to N) at position 31 (D31N) (Bhattacharyya et al, 2001). The D31N genetic mutation severely affects the catalytic function of the enzyme, resulting in significantly reduced SGSH activity.

The original MPS IIIA mouse exhibited a mixed genetic background, featuring the 129SvJ, CD1, C57BL/6, and SJL strains (Bhaumik et al., 1999; Bhattacharyya et al., 2001). To improve genetic stability and homogeneity in the murine progeny, the MPS IIIA mouse was back-crossed onto the C57BL/6 mouse strain (B6.Cg-Sgsh^{mps3a} ; Crawley et al., 2006). Congenic MPS IIIA mice exhibit a disease phenotype by approximately seven- to eight-weeks of age, with facial dysmorphism, dishevelled fur, hepatosplenomegaly, and an increasingly severe hunched posture with age (Crawley et al., 2006). The lifespan of the MPS IIIA mouse is up to approximately nine-months of age (Fu et al., 2016).

The original mixed MPS IIIA mouse strain exhibited hyperactivity at three-weeks of age followed by hypoactivity (Hemsley and Hopwood, 2005). Congenic MPS IIIA mice do not display early hyperactivity, however, hypoactivity is seen in the Open Field test by 12- to 15-weeks of age, and reduced anxiety is noted in the Elevated Plus Maze test, with a tendency to explore open arms more so than corresponding controls (Crawley et al., 2006; Lau et al, 2008). The absence of hyperactivity in congenic mice at three-weeks of age could be due to masking in the highly active C57BL/6 strain (Voikar et al., 2004; Crawley et al, 2006). Neuromuscular grip strength and negative geotaxis are affected in both strains as early as six-weeks of age, and the Morris Water Maze test reveals memory and spatial learning impairments by 20-weeks of age (Crawley et al, 2006).

The major histopathological feature in the MPS IIIA mouse is the primary accumulation of partially digested HS in most cells. Under normal conditions, HS interacts with cell surface proteins to modulate the surrounding area and bind with proteoglycans to elicit more precise cellular functions (Miller et al, 2014). Located within the nucleus, extracellular matrix, and cell membrane, proteoglycan-bound sulphated compounds are involved with cell proliferation, cell-cell recognition and adhesion, matrix formation, and cell-matrix

interactions (Fig 1.5; Kjellén and Lindahl, 1991; Schaefer, 2014; Lindsay et al., 2020). Heparan sulphate proteoglycans (HSPGs) and chondroitin sulphate proteoglycans (CSPGs) are located around and between the somas of neurons and glia within the CNS (Fig 1.5A). Within the plasma membrane and extracellular matrix, HSPGs and CSPGs interact with the amino acid residues of chemokines, cytokines, growth factors, proteases, adhesion molecules, and lipid-binding proteins to ultimately regulate cell signalling in a predominantly pro-regenerative manner (Fig 1.5B; Xu et al., 2018; Lindsay et al., 2020).

GM2 and GM3 gangliosides, which reside within the neuronal plasma membranes of the CNS, also accumulate in the MPS III brain (McGlynn et al., 2004; Breiden and Sandhoff, 2019). Moreover, the number of neurons containing engorged lysosomes, and the number of inclusions themselves, increases as the disease progresses (Fig 1.6; Crawley et al, 2006). Electron micrographs have shown vacuolar inclusions of HS within the soma of neurons at six- and 12-weeks of age (Savas et al., 2004), 18-weeks of age (Fraldi et al., 2007; Hemsley et al., 2007), six-months of age (Ohmi et al., 2003; Crawley et al., 2006) and eight-months of age (Wilkinson et al., 2012). Immunohistochemical lysosomal integral membrane protein-2 (LIMP-II) staining also highlighted lysosomal inclusions within neurons from four-weeks and up to 21-weeks of age (Hemsley et al., 2009; Hassiotis et al., 2014a), and storage of secondary substrates also including GM2-gangliosides (Fraldi et al., 2007) up to 10-months of age.

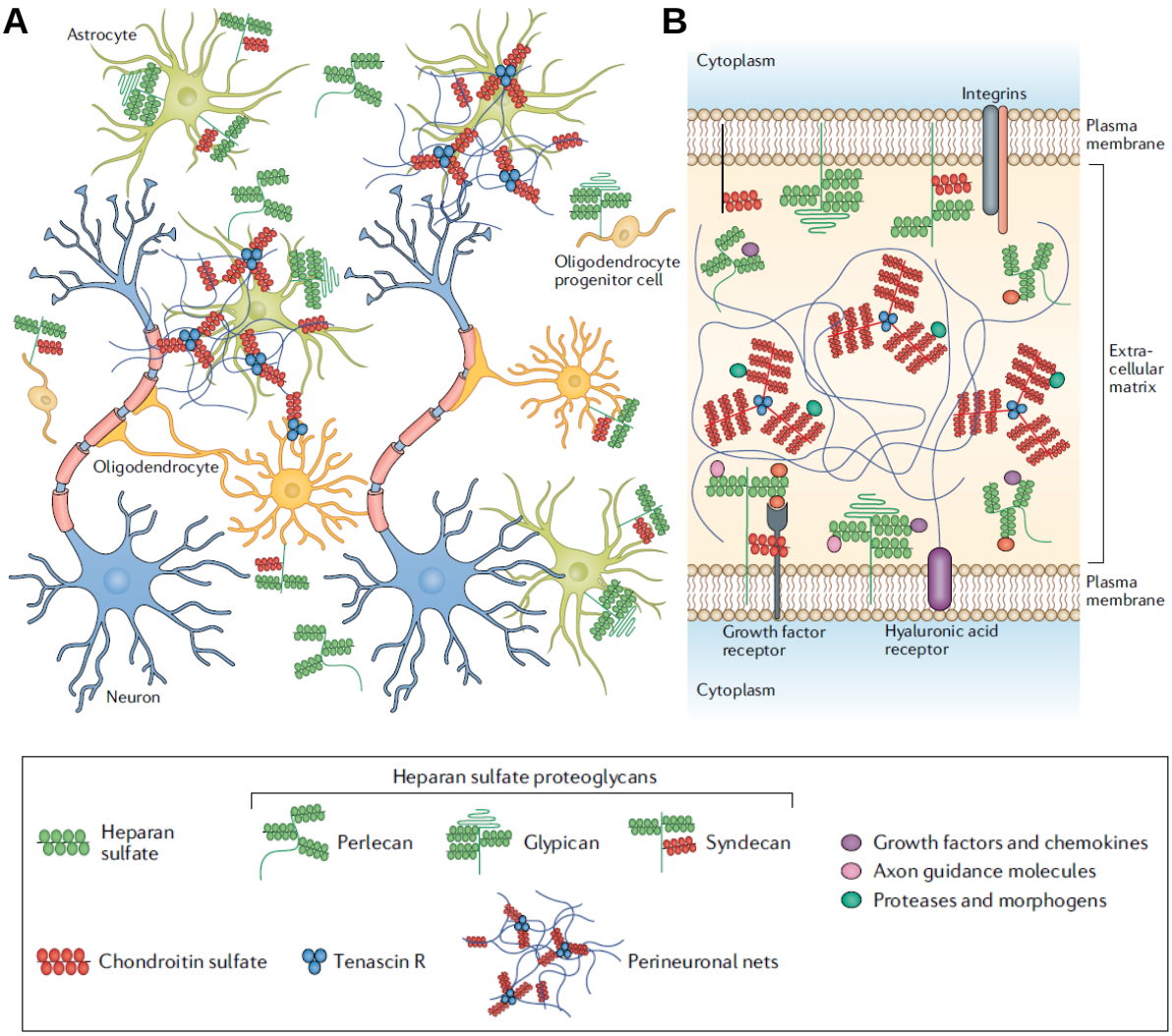


Figure 1.5 – **Heparan sulphate localisation in the CNS.** HSPGs and chondroitin sulphate are located around and between the cell bodies of neurons and glia within the CNS (A). HSPGs are located within the extracellular matrix and promote the binding of growth factors and chemokines (B). (Lindsay et al., 2020).

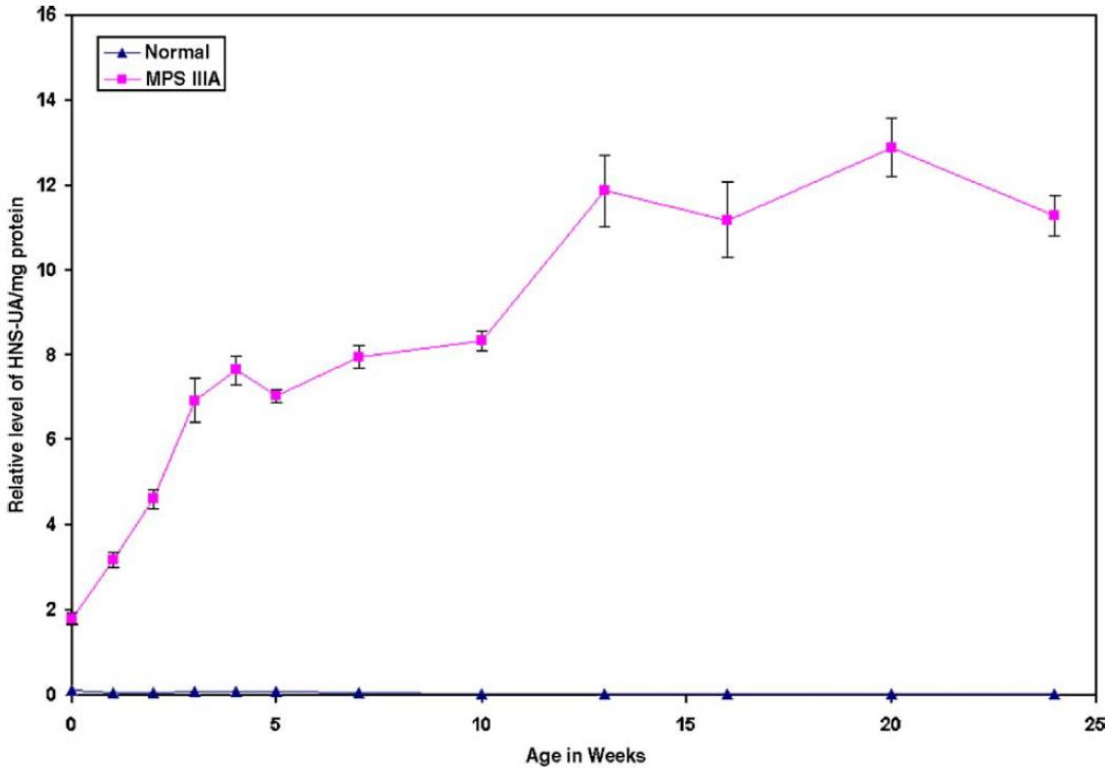


Figure 1.6 – **Heparan sulphate levels in the congenic MPS IIIA mouse.** HS levels in the brain of congenic MPS IIIA mice measured from birth to approximately 25-weeks of age. N=3/genotype/age. Data are mean ± SEM. (Crawley et al., 2006).

1.7 Therapeutic Approaches

Although some treatment strategies are available for several LSDs, there is no approved treatment for MPS III patients. Treatment approaches currently under evaluation for patients include bone marrow transplantation, gene therapy, enzyme replacement therapy, substrate reduction therapy, and chaperone therapy (Fig 1.7; Leal et al., 2020).

1.7.1 Symptom Management

For patients lacking the option of an effective treatment, particularly those with CNS pathology, supportive care measures are implemented to assist in symptom management (Table 1.2). These include access to physical, occupational, and speech therapists. Behavioural therapy, however, is unlikely to be effective, especially since any improvements are often lost with disease progression. The drug Risperidone has been considered for treatment of hyperactivity (Kalkan Ucar et al., 2010), whilst melatonin has been used to treat sleep disorders (Mahon et al., 2014). Assisting devices such as canes and wheelchairs are also used as the disorder progresses, alongside vitamin D supplements for low bone mineral densities (Nur et al., 2017). Due to the clinical complexity of these disorders, at present a combination of therapies and supportive care is necessary to manage symptoms.

1.7.2 Haematopoietic Stem Cell (Bone Marrow) Transplantation

Bone marrow transplantation was developed with the aim of providing a greater source of bone marrow-derived cells that would alleviate the enzyme deficiency in LSD patient cells. Bone marrow-derived cells are of the monocyte/macrophage lineage and their efficacy hinges on their ability to traverse the blood-brain barrier and subsequently

Table 1.2 – **Symptom management for MPS III.** Clinical manifestations in MPS III and the current methods of treatment. Adapted from Wagner and Northrup (2019).

Manifestation	Treatment
Seizures	Antiepileptic drugs as determined by neurologist
Neurodevelopmental delays	Supportive therapies (speech, occupational, physical)
Psychiatric / Behavioural issues	Treatment as determined by psychiatrist Creation of physically safe environment at home
Sleep disorders	Use of melatonin or other medication Polysomnogram if suspicion of sleep apnoea
Musculoskeletal	Treatment as determined by orthopaedist Physical therapy or hydrotherapy for joint stiffness Vitamin D therapy in the context of low bone mineral density
Hearing loss	Ear tube insertion or hearing aid use
Recurrent respiratory infections	Treatment as determined by otolaryngologist Airway clearance therapy, particularly in later disease stages
Cardiovascular anomalies	Treatment as determined by cardiologist
Feeding difficulties / malnutrition	Gastrostomy tube placement
Visual impairment	Treatment as determined by ophthalmologist
Palliative care	As per palliative care specialist

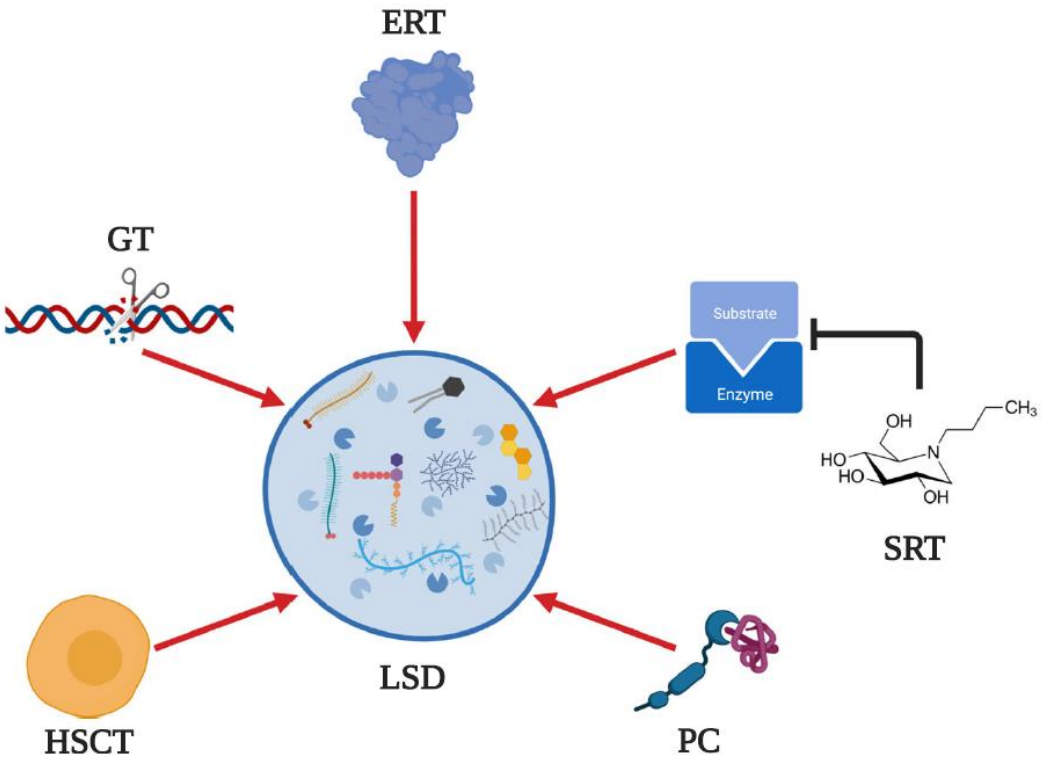


Figure 1.7 – Treatment strategies for LSDs. Illustrated are the current approaches in place to minimise the effects of accumulating substrate within the lysosomes of LSDs. ERT, enzyme replacement therapy; GT, gene therapy; HSCT, hematopoietic stem cell transplantation; LSD; lysosomal storage disorder; PC; pharmacological chaperones; SRT, substrate reduction therapy. (Leal et al., 2020).

differentiate into microglia, which are the primary macrophage cells of the brain (Hess et al., 2004). Donor cells carry the necessary genes for encoding the deficient enzyme into cells of the target organ system, where transduced cells subsequently secrete recombinant enzyme into the blood, CSF, and surrounding tissues. Enzyme-deficient cells then incorporate enzyme via MPRs of the endo-lysosomal pathway for effect (Fig 1.8; Sands and Davidson, 2006). Like most treatments, bone marrow transplantation offers the greatest success when patients are young (Poe et al., 2014). Exclusively, it is not currently deemed an effective treatment option for MPS III. Indeed, in pre-clinical studies on MPS IIIA mice, bone marrow transplantation struggled to arrest the clinical progression of disease and improve neuropathology despite penetration into the CNS (Lau et al., 2010). However, when used in conjunction with a lentiviral vector expressing SGSH, MPS IIIA mice showed a restoration of behavioural phenotype (Langford-Smith et al., 2012). The vector facilitates cross-correction of the haematopoietic stem cells to over-express the therapeutic enzyme (Aronovich and Hackett, 2015).

1.7.3 Enzyme Replacement Therapy (ERT)

ERT involves the administration of a recombinant form of the deficient lysosomal enzyme, which is incorporated into cells by endocytosis and then packaged into lysosomes through endosome and lysosome fusion to become functionally active. However, the blood-brain barrier prevents the uptake of the intravenously delivered enzyme into the brain, and thus does not effectively target the neuropathological features of LSDs (Desnick and Schuchman, 2012). Indeed, intravenous injection of SGSH into MPS IIIA mice at birth successfully ameliorated cognitive deficits but failed to effectively cross the blood-brain barrier after the neonatal stage (Gliddon and Hopwood, 2004). However, intrathecal injection of SGSH into the CSF normalised substrate storage

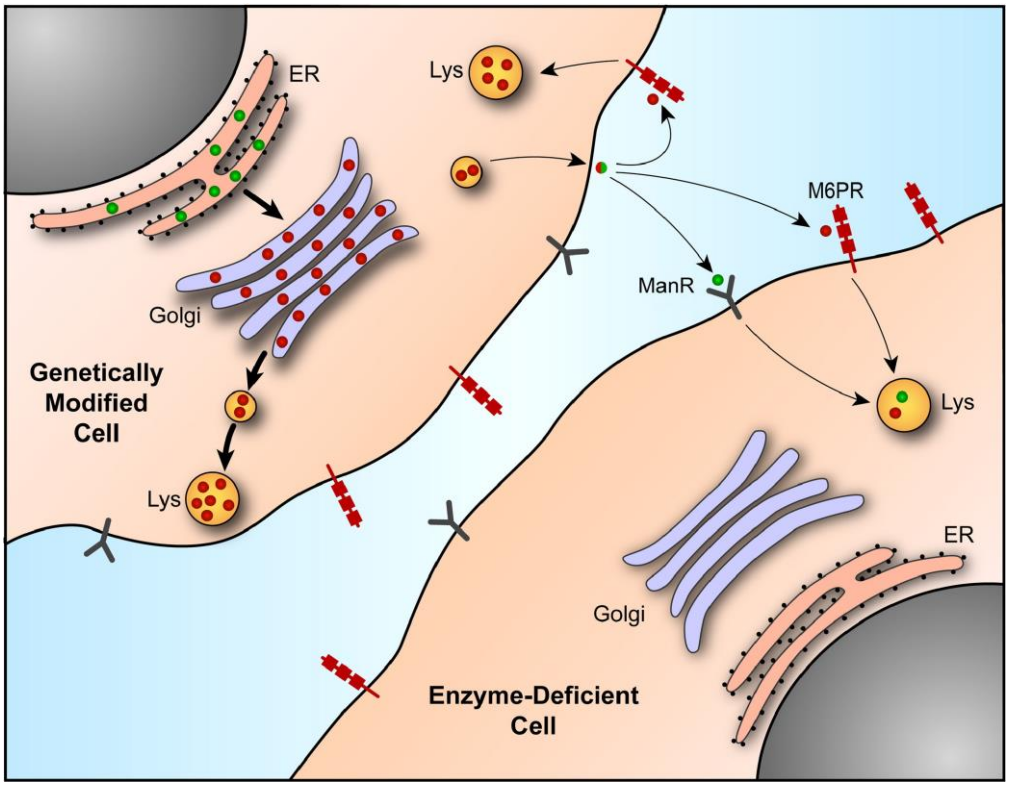


Figure 1.8 – Genetically modified therapeutic mechanism of action. Donor and gene therapies carry genes encoding the deficient enzyme into cells of an organ system where transduced cells secrete recombinant enzyme into the blood, CSF, and surrounding tissues. Enzyme-deficient cells subsequently incorporate enzyme through MPRs of the endo-lysosomal pathway. (Sands and Davidson, 2006).

in the CNS of MPS IIIA dogs (Hemsley et al., 2009), MPS IIIA mice (Beard et al., 2015; King et al., 2016), which has also successfully translated to human patients (Jones et al., 2016). Similar success with pathological amelioration has also been observed in the MPS IIIB mouse (Kan et al., 2014).

1.7.4 Substrate Reduction Therapy (SRT)

SRT utilises small molecules to block the synthesis of HS macromolecules within the lysosome, thereby slowing substrate accumulation (Aerts et al., 2006). Miglustat, the first SRT approved for human use, acts by inhibiting glucosylceramide synthase (the substrate that accumulates in the LSD Gaucher disease), thus halting the glucosylceramide synthesis pathway (Yue et al., 2019). An *in vitro* study on MPS IIIC patient fibroblasts showed a reversal of the disease phenotype through siRNA targeting of genes involved in HS synthesis (Canals et al., 2015). Genistein (a soy-derived isoflavone acting as a tyrosine kinase inhibitor) has also shown success at inhibiting HS synthesis, and thereby reducing HS accumulation in plasma and urine (de Ruijter et al., 2012). It blocks the epidermal growth factor plus additional growth factor receptors that together regulate the transcription of HS synthesis genes. A major benefit of genistein is it can reportedly cross the blood-brain barrier, thus making it a potential option for intravenous administration to MPS III patients (de Ruijter et al., 2012). Administration of genistein at low dosage did not, however, improve MPS III manifestations and therefore requires further testing at a higher dosage (de Ruitjer et al., 2012). Rhodamine B is an alternate small molecule of interest, administration of which ameliorated disease pathology in MPS I and MPS IIIA mice by inhibiting the formation of HS and dermatan sulphate (Derrick-Roberts et al., 2017).

1.7.5 Pharmacological Chaperone Therapy (PCT)

PCT is an approved treatment option for non-LSDs but remains under evaluation in MPS III. In the LSDs, this approach assists in restoring the natural folding and trafficking of the dysfunctional enzyme through the lysosome's degradative machinery to improve its efficacy (Hughes et al., 2017). A significant advantage of the smaller chaperones is that they can cross the blood-brain barrier without affecting their integrity to target the lysosomal enzymes in the CNS. Testing of pharmacological chaperones has expanded to target the neuropathology in MPS IIIC (Matos et al., 2014). To correct the aberrant folding of enzyme in MPS IIIC, use of a glucosamine chaperone was shown to partially recover the folding of the enzyme and its subsequent activity (Matos et al., 2014).

1.7.6 Gene Therapy

Recently, gene therapy has emerged as a less transient and more permanent therapeutic strategy to combat CNS pathology. As LSDs are genetic disorders, a functional copy of the gene encoding the deficient enzyme is utilised to target cells of any organ system (Sands and Davidson, 2006). Dosing frequency with gene therapy is lower compared with alternative LSD treatment approaches, including enzyme replacement therapy, because a smaller number of transduced cells are required to produce enough functional enzyme to be taken up by enzyme-deficient cells, as mediated by the MPRs (Haskins, 2007). Following delivery, the transduced cells secrete the recombinant enzyme into the blood, CSF, and surrounding tissues, which are then incorporated via the endo-lysosomal pathway, as described in Section 1.7.2 (Fig 1.7; Sands and Davidson, 2006; Platt et al, 2018). The viral vector can be in the form of an adeno-associated virus (AAV), canine adenovirus, lentivirus, or non-viral gene therapy (Aronovich et al, 2017). Lentiviral therapies have in fact reached the clinical trial stage for a few LSDs, including metachromatic leukodystrophy and Fabry disease (reviewed in Platt et al., 2018).

Multiple AAV serotypes, including AAV2/5, 4, 8, 9, and rh10 have been tested extensively in several MPS III animal models. AAV2/5 carrying N-acetyl-alpha-glucosaminidase (*NAGLU*) was injected into the intrastriatal putamen of MPS IIIB mice with successful reduction in lysosomal storage and improvement in behavioural outcomes (Cressant et al, 2004). *NAGLU* has also been administered to MPS IIIB mice intravenously via AAV9 and, with its ability to cross the blood-brain barrier, was able to restore enzyme levels and improve lysosomal pathology and behavioural outcomes in adult MPS IIIB mice (Fu et al, 2011). An additional trial utilising recombinant AAV2/5 encoding *NAGLU* in MPS IIIB children involved intraparenchymal injection (Tardieu et al., 2017). The study reported the prevention and slowing of cognitive decline, particularly when children were diagnosed at an early age (Tardieu et al 2017). Whilst AAV8 has reported enhanced transduction of *NAGLU* in MPS IIIB mice (Gilkes et al., 2016), AAV9 encoding *NAGLU* administered intravenously to MPS IIIB mice was reported with a near-complete correction of serum metabolite abnormalities (Fu et al., 2017).

AAV4 containing modified *SGSH* was intraventricularly administered to eight-week-old MPS IIIA mice and resulted in increased enzyme activity and improved behavioural outcomes (Chen et al, 2018). AAV2/5 carrying the therapeutic genes sulphatase modifying factor-1 (*SUMF1*) and *SGSH* has been intraventricularly injected into MPS IIIA mice and shown to reduce lysosomal storage and improve motor and cognitive function (Fraldi et al, 2007). AAV9 encoding *SGSH* has been injected into MPS IIIA mice via intra-CSF or intravenous delivery, and MPS IIIA dogs via intracisternal or intracerebroventricular delivery with successful elevation of SGSH activity (Ruzo et al, 2012; Haurigot et al, 2013). AAV9 was also administered intravenously to MPS IIIA mice, and when treated up to three-months of age, learning ability was improved and lifespan normalised (Fu et al, 2016). AAVrh10 carrying *SGSH* evaluated in pre-symptomatic MPS IIIA mice showed a

similar level of success in reducing lysosomal pathology through intraparenchymal administration (Winner et al, 2016). This same vector was also used in a phase I/II trial in MPS IIIA children, and indicated a moderate improvement in behaviour, attention, and sleep, with the youngest patient most likely to receive the greatest benefit (Tardieu et al, 2014). More recently, the AAVrh10 vector encoding *SGSH* has recorded success at ameliorating pathology in MPS IIIA dogs and cynomolgus monkeys through direct intraparenchymal injection into the brain (Hocquemiller et al., 2019).

1.8 Neuronal Pathology

1.8.1 Neurodegeneration in MPS III

Despite the abnormal intracellular pathology described in MPS IIIA, gross neuronal cell loss has not been reported in MPS IIIA, IIIB and IIIC mouse models until end-stage disease (~12-months-old), well beyond the symptomatic age of three- to four-months-old (Heldermon et al, 2007; Wilkinson et al, 2012; Pshezhetsky, 2015; Beard et al, 2017). Despite no overall cerebellar atrophy in older MPS IIIB mice, Purkinje cell death has, however, been reported in the MPS IIIA dog (by 40.9-months of age; Hassiotis et al., 2014b) and MPS IIIB dog (Ellinwood et al., 2003), coinciding with symptom onset.

Moreover, ubiquitin-positive lesions have been identified within the axonal processes of MPS IIIA mouse neurons (Savas et al., 2004). These lesions, present by seven-weeks of age in the MPS IIIA mouse, have been further linked to axonal dystrophy in dopaminergic, cholinergic, and GABAergic neurons (Beard et al., 2017). In the Huntaway canine MPS IIIA model, whilst cell death was reported at a later disease stage, axonal lesions were detected from the pre-symptomatic age of 4.3-months (Hassiotis et al., 2014b). Functionally, these lesions may disrupt axonal transport of intracellular organelles and vesicles to and from the synapse thus hindering neurotransmission (Beard et al., 2017). Together, this suggests neurological dysfunction does not arise from cellular loss but rather from discrete structural or functional changes in the neurons themselves.

1.8.2 Synaptic Pathology of Neurons

The cortical, hippocampal, striatal and cerebellar regions of the brain are home to groups of “spiny” neurons. These neurons develop protrusions on their dendrites termed dendritic spines, which were first discovered by Santiago Ramón y Cajal in 1888. He was able to visualise the fine structure of neurons under a light microscope using the Golgi silver-impregnation staining method (Ramón y Cajal, 1888). Dendritic spines contain a head

(~<1µm in diameter) and a thin neck (<0.1µm thick and ~1µm long), which extends from the dendrite branch (Phillips and Pozzo-Miller, 2015).

During maturation, dendritic spines progress through a change in morphology, from 'filopodia' and 'stubby' through 'thin' to 'mushroom' spines (Figure 1.9). The morphological distinctions were first proposed in 1970 (Peters and Kaiserman-Abramof, 1970), and changes in spine morphology were initially suggested to correlate with changes in strength of synaptic function (Schikorski and Stevens, 1999; Arellano et al., 2007; Colgan and Yasuda, 2014). Filopodia are long and motile needle-like projections which are highly active and abundant, particularly in the developing brain (Hering and Sheng, 2001; Zuo et al., 2005). Filopodia receive predominantly chemically transmitted excitatory input from neighbouring pre-synaptic terminals in the form of glutamate neurotransmitters and can transition into more stable spine morphologies. Transmission is intermittent and depends on the pre-synaptic action potential. Moreover, only a small percentage (0.2%) evolve into stubby spines following synaptic stimulation (Bhatt et al., 2009; Chidambaram et al., 2019). This could suggest they provide a fast-plasticity mechanism, particularly in the developing brain (Zuo et al., 2005; Ozcan, 2017). Short 'stubby' spines do not have a proper spine neck; long 'thin' spines have a long neck with small head; and large 'mushroom' spines have a defined neck and bulbous head (Bourne and Harris, 2007).

Dendritic spines comprise the post-synapse and pair with pre-synaptic boutons on axon terminals of a neighbouring neuron to form a communication point between two neurons (Fig 1.10). Spines typically function as excitatory post-synapses, whereas inhibitory synapses are located on the dendritic shaft itself (Arellano et al., 2007). Whilst age, cell type, and location determines the total dendritic spine density, it is estimated that each neuron possesses over 100,000 dendritic spines (Yuste, 2011; Chidambaram et al., 2019).

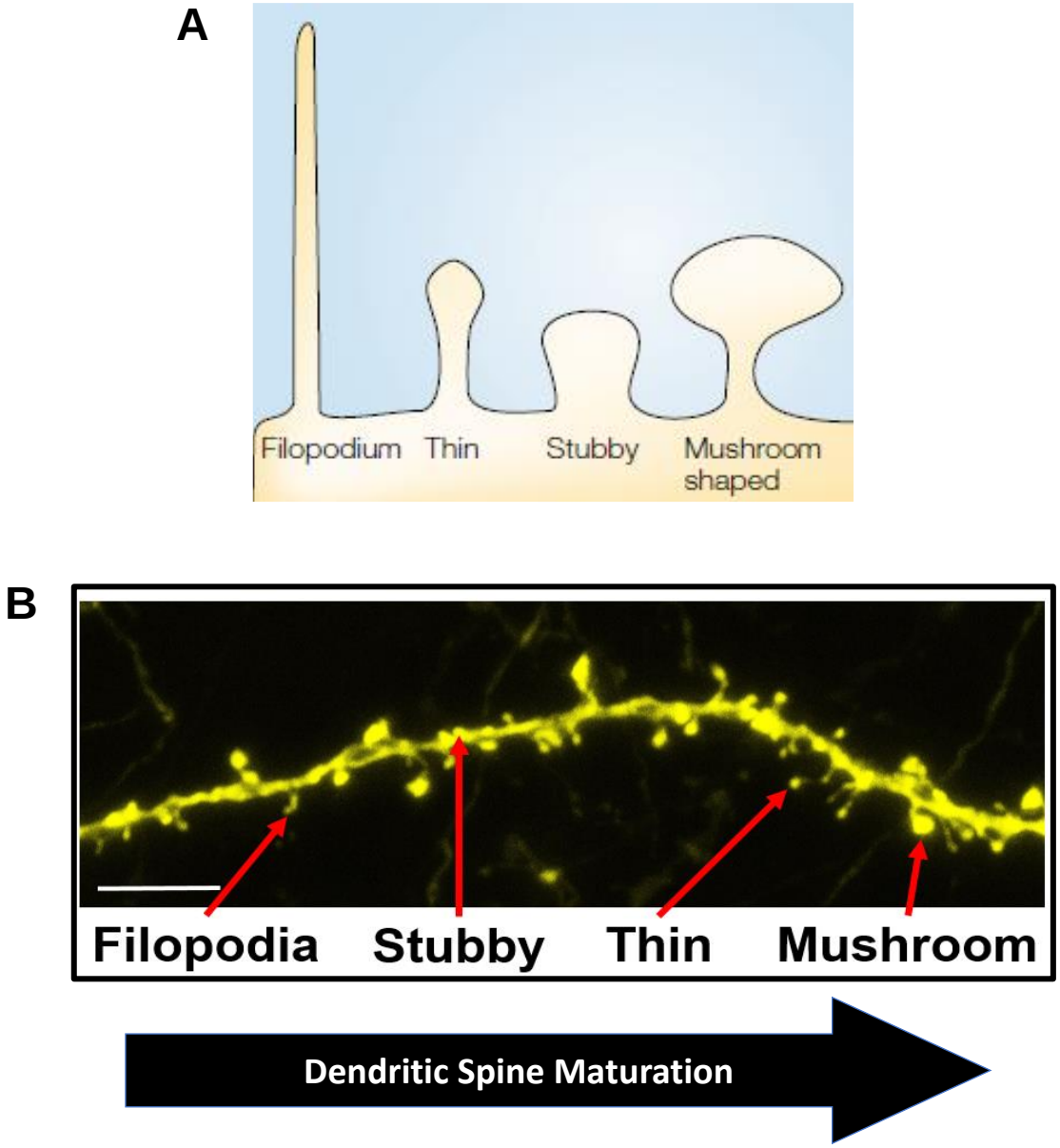


Figure 1.9 – Dendritic spine morphologies. The illustrated differences in dendritic spine morphology from filopodia to stubby (immature), and long-thin to fully mature mushroom spines (A; Hering and Sheng, 2001). A microscopic image highlighting the morphologies on a cortical neuron (B). Scale bar is 5µm.

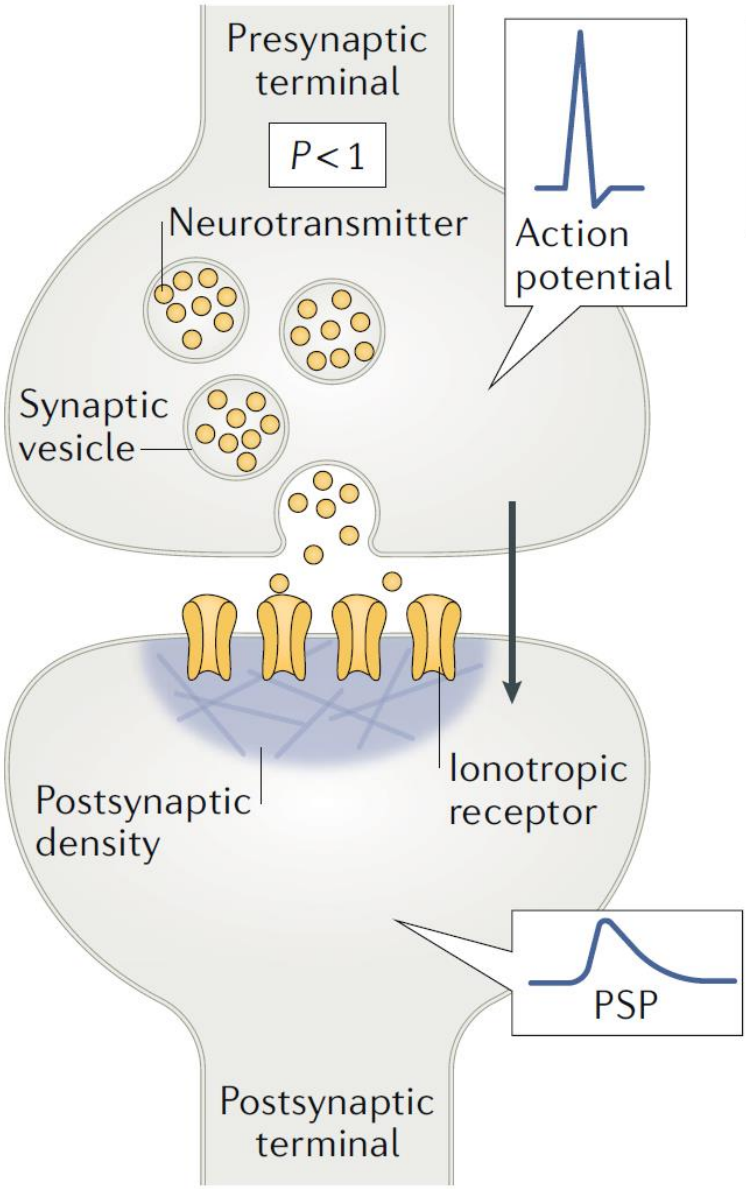


Figure 1.10 – Action potential traversing the synapse. The action potential travels down the axon to the pre-synapse to trigger the release of pre-synaptic vesicles which contain signalling molecules and neurotransmitters. These molecules bind to ligand-gated ion channels in the post-synaptic membrane and open, which triggers a change in membrane potential in the post-synaptic cell. (PSP, post-synaptic potential). (Alcami and Pereda, 2019).

Whilst most synapses are functional, the physical size of the spine head is reported to be directly proportional to the reliability and strength of the synapse (Arellano et al., 2007). Providing physical structure to the formation of spines are the cytoskeleton, membrane neurotransmitter receptors (N-methyl-D-aspartic acid (NMDA) and α-amino-3-hydroxy-5-methyl-4-soxazolepropionic acid (AMPA)), the post-synaptic density (PSD) region, molecular motors, trans-synaptic cell adhesion molecules, and the extracellular matrix (Kilinc, 2018; Chidambaram et al., 2019). Actin is the main component of the cytoskeleton of dendritic spines, with levels reported to be six-times higher than what is found in the dendritic shaft (Honkura et al., 2008). Within the spine, actin is either a polymerised filamentous form (F-actin) or the less prevalent soluble depolymerised form (G-actin) (Honkura et al., 2008). The branching and bundling of the cross-linked filaments provide stability, while the changes in polymerisation determine the growth and shape during maturation. Myosin II assists with the contraction and bundling of actin, is localised within the dendritic spine head, and is crucial in shaping the size of the spine head (Ryu et al., 2006). Myosin II is also highly abundant within the post-synaptic density (PSD), a protein-rich area located on the spine head adjacent to the pre-synaptic bouton, which marks a synaptic contact (Arellano et al., 2007). In addition to the cytoskeletal proteins the PSD contains cell surface receptors, adhesion molecules, synaptic vesicles, and the dominant scaffolding protein PSD95 (Chidambaram et al., 2019). AMPA receptors are located towards the edge of the PSD, and NMDA receptors are located within the centre of the PSD (Kharazia and Weinberg, 1997). Stimulation of the NMDA receptors promotes actin mobilisation, whilst the activity of AMPA receptors reduces actin motility and thus improves spine stability (Fischer et al., 2000).

Furthermore, spine head volume has been shown to be proportional to the PSD area, post-synaptic receptor number, and pool of transmitters (Harris and Stevens, 1989; Dobrunz and

Stevens, 1997; Nusser et al., 1998). A small neck slows diffusion and reduces movement of signalling molecules out of the spine (Adrian et al., 2014). Indeed, spines can act as isolated biochemical and electrical compartments of the neuron due to the diffusion-resistant nature of the spine neck (Nishiyama, 2019). Dendritic spine morphology is highly plastic and variable, even within the dendritic arbour of the same neuron. The size and shape of spines is regulated in an activity- and learning-dependent manner and can persist from seconds to decades (Grutzendler et al., 2002; Trachtenberg et al., 2002; Alvarez-Castelao and Schuman, 2015).

Synapses are categorised into either electrical or chemical groups and are thought to play a key role in brain plasticity and memory storage (Kasai et al, 2010). The spine neck acts as a barrier to the diffusion of biochemical and electrical signals, permitting each individual spine to function as an isolated unit (Yuste and Denk, 1995; Nevian and Sakmann, 2004). Electrical synapses directly transfer small molecules and charged ions through gap junctions (reviewed in Rouach et al, 2002). Chemical synapses involve the transfer of electrical activity from the pre-synapse of one neuron to the post-synapse of another neuron via chemical mediators. Generated action potentials move down axons, stimulating neurotransmitter release from pre-synaptic vesicles into the synaptic cleft (between the pre- and post-synapse), which activate ionotropic receptors in the post-synapse and convert back to an electrical signal to depolarise the post-synaptic neuron and carry the action potential onwards as a post-synaptic potential (Fig 1.10; reviewed in Lepeta et al, 2016; Alcami and Pereda, 2019). The primary neurotransmitter to elicit an excitatory response is glutamate, and gamma-aminobutyric acid (GABA) is the primary inhibitory neurotransmitter. As chemical synapses regulate excitatory and inhibitory signals, they therefore regulate the increasing or decreasing possibility for action potentials to propagate down a target neuron.

Therefore, dendrite and dendritic spine operation is important for the maintenance of a functioning neuronal network. In fact, altered dendritic spine structure and function has been observed in a number of neurocognitive disorders (Table 1.3; reviewed in Chidambaram et al., 2019). These observations extend to Alzheimer's disease (Braak and Braak, 1997; Zempel et al, 2010; Attar et al., 2012), schizophrenia (Garey et al, 1998; Sweet et al., 2009; reviewed in Hayashi-Takagi, 2017), and even part of the autism spectrum disorders (Raymond et al, 1996; Hutsler and Zhang, 2010; Stephenson et al, 2017). Since altered number and function of dendrites and dendritic spines can occur prior to neuronal death, correct brain function may be dependent on synaptic output, with dysfunction ultimately and directly resulting in neurological disease.

1.8.3 Lysosomal Function at the Synapse

Research into lysosomal function in neurons to date has primarily focused to the soma and axon. The earliest studies reveal endosomal compartments in the synapse and endosomes contributing to the formation of synaptic vesicles (Heuser and Reese, 1973; Teichberg et al., 1975). Whilst Parton et al. (1992) confirmed the presence of lysosomes in the soma and axon of neurons, they postulated that trafficking between the peripheral endosomes of the synapse and lysosomes is an important process for degrading and recycling pre- and post-synaptic components. Lysosomes have also been shown to degrade AMPA receptors (AMPARs) (Ehlers, 2000; Schwarz et al., 2010). AMPARs form an integral part of the synaptic membrane to receive glutamate on excitatory synapses, thus further alluding to a lysosomal role in synaptic and neurotransmitter function. Potentially impacting the exocytic process, inactivation of cathepsin D (located in GABAergic pre-synaptic endosomes and associated with Batten disease) was found to result in enlarged pre-synaptic endosomes, reducing the readily releasable pool and impairing synaptic transmission (Li et al., 2019), further suggestive of the impact of storage material on

Table 1.3 – **Dendritic spine changes in CNS disease.** A summary of reported dendritic spine abnormalities in various CNS diseases. Adapted from Chidambaram et al. (2019).

Neurological Disease	Dendritic Spine Pathology	Reference
Alzheimer's Disease	↓ total spine density ↑ premature spines	Spires et al., 2005; Jacobsen et al., 2006; Serran-Pozo et al., 2011; Attar et al., 2012
Parkinson's Disease	↓ total spine density	Stephens et al.,2005; Zaja-Milatovic et al., 2005; Villalba and Smith, 2013
Huntington's Disease	↑ total spine density (mild cases) ↓ total spine density (advanced cases)	Graveland et al., 1985; Guidetti et al., 2001; Xie et al., 2010
Autism Spectrum Disorder	↑ total spine density	Hutsler and Zhang, 2010; Tang et al., 2014
Fragile X Syndrome	↑ total spine density ↑ immature spines	Cruz-Martin et al., 2010; Cook et al., 2014
Rett Syndrome	↓ total spine density ↓ mushroom spine density	Chapleau et al., 2009; Landi et al., 2011; Chapleau et al., 2012; Castro et al., 2014
Down's Syndrome	↓ total spine density ↑ spine head size	Belichenko et al., 2007; Belichenko et al., 2009
Schizophrenia	↓ total spine density	Garey et al., 1998; Sweet et al., 2009
Depression	↓ total spine density ↓ spine function	Christoffel et al., 2011; Wang et al., 2013
Epilepsy	↑ total spine density ↓ total spine density ↑ loss of spines	Ampuero et al., 2007; Zeng et al., 2007; Nishimura et al., 2008
Stroke	↓ total spine density	Babu and Ramanathan, 2011; Kalaivani et al., 2014
Prion Disease	↓ total spine density	Belichenko et al., 2000; Siskova et al., 2009
Sleep Disorders	↓ spine dynamics	Yang and Gan, 2012; Yang et al., 2014

neurotransmission within neuronal lysosomes.

1.8.4 Morphological Changes of Neurons in Lysosomal Storage Disorders

Morphometric analysis of neurons has been conducted in LSD brains over several decades. The Golgi stain method was used by Purpura and Suzuki (1976) who first identified "meganeurites" on LSD cortical neurons and suggested they were engorged neuronal processes containing accumulated substrate. These swellings projected dendritic spines and additional spinous processes. Meganeurites are considered to be exclusive to disorders of the endosomal-lysosomal system (Walkley, 2004; Walkley and Suzuki, 2004). Walkley et al. (1981) examined neuronal morphology in a feline model of mannosidosis using the Golgi staining method and found dendritic spine loss on cortical neurons in association with meganeurites. Human case studies by Takashima et al. (1985) utilising the Golgi stain method also revealed reductions in the level of dendritic complexity in Tay-Sachs disease (a neurodegenerative LSD) and MPS-I. Over the years, dendritic arborisation and meganeurite assessment helped to characterise neurons in MPS I (Walkley et al, 1988), GM1-gangliosidosis (Walkley, 1987), and GM2-gangliosidosis (Siegel and Walkley, 1994). Pyramidal and non-pyramidal cerebral cortical neurons from feline models of Niemann-Pick disease types A and C (both neurodegenerative LSDs) showed axonal dystrophy plus a decrease in dendritic spine density (Walkley and Baker, 1984; Higashi et al, 1993).

Dendritic spine characteristics have been investigated in other LSDs (including MPS III; Table 1.4). In two mouse models of Batten disease (the most common autosomal recessive neurodegenerative disease of childhood) – *Ppt1*$^{-/-}$ and *Cln6*^{nclf}, presented deficiencies in synaptic density in the thalamus from an early-symptomatic age, and sensory regions of the cortex showed a further decrease in synaptic density with age, but not as markedly as the

Table 1.4 – **Dendritic spine changes in LSDs.** A summary of reported dendritic spine densities in cultured neurons, animal models, and post-mortem studies of the mucopolysaccharide disorders and other LSDs.

Lysosomal Storage Disorder	Neuronal Type / Location	Dendritic Spine Density	Reference
CLN1	Hippocampus	Decrease	Peng et al., 2015
CLN3	Cerebral organoid	Decrease	Gomez-Giro et al., 2019
CLN5	Cortex	Decrease	Amorim et al., 2015
CLN6	Thalamus; Cortex	Decrease	Kielar et al., 2009
GM2 Gangliosidosis	Cortex; Cerebellum	Decrease	Takashima et al., 1985; Siegel and Walkley, 1994; Hooper et al., 2016
Manosidosis	Cortex	Decrease	Walkley et al., 1981; Stroobants et al., 2017
Niemann-Pick A	Cortex	Decrease	Walkley and Baker, 1984; Arroyo et al., 2014
Niemann-Pick C	Cerebellum	Decrease	Higashi et al., 1993
Niemann-Pick C	Hippocampus	No change	Xu et al., 2010
Sialidosis	Cortex	Decrease	Takashima et al., 1985

thalamus. Changes in neuronal morphology have also been observed in larger animal models. In a $CLN5^{-/-}$ sheep model of Batten disease, whilst Amorim et al (2015) did not find changes in the cerebellum, they did show synaptic loss in the motor cortex at the symptomatic age of approximately two-years. This has significant implications as the major neuropathological features in the sheep closely mirror the human disease. It was noted, however, that further examination of synaptic changes was required at pre- and early-symptomatic ages to determine whether synaptic loss precedes or occurs in conjunction with gross neuropathological changes (Amorim et al., 2015).

1.8.5 Functional Changes of Neurons in Lysosomal Storage Disorders

Models of other LSDs, including Niemann-Pick disease type C, have presented some conflicting results on synaptic morphology and function. Functional changes were hypothesised to be linked to substrate storage within the synapse, as storage in the lipid matrix has been shown to influence the electrophysiological properties of ion channels in plasma membranes (Lundbaek et al., 1996; Jennings et al., 1999). One study utilising brain slices and primary neuronal cultures from a Niemann-Pick disease type C mouse model revealed no differences in membrane potential, action potential amplitude, post-synaptic potentials, reversal potential, or intracellular concentrations of free Ca^{2+} (Deisz et al., 2005). More recently, and conflictingly, a study in a different Niemann-Pick disease type C1 (NPC1) model using induced pluripotent stem cell (iPSC)-derived neurons reported a reduction in membrane potential (Rabenstein et al., 2017). A similar finding was observed in iPSC-derived neurons from patients with Gaucher disease (Sun et al., 2015). A significant reduction in the influx of Ca^{2+} via AMPARs was also seen in the Niemann-Pick disease type C1 iPSC-derived neurons. This may possibly be due to Ca^{2+}-impermeable AMPARs resulting from cholesterol storage in the lipid membrane of synapses disturbing the trafficking of glutamine receptor subunits for AMPARs and an up-regulation in the

Ca^{2+}-impermeable glutamine receptor GluA2 subunit (Rabenstein et al., 2017). Storage within neurons has also been found to increase cell capacitance in a Fabry rat model, most likely due to the increased size of the soma (Miller et al., 2018). Whilst the cell membrane was also more fragile as a result of the enlargement, no differences in neuronal excitability were recorded. This is despite previous patch-clamp studies in Fabry disease mice showing changes in the conductance of voltage-gated sodium, potassium, and calcium channels (Choi et al., 2015; Namer et al., 2017). Rabenstein and colleagues expanded on their previous cultured work into an *ex vivo* model with cerebellar slices of Niemann-Pick disease type $C1^{-/-}$ mice and found increased frequency of GABAergic inhibitory post-synaptic currents in Purkinje cells preceding neuronal loss (Rabenstein et al, 2019).

Moreover, a murine model of the neurological LSD Sandhoff disease showed GM2-ganglioside accumulation in the hippocampus reduced the amplitude of AMPAR-mediated currents, despite no difference in overall number of GluR1 receptors until late-symptomatic disease (Hooper et al., 2016). This dysregulation of the glutamatergic system suggests that sub-cellular receptor trafficking rather than actual protein levels could be directly influencing neuronal function, and that the loss of AMPARs is detrimental and not protective (Hooper et al., 2016).

Further to sub-cellular trafficking, Npc1 (Niemann-Pick type C1) is reported to be abundant in recycling endosomes of pre-synaptic terminals (Karten et al., 2006). The subsequent enzyme deficiency in Npc1 leads to morphological changes in excitatory and inhibitory pre-synaptic terminals, synaptic vesicle turnover, and reduction in the number of glutamatergic and synaptic inputs to Purkinje cells (Karten et al., 2006; Buard and Pfrieger, 2014; Caporali et al., 2016).

Reduced synaptic vesicle pool size and synaptic currents were observed in $CLN1^{-/-}$, $CLN6^{nclf}$ and $Ppt1^{-/-}$ Batten mice (Kielar et al., 2009; Peng et al., 2015). A neuronal culture model of Batten disease ($CLN6^{-/-}$) has been utilised to examine the mechanism of synaptic endocytosis in the re-uptake and recycling of neurotransmitters and synaptic vesicle components. It was discovered the affected $CLN6^{-/-}$ cells showed a significant reduction in recycling and re-uptake capacity, suggesting that activity-dependent bulk endocytosis and synaptic vesicle production is compromised with lysosomal storage in neurons (Best et al., 2017). Complementary to this, an electrophysiological time-course was conducted in a mouse model of Batten disease (Burkovetskaya et al, 2017), where deficits in axonal and synaptic excitability were observed in neurons of the hippocampus and visual cortex prior to neuronal loss. However, morphometric analysis was not included in this time-course.

There were no changes to electrophysiological kinetics or functional deficits in Ca^{2+} flux in a feline model of MPS VI (Lischka et al., 2008). The same study also found functional Ca^{2+} flux mechanisms and similar voltage-activated ion currents (compared to controls) in a feline model of MPS I, yet alluded to impairments in signalling components related to second messenger-mediated signal transduction cascades. This may have affected the flux mechanisms tested during pharmacological manipulations in the calcium imaging component of the study (Lischka et al., 2008). To support this claim, an MPS IV model revealed a defect in the calcium transporter, mucolipin 1, which altered the exocytic process (LaPlante et al., 2006).

More recent investigation into lysosomal motility has revealed trafficking of lysosomes to distal dendrites and dendritic spines themselves in an activity-dependent manner (Goo et al, 2017). In fact, this recruitment is potentially due to local AMPAR activation (Goo et al, 2017). Trafficking could occur via interactions with motor proteins located on

microtubules within dendrites (Maday et al, 2014). The presence of lysosomes in dendritic spines suggests that synaptic plasticity and remodelling occurs with the assistance of localised degradation, and not relying on transport to the soma (Goo et al, 2017).

Interestingly, inhibition of lysosomal function and motility has been shown to reduce dendritic spine growth and number (Goo et al, 2017; Padamsey et al, 2017a). Padamsey et al. (2017b) also revealed that lysosomes mediate activity-dependant Ca^{2+} dendritic signalling and play a role in the long-term maintenance of synaptic plasticity. With growing evidence suggesting lysosomes contain internal Ca^{2+} stores (Galione et al 2010; 2015), lysosomal inhibition could also be reducing the release of Ca^{2+} required for neurotransmitter release (Brailoiu et al, 2003; McGuinness et al, 2007).

The predominant mechanism for growth or changes in dendritic spine morphology is the modulation of actin filaments during long-term potentiation (prolonged stimulation) of a synapse (Lin et al., 2005). NMDA receptors are activated by the initial stimulation, control intracellular Ca^{2+} levels, and translocate stabilising and scaffolding proteins to alter the length and diameter of the spine in response to the stimulation (Okamoto et al., 2004; Noguchi et al., 2005). A greater stimulation leads to an enlargement of the spine head, also due to higher levels of AMPA glutamate receptors (Matsuzaki et al., 2001). The recruitment of receptors to the synaptic junction is further implicated in synaptic dynamics, as blockage of both NMDA and AMPARs reduces the overall density of dendritic spines (McKinney et al., 1999; Kang et al., 2009). Therefore, with evidence highlighting the role of the lysosome in regulating synaptic plasticity, it is possible that lysosomal dysfunction impairs recruitment of neurotransmitters and receptors to the pre- and post-synapse, thus resulting in dendritic spine changes in LSDs.

1.8.6 Morphological and Functional Changes of Neurons in MPS III

There has been one reported examination of dendritic structure and spine density in post-mortem human tissue from an MPS IIIA patient (Takashima et al., 1985). Whilst camera lucida studies suggested no change in dendritic arborisation within the visual cortex (Fig 1.11A-B), they did detect large swellings on the dendrites, dubbed "meganeurites". Moreover, there was a reported decrease in dendritic spine density along apical and basal dendrites (Fig 1.11B) on layer 3 visual cortical pyramidal neurons (Takashima et al., 1985).

Reductions in pre-synaptic (axonal bouton) proteins have been identified in the MPS I and MPS III murine cerebral cortex at symptomatic ages (Vitry et al., 2009; Wilkinson et al., 2012). The study by Vitry and colleagues showed that the decrease in the pre-synaptic protein, synaptophysin, in the MPS IIIB mouse cerebral cortex was caused by HS oligosaccharide-induced degradation by the proteasome.

Assessments into synaptic characteristics of MPS IIIA mouse chromaffin cells have shown a reduction in the total number of secretory vesicle exocytotic events (Keating et al., 2012). Further analysis of these amperometric recordings showed no difference in the kinetics of these events or Ca^{2+} flux. Focusing within the CNS, preliminary work by Shoubridge (2013) examined the architecture of pyramidal neurons in the MPS IIIA mouse cerebral motor cortex at the symptomatic age of 20-weeks (Fig 1.12) with the use of a modified Golgi-Cox histological stain (Ranjan and Mallick, 2010). Whilst no significant differences were found in the degree of complexity within the dendritic arborisation between genotypes (Fig 1.12B-F), decreases in post-synaptic dendritic spine number were recorded across multiple orders of dendrites (Fig 1.13). These findings were then verified in the MPS IIIB mouse cerebral motor cortex, and the deficits in dendritic spine density was

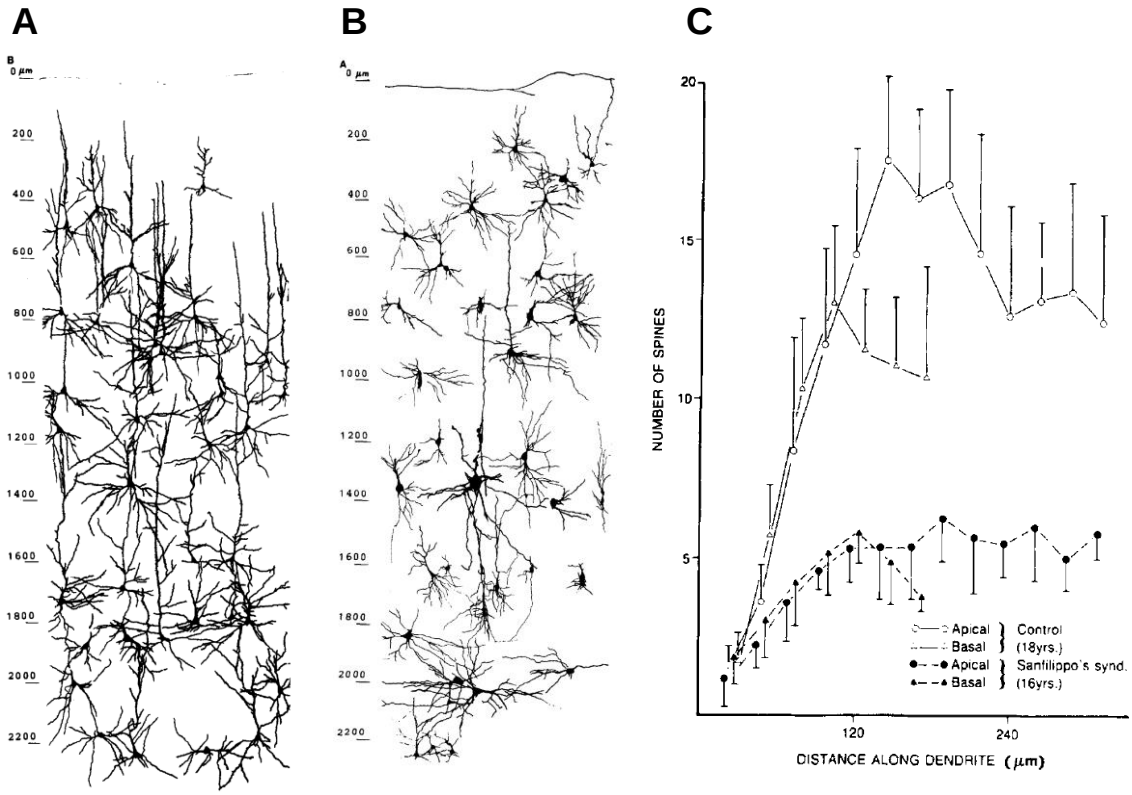


Figure 1.11 – Historical human post-mortem MPS IIIA neuronal morphological assessment. The single reported examination of neuronal morphology in human MPS IIIA brain tissue occurred in the visual cortex of a 16-year-old male. Camera lucida drawings of neuronal dendritic arborisation in an 18-year-old control (A) and MPS IIIA male (B), followed by dendritic spine analysis (C). (Takashima et al., 1985).

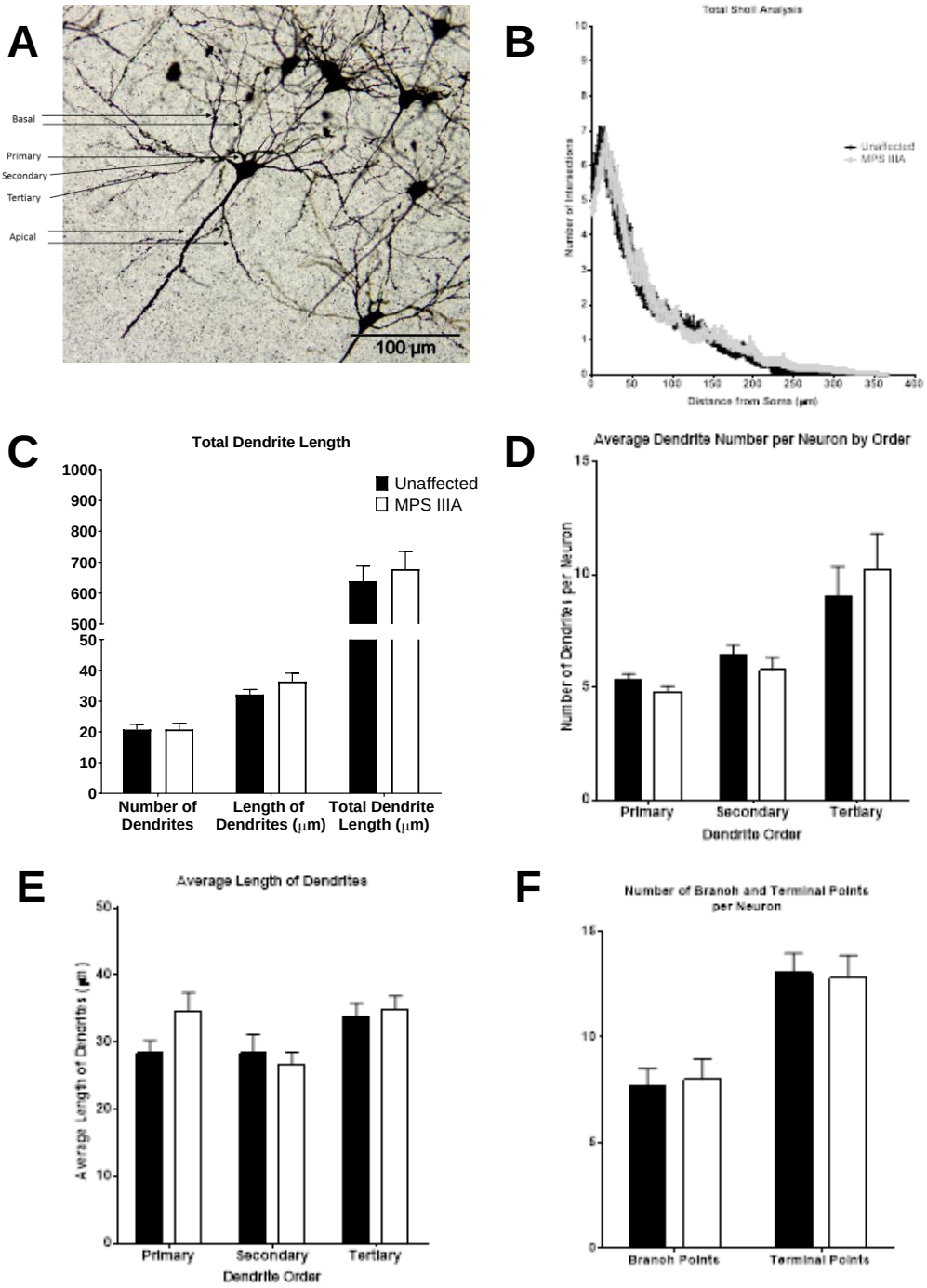


Figure 1.12 – The complexity of dendritic arbours in MPS IIIA mice at 20-weeks. An example of a pyramidal neuron in the mouse motor cortex of the cerebrum stained using the Golgi-Cox method (A). Total Sholl analysis (B) revealed no overall differences between unaffected and MPS IIIA dendritic arborisation at 20-weeks of age. Localised assessments (C-F) further highlighted no significant differences ($p>0.05$) in dendritic complexity between unaffected and MPS IIIA mice. Data are mean ± SEM (n=5/genotype).

again observed (Fig 1.14; Shoubridge et al., unpublished).

An elevation in the number of mushroom (mature) dendritic spines has been observed in the MPS IIIA mouse model at a pre-symptomatic age, although localised to the somatosensory cortex (Dwyer et al 2017). Glutamatergic excitatory post-synaptic strength in pyramidal neurons of the somatosensory cortex was reduced in MPS IIIA mice despite no overall change in spine number or pre-synaptic neurotransmitter vesicle release (Dwyer et al, 2017). Decreases in the number of synaptic vesicles at the pre-synapse, and pre-synaptic spine head volume were seen in an aged MPS IIIA mouse model (Sambri et al., 2017); these authors also found a significant reduction in the excitatory post-synaptic potential in six-month-old MPS IIIA mouse hippocampal slices (Sambri et al., 2017).

More recently, de Aragao et al. (2020) recorded total spine deficiencies in MPS IIIC mouse hippocampal neurons from as early as 10-days of age. Utilising an immunofluorescence stain for PSD protein 95 (PSD95), they also reported reductions in PSD95 puncta in the post-mortem human cortex of MPS IIIA, MPS IIIC, and MPS IIID patients (de Aragao et al., 2020). They recorded reductions in frequency and amplitude for both inhibitory and excitatory post-synaptic events in hippocampal *ex vivo* slices from approximately seven-week-old MPS IIIC mice, and also reported reductions in the motility of synaptic vesicles in cultured MPS IIIC hippocampal neurons after 21-days *in vitro*. Lastly, both synapsin and synaptophysin levels were reduced in MPS IIIC hippocampal neurons after 21-days *in vitro* (de Aragao et al., 2020).

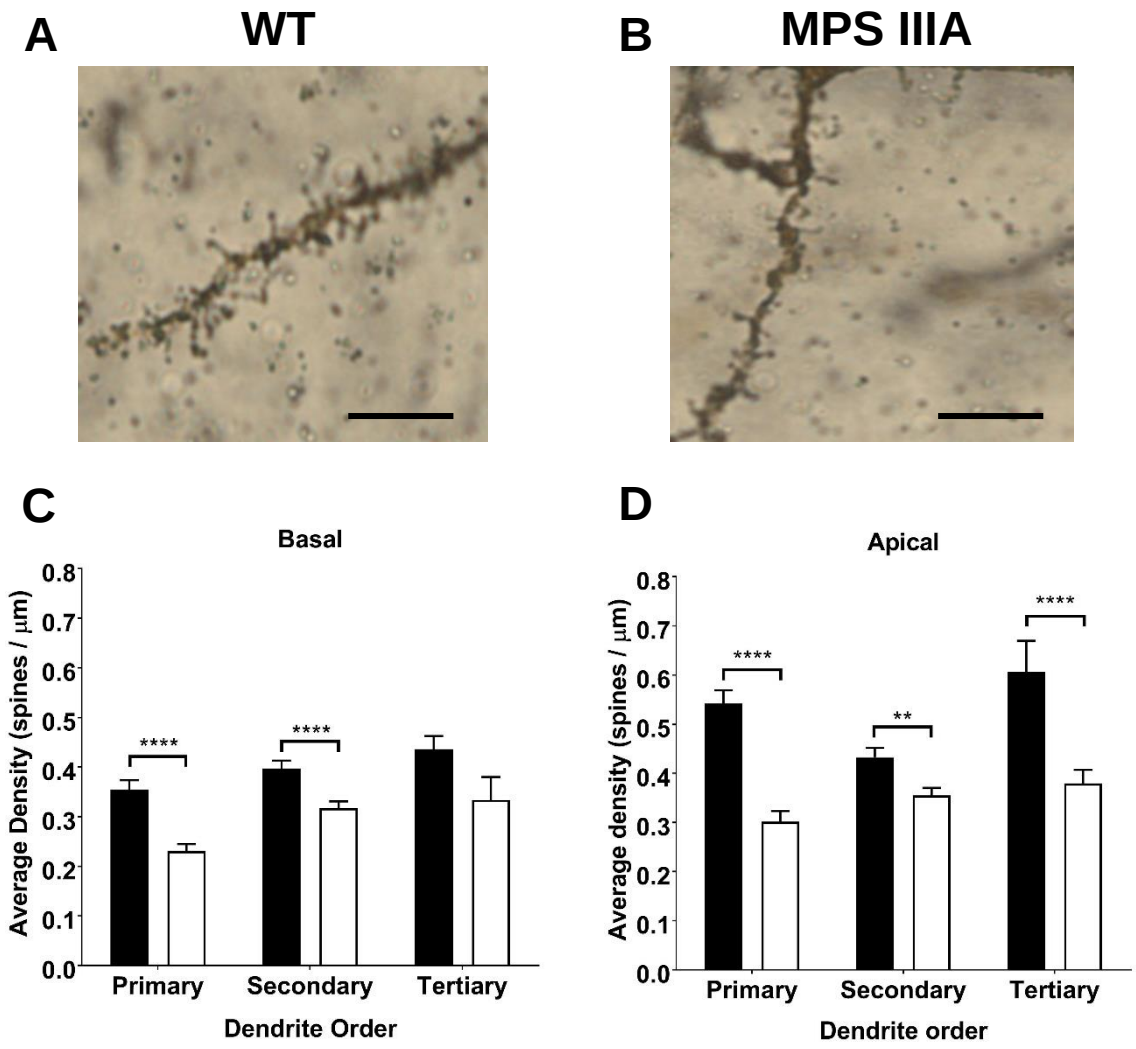


Figure 1.13 – Dendritic spine density is decreased in MPS IIIA mice at 20-weeks.

Examples of a Golgi-Cox-stained dendrite in wild-type (WT) (A) and MPS IIIA (B) mouse cerebral motor cortex. Dendritic spine density was decreased in MPS IIIA basal (C) and apical (D) dendrites of cortical pyramidal neurons. **p<0.01; ****p<0.0001. Scale bar = 5μm. Data are mean ± SEM (n=5/genotype).

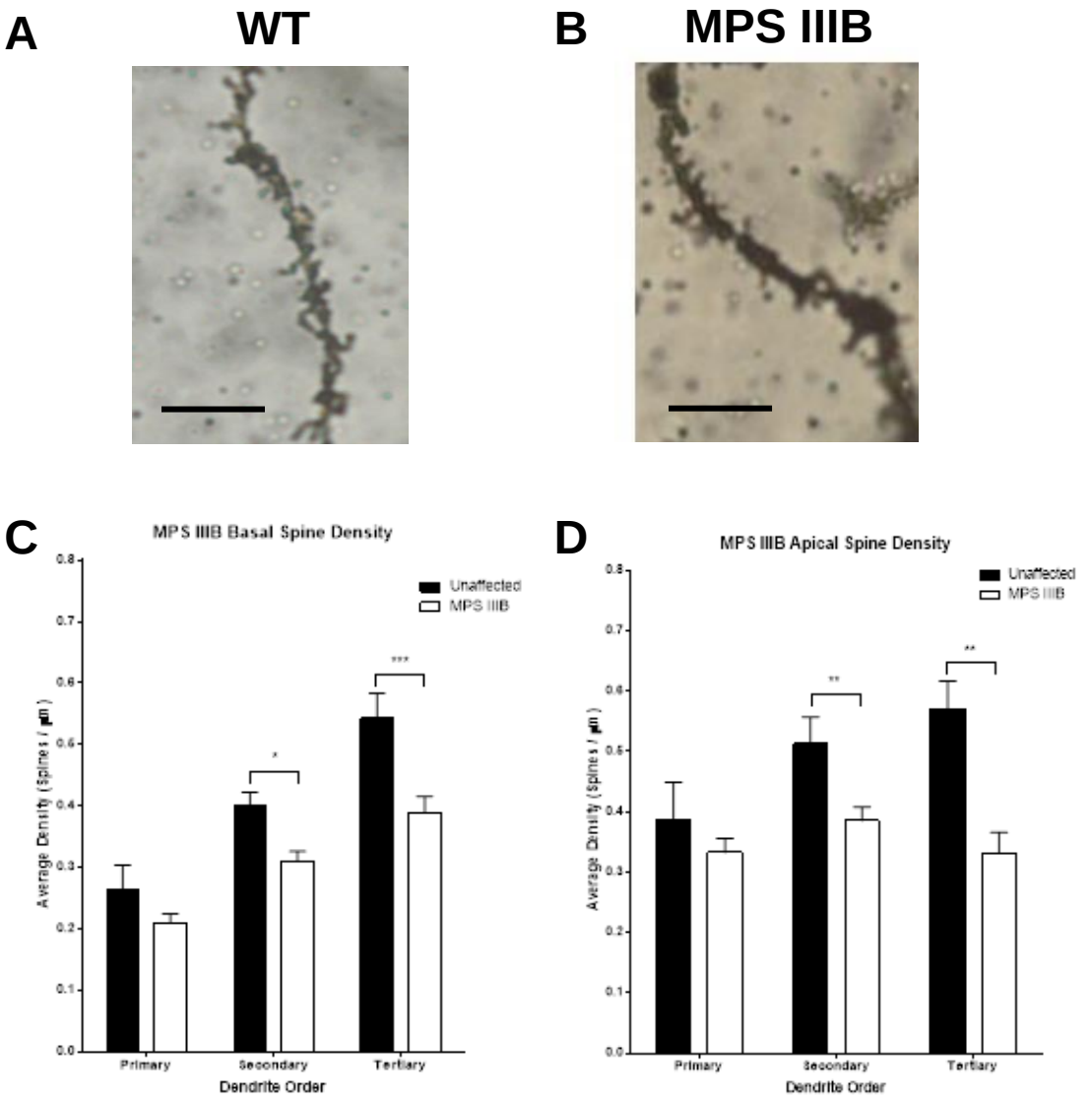


Figure 1.14 – Dendritic spine density is decreased in MPS IIIB mice at 20-weeks. Examples of a Golgi-Cox-stained dendrite in wild-type (WT) (A) and MPS IIIB (B) mouse cerebral motor cortex. Dendritic spine density was decreased in MPS IIIB basal (C) and apical (D) dendrites of cortical pyramidal neurons. *p<0.05; **p<0.01; ***p<0.001. Scale bar = 5µm. Data are mean ± SEM (n=5/genotype).

Assessments of neuronal pathology, including synaptic properties, within MPS III models are summarised in Table 1.5. Collectively these data suggest that changes to dendritic spine morphology and function could be contributing to the neurological dysfunction associated with MPS III.

Table 1.5 – Summary of the outcomes of studies evaluating synaptic changes in MPS III. A summary of the current knowledge about synaptic pathology in MPS III. The arrows denote a phenotypic difference of 'increase', 'decrease', or 'no change'. EM, electron micrograph; IF, immunofluorescence; IHC, immunohistochemistry; WB, western blot.

Disease Model	Brain Region	Synaptic Assessment	Symptomatic Time-Point	Difference	Method	Reference
MPS IIIA human (in vivo)	Cortex (visual)	Dendritic spine density	Post-mortem (16-years)	↓	Golgi-Cox	Takashima et al., 1985
MPS IIIB mouse (in vivo)	Cortex (frontal)	Pre-synapse (synaptophysin)	Pre-symptom (10 days)	↓	IF + WB	Vitry et al., 2009
			Late-symptom (8-months)	↓		
		Synaptic density (synaptobrevin)	Pre-symptom (10 days)	↔	IF	
			Late-symptom (8-months)	↔		
MPS I, IIIA, IIIB mouse (in vivo)	Cortex (motor, somatosensory, parietal)	Pre-synapse (protein expression)	Early-symptom (4-months)	↓	IHC	Wilkinson et al., 2012
			Late-symptom (9-months)	↓		
		Synaptic density (synaptophysin)	Early-symptom (4-months)	↔		
			Late-symptom (9-months)	↔		
MPS IIIA mouse (in vitro)	Adrenal gland (chromaffin cell)	Synaptic vesicle exocytosis	Late-symptom (>20-weeks)	↓	Ampero-metry	Keating et al., 2012
MPS IIIA mouse (in vivo)	Cortex (somatosensory)	Dendritic spine density	Pre-symptom (3-weeks)	↑	Golgi-Cox	Dwyer et al., 2017
MPS IIIA, IIIB mouse (in vivo)	Cortex (motor)	Dendritic spine density	Late-symptom (20-weeks)	↓	Golgi-Cox	Shoubridge et al., 2013; unpublished
MPS IIIA mouse (in vivo)	Cortex (unspecified)	Pre-synaptic head size	Early-symptom (12-weeks)	↔	EM	Sambri et al., 2017
			Late-symptom (6-months)	↔		
			Late-symptom (10-months)	↓		
MPS IIIC mouse (in vivo and in vitro)	Hippocampus (unspecified)	Pre-synapse (synaptophysin)	Pre-symptom (3-weeks)	↓	IF	Aragao et al., 2020
		Dendritic spine density	Pre-symptom (3-weeks)	↓	3-D confocal	
			Early-symptom (12-weeks)	↓		
			Late-symptom (8-months)	↓		

1.9 Inflammation in the Central Nervous System

1.9.1 Adaptive Immunity

In addition to the intracellular dysfunction of neurons in MPS III, impaired neuronal function may potentially be exacerbated by inflammatory processes within the CNS, particularly involving the innate immune system (Ohmi et al., 2003; Ausseil et al., 2008). Of the two immune responses in the CNS, the adaptive immune response is not as prevalent yet it is more specific in nature. It constitutes primarily T- and B-cell lymphocytes that are located within the blood, CSF, and brain tissue, and secrete pro-inflammatory (Th1 or Th17) or anti-inflammatory (Th2) cytokines (Stephenson et al., 2018). However, the primary effect of the adaptive immune response comes via CD4 T-cells located within the meningeal spaces of the brain (Norris and Kipnis, 2019). These cells are responsible for secreting cytokines which modulate the local inflammatory environment and can directly impact neuronal activity (Fig 1.15). Interleukin (IL)-4 and IL-13 are secreted from CD4 T-cells and have been shown to promote the production of brain-derived neurotrophic factor and boost cognition (Derecki et al., 2010; Brombacher et al., 2017). Interferon (IFN)-γ signalling has also been shown to impact on social behaviours in mice (Filiano et al., 2016). Whilst other cytokines have been detected as biomarkers, their effects within the CNS remain to be defined.

1.9.2 Innate Immunity

Within the CNS, the types of innate immune cells include macrophages, microglia, astrocytes, mast cells, natural killer cells, and polymorphonuclear neutrophils (Presta et al., 2018). These cells act in a non-specific manner by recognising the stress of host cells and assisting with tissue repair and clearance of cellular debris. Binding to damage-associated molecular patterns or pathogen-associated molecular patterns by innate immune cell pattern recognition receptors leads to their activation and subsequent function (Presta et al.,

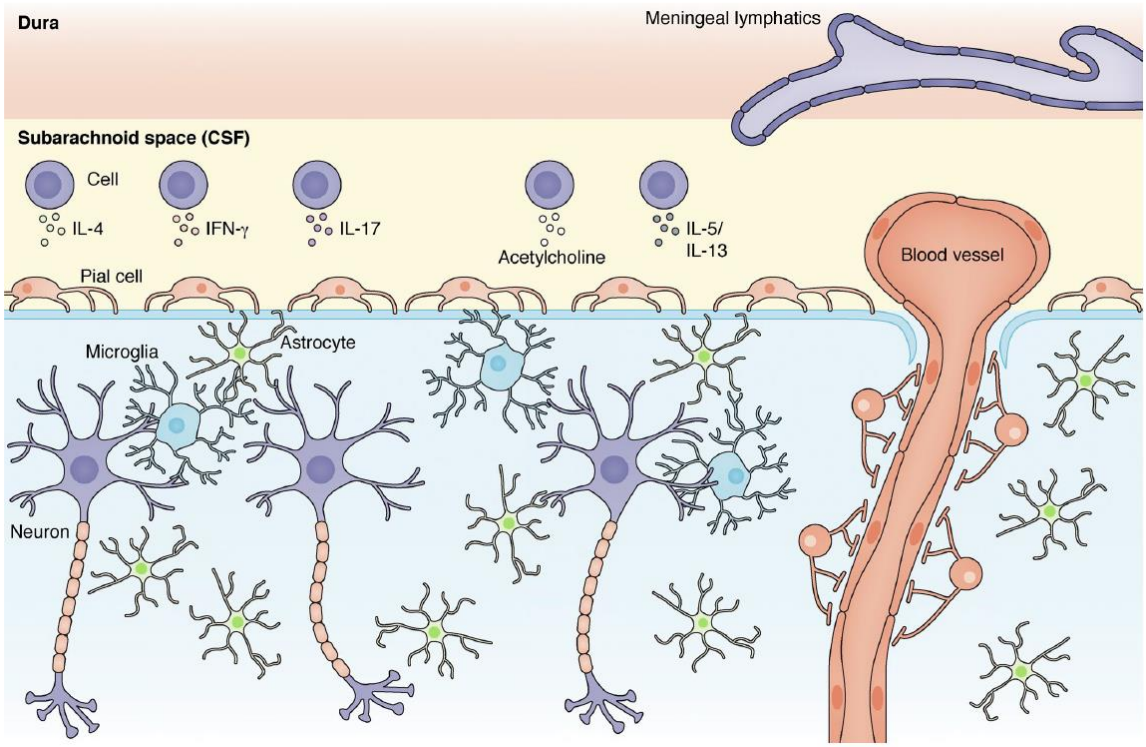


Figure 1.15 – **Cytokine release by adaptive immunity in the CNS.** Regulation of neuronal function by the cytokine-secreting CD4 T-cells residing in the meninges of the CNS. (Norris and Kipnis, 2018).

2018; Stephenson et al., 2018). As microglia are the major immune cells in the brain, most of the innate immune response involves polarising the microglial population towards a pro- or anti-inflammatory state, which can be identified through expression of markers, including IL-6, CD206, or CD163 (Presta et al., 2018). Together, these innate immune cells aid the clearance of dying cells, myelin debris, aggregated proteins, and cell reprogramming (Stephenson et al., 2018).

1.9.3 The Complement Cascade

Innate inflammation also involves initiation of the complement cascade and recruitment of inflammatory cells (microglia and astrocytes) to the site of inflammation specifically to remove debris and reprogram cellular function, most notably during development of synaptic circuits early in life (reviewed in Stephenson et al., 2018). Synthesis of components of the complement cascade has been shown to occur in the CNS, with neurons also expressing receptors to these components (Stephenson et al., 2018; Morimoto and Nakajima, 2019). The stage of synthesis of each element, as well as the location of inhibition for each of the three regulatory factors is shown in Figure 1.16.

Complement proteins are produced by a variety of cell types and locations, permitting the complement cascade to be initiated locally and systemically in response to infectious and non-infectious circumstances (Morimoto and Nakajima, 2019). In the majority of non-self-targets, complement component 1q (C1q) is activated and identifies the target for removal, with C2, C3 and C4 fragments opsonising it. In the steps leading-up to formation of the Membrane Attack Complex, C3a, C4a and C5a fragments stimulate inflammation and promote phagocytosis. The Membrane Attack Complex inserts itself into the non-self-target cell membrane and lyses the cell (Yasojima et al., 1999). C1 Inhibitor prevents C1q

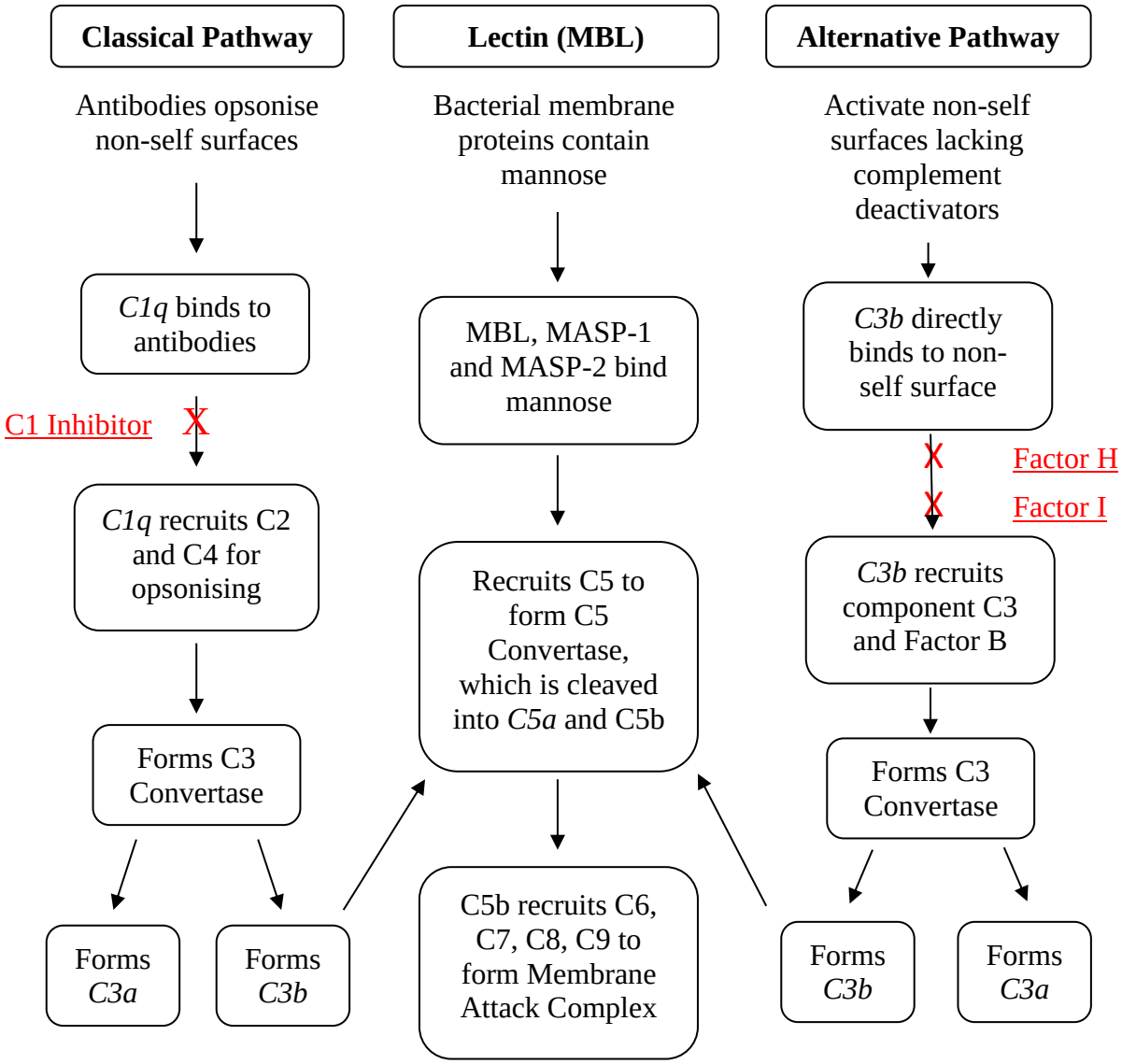


Figure 1.16 – **The complement cascade.** Synthesis of the complement components within the three pathways constituting the complement cascade and (highlighted) regulatory factors. (Adapted from Yanamadala and Friedlander, 2010; Yasojima et al., 1999).

from initiating the classical pathway, while Factors H and I prevent C3b from continuing along the alternative pathway. Both pathways are very similar, and inhibition of each not only hinders inflammation but also degeneration of the non-self-target. Complement cascade components localise to developing synapses from astrocytes and mediate phagocytosis of the synapse by microglia, refining and strengthening the remaining synaptic connections in the CNS through "synaptic pruning" (Pfrieger and Barres, 1997; Schafer et al., 2012). Disruption of the C3 receptor is specific to microglia in the brain and has a severely negative effect on brain wiring, with pre-synaptic inputs targeted preferentially over post-synaptic inputs. A disruption to the genetic material for complement activation also appears to disrupt microglial function, resulting in an incomplete ability to remodel synapses (Schafer et al., 2012).

Using a mouse model of glaucoma, it was deduced that during development, astrocytes permit activity-dependent signalling for synaptic survival and elimination (Stevens et al., 2007). This process resurfaces following neuronal injury or in neurodegenerative diseases based on the localisation of C1q to synapses. Stevens et al. (2007) showed that C1q was up-regulated and localised to retinal synapses during the early stages of glaucoma prior to obvious neurodegeneration. C3 is recruited to C1q, which then binds to the C3 receptor on microglia, suggesting that the complement cascade is involved in synaptic loss in neurodegenerative diseases (Fig 1.17; Klein, 2020).

1.9.4 Glial Cell Inflammatory Activation

The functionality of astrocytes and microglia in inflammatory responses includes both pro- and anti-inflammatory effects. Microglia are the primary innate immune cell of the CNS and constitute approximately 80% of all brain immune cells (Morimoto and Nakajima,

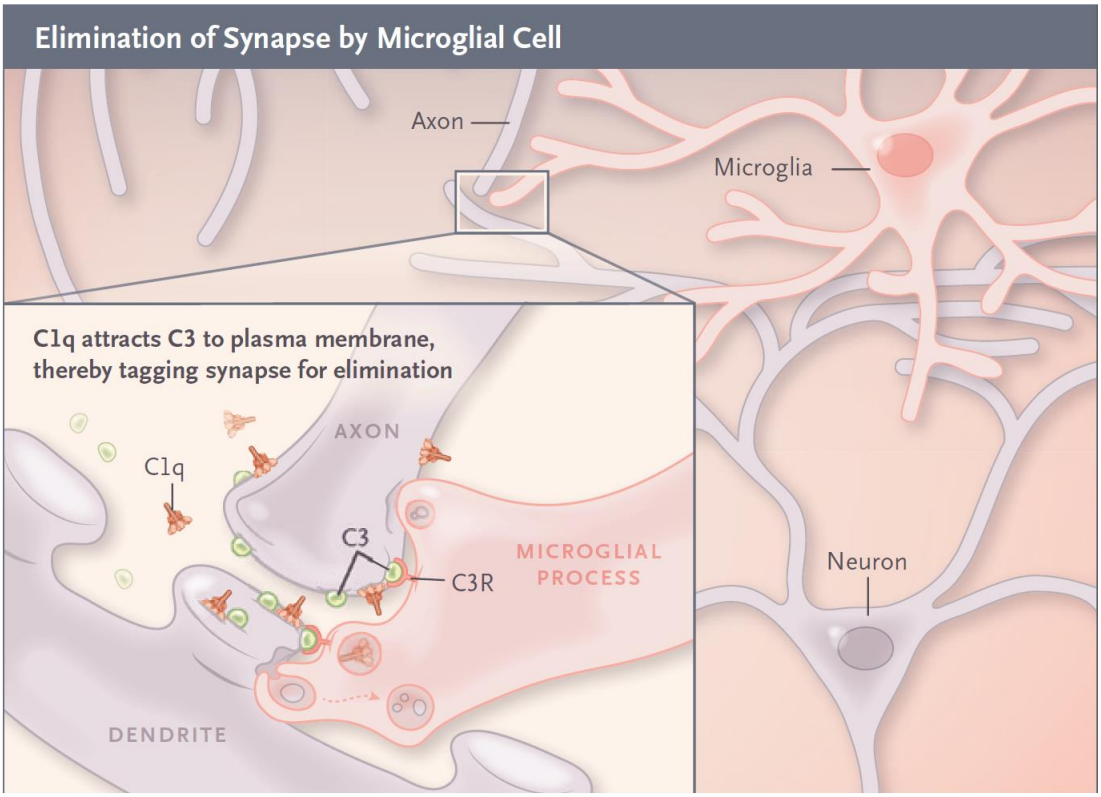


Figure 1.17 – **Synaptic pruning process.** Illustration of the complement-mediated pruning process with synaptic elimination by activated microglia. (Klein, 2020).

2019). Microglia are particularly heterogeneous, with their functionality spanning a range of phenotypes. One distinct pro-inflammatory type (termed 'M1-like') presents up-regulated inflammatory components Tumor Necrosis Factor (TNF), IL-1b and reactive oxygen species (Block et al., 2007). At the other end of the spectrum is the immunosuppressive type ('M2-like'), which is distinguished by up-regulated Chitinase-like 3, Frizzled class receptor 1, and Arginase 1 (Boche et al., 2013). The classification of microglial activation is currently being reviewed, however, because macrophages and microglia can display more than these two polarised states (Martinez and Gordon, 2014; Heppner et al., 2015; Liddelow and Barres, 2017).

Similar with microglia in both phenotype and nomenclature, two distinct types of reactive astrocytes have been identified: A1 and A2. A1 neuroinflammatory reactive astrocytes up-regulate complement cascade genes C1r, C1s, C3 and C4, which have previously been reported to be harmful to synapses (Zamanian et al., 2012). A2 reactive astrocytes promote survival and growth of neurons via up-regulation of neurotrophic factors in addition to thrombospondins, which promote the repair of synapses and generate greater populations of synapses (Eroglu and Barres, 2010; Liddelow and Barres, 2017).

The link between microglial and astrocytic interaction has been further characterised by Liddelow et al. (2017). They found activated microglia secrete IL-1α, TNF and C1q to induce A1 astrocyte activation, which lost many traditional functions, including the promotion of synapse formation and function, and overall neuronal survival. Liddelow and colleagues also showed *C3* is one of the most highly up-regulated genes in A1 astrocytes and is not present in A2 astrocytes. Additionally, C3-positive A1 reactive astrocytes were discovered in the human caudate nucleus in Huntington's, in the hippocampus and prefrontal cortex in Alzheimer's, in the motor cortex of amyotrophic lateral sclerosis, in

the substantia nigra of Parkinson's, and in multiple sclerosis neurodegenerative disease tissues (Liddelow et al., 2017; Vilalta and Brown, 2018). A1 astrocytes have since been implicated in mechanisms of synaptic pruning in patient-derived models of schizophrenia (Joshi et al., 2019), further linking inflammation and synaptic function in neurodegenerative disease.

1.9.5 Inflammation in MPS III

The presence of gliosis was first described in the MPS IIIA mouse model by Savas et al. (2004). Astrocytic activation was higher in MPS IIIA mice at 24-weeks of age compared with age-matched controls; in particular, gliosis was observed in the brainstem, superior colliculus, cortex, and white matter tracts.

Hemsley et al. (2009) reported a significantly greater activation of glial cells in the MPS IIIA mouse brain at the younger age of 21-weeks, compared with age-matched unaffected mice. Observed microglial activation was described in the medial, rostral, caudal, cerebral cortical regions, colliculi, cerebellum, thalamus, and hippocampus; activation of astrocytes was also observed in the affected model within similar regions of the mouse brain. Following intravenous and intra-CSF injection of SGSH, there was a marked decrease in the total number of activated microglia, with fewer storage vesicles containing accumulated material in the remaining cells (Hemsley et al., 2009).

In a more recent time-course study, the MPS IIIA mouse model exhibited significant accumulation of lysosomal inclusions corresponding with inflammation from four-weeks through to 18-weeks of age across the cortex, hippocampus, amygdala, and superior and inferior colliculi (Hassiotis et al., 2014a). Such accumulations were also seen throughout the CNS of MPS IIIA and MPS IIIB mouse models, priming microglial activation through

interaction of the toll-like receptor (TLR) 4 and adaptor protein MyD88. This resulted in neuroinflammation and neurodegeneration with the release of pro-inflammatory cytokines IL-1, TNF-α, MCP-1, and MIP-1α (Ausseil et al., 2008; Arfi et al., 2011; Wilkinson et al., 2012; Martins et al., 2015).

In the MPS IIIB mouse model, Ohmi et al. (2003) examined the cortex for the presence of activated microglia. They reported that microglia, regardless of position relative to a neuron, contained large vacuoles with a characteristic appearance of lysosomes engorged with HS and secondary lipids. Moreover, microarray analysis of the same region revealed inflammatory components *C1qa, C1qb, C1qc, C4,* and *Gfap* cDNA transcripts were elevated at three-months of age (Ohmi et al., 2003).

Attempts to treat inflammation and potentially alleviate CNS pathology in MPS III started with the pre-clinical use of a general anti-inflammatory drug, aspirin. In MPS IIIA mice, it effectively lowered inflammation and oxidative stress (Arfi et al., 2011). However, the effects of aspirin on clinical symptoms were not assessed. Another anti-inflammatory drug, prednisolone, was tested and found to be effective at reducing inflammation in peripheral tissues in MPS IIIB mice but failed to have an effect in the brain (Holley et al., 2018). In attempts to alleviate clinical symptoms, anti-inflammatory therapies have undergone early trials in MPS III children, such as the currently active trial (NCT04018755) utilising anakinra, which decreases IL-1 levels in the body. This trial was initiated after pre-clinical experiments in an MPS IIIA mouse model, which underwent genetic knockout of the IL-1 receptor, showed reduced gliosis and prevented behavioural phenotypes (Parker et al., 2020). As the trial is currently active, and it is the first of its kind in MPS III patients, the translatable effects of anti-inflammatories are not yet known.

1.9.6 Inflammation in Lysosomal Storage Disorders

Natural modification of inflammatory factors also occurs in other LSDs, particularly Niemann-Pick disease type C. Indeed, throughout the Niemann-Pick disease type C disease course, the largest group of genes modified involve the immune response and inflammatory pathway. Initiating the complement cascade in this disorder, C1q acts as the primary mediator in synapse removal and marking apoptotic neurons for clearance (Lopez et al., 2012). However, C1q was not up-regulated in areas of neuronal loss or microglial activation in the Niemann-Pick C mouse model, but was up-regulated in other areas, namely the deep cerebellar nuclei and hippocampus. These studies indicated that neuronal death could be driven by isolated cell mechanisms with minimal regulation by the immune response, and neuronal loss therefore occurring without direct influence from complement components (Lopez et al., 2012). Similar with the study by Yasojima et al. (1999), Lopez et al. (2012) observed only the activating complement components and none of the three regulatory factors.

Further investigation into the Niemann-Pick C mouse model sought to determine the effect of elevated complement components on microglia in the cerebellum (Kavetsky et al., 2019). It was discovered that microglia are activated and in contact with dendrites of Purkinje cells at an early age, prior to the onset of cell degeneration. As the cell degeneration progressed with age, accumulation of dendritic material inside the microglia was evident, suggesting microglia contribute to the neurodegeneration in Niemann-Pick disease type C (Kavetsky et al., 2019).

1.10 Research Significance and Outcomes

Evidence of connections between the synapse and the lysosome is strengthening as investigations into the synaptic health in LSDs propagate. However, more comprehensive analyses are required, including the establishment of time-course assessments across various LSDs to evaluate synaptic plasticity over disease course. It would also help to identify the onset of synaptic changes and any possible deterioration or contribution to disease.

Similarly, the emergence of impaired electrophysiological function in LSDs should not go unnoticed. Moreover, mechanistic studies investigating the processes of complement-mediated synaptic pruning following neurodevelopment in the pro-inflamed LSDs would prove useful. Indeed, targeting therapies to restore synaptic function in LSDs could potentially reinforce the foundations leading to stable and improved brain function, and prevent cognitive decline.

This evidence could well lead the LSD field into joining the growing classification of disorders termed ‘synaptopathies’. The status of the lysosome should also perhaps be considered in already classified synaptopathies. By expanding our vision to encompass all synaptic components, we can continue the current rate of progress towards treating neurological diseases and preserve the healthy neuronal circuit.

1.10.1 Hypothesis

To expand understanding on the underlying mechanisms of symptom development in MPS IIIA, this review has highlighted that the synapse warrants further investigation. The hypothesis of this study was that:

Changes in synaptic morphology and function underlie neurological decline in the paediatric neurodegenerative disorder Sanfilippo syndrome (MPS III), and they can be prevented by gene therapy.

1.10.2 Aims

The overall aim of this study was to explore synaptic morphology and function in MPS III, a paediatric-onset lysosomal storage disorder. The specific objectives to achieve this were to:

1. Establish a time-course of changes in the morphology and number of dendritic spines in the cerebral cortex of MPS IIIA mice.
2. Use electrophysiology to elucidate the biological impact of synaptic dysfunction on neuronal activity in MPS IIIA mice.
3. Determine underlying mechanisms contributing to dendritic spine dysgenesis/loss and dysfunction in MPS IIIA.
4. Administer AAV-based gene therapy to MPS IIIA mice prior to the onset of synaptic degeneration to determine whether neurological decline can be prevented.

Overall, the outcomes of this study will increase our understanding of neurological dysfunction in MPS IIIA, and potentially provide therapeutic targets for this presently untreated neurodegenerative disease.

– CHAPTER 2 –

MATERIALS AND METHODS

2.1 Materials

2.1.1 Animal Husbandry

1.5mL Eppendorf Tubes	0030120086; Eppendorf, NSW, Australia
70% Ethanol	EA061-2.5L-P; Chem-Supply, SA, Australia
Rodent Ear Punch	AS500077; Able Scientific, Australia

2.1.2 Genotyping

1.5mL Eppendorf Tubes	0030120086; Eppendorf, NSW, Australia
2x Taqman Gene Expression Master Mix	4369016; ThermoFisher Scientific, MA, USA
2x Taqman Genotyping Master Mix	4371353; ThermoFisher Scientific, MA, USA
40x Custom MPS IIIA Assay Working Stock	CCU001SNR; ThermoFisher Scientific, MA, USA
Chelex 100 Resin	142-1253; Bio-Rad Laboratories, USA
Custom SNP Assay for YFP	CCU001S; ThermoFisher Scientific, MA, USA
Custom Taqman Copy Number Assay for YFP	4331348; ThermoFisher Scientific, MA, USA
MicroAmp Adhesive Film Applicator	4333183; ThermoFisher Scientific, MA, USA

MicroAmp Optical 384-well Reaction Plates	4309849; ThermoFisher Scientific, MA, USA
MicroAmp Optical Adhesive Film	4311971; ThermoFisher Scientific, MA, USA
MicroAmp Support Base	4379590; ThermoFisher Scientific, MA, USA
Sterile Water	2037157; Clifford Hallam Healthcare, SA, Australia
Taqman Copy Number Reference Assay	4458366; ThermoFisher Scientific, MA, USA

2.1.3 Tissue Collection

1mL Syringes	Becton Dickinson, USA
10x Phosphate Buffered Saline (PBS) – Stock (in Milli-Q water)	
1.37M sodium chloride	465-2.5KG; Science Supply Australia, Vic, Australia
27mM potassium chloride	383-500G; Science Supply Australia, Vic, Australia
80mM disodium hydrogen orthophosphate	SA026-500G; Chem-Supply, SA, Australia
20mM potassium dihydrogen orthophosphate	391-500G; Science Supply Australia, Vic, Australia
23G Butterfly Needles	Hamilton Company, NV, USA
50mL Syringes	Becton Dickinson, USA
Anodised Aluminium Brain Slicer	Braintree Scientific, Inc., USA
GEM Stainless Steel Blades	Personna, USA
Paraformaldehyde	P6148-1KG; Sigma-Aldrich, NSW, Australia

2.1.4 Histology

10x Phosphate Buffered Saline (PBS) – Stock (in Milli-Q water)	
1.37M sodium chloride	465-2.5KG; Science Supply Australia, Vic, Australia
27mM potassium chloride	383-500G; Science Supply Australia, Vic, Australia
80mM disodium hydrogen orthophosphate	SA026-500G; Chem-Supply, SA, Australia
20mM potassium dihydrogen orthophosphate	391-500G; Science Supply Australia, Vic, Australia
100% Ethanol	EA043-20L; Chem-Supply, SA, Australia
Acetone	AA008-2.5L; Chem-Supply, SA, Australia
Double-edge Stainless Blades	82133316; Wilkinson Sword, UK
Glycerol	GA010-500M; Chem-Supply, SA, Australia
Low Melt Agarose	1613111; Bio-Rad Laboratories, USA
Normal Donkey Serum	017-000-121; Jackson Immunoresearch Lab, USA
Shandon Embedding Cryomold	1841; ThermoFisher Scientific, MA, USA
Superfrost Plus Coverslips	Menzel-Glaser, Germany
Superfrost Plus Microscope Slides	Menzel-Glaser, Germany
Triton X-100	X100; Sigma-Aldrich, NSW, Australia

2.1.5 Antibodies

Donkey anti-rabbit-Cy3	711-165-152; Jackson Immunoresearch Lab, USA
Donkey anti-rat-Alexa Fluor 594	712-585-153; Jackson Immunoresearch Lab, USA
Rabbit anti-GFAP	Z0334; Dako, Agilent, CA, USA
Rabbit anti-Iba1	019-19741; FUJIFILM Wako Chemicals, USA
Rabbit anti-LAMP1	ab24170; Abcam, Cambridge, UK
Rat anti-C1q	ab11861; Abcam, Cambridge, UK
Rat anti-C3	ab11862; Abcam, Cambridge, UK

2.1.6 Electrophysiology

10x Artificial Cerebrospinal Fluid (ACSF) –

Stock (in Milli-Q water)

125mM sodium chloride	465-2.5KG; Science Supply Australia, Vic, Australia
25mM sodium bicarbonate	S5761-500G; Sigma-Aldrich, NSW, Australia
3mM potassium chloride	383-500G; Science Supply Australia, Vic, Australia
1.25 mM sodium dihydrogen phosphate	S9638-250G; Sigma-Aldrich, NSW, Australia
Acetone	AA008-2.5L; Chem-Supply, SA, Australia
Sodium hypochlorite	ST044-500M; Chem-Supply, SA, Australia

2.1.7 Gene Therapy

27 G Needles	Hamilton Company, NV, USA
70% Ethanol	EA061-2.5L-P; Chem-Supply, SA, Australia
Sodium hypochlorite	ST044-500M; Chem-Supply, SA, Australia

2.1.8 Mass Spectrometry

2,2-Dimethoxypropane	D136808-25ML; Sigma-Aldrich, NSW, Australia
3M Butanolic hydrochloride	87472-50ML-F; Sigma-Aldrich, NSW, Australia
96-Well microtitre plate	655101; Interpath Services, Vic, Australia
Heparan sulphate sodium salt	HO-3105; Celsus Laboratories, USA

2.2 Methods

2.2.1 YFP$^{+/-}$-MPS IIIA Mouse Colony Establishment and Maintenance

In the year prior to commencing this study, a novel YFP$^{+/-}$-MPS IIIA mouse colony was established in the Childhood Dementia Research Group (CDRG) by Mr Andrew Shoubridge to improve the resolution and quality of neuromorphological assessments. The model uses a murine *Thy1* promoter (thymus cell antigen 1) at transgenic (reporter) insertion H to express yellow fluorescent protein (YFP). The regulatory elements comprise a 6.5 kilobase fragment obtained from the 5' portion of the *Thy1* gene, extending from the promoter to the intron, following exon 4, but lacking exon 3 and the flanking introns, resulting in subsets of neurons expressing the YFP. The deleted sequences cause no detectable expression in non-neuronal cells. The line was termed '*thy1-YFP-H'* due to the type of fluorescent protein expressed and transgenic insertion location and was one of multiple strains originally developed to image multiple neuronal subsets with differing spectral variants (Feng et al., 2000). Approximately 10-30% of sensory neurons are labelled in the dorsal root ganglia; layer 5 pyramidal neurons are selectively labelled in the cerebral cortex; pyramidal neurons are selectively labelled in the hippocampus; mossy fibres are labelled in the cerebellar cortex; and approximately 10-30% of retinal ganglion cells are labelled in the retina. Neurons are illuminated all the way to synaptic terminals for a strong and specific Golgi-like stain, with minimal labelling of nearby axons (Figure 2.1).

Two female and two male YFP hemizygous mice (B6.Cg-Tg(Thy1-YFP)HJrs/J; JAX Stock #003782) were purchased from the Jackson Laboratory, Bar Harbour, Maine, USA. Two female and two male congenic MPS IIIA mice (B6; Cg-Sgsh^{mps3a}) were obtained from the in-house colony established and maintained at the Women's and Children's Hospital Health Network, North Adelaide, South Australia, Australia. All husbandry, procedures,

and experiments were undertaken in the Animal Care Facility at the Women's and Children's Hospital Health Network, with the approval of the Animal Ethics Committees of the University of Adelaide (M-2017-118) and Women's and Children's Hospital Health Network (AE#1030/12/2018, AE#1032/12/2018, AE#1073/11/2020, AE#1091/06/2021, AE#1108/12/2021). Gene technology approval (B144/12/2020) was obtained from the Biosafety Committees of the Women's and Children's Hospital Health Network and the University of Adelaide. All research was conducted in accordance with the National Health and Medical Research Council's *Australian Code for the Care and Use of Animals for Scientific Purposes (8th Edition)*.

Mice were housed in a constant temperature and humidity-controlled facility with a 14-hour light to 10-hour dark cycle, with food and water provided *ad libitum*. For environmental enrichment, mice were provided with plastic houses, cardboard, and tissue paper. The date of birth for mouse pups was recorded as the date on which the pups were first observed. For identification, mice were ear-notched between 14- to 21-days of age; the notched tissue was subsequently utilised for genotyping. Weaning of mice occurred at approximately 21-days of age, after which they were housed in same-sex groups of similar ages. The mice were monitored daily, and body weight was measured weekly. The overall physical health of newborn pups through to adult animals was assessed, with any abnormalities or changes recorded. After five generations, the mice were backcrossed to the C57Bl/6 colony to restore any genetic drift. Following the backcross for these studies, mice were bred, and tissues harvested, for up to five generations.

Hemizygous single-copy YFP ($YFP^{+/-}$) with heterozygous or unaffected MPS IIIA ($SGSH^{+/+}$ / $SGSH^{+/-}$) mice were classified as wild-type, and $YFP^{+/-}$ with homozygous MPS IIIA ($SGSH^{-/-}$) classified as MPS IIIA mice. Both sub-types were used in the

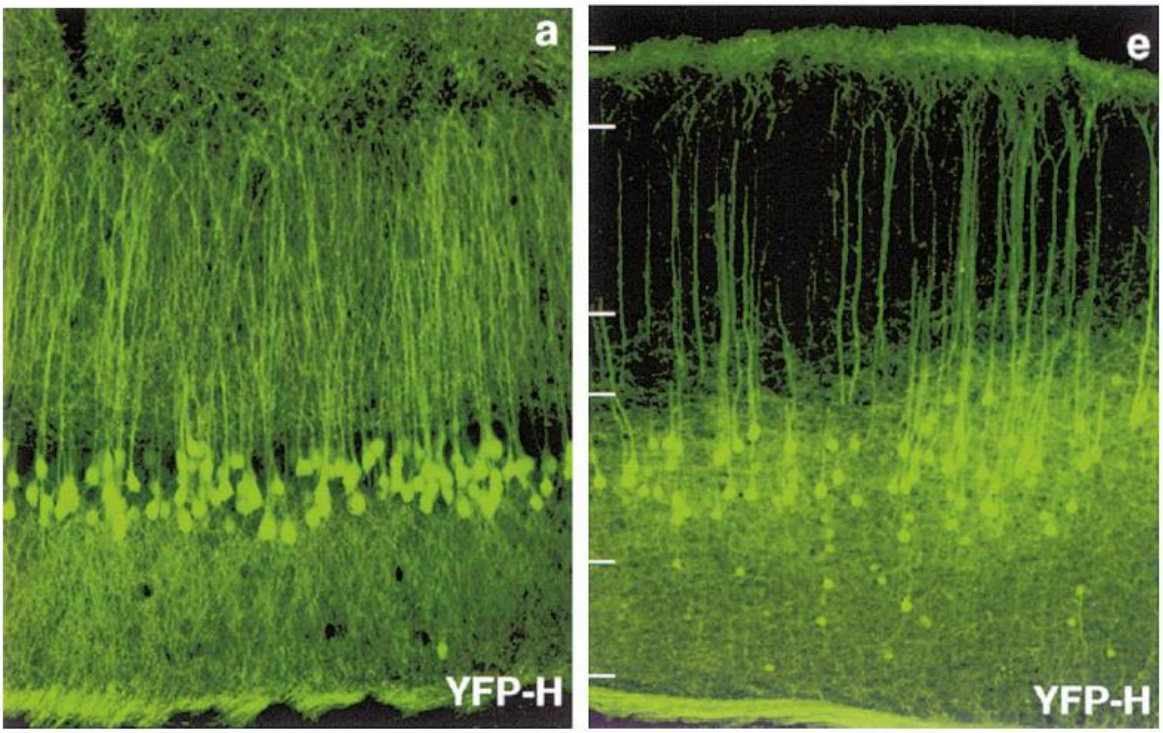


Figure 2.1 – Expression of fluorescent protein in transgenic mice. Representative images of neuronal subsets expressing fluorescent protein within the YFP-H transgenic mouse line. Expression can be seen in the hippocampus of multiple neurons (A). This project utilised the YFP-H line which specifically highlighted layer 5 pyramidal neurons in the cerebral cortex (E). (Adapted from Feng et al. 2000).

histological, electrophysiological, and behavioural assessments constituting this project.

2.2.2 Mouse Ear Notching

Between 14- to 21-days of age, mice were moved from the mother's cage and placed on soft tissue in a separate cage. Individual mice were then handled on a bench-coat and notched at the ear with small ear punch scissors, corresponding to a designated identification number (Figure 2.2). The scissors and forceps were sterilised with 70% ethanol and wiped dry prior to each punch. Using the forceps, the notched tissue was placed into a sterilised 1.5 mL Eppendorf tube and temporarily stored on ice. After notching, the mice were returned to the dam ahead of weaning and monitoring. The tubes on ice were transferred to -20^{o}C for long-term storage and subsequent genotyping.

2.2.3 Genotyping YFP$^{+/-}$-MPS IIIA Mice

2.2.3.1 Genomic DNA Lysis from Mouse Tissue

Under sterile conditions, 100µL of well-vortexed 10% (w/v) Chelex-100 in sterile water was added to a tube containing the mouse tissue. Tubes were then vortexed briefly, ensuring the tissue was immersed in the Chelex-100 solution, and then immediately transferred to a heating block set at 100^{o}C for 10 minutes. Tubes were then vortexed briefly and returned to the heating block at 100^{o}C for a further 10 minutes. Following the incubation, cellular debris and Chelex-100 particles were pelleted by spinning in a bench centrifuge for two minutes at 13,000 rpm. The supernatant containing genomic DNA was then used immediately for quantification or stored at -20^{o}C.

2.2.3.2 Quantification of Genomic DNA

Genomic DNA was quantified using a NanoDrop 1000 Spectrophotometer (ND-1000; ThermoFisher Scientific, Waltham, MA, USA) loaded with the ND-1000 v3.7.0 software

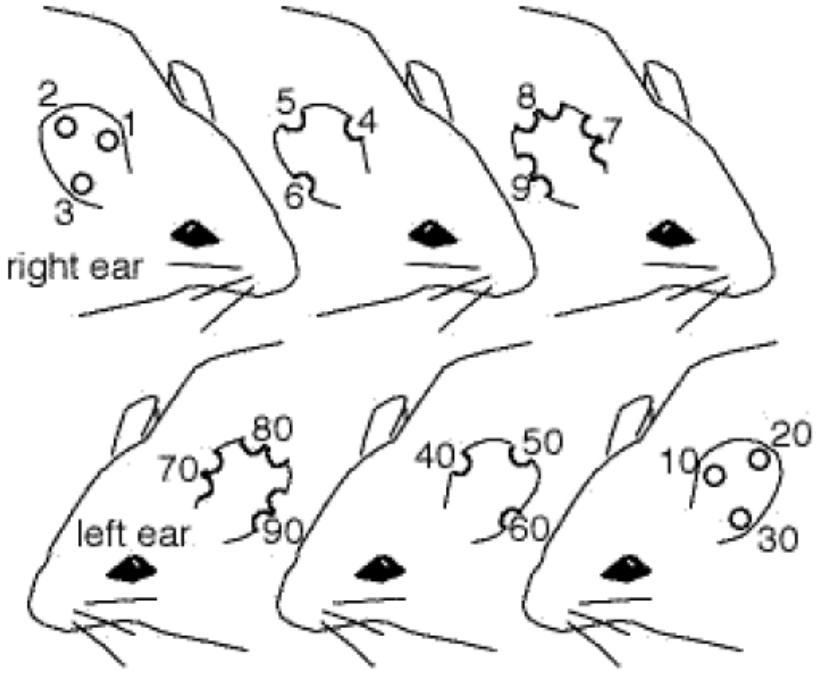


Figure 2.2 – Mouse ear-notching chart. Illustrated guide for the different patterns of ear-notching for identification. Notched tissue was also used for genotyping the mice.

under the “Nucleic Acid” selection. Following the software directions, the ND-1000 was calibrated by loading 2µL of Milli-Q water onto the ND-1000 pedestal. Following the software directions, the ND-1000 was then “blanked” using a new loading of 2µL of Milli-Q water. Genomic DNA was measured by subsequent loadings of 1µL of DNA sample onto the ND-1000 pedestal. The amount of DNA (ng/µL) was recorded, and the pedestal wiped clean between samples. From the recordings, genomic DNA dilutions were calculated to a final concentration of either 5ng or 1ng in 1µL of sterile water using the following equations:

Genomic DNA volume (µL) = 200ng / [neat genomic DNA recording (ng/µL)]

Sterile water volume (µL) = 200µL – genomic DNA volume (µL) (for 1ng/µL)

or

Sterile water volume (µL) = 40µL – genomic DNA volume (µL) (for 5ng/µL)

The genomic DNA dilutions of 1ng/µL and 5ng/µL were used immediately for genotyping or stored at -20^{o}C.

2.2.3.3 Genotyping Assay for Sulphamidase in YFP$^{+/-}$-MPS IIIA Mice

All genotyping assays were conducted with thawed DNA samples as prepared in Methods (2.2.3.1 and 2.2.3.2). The genotyping assays were conducted in sterile conditions within a designated pre-PCR cabinet. Genotyping assays were established under the guidance of Dr Adeline Lau (CDRG). A Taqman custom single nucleotide polymorphism (SNP) genotyping assay was used to differentiate the zygosity of the *SGSH* gene in YFP$^{+/-}$-MPS IIIA tissue. In a sterile Eppendorf tube, a “master-mix” was created, with each component multiplied by the number of samples being tested. Also included were two negative control samples (using sterile water in place of genomic DNA), three positive controls (unaffected,

heterozygous, and homozygous recessive), and one spare for pipetting inaccuracies. The master-mix contained 3.75µL of sterile water, 5µL of 2x Taqman Genotyping Master Mix, and 0.25µL of 40x MPS IIIA SNP Custom Assay Working Stock. The MPS IIIA SNP Custom Assay Working Stock contained the forward primer (5' ACG CCC TCT GCT CTG TCT TC 3'), reverse primer (5' GCG ATG GCA GTG TTG TTG TAT AC 3'), wild-type probe (5' VIC-TCA GCG GAT GAC GG-NFQ-MGB 3'), and mutant probe (5' FAM-TCA GCG AAT GAC GG-NFQ-MGB 3'). The master-mix was then vortexed, and 9µL was aliquoted into each well of a 384-well reaction plate, followed by 1µL of the negative control into two of the wells. The plate was transferred to a separate bench, where 1µL of 1ng/µL genomic DNA was added to each corresponding well. The plate was sealed, centrifuged for about 20 seconds in a plate centrifuge, and inserted into the QuantStudio 7 Flex Real-Time Polymerase Chain Reaction (PCR) System. The targeted sequences were amplified with a 30-second pre-read stage at 60^{o}C, a 10-minute holding stage at 95^{o}C, 40 cycles at the PCR amplification stage with 15-seconds of 95^{o}C followed by 1-minute of 60^{o}C, concluding with a 30-second post-read stage. At the conclusion of the reaction, data were exported to a PC for use with the QuantStudio Real-Time PCR software to generate an Allelic Discrimination Plot, which visualises the SGSH genotype for each sample (Figure 2.3A).

2.2.3.4 Genotyping Assay for YFP *in YFP$^{+/-}$-MPS IIIA Mice*

A Taqman custom SNP genotyping assay was used to differentiate the zygosity of the *YFP* transgene in YFP$^{+/-}$-MPS IIIA tissue under the guidance of Dr Adeline Lau (CDRG). In a sterile Eppendorf tube, a "master-mix" was created, with each component multiplied by the number of samples being tested. Also included were two negative control samples (using sterile water in place of genomic DNA), and two positive controls (a hemizygous YFP

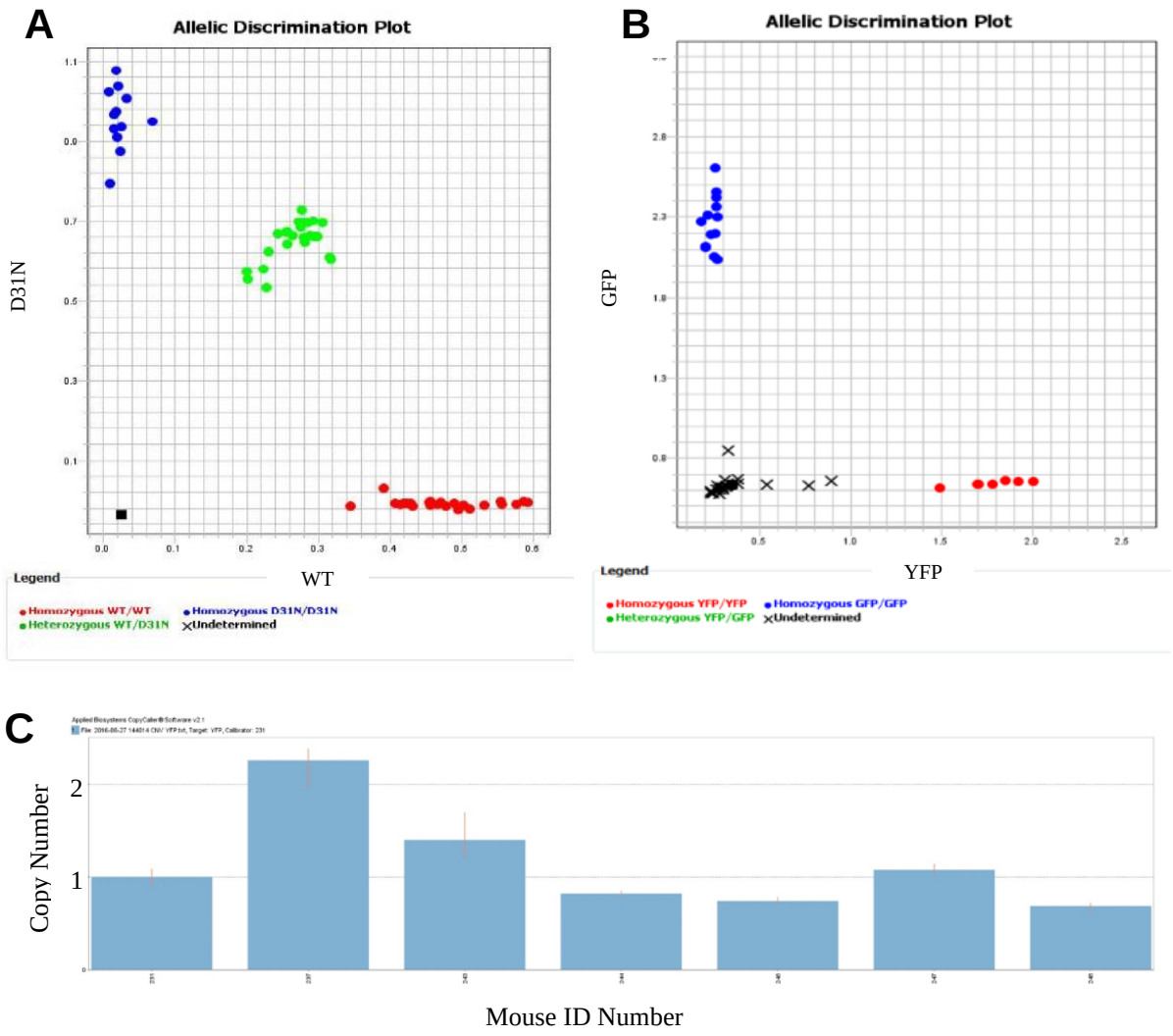


Figure 2.3 –Outputs of genotyping assays. Representative images of the outputs generated by Taqman custom SNP genotyping assays for YFP$^{+/-}$-MPS IIIA mice. The allelic discrimination plot for the *SGSH* gene (A) visualises the genotypes of individual mice as MPS IIIA (blue), heterozygous (green), unaffected (red), and negative control (black). The allelic discrimination plot for the *YFP* transgene (B) visualises positive expression in individual mice of YFP (red), and non-fluorescence (black). The CopyCaller histogram (C) visualises the zygosity of individual mice expressing YFP with copy number on the y-axis, and individual samples listed on the x-axis.

single-copy and a homozygous YFP double-copy), and one spare for pipetting inaccuracies. The master-mix contained 1.75µL of sterile water, 2.5µL of 2x Taqman Genotyping Master Mix, and 0.25µL of 20x YFP-VIC SNP Custom Assay Working Stock. The YFP-VIC SNP Custom Assay Working Stock contained the forward primer (5' GCA CCA CCG GCA AGC T 3'), reverse primer (5' AGT CGT GCT GCT TCA TGT GGT 3'), and YFP probe (5' VIC-ACC ACC TTC GGC TAC G-NFQ-MGB 3'). The master-mix was then vortexed; 4.5µL was aliquoted into each well of a 384-well reaction plate, followed by 0.5µL of the negative control into two of the wells. The plate was transferred to a separate bench, where 0.5µL of 5ng/µL genomic DNA was added to each corresponding well. The plate was sealed, centrifuged for about 20-seconds in a plate centrifuge, and inserted into the QuantStudio 7 Flex Real-Time PCR System (ThermoFisher Scientific, Waltham, MA, USA). The targeted sequences were amplified with a 30-second pre-read stage at 60^{o}C, a 10-minute holding stage at 95^{o}C, 40 cycles at the PCR amplification stage with 15-seconds of 95^{o}C followed by 1-minute of 60^{o}C, concluding with a 30-second post-read stage. At the conclusion of the reaction, data were exported to a PC for use with the QuantStudio Real-Time PCR software to generate an Allelic Discrimination Plot, which visualises the YFP-expressing genotype for each sample (Figure 2.3B).

2.2.3.5 Genotyping Assay for YFP *Copy Number in YFP$^{+/-}$-MPS IIIA Mice*

A Taqman custom SNP genotyping assay was also used, under the guidance of Dr Adeline Lau (CDRG), to differentiate expressing hemizygous YFP single-copy from homozygous YFP double-copy in YFP$^{+/-}$-MPS IIIA tissue. In a sterile Eppendorf tube, a "master-mix" was created, with each component multiplied by the number of samples being tested. Also included were two negative control samples (using sterile water in place of genomic DNA), and two positive controls (a hemizygous YFP single-copy and a homozygous YFP

double-copy), and one spare for pipetting inaccuracies. The master-mix contained 2µL of sterile water, 5µL of 2x Taqman Genotyping Master Mix, 0.5µL of Taqman Copy Number Reference Assay, and 0.5µL of 20x YFP-FAM SNP Custom Assay Working Stock. The YFP-FAM SNP Custom Assay Working Stock contained the forward primer (5' GCA CCA CCG GCA AGC T 3'), reverse primer (5' AGT CGT GCT GCT TCA TGT GGT 3'), and YFP probe (5' FAM-ACC ACC TTC GGC TAC G-NFQ-MGB 3'). The master-mix was then vortexed; 8µL was aliquoted into each well of a 384-well reaction plate, followed by 2µL of the negative control into two of the wells. The plate was transferred to a separate bench, where 2µL of 5ng/µL genomic DNA was added to each corresponding well. The plate was sealed, centrifuged for about 20-seconds in a plate centrifuge, and inserted into the QuantStudio 7 Flex Real-Time PCR System (ThermoFisher Scientific, Waltham, MA, USA). The targeted sequences were amplified with a 2-minute pre-read stage at 50^{o}C, a 10-minute holding stage at 95^{o}C, 40 cycles at the PCR amplification stage with 15-seconds at 95^{o}C followed by 1-minute at 60^{o}C. At the conclusion of the reaction, data were exported to a PC for use with the QuantStudio Real-Time PCR software and CopyCaller v2.1 software to generate a histogram which visualises the number of YFP copies for each sample against the positive controls (Figure 2.3C).

2.2.4 Perfusion Fixation

Fixative constituting 4% paraformaldehyde (PFA; w/v) in 1x PBS (pH 7.4) was prepared fresh each morning of euthanasia and tissue collection and kept at 4^{o}C or on ice until use. Mice were humanely euthanised in an isolated holding chamber to minimise distress to all animals. Euthanasia occurred via CO_2 overdose at a rate of 0.5-1 L/minute, with confirmation of death by the absence of a corneal reflex and a pain reflex by a toe pinch.

Within a fume hood, individual mouse limbs were pinned to a Styrofoam board to anchor the mouse steady. Using surgical scissors, the abdominal cavity was opened to reveal the diaphragm. The diaphragm and rib cage were carefully cut away to expose the heart; a 23G butterfly needle connected to the perfusion apparatus was then used to puncture the left ventricle of the heart. The butterfly needle was anchored to the Styrofoam board with pins to maintain the connection with the heart during the perfusion process. Using surgical scissors, the right auricle was cut to provide an escape route for blood and initial perfusate of ice-cold PBS. Approximately 10-20 mL of PBS was perfused prior to switching to 4% PFA to ensure blood was cleared from tissues. A sufficiently cleared sample was determined by a pale-brown liver compared with the fresh red-brown liver. Approximately 20 mL of 4% PFA was perfused to ensure fixation of the tissue, which was confirmed by muscle stiffening and tail/limb twitching.

After approximately 20 mL of 4% PFA was perfused through the mouse, the head was decapitated, and the brain swiftly removed. The brain was placed into an ice-cold brain slicer and cut sagittally down the mid-line using a GEM blade to separate the two hemispheres. The hemispheres were separately and immediately immersed in 4% PFA for seven-days at 4^{o}C and then transferred to PBS for long-term storage at 4^{o}C. In addition to the brain, eyes, liver, and spleen were also collected.

2.2.5 Dendritic Spine Visualisation and Quantification

In the year prior to this PhD candidature, YFP$^{+/-}$-MPS IIIA mice were bred and aged to three- and six-weeks (pre-symptomatic), 12-weeks (early-symptomatic), and 20-weeks (late-symptomatic). For dendritic spine characterisation, six mice per genotype per age were allocated. Following euthanasia and perfusion fixation, the left-brain hemisphere was kept at 4^{o}C in PBS until use for sectioning and imaging.

2.2.5.1 Brain Section Preparation

Firstly, a spirit level was used to identify a flat area on the work bench. Cryomolds were then placed on this area. Six-percent low-melt agarose (w/v) in 1x PBS was gently heated in a microwave until dissolved, and mixed. The agarose solution was monitored with a thermometer and left to cool to approximately 37^{o}C. Using a brain slicer and GEM blade, a coronal cut was made into the cerebellum of the left hemisphere to create a flat surface on the posterior side of the brain. The brain tissue was then transferred into a cryomold on the flat surface, and the cooled agarose was carefully poured into the cryomold until the tissue was completely covered, taking care to ensure no bubbles were present around the tissue. The mold was left on the bench to set (gel turned opaque and firm). Once cooled and hardened, the embedded tissue was removed from the cryomold and stored in PBS at 4^{o}C in the dark until use for sectioning.

Embedded tissues were then fixed to the mounting stage of a Leica VT1000S Vibrating-Blade microtome (vibratome) (Leica, Germany) with superglue. Once the glue was set, the stage was then secured inside the sample chamber affixed to the vibratome. Chilled PBS was then poured into the chamber until the tissue was completely immersed. The vibrating blade was programmed to move at a slow speed and high frequency due to the softer nature of the sample. The razor blade was gently and carefully wiped with acetone to remove any oil residue, washed in 100% ethanol, then dried before carefully securing in the blade-holder. To ensure slices were thin enough to be viewed completely by confocal microscopy yet retain a high level of dendritic branching for characterisation, sections were cut at a thickness of 90µm. Using a mouse brain atlas for guidance (Paxinos and Franklin, 2004), serial coronal sections were collected for assessment from approximately 6.26mm interaural (2.46mm from bregma), which included the motor cortical region. Sections were mounted onto slides with anti-fade medium constituting glycerol and PBS (ratio of 9:1),

and cover-slipped. Slides were sealed with nail polish, and then stored at 4^{o}C in the dark until use for imaging. Remaining embedded tissue was carefully removed from the mounting stage with a blade and returned to storage in PBS at 4^{o}C in the dark.

2.2.5.2 Dendritic Spine Imaging and Analysis

Prior to imaging, mouse genotypes and ages were blinded to the candidate. To produce the resolution necessary to characterise dendritic spine density and morphology, sections were imaged on a Leica TCS SP8 X spectral scanning confocal microscope (Leica, Wetzlar, Germany) with an oil-immersion 63x objective lens and a 2x digital zoom. Voxel size was cubic at 0.09x0.09x0.09µm for greatest image accuracy as data were not stretched between z-planes, which would occur with larger z-steps. Larger pixel sizes could also fail to capture smaller/thinner spines (Dickstein et al., 2016). Lines were accumulated twice, and final frames averaged three-times per image acquisition to reduce noise. The YFP was excited with 514nm excitation at 15% power and visualised with a PMT detector at 521nm-565nm emission range, gain 613V, and offset -0.21%. Six dendritic segments per neuron, six neurons per mouse, and six mice per genotype per age were evaluated.

The z-stacks acquired by confocal microscopy were then exported and processed with Imaris software (v9.3.1; Bitplane, Belfast, UK). Raw images were rendered as maximum intensity stacks (Fig 2.4A), and a threshold was used to identify the dendrite and dendritic spine structures (Fig 2.4B). The Imaris software then generated a three-dimensional model for analysis (Fig 2.4C), highlighting the total population of dendritic spines along the dendrite. Combined with the use of a “Classify Spines” plug-in by MATLAB (vR2017b; MathWorks, MA, USA), dendritic spines were classified into the different morphologies of filopodia, stubby, thin, and mushroom, and then quantified (Fig 2.4D). Resultant data were subsequently exported for unblinding and statistical analysis.

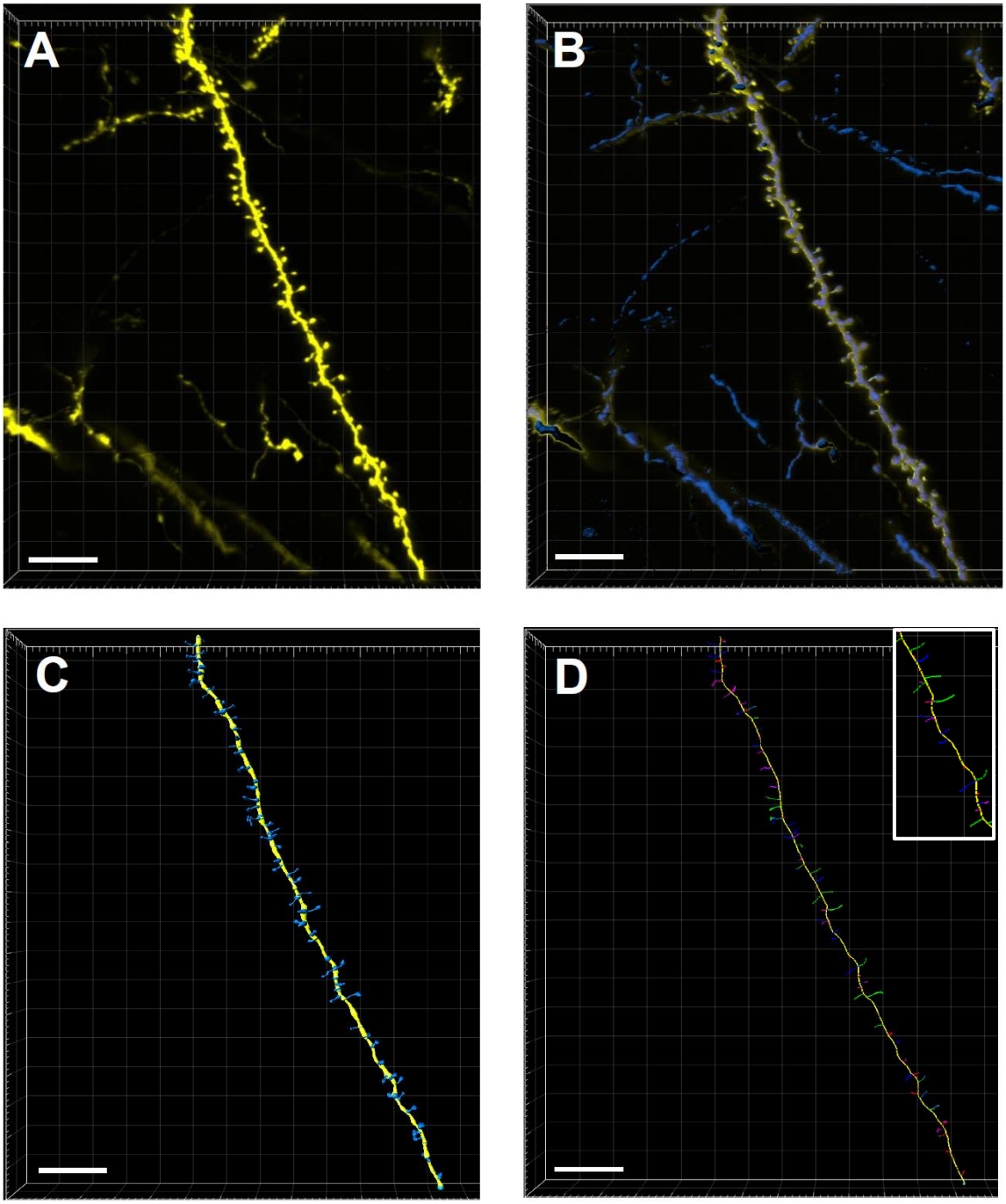


Figure 2.4 – Visualisation and quantification of dendritic spines. Representative images of a YFP dendrite undergoing dendritic spine classification with Imaris software. The software used a raw confocal image (A) to establish a threshold for the dendrite and dendritic spine structures (B) and created a model for three-dimensional analysis (C). Spines were then classified into their sub-types and quantified (D). The magnified insert shows filopodia (purple), stubby (red), thin (blue), and mushroom (green). Scale bar is 10µm.

2.2.6 Immunofluorescence

2.2.6.1 Immunofluorescence Staining

All immunofluorescence assays were conducted with the same protocol, on free-floating sections. Coronal sections of 20µm thickness from the same samples described in 2.2.5.1 containing the motor cortical region for assessment were cut on a Lecia VT1000S vibratome (Leica, Germany). On a rocking platform and at room temperature for all steps, sections were initially washed with 0.3% Triton in 1x PBS (pH 7.4). Sections were then blocked with 5% normal donkey serum (NDS) in 0.3% Triton in 1x PBS (pH 7.4) for two-hours. Overnight, sections were incubated with primary antibodies in 5% NDS in 0.3% Triton in 1x PBS (pH 7.4). The primary antibody specifications are illustrated in Table 2.1. The next day, sections were washed with 0.3% Triton in 1x PBS (pH 7.4), and then incubated with secondary antibodies in 1x PBS (pH 7.4) for three-hours in the dark. The secondary antibody specifications are illustrated in Table 2.2. Lastly, in the dark, sections were washed in 1x PBS (pH 7.4) and mounted onto slides with anti-fade medium constituting glycerol and 1x PBS (ratio of 9:1), and cover-slipped. Slides were sealed with nail polish, and then stored at 4^{o}C in the dark until use for imaging

2.2.6.2 Immunofluorescent Imaging

Mouse genotypes and ages were blinded to the candidate. Slides were imaged on a Leica TCS SP8 X spectral scanning confocal microscope (Leica, Wetzlar, Germany) with an oil-immersion 40x objective lens. Voxel size was cubic at 0.3x0.3x0.3µm. Lines were accumulated twice, and final frames averaged three-times per image acquisition to reduce noise. The YFP was excited with 514nm excitation at 15% power and visualised with a PMT detector at 521nm-565nm emission range, gain 671V, and offset 0%. C1q was visualised at 588nm excitation with 15% power and captured with a HyD detector at

Table 2.1 – Primary antibodies used and their dilutions.

Primary Antibody	Dilution
Rat anti-C1q	1:50
Rabbit anti-Iba1	1:200
Rat anti-C3	1:400
Rabbit anti-GFAP	1:3200
Rabbit anti-LAMP1	1:200

Table 2.2 – Secondary antibodies used and their dilutions.

Secondary Antibody	Dilution
Donkey anti-rat-Alexa Fluor 594 (C1q)	1:200
Donkey anti-rabbit-Cy3 (Iba1)	1:200
Donkey anti-rat-Alexa Fluor 594 (C3)	1:600
Donkey anti-rabbit-Cy3 (GFAP)	1:200
Donkey anti-rabbit-Cy3 (LAMP1)	1:200

603nm-651nm emission range, gain 19V, and offset 0%. Ionised calcium-binding adaptor molecule 1 (Iba1) was visualised at 548nm excitation with 15% power and captured with a HyD detector at 560nm-594nm emission range, gain 21V, and offset 0%. Complement component 3 (C3) was visualised at 588nm excitation with 15% power and captured with a PMT detector at 598nm-650nm emission range, gain 655V, and offset 0%. Glial fibrillary acidic protein (GFAP) was visualised at 554nm excitation with 15% power and captured with a PMT detector at 556nm-599nm emission range, gain 513V, and offset 0%. LAMP1 was visualised at 554nm excitation with 15% power and captured with a PMT detector at 556nm-599nm emission range, gain 516V, and offset 0%. Z-stacks were then exported for image analysis.

2.2.6.3 Immunofluorescent Analysis

To calculate the levels of inflammatory cytokines, glial cells, and the effect of gene therapy in the motor cortical area, Fiji (ImageJ) software (Schindelin et al., 2012) was used. Controls without primary and secondary antibodies were included within each assay to establish an individual threshold for each fluorophore, which was then applied consistently to each image. Data were obtained as the percentage of positive immunofluorescence within the imaged region. The number of A1-type astrocytes was determined by manually counting the number of GFAP-positive astrocytes that were also positive for C3, as a percentage of the total GFAP-positive astrocytes within the imaged region. All data were then exported for unblinding and statistical analysis.

To quantify the recruitment of glial cells to YFP neurons, the z-stacks acquired by confocal microscopy were processed with Imaris software (v9.3.1; Bitplane, Belfast, UK). The GFAP, Iba1, and YFP channels were individually thresholded to determine positively-stained area and were then rendered into three-dimensional surfaces. Using the “Distance

Transformation XTension", the distance between the two surfaces was measured for individual voxels, and then listed for each surface. Resultant data were subsequently exported for unblinding and statistical analysis.

2.2.7 Electrophysiology

2.2.7.1 Brain Slice Preparation

To conduct electrophysiological recordings, *ex vivo* brain slices were prepared from three-, six-, and 12-week-old $YFP^{+/-}$-MPS IIIA mice. On the morning of tissue collection, fresh artificial cerebrospinal fluid (ACSF) was prepared for slicing, containing 125mM NaCl, 25mM $NaHCO_3$, 3mM KCl, 1.25mM NaH_2PO_4, 25mM glucose, 3mM sodium pyruvate, 1mM $CaCl_2$, 6mM $MgCl_2$, pH 7.4, oxygenated with 95% oxygen and 5% carbon dioxide, and stored at 4^{o}C. Due to the separate location of the animals in the Animal Care Facility at the Women's and Children's Hospital Health Network, North Adelaide, South Australia, Australia, and the experiments conducted at the South Australian Health and Medical Research Institute (SAHMRI), North Terrace, Adelaide, South Australia, Australia, a portion of the oxygenated slicing ACSF was made into a frozen slushy. The slushy was designed to drastically reduce the metabolism of the tissue and preserve cellular integrity during transport between facilities.

At the animal facility, animals were anesthetised by inhalation of isoflurane and then decapitated. Isoflurane was used in place of carbon dioxide (used for all other euthanasia procedures), as carbon dioxide overdose creates a hypoxic environment for the brain which leads to neuronal death. The brain was rapidly removed, with ACSF from the slushy periodically applied to the brain to slow tissue deterioration. The brain was then separated into the left and right hemispheres, and then submerged in the ACSF frozen slushy (surrounded by wet ice) for transport.

Upon arrival at SAHMRI, the left hemisphere was fixed with superglue to the mounting stage of a Leica VT1000S vibratome (Leica, Germany) on a bed of ice. ACSF from the slushy was periodically applied to the brain while the glue set to slow tissue deterioration. Once the glue had set, the stage was then secured inside the sample chamber affixed to the vibratome, which was filled with ice-cold ACSF slicing solution. The bath surrounding the chamber was filled with ice to keep the solution and tissue cold. The vibrating blade was aligned at a 15^{o} angle to the coronal plane and programmed to move at a slow speed and high frequency, due to the softer nature of the sample. Single-use, double-bevelled stainless-steel blades (Part No. 7550/1/SS; Campden Instruments, Leicester, England, UK) were specially chosen to provide the cleanest cuts into the brain and minimise tearing and rough-cutting trauma to the tissue. The blades were gently and carefully wiped with acetone to remove any oil residue, washed in 100% ethanol, then dried prior to securing in the blade-holder. Regardless of the quality of the blade, the cells nearest to the cut edges of the tissue were highly likely to die. Therefore, hemi-coronal sections were cut at a thickness of 300µm to ensure healthy cells were captured and to preserve their dendritic tree. Using a mouse brain atlas for guidance (Paxinos and Franklin, 2004) sections were cut to approximately 2.86mm interaural distance (-0.94mm from bregma), which included the motor cortical region (consistent with the other experimental assessments). As they were cut, *ex vivo* slices were carefully transferred to a holding chamber within a Braincubator^{TM} (Western Sydney University, Kingswood, NSW, Australia) containing fresh recording ACSF for 10- to 30-minutes at 32^{o}C. Ten-minutes after the final slice was transferred to the Braincubator, the temperature was reduced to 15^{o}C where it remained. The Braincubator was designed to administer carbogen (95% oxygen and 5% carbon dioxide) and carefully regulate the temperature in addition to pH of the ACSF while it was passed through a UVC filtration system to minimise bacteria levels. Collectively, this dramatically increased the lifespan and integrity of the brain slices (Buskila et al., 2014;

Cameron et al., 2017). The recording ACSF contained 125mM NaCl, 25mM $NaHCO_3$, 3mM KCl, 1.25mM NaH_2PO_4, 25mM glucose, 3mM sodium pyruvate, 2mM $CaCl_2$, 1mM $MgCl_2$, pH 7.4, and was oxygenated with 95% oxygen and 5% carbon dioxide. Slices were given at least 45-minutes to recover from the cutting procedure. Recordings from slices were made between one- and nine-hours after slice preparation.

2.2.7.2 Whole-cell Patch-clamp Recording

Individual brain slices were transferred as needed from the Braincubator into a recording chamber at room temperature (21˚C). The recording chamber was continually perfused at 0.32 mL/minute with recording ACSF solution, and continuously bubbled with 95% oxygen and 5% carbon dioxide. The recording chamber was situated on a Scientifica Motorised Movable Top Plate (Scientifica, East Sussex, England, UK) (Fig 2.5; yellow arrow). Recordings were made on YFP-positive layer 5 pyramidal neurons within the motor cortical region. To visualise these cells, a combination of infrared Differential Interference Contrast microscopy and fluorescent microscopy was utilised. A PCO.Panda 4.2 digital camera (PCO Imaging, Kelheim, Germany) (Fig 2.5; red arrow) attached to an upright Olympus BX51WI microscope (Olympus, Tokyo, Japan) equipped with a 40x water-immersion objective lens and infrared filter, helped to navigate the tissue. A CoolLED pE-300 illumination unit (CoolLED, Andover, England, UK) was used to emit light at 475nm to stimulate neurons expressing YFP, and then visualised with a YFP filter. The infrared DIC was used to visualise the health of the neurons. Neurons were healthy if they presented with a round and plump soma. Shrunken somata, or somata with a sharp visual contrast were not selected for patching.

Patch-clamp pipettes were prepared from fire-polished borosilicate glass capillaries with an external diameter of 1.5mm and internal diameter of 0.86mm (Item No. BF150-86-10;

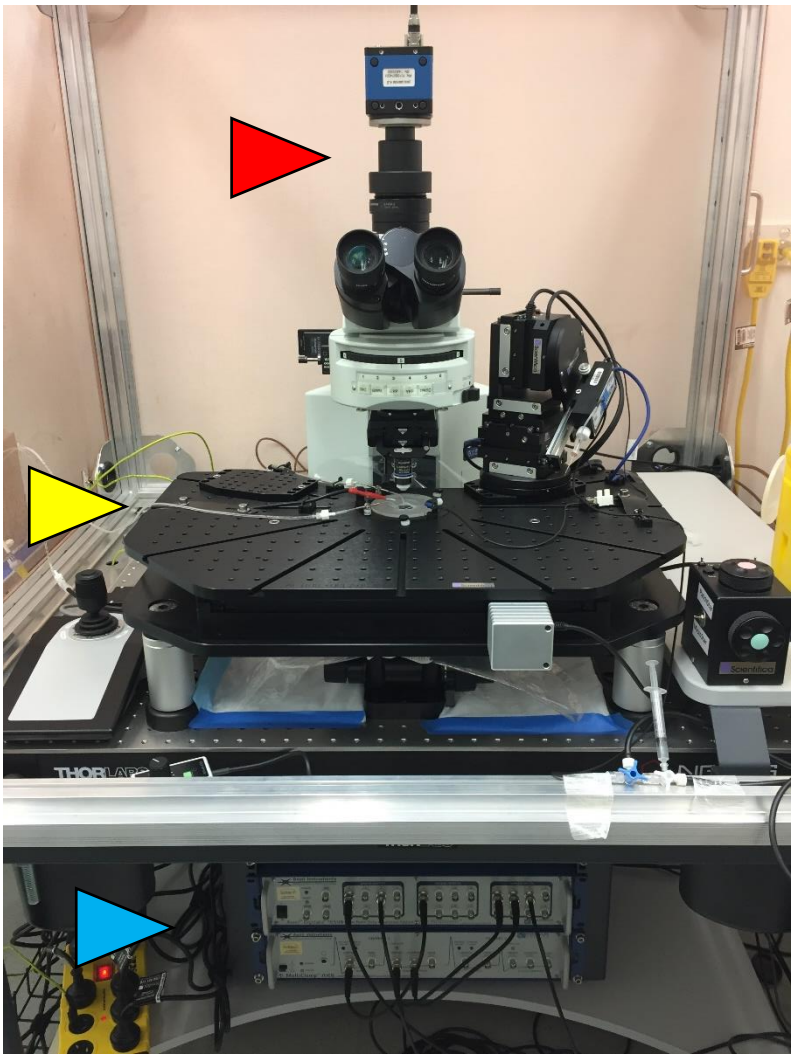


Figure 2.5 – Equipment set-up for electrophysiology. The arrangement of equipment within the electrophysiology rig for whole-cell patch-clamp recordings. A digital camera (red arrow) attached to an upright microscope captured the images of YFP-positive neurons in *ex vivo* brain slices. Brain slices were held in the recording chamber on the motorised stage (yellow arrow) during recordings. Trace data of recordings were amplified and digitised (blue arrow) prior to display and analysis. The rig was surrounded by a copper wire Faraday cage to minimise external electrical noise.

Sutter Instrument, Novato, CA, USA) on a P-1000 Micropipette puller (Sutter Instrument, Novato, CA, USA). Recording pipettes were then filled with internal solution containing 130mM potassium gluconate, 6mM KCl, 4mM NaCl, 10mM Na-HEPES, 0.2mM potassium-EGTA, 0.3mM GTP, 2mM Mg-ATP, 0.2mM cAMP, 10mM D-glucose, 0.15% biocytin, and 0.06% rhodamine, with a final open tip resistance of 3-5 MΩ. The pH and osmolarity of the internal solution were close to physiological conditions (pH 7.3; 290–300mOsmol).

Whole-cell recordings were amplified and digitised via a Digidata 1550B and MultiClamp series 700B (Molecular Devices, San Jose, CA, USA) (Fig 2.5, blue arrow). All current and voltage recordings were low-pass filtered (DC to 20 kHz), and acquired by pClamp software (v10.3; Molecular Devices, San Jose, CA, USA). Whole-cell recorded membrane potential values were adjusted and accounted for pipette offset, and the recording electrode capacitance was compensated for in cell-attached mode. Evoked action potentials were recorded in current-clamp at the resting membrane potential and at -60mV, which was close to the anion reversal potential. Spontaneous action potentials were recorded at resting membrane potential in current-clamp. Synaptic events were observed exclusively in voltage-clamp at -60 mV. Spontaneous synaptic events were recorded with a supplementation to the recording ACSF of 1µM tetrodotoxin to block sodium channels. Recorded tracings were analysed with Clampfit software (v10.3; Molecular Devices, San Jose, CA, USA) and were corrected for liquid junction potentials (-10 mV). Resultant data were then exported for statistical analysis.

2.2.8 Gene Therapy by Intraventricular Injection

2.2.8.1 Breeding for Day 0 Injection

To ensure the YFP$^{+/-}$-MPS IIIA mice received the correct treatment type at birth (AAV9-*SGSH* or vehicle), knowledge of mouse genotype was required at Day 0. Additionally, it was necessary for all groups to undergo behavioural testing together to minimise any variance within the tests. Therefore, a strict breeding plan was constructed to ensure enough mice were born with a presumed genotype and within a narrow timeframe. The outline of this breeding plan is shown in Figure 2.6. Ultimately, for wild-type progeny, one parent was required to possess zero copies of YFP, one parent to possess two copies of YFP, either parent to be homozygous wild-type, and the other to be heterozygous or homozygous unaffected. For MPS IIIA progeny, one parent was required to possess zero copies of YFP, one parent to possess two copies of YFP, and both parents to be homozygous MPS IIIA. Based on these requirements and the available supply of mice, pairings of predominantly hemizygous single-copy YFP were used with heterozygous MPS IIIA for the first generation (Gen 2 F1). Probability ratios for resultant offspring were calculated, with predictions for optimal outcomes showing the earliest generation for the experimental parents to be the fifth (Gen 2 F5). Based on historical data from the CDRG, four pups per litter were assumed for both wild-type and MPS IIIA pairings, as the YFP$^{+/-}$-MPS IIIA colony average was 4.5 pups per litter. For the experimental generation, an additional 30% in pup number was planned for each genotype in case of failed pairings or significantly delayed pairings. Therefore, 11 wild-type pairings and 20 MPS IIIA pairings were required to generate the necessary 90 experimental animals of 45 females and 45 males. The females were designated for tissue collection at multiple time-points, including the periods of behavioural testing, while the males were designated for behavioural testing.

	Parent 1	Parent 2	Probability ratio of generated offspring								
			YFP/+ ; Norm	**YFP/+** ; Het	**YFP/+** ; MPS	**YFP/YFP** ; Norm	**YFP/YFP** ; Het	**YFP/YFP** ; MPS	+/+ ; Norm	+/+ ; Het	+/+ ; MPS
Gen 2 F1	**YFP/+** ; Het	**YFP/+** ; Het	1:8	1:4	1:8	1:16	1:8	1:16	1:16	1:8	1:16
Gen 2 F1	**YFP/+** ; Het	+/+ ; Het	1:8	1:4	1:8	0	0	0	1:8	1:4	1:8
Gen 2 F1	**YFP/+** ; Het	**YFP/+** ; Het	1:8	1:4	1:8	1:16	1:8	1:16	1:16	1:8	1:16
Gen 2 F1	**YFP/+** ; Het	**YFP/+** ; Het	1:8	1:4	1:8	1:16	1:8	1:16	1:16	1:8	1:16
Gen 2 F2	**YFP/+** ; MPS	+/+ ; Het	0	1:4	1:4	0	0	0	0	1:4	1:4
Prediction based on best ratios:											
Gen 2 F3	**YFP/+** ; Het	**YFP/+** ; MPS	0	1:4	1:4	0	1:8	1:8	0	1:8	1:8
	+/+ ; Het	+/+ ; MPS	0	0	0	0	0	0	0	1:2	1:2
Gen 2 F4	**YFP/YFP** ; Het	**YFP/YFP** ; MPS	0	0	0	0	1:2	1:2	0	0	0
	YFP/YFP ; Het	**YFP/+** ; MPS	0	1:4	1:4	0	1:4	1:4	0	0	0
Gen 2 F5	**YFP/YFP** ; Het	**YFP/YFP** ; MPS	0	0	0	0	1:2	1:2	0	0	0

	YFP	+
YFP	**YFP/YFP**	**YFP/+**
+	**YFP/+**	+/+

	MPS	Norm
MPS	MPS	Het
Norm	Het	Norm

	+	+
YFP	**YFP/+**	**YFP/+**
+	+/+	+/+

	MPS	Norm
MPS	MPS	Het
MPS	MPS	Het

	YFP	+
YFP	**YFP/YFP**	**YFP/+**
YFP	**YFP/YFP**	**YFP/+**

Figure 2.6 – Breeding plan for Day 0 mouse intraventricular injections. The breeding plan constructed and followed to produce the necessary experimental mice for intraventricular injections of AAV9-*SGSH* or vehicle at birth. The probability ratios for resultant offspring were calculated, with predictions for optimal outcomes showing the earliest generation for the experimental parents to be the fifth. +/+ denotes no expression of YFP; YFP/+ denotes a single-copy of YFP; YFP/YFP denotes two copies of YFP; Norm denotes homozygous expression of *SGSH*; Het denotes heterozygous expression of *SGSH*; MPS denotes no expression of *SGSH*.

2.2.8.2 Intraventricular Injection at Day 0

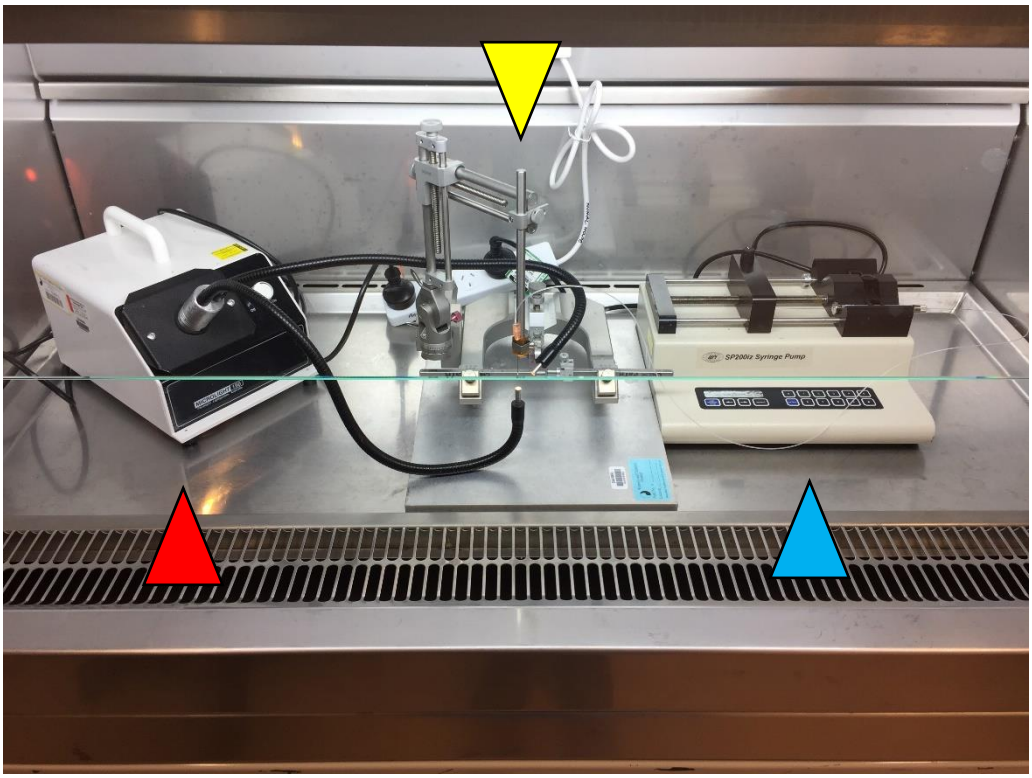
For the intraventricular injections of Day 0 YFP$^{+/-}$-MPS IIIA mice, a custom-designed viral vector (AAV9-CMV-*SGSH*; hereafter referred to as AAV9-*SGSH*; Vector Biolabs, PA, USA) was obtained. The titre supplied was 5.7x10^{10} genome copies (gc)/µL. Based on the dosage in previous administrations of AAV9 to adult MPS IIIA mice via intracisternal injection (5x10^{10} gc/mouse; Haurigot et al., 2013) and AAV2/5 in newborn mice via intraventricular injection (3x10^{10} gc/mouse; Fraldi et al., 2007), a dose of 5x10^{10} gc/mouse was selected. Injections were made into each brain hemisphere, with virus diluted in sterile PBS (Sigma-Aldrich, NSW, Australia) to 2.5x10^{10} gc/µL.

Following the breeding plan described in 2.2.8.1, 90 experimental mice were born within the timeframe of 11 days: 30 of the mice born were wild-type and received the vehicle of sterile PBS (Sigma-Aldrich, NSW, Australia); 30 of the MPS IIIA mice also received the vehicle; and the remaining 30 MPS IIIA mice received the AAV9-*SGSH* vector treatment. Injections were administered to entire litters, and the treatment injected noted for each cage. On the day of birth, cages containing the dam/nest and pups were transferred to one of the experimental rooms. Quietly and gently, pups were removed from the cage and placed in a tissue-lined dish (Fig 2.7A). Half of the litter was taken at a time to minimise distress to the mother. Prior to receiving the injections, the mice were individually cryoanaesthetised in dry (not watery) ice for two-minutes. The pups were deemed to be anaesthetised when they did not respond to a pinch of the tail. Moving quickly, pups were taken out of the ice and carried to a biosafety cabinet. They were then placed over a MicroLight 150 Cold Light Fibre Optic Illuminator (Fibreoptic Lightguides, VIC, Australia) to transilluminate the brain and ventricles whilst preserving the cryoanaesthesia (Fig 2.7B; red arrow). Using a stereotaxic frame for guidance (David Kopf Instruments, CA, USA), a 27G dental needle was positioned directly over the lateral ventricles

A



B



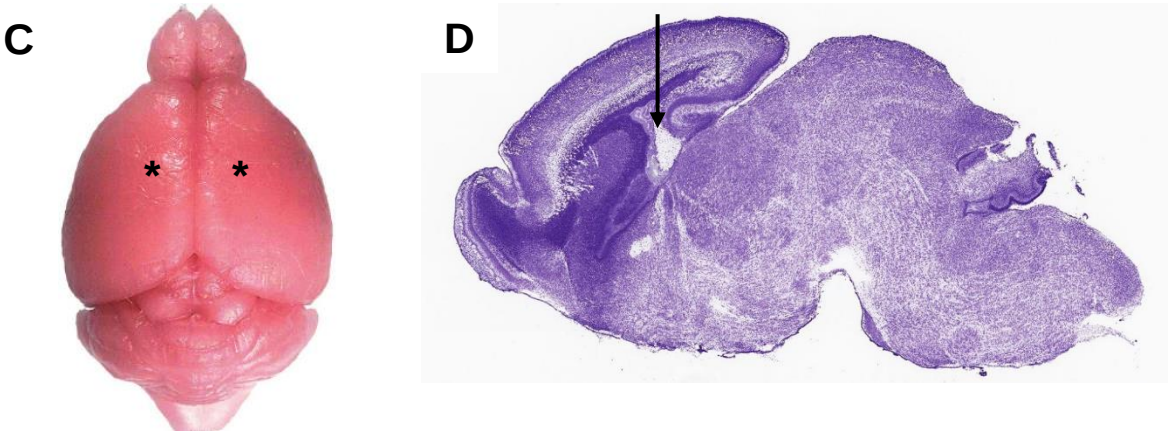


Figure 2.7 – Administering intraventricular injections to YFP$^{+/-}$-MPS IIIA mice. The equipment set-up for bilateral intraventricular injections of Day 0 YFP$^{+/-}$-MPS IIIA mice. Pups removed from their mother were kept in tissue-lined dishes under a heat lamp (A). A cold light source (B, red arrow) illuminated the sites for injection. Injections occurred via a 27G dental needle attached to a stereotaxic frame (B, yellow arrow) and a syringe slow-infusion pump (B, blue arrow). The needle was lowered in the dorsal position for the left and right hemispheres (C, asterisks), and inserted into the lateral ventricles (D, arrow).

(Fig 2.7; yellow arrow). Inert plastic polyethylene tubing (Becton Dickinson, USA) contained either the PBS vehicle or AAV9-*SGSH* viral vector for injection and was connected to the needle and a SP200iz Syringe Infusion Pump (World Precision Instruments, Sarasota, FL, USA) (Fig 2.7B; blue arrow). The needle was positioned over the left lateral ventricle (Fig 2.7C; left asterisk), then carefully lowered and inserted into the ventricle (Fig 2.7D); 1µL of solution was then injected at a rate of 1µL/minute and given 15-20 seconds to sufficiently disperse prior to withdrawal of the needle. The mouse pup was then placed in a tissue-lined dish under a heat lamp to recover. Mice were deemed fully recovered with a bright-pink appearance and response to touch. Once all pups had received one injection, the cycle was repeated with the cryoanaesthesia and the initial pup, but in the right lateral ventricle (Fig 2.7C, right asterisk). Once completely recovered, the pups were rolled in some of the bedding from the home cage, returned to the home cage and rotated with the other half of the litter. Mice were subsequently monitored weekly to record overall health until tissue collection.

2.2.9 Behavioural Testing

Behavioural tests were performed on cohorts of individually housed male mice to avoid any inter-gender influences on behaviour performance and to prevent fighting amongst individuals. Individual housing also ensured each mouse was exposed to the same testing environment for identical durations and was naïve to all tests. Mice underwent Open Field testing at 15-weeks of age, and Pole, Negative Geotaxis, and Grip Strength testing at 20-weeks of age. All testing was conducted between the hours of ~0700 and 1200 under normal lighting conditions. Animals were transported from the holding room to the behavioural testing room 48-hours prior to testing to provide the opportunity to acclimatise to the environment. Curtains were also erected in front of the mice to shield them from the activity in the testing area and to preserve naivety. After testing, mice were returned to the

holding room. Mice were tested in a randomised order, with genotype and identification blind to the experimenter.

2.2.9.1 Open Field Test

The Open Field behavioural test involved both manual and electronic recordings via a video camera (Figure 2.8A). The testing area utilised a 30 x 50cm plastic box with an open top, divided into a 3 x 5 grid (9 x 10cm; Figure 2.8B) (Hemsley and Hopwood, 2005). Each mouse was placed into the testing area in the same spot (Figure 2.8B). The test duration for each mouse was five-minutes, and the manual data recorded included the frequency at which a mouse groomed, reared up on its hind-limbs, and crossed a grid-line. The total distance travelled and number of grid-lines crossed were recorded by the camera and data were communicated to a computer fitted with HVS Image Field 2020 Software (www.hvsimage.com). Between each mouse tested, the box was cleaned with 70% ethanol-soaked tissues and dried thoroughly to remove any traces of mouse scent.

2.2.9.2 Pole Test

The Pole motor behavioural test involved manually recording the time taken for each mouse to navigate the roughened wooden pole (Lau et al., 2017). The pole had a height of 55cm and a diameter of 8mm. The mouse was placed at the top of the pole with its head facing toward the ceiling. Utilising a timer, the time taken for the mouse to orientate down towards the base of the pole was recorded, and then the time taken to descend the pole was also recorded. The maximum time permitted to record was 120-seconds. If the mouse fell during the test, it would land into shredded paper and a time of 120-seconds was recorded (Figure 2.9). The test was repeated four-times for a total of five tests. At the conclusion of the fifth test, the mouse was returned to its cage and the pole was cleaned with 70% ethanol-soaked tissues and dried thoroughly to remove any traces of mouse scent.

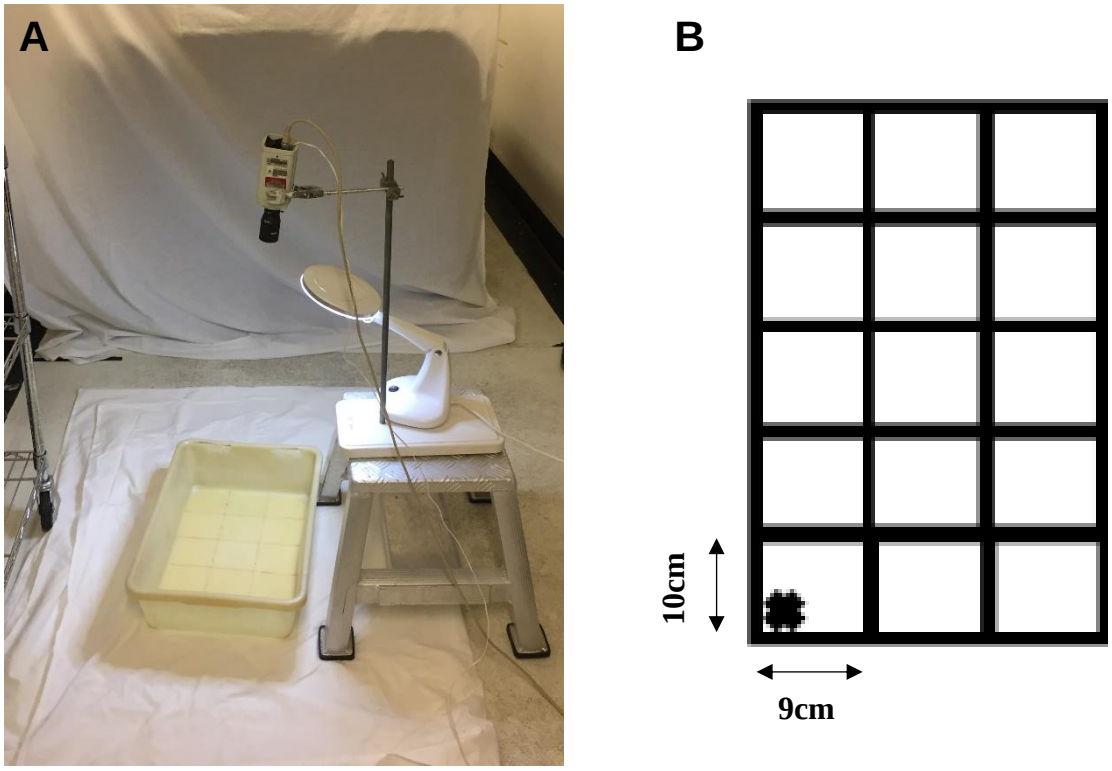


Figure 2.8 – Open Field Test. Images illustrating the set up for the Open Field test. The testing area shielded with curtains and utilising a video camera to monitor mouse movement (A). The testing area utilised a 30 x 50cm plastic box with a 3 x 5 grid of 9 x 10cm (B). Mice were placed in the same spot of the testing area to maintain consistency (cross).



Figure 2.9 – Pole Test. Set up used for the Pole motor behavioural test. The rough wooden pole was 55cm high with a diameter of 8mm and was embedded in a 30 x 50cm plastic box filled with shredded paper. For subsequent motor tests, the pole was removed.

2.2.9.3 Negative Geotaxis Test

The Negative Geotaxis motor behavioural test involved manually recording the time taken for each mouse to right itself on a metal cage lid (Hemsley and Hopwood, 2005). Each mouse was placed onto the cage lid, which was suspended approximately 30cm above a 30 x 50cm plastic box of shredded paper. The distance could not be lower as the mouse would not see an incentive to hold on and would drop, and a higher distance risked injury to the mouse. The lid was slowly and gently oriented until the mouse was vertical and facing downwards towards the shredded paper, and then the timer was started. The time taken for the mouse to turn and face upwards was recorded, with a maximum time of 30-seconds. The lid was then carefully righted so the mouse was upright, and then returned to its cage. If the mouse fell into the paper, the time of falling was recorded and deemed a failed test, and the mouse was returned to its cage. Between each mouse tested, the lid was cleaned with 70% ethanol-soaked tissues and dried thoroughly to remove any traces of mouse scent.

2.2.9.4 Grip Strength Test

The Grip Strength motor behavioural test involved manually recording the time taken for each mouse to grip the metal bars of a cage lid (Hemsley and Hopwood, 2005). Each mouse was placed onto the cage lid, which was suspended approximately 30cm above a 30 x 50cm plastic box of shredded paper. The distance could not be lower as the mouse would not see an incentive to hold on and would drop, and a higher distance risked injury to the mouse. The lid was gently moved from side to side to encourage the mouse to grip the metal bars. The lid was then carefully inverted so the mouse was hanging upside down over the shredded paper. The timer was started and recorded for the duration of the test until the mouse could no longer grip and fell into the paper, up to a maximum of 60-seconds. The test was regarded as a fail if the mouse fell, and the mouse was then returned

to its cage. If the mouse did not fall, 60-seconds was recorded and the test was regarded as a pass. The lid was then carefully righted and the mouse returned to its cage. Between each mouse tested, the lid was cleaned with 70% ethanol-soaked tissues and dried thoroughly to remove any traces of mouse scent.

2.2.10 Tissue Collection

Fixative was prepared as per Methods (2.2.4). The head was quickly decapitated, and the brain swiftly removed. The brain was placed into an ice-cold brain slicer and cut sagittally down the midline using a GEM blade to separate the two hemispheres. The left hemisphere was immediately immersed in 4% PFA for seven-days at 4^{o}C, and then transferred to 1x PBS for long-term storage at 4^{o}C. The right hemisphere was sliced into five hemi-coronal sections, divided into labelled Eppendorf tubes, and placed into liquid nitrogen for transport and subsequent long-term storage at -80^{o}C. The left hemisphere was collected for immunofluorescence assays and dendritic spine analysis, while the slices of the right hemisphere were collected for mass spectrometry analysis of HS. In addition to the brain, eyes, blood, liver, and spleen were also collected.

2.2.11 Homogenisation of Brain Tissues

To prevent protein degradation, Fast Prep-24 2mL lysing matrix D tubes containing 1.4mm ceramic spheres (116913050-CF; MP Biomedicals, USA) were cooled on ice prior to the homogenisation process. Five-hundred µL of ice-cold Tris-NaCl homogenising buffer (0.02M Tris and 0.5M NaCl in Milli-Q water; pH 7.4) was added to each tube. The brain slice was thawed from -80^{o}C on ice, and then transferred to the homogenising tube containing the buffer. In a 4^{o}C cold room, samples were homogenised twice using a Precellys 24 Homogeniser (Bertin Technologies, France) at 6500 rpm at 20-second

intervals to prevent the samples from heating. The homogenised tissue was then kept on ice and immediately assayed for total protein content or stored at -80^{o}C until analysis.

2.2.12 Bicinchoninic Acid Protein Assay

To determine the total protein content of the brain slice homogenates, a micro-bicinchoninic acid (BCA) protein assay method was identified (Smith et al., 1985) and performed according to the manufacturer's instructions (23225; ThermoFisher Scientific, Waltham, MA, USA). To summarise, a standard curve was prepared from bovine serum albumin which encompassed the total protein levels of 1-20mg. The standard curve was then added, in duplicate, to a non-protein-binding 96-well plate (655901; Interpath Services, Vic, Australia) in addition to duplicates of MPS IIIA mouse brain quality control samples. The brain homogenates were diluted in Milli-Q water (1:5), then 5µL was subsequently added (in duplicate) to the plate. Milli-Q water was added to each well to ensure an equal volume of 100µL for all wells; 100µL of micro-BCA working reagent was then administered to each well to give a final volume of 200µL. The plate was then sealed (76-401-05; Jomar Life Sciences, Vic, Australia) and incubated at 37^{o}C for two-hours. Using a Victor 3 Multilabel Counter (Perkin Elmer 1420, USA), total protein concentration was determined by measuring the absorbance wavelength at 562nm. The quality of the plate was rejected if two of the calculations from the standard curve presented a coefficient of variation (%CV) greater than 10%. A sample was rejected and required repeating if one or both of its corresponding wells presented a %CV value greater than 10% and/or the protein concentration value was not between the range of 2-16µg of the standard curve.

2.2.13 Mass Spectrometry

2.2.13.1 Heparan Sulphate Isolation from Brain Tissue

To determine the levels of HS within the brain slice homogenates prepared in 2.2.11, the method developed by Trim et al. (2015) was followed. From the protein calculations obtained in 2.2.12, 100µg of total homogenate protein was added to 12mL glass tubes and freeze-dried overnight in a SpeedVac Vacuum Concentrator (ThermoFisher Scientific, Waltham, MA, USA). Also included were samples for a disaccharide standard curve which contained protein levels covering the range of 1-2000ng. Additionally, a control sample of 10ng undigested HS was made, plus one blank tube. The next day, the dried samples were resuspended with 50µL of 2,2-dimethoxypropane followed by 1mL of 3M butanolic hydrochloric acid. Tubes were sealed with lids and heated for two-hours at 100^{o}C, then supplied with nitrogen gas at 45^{o}C for one-hour, or until completely dry. Dried samples were subsequently reconstituted in 200µL of a 100ng/mL HS internal standard (prepared by Dr Paul Trim, Mass Spectrometry Core Facility, SAHMRI, Adelaide, SA, Australia), vortexed and pulsed twice in a centrifuge at 1200rpm, then mixed on a rotary shaker for 30-minutes (Ratek Instruments, Boronia, Vic, Australia). Samples were briefly centrifuged before transfer to Eppendorf tubes and centrifuging at 13000rpm for 15-minutes in a Biofuge Pico (Heraeus, Germany); 180µL of the supernatant was transferred to a 96-well microtitre plate, including the standard curve, HS quality control, HS internal standard, and Milli-Q water blanks. The plate was then sealed and provided to the Mass Spectrometry Core Facility for analysis.

2.2.13.2 Liquid Chromatography/Mass Spectrometry of Heparan Sulphate

Liquid chromatography-tandem mass spectrometry (LC-MS/MS) analysis of butanolysis samples to determine total HS as prepared in 2.2.13.1 was performed by Dr. Paul Trim (Mass Spectrometry Core Facility, SAHMRI, Adelaide, SA, Australia). To generate the

measurements, samples were analysed with an Acquity Ultra Performance Liquid Chromatography system (UPLC) (Waters Corporation, MA, USA) utilising a 2.1mm x 50mm UPLC Ethylene Bridged Hybrid C18 column with a 1.7µm particle size (Waters Corporation, MA, USA; P/N. 186002350), combined with an API 4000 Q-Trap triple-quadrupole mass spectrometer (AB Sciex, Ontario, Canada).

Liquid chromatography separation was achieved by injecting 2µL of sample extract onto the UPLC column at 350mL/min using the initial gradient conditions of 99% mobile phase A (MP-A) containing 0.1% formic acid in Milli-Q water (1:999 w/v). The chromatographic gradient used for the analysis of butanolysis-digested HS is shown in Figure 2.10. The gradient ran from 99% to 90% MP-A over 270-seconds at the same flow rate. The column was then washed for 66-seconds with 99% mobile phase B (MP-B) containing 0.1% formic acid in acetonitrile (1:999 w/v), followed by column equilibration with 99% MP-A for 140-seconds.

Mass spectrometric analysis of HS was performed in positive ion multiple reaction monitoring mode using an ion-spray source temperature of 450^{o}C and voltage of 5500V. Nitrogen was used as the collision gas at a pressure of $2x10^{-5}$Torr. Three transitions were monitored for 50ms each for HS disaccharides (mass-to-charge ratio (*m/z*) 468.245 to 162.077), deuterated HS internal standard (*m/z* 486.384 to 162.077), and spiked internal standard and chondroitin sulphate/dermatan sulphate disaccharides (*m/z* 510.255 to 278.160). Samples were randomised prior to analysis, then a blank injection followed by the first quality control conditioned the column. The quality control was repeated at the middle and end of the run, and a blank injection of Milli-Q water was administered every three samples for all other samples. The peak areas were determined using Analyst software (v1.6.2, AB Sciex), and final HS total values were calculated for all individual

samples by the ratio of HS peak area to internal standard peak area. The dominant peak for each sample was incorporated for analysis.

A

Time (min)	% MP-A	% MP-B	Curve
Initial	99	1	-
2.00	95	5	6
2.01	80	20	6
5.00	75	25	6
5.01	1	99	1
7.50	99	1	11
8.50	99	1	6

B

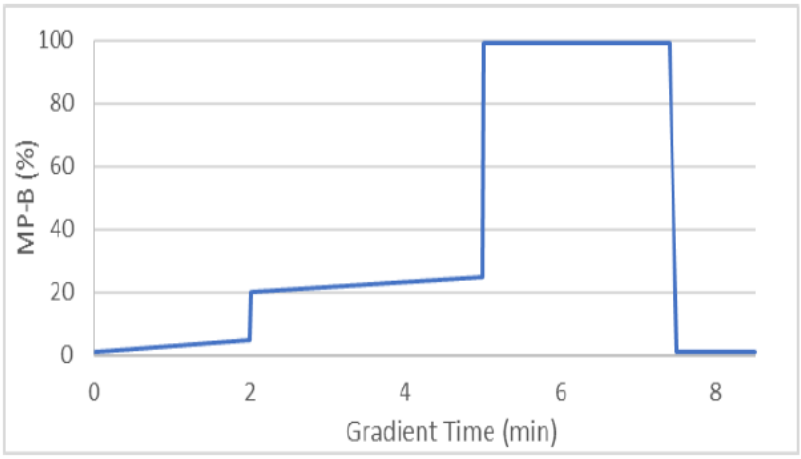


Figure 2.10 – Chromatographic gradient for analysis of heparan sulphate. The liquid chromatography separation of butanolysis-digested HS samples was administered through a chromatographic gradient with two mobile phases over time (A), with an example of a visualised gradient curve for the administration of mobile phase B (B).

2.2.14 Statistical Analysis

Statistical analysis of glial cell proximity to neuron data was performed in consultation with Ms. Suzanne Edwards of the Data, Design and Statistics Service, University of Adelaide. The raw data were transformed to long format with columns for Frequency, Distance, Week, and Group. Negative binomial regression models were used with a log link function to investigate the association between Frequency (a dependent count variable) and a three-way interaction of Distance, Week, and Group. If the three-way interaction was significant ($p<0.05$) four two-way interaction models were then performed to lessen the complexity that could occur in a four-way interaction model. Each model was performed for a different week, generating four total models (with a three-way interaction). Post-hoc comparisons were performed, and results presented as Incidence Rate Ratios (IRRs), 95% confidence intervals (CIs) and interaction, comparison and global p-values. The statistical software used was SAS 9.4 (SAS Institute Inc., Cary, NC, USA).

All other data were analysed using GraphPad Prism software (v8.0.0; GraphPad Prism Software Inc., San Diego, CA, USA), and presented as mean ± standard error of the mean (s.e.m.), with statistical significance determined when $p<0.05$. Outliers were identified using the ROUT method for Q=1% and included for presentation but excluded from statistical analysis. Electrophysiological data were analysed with parametric unpaired t tests. All remaining data were treated with analysis of variance (ANOVA), followed by *post-hoc* Bonferroni correction to adjust for multiple group comparisons.

– CHAPTER 3 –

TEMPORAL CHARACTERISATION OF DENDRITIC SPINES ON LAYER 5 PYRAMIDAL NEURONS IN THE MPS IIIA MOUSE MOTOR CORTEX

3.1 Introduction

MPS IIIA mouse cortical pyramidal neurons have been repeatedly shown to present with an abnormal pathology. Electron micrographs revealed vacuolar inclusions of HS within the soma of mouse cortical pyramidal neurons at 12-weeks of age (Fig 3.1A; Fraldi et al., 2007), 18-weeks of age (Hemsley et al., 2007), six-months of age (Crawley et al., 2006), and eight-months of age (Wilkinson et al., 2012). Immunohistochemical staining of LIMP-II also highlighted lysosomal inclusions within the cortical neurons at four-weeks of age (Hassiotis et al., 2014a), and storage of HS (Fig 3.1B) and secondary substrates, including GM2- (McGlynn et al., 2004; Fraldi et al., 2007; Hassiotis et al., 2014a) and GM3-gangliosides from four-weeks up to 10-months of age (Fig 3.1C; McGlynn et al., 2004). Collectively, these data highlight expansion of the lysosomal compartment in cortical pyramidal neurons in the MPS IIIA brain.

As described in Chapter 1, preliminary work by the candidate (Shoubridge, 2013) examined the architecture of pyramidal neurons in the MPS IIIA mouse cerebral motor cortex with the use of a modified Golgi-Cox histological stain (Ranjan and Mallick, 2010). Whilst no significant differences were found in the degree of complexity within the dendritic arborisation between genotypes, decreases in dendritic spine number were

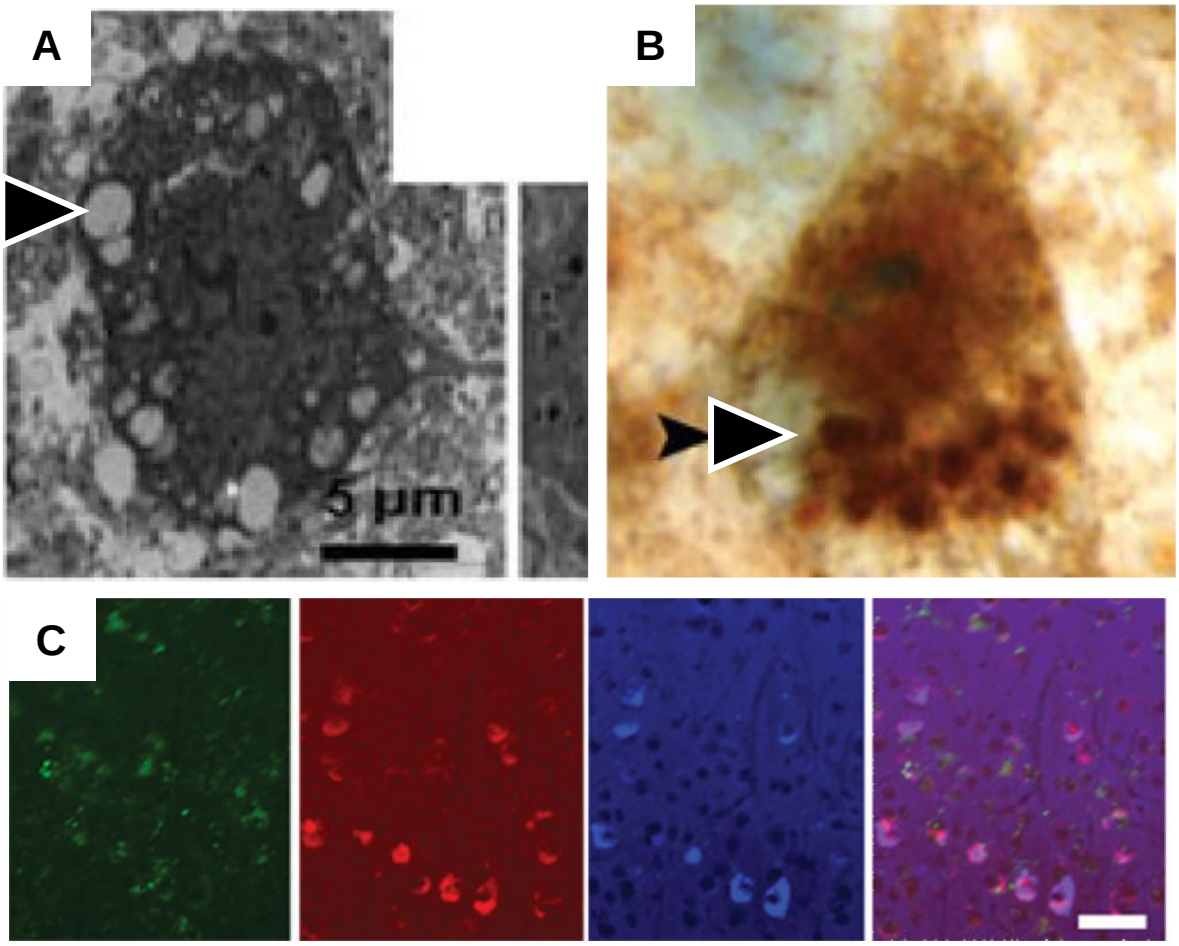


Figure 3.1 – Substrate storage within MPS IIIA cortical neurons. Representative images of substrate storage within cortical pyramidal neurons of the MPS IIIA mouse. An electron micrograph of a cortical neuron with vacuolar inclusions highlighted by arrow (A; Fraldi et al., 2007). An immunohistochemical image of a cortical pyramidal neuron stained for HS with aggregates highlighted by an arrow (B; McGlynn et al., 2004). Layer 5 pyramidal neurons in the cerebral cortex of MPS IIIA mice stained for secondary substrates, including gangliosides (C; Scale bar 75µm; McGlynn et al., 2004).

recorded across multiple orders of dendrites. These findings were then verified in the MPS IIIB mouse cerebral motor cortex (Shoubridge et al., unpublished). These data suggest changes to dendritic spine density on motor cortical pyramidal neurons could contribute to the neurological dysfunction associated with MPS III.

However, these preliminary investigations were at a single time-point (20-weeks of age), when symptoms are well-established in MPS III mice. Therefore, it cannot therefore be conclusively stated whether synaptic changes were potentially contributing to the onset of symptoms. Additionally, the Golgi-Cox stain presented major challenges. Whilst it allowed for whole-cell resolution by staining 1-5% of neurons with an absence of background, the staining of neurons was arbitrary (Milatovic et al., 2010). There was also a lack of 3-D resolution with the Golgi-Cox stain due to the use of conventional brightfield microscopy (Feldman and Dowd, 1975). Therefore, it was likely that synaptic density was under-estimated as it was not possible to visualise the entire neuronal structure. Thus, further investigations are required to elucidate the time course of dendritic spine changes, whether they are deficient pre-symptomatically, or whether temporal changes correlate with the onset of symptoms. Lastly, further assessments are required with a more robust method to comprehensively capture the entire neuronal structure.

The investigations in this study focused on the structure and function of layer 5 pyramidal neurons within the motor cortex. This is an under-studied brain region because across the MPS IIIA models, particularly mice, performance in motor function behavioural tests are a key determinant of disease phenotype (Hemsley et al., 2005; Crawley et al., 2006). Indeed, motor behavioural performance has been a primary indicator of therapeutic efficacy in recent assessments of various genetic therapies (Fraldi et al., 2007; Ruzo et al., 2012; Haurigot et al., 2013; Winner et al., 2016; Chen et al., 2018).

The motor cortex contains multiple types of pyramidal neurons, which are organised by cortical layer and projected pathway to their target (Fig 3.2; Papale and Hooks, 2018). Additionally, the mouse motor cortex receives input from similar brain areas as higher order mammals (Papale and Hooks, 2018). Connections to the motor cortex predominantly originate from the thalamus or other cortical regions, and are excitatory in nature (Kuramoto et al., 2009, 2015; Ohno et al., 2012). In brief, the circuitry information for initiation and control of movement is transmitted to pyramidal neurons in layers 2 and 3 (Brodmann, 1909), projected to layer 5 neurons (Weiler et al., 2008), and subsequently projected out to the distal regions, including the striatum, thalamus, and brainstem/spinal cord to elicit a functional output (Shepherd, 2013; Gerfen et al., 2018).

We made use of a reporter strain (the *thy1-YFP-H* line) in which layer 5 pyramidal neurons in the cerebral cortex are YFP-positive. These mice were paired with congenic MPS IIIA mice from an in-house colony to produce the $YFP^{+/-}$-MPS IIIA mouse model used in this study.

Overall, the experiments in this Chapter aimed to explore synaptic morphology in MPS IIIA and expand our understanding of neurological dysfunction to provide potential therapeutic targets for this currently untreated disease. At the time of this study, the literature revealed limited investigations of synaptic structure across multiple ages within the same model - particularly within the motor region – so a definitive link between neuronal structure and function with symptom development has not been established. Thus, this Chapter aimed to establish a time course of changes in the morphology and number of dendritic spines in the motor cerebral cortex of MPS IIIA mice.

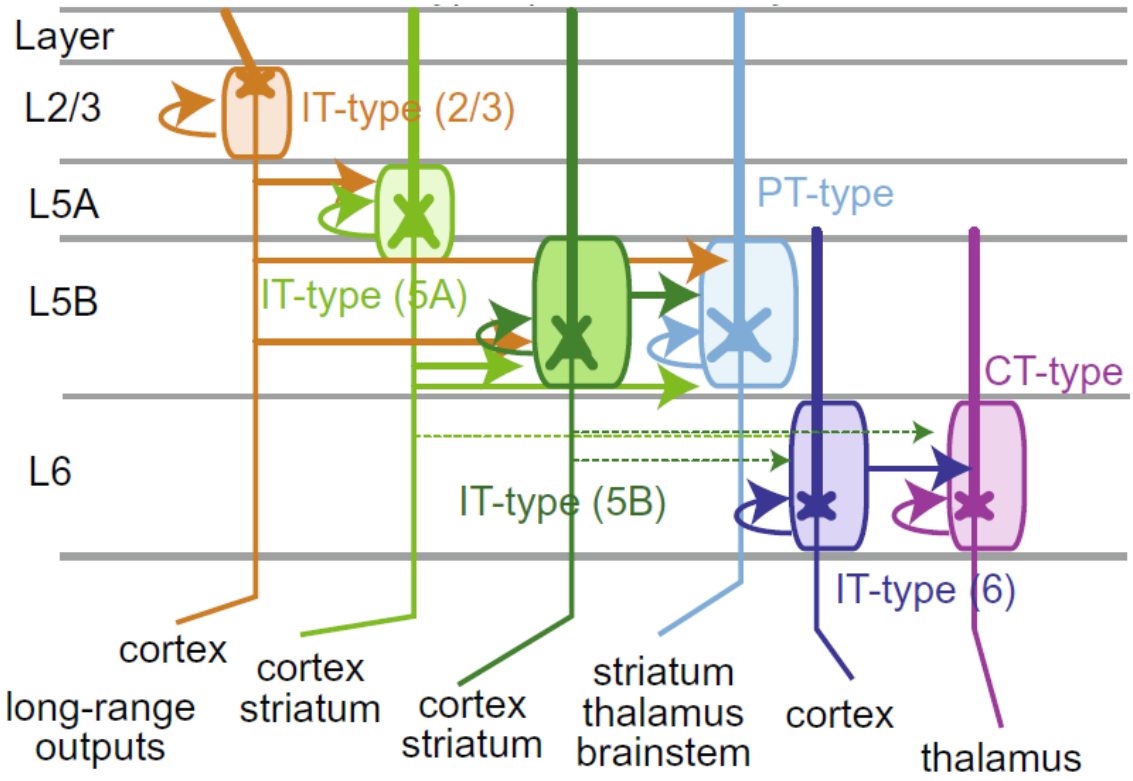


Figure 3.2 – Major excitatory connections within the motor cortex. The cortical neuronal circuitry within different layers of the motor cortex and projections to specific targets. The major local projections are illustrated with arrows. Layer 5 pyramidal neurons receive strong local input but do not send strong local output back to these neurons. CT, corticothalamic; IT, intra-telencephalic; PT, pyramidal tract. (**Papale and Hooks, 2018**).

3.2 Results

3.2.1 Visualisation of dendritic spines on YFP neurons

To assess dendritic spine density and morphology on layer 5 pyramidal neurons in the motor cortex, hemi-coronal brain slices were obtained from male and female $YFP^{+/-}$-MPS IIIA mice (Fig 3.3A). The 90µm-thick slices permitted visualisation and characterisation by confocal microscopy (Fig 3.3B-C). The z-stacks acquired by confocal microscopy, when compiled and remodelled, clearly distinguished the differences in dendritic spine morphology on the YFP neurons (Fig 3.3D). For reference, the arrow in Fig 3.3 indicates the direction of transition of spine maturity, i.e. mushroom spines are the most stable and mature post-synapses.

3.2.2 Total densities of dendritic spines are reduced on MPS IIIA neurons

In the year prior to this PhD candidature, $YFP^{+/-}$-MPS IIIA mice were bred and aged to three- and six-weeks (pre-symptomatic), 12-weeks (early-symptomatic), and 20-weeks (late-symptomatic). Characterisation of neurons was undertaken during the PhD candidature. Symptom onset refers to deficits in motor function and hypoactivity (Hemsley and Hopwood, 2005). In brief, partial deficiencies in motor performance during behavioural testing can be measured at ~12-weeks of age, whilst significant differences can be recorded in all tests of neuromuscular strength, negative geotaxis, and gait from 20-weeks of age (Hemsley and Hopwood, 2005). Representative images of dendritic spine characteristics are shown in Figure 3.4.

There was a decrease in total dendritic spine density on MPS IIIA mouse neurons compared with their respective age-matched controls by the pre-symptomatic age of six-weeks ($p<0.01$; Fig 3.5). Unexpectedly, there was no difference between groups at 12-

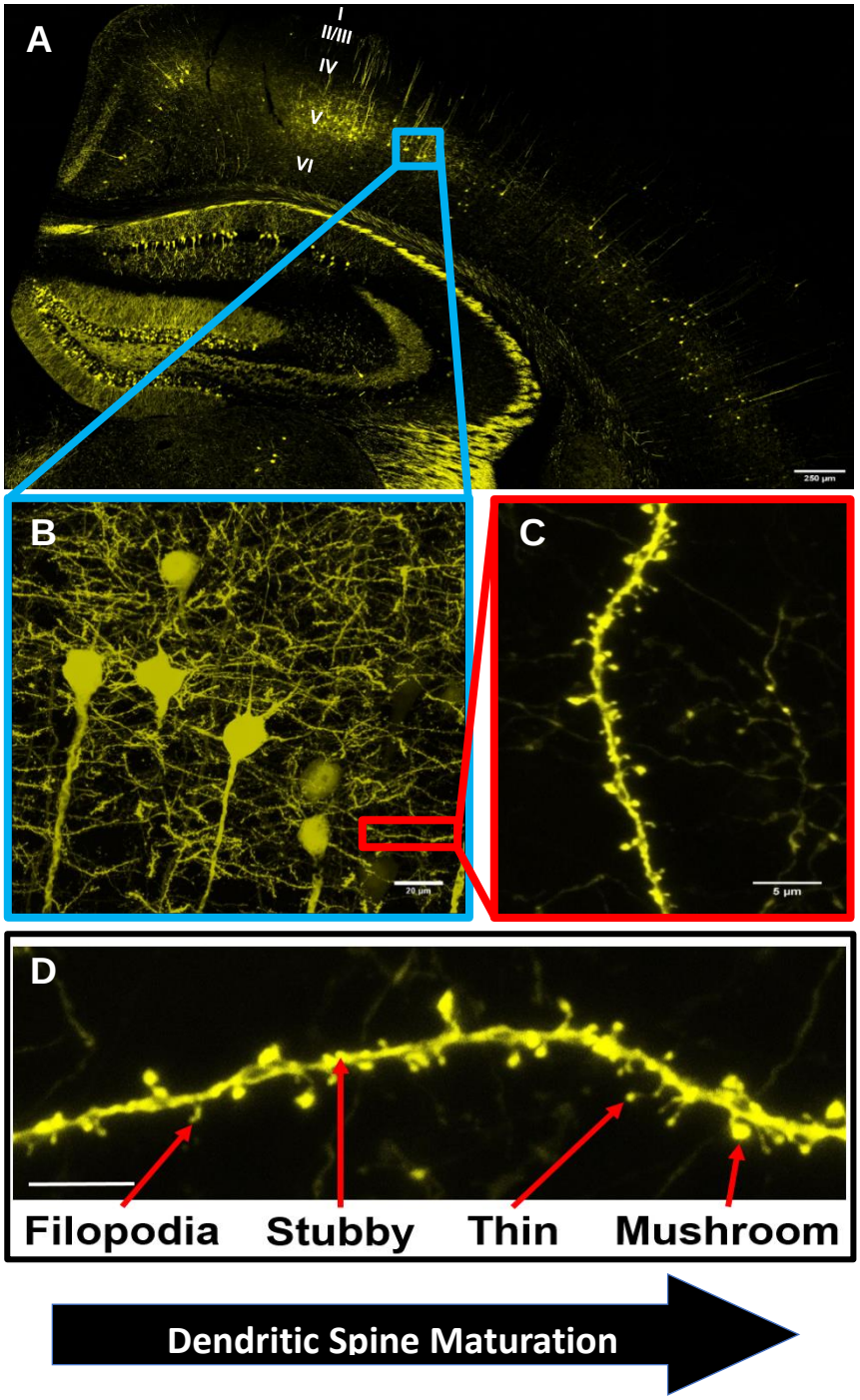


Figure 3.3 – Visualisation of dendritic spines on YFP neurons. Hemi-coronal sections highlight subsets of YFP-positive neurons in the cerebral cortex and hippocampus, with cortical layers identified (A). Layer 5 pyramidal neurons in the cerebral cortex of $YFP^{+/-}$-MPS IIIA mice (B) show high resolution of individual dendritic spine morphologies (C-D). Progression to spine morphological maturity is indicated (arrow). Scale bar is 250µm (A), 20µm (B), and 5µm (C-D).

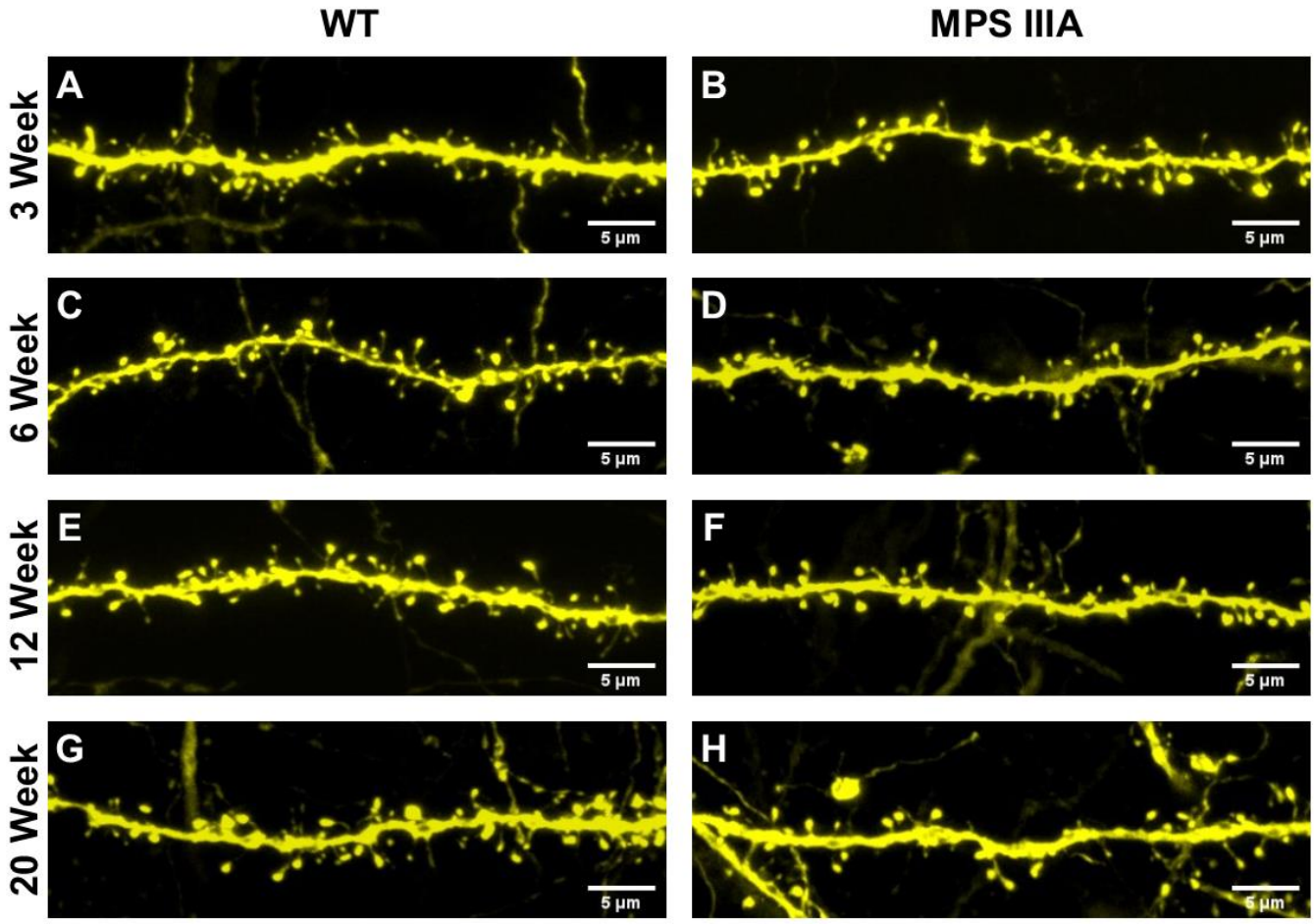


Figure 3.4 – Representative images of dendritic spine densities. Dendrites of layer 5 pyramidal neurons in the cerebral motor cortex of wild-type (WT) and MPS IIIA mice at three- (A-B), six- (C-D), 12- (E-F), and 20-weeks of age (G-H). Scale bar is 5µm.

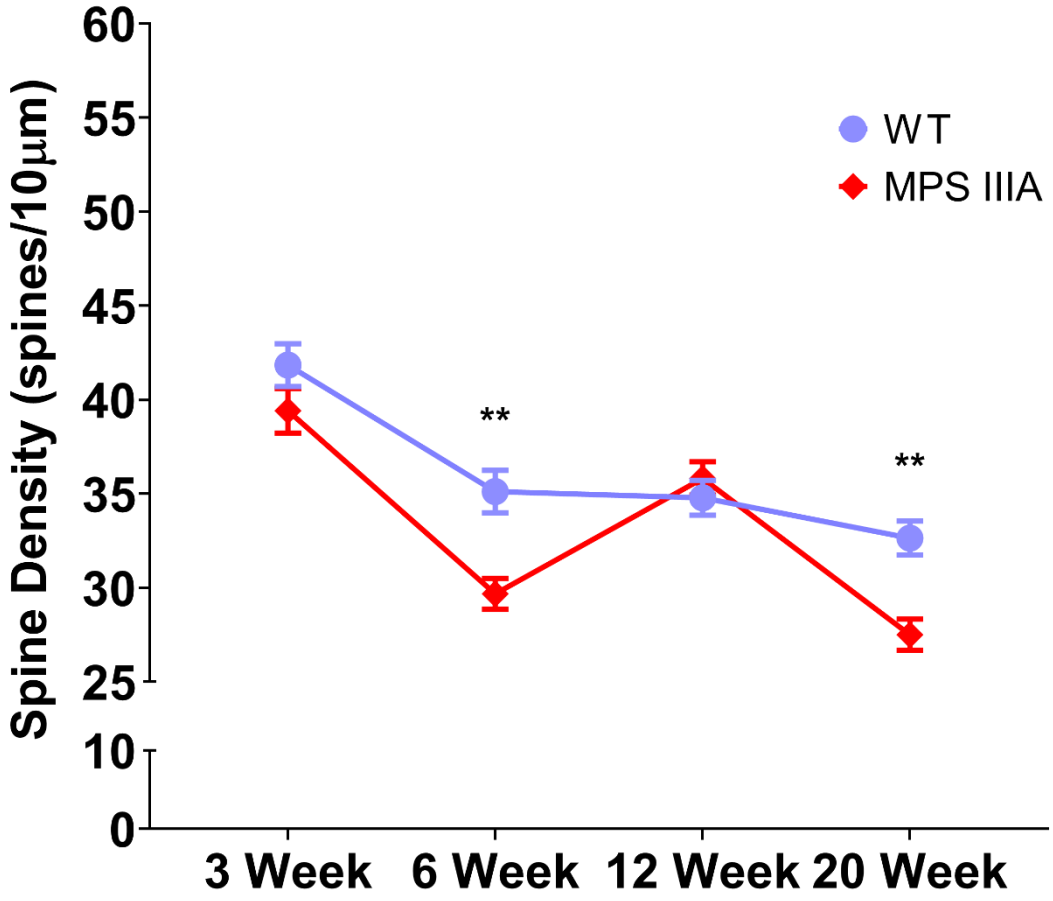


Figure 3.5 – Total dendritic spine densities. Dendritic spine densities of layer 5 pyramidal neurons in the cerebral motor cortex of wild-type (WT) and MPS IIIA mice at three-, six-, 12-, and 20-weeks of age. N=6 dendritic segments per cell; six cells per animal; six animals per genotype per age. **p<0.01; two-way ANOVA with Bonferroni's multiple comparisons. Data are mean ± SEM. Experimenter blinded to genotype and age.

weeks of age, with an increase in spine density from six-weeks on MPS IIIA neurons. At the late-symptomatic age of 20-weeks, a significantly reduced density of spines was observed on MPS IIIA neurons compared to wild-type ($p<0.01$). Whilst trending down, there was no significant decrease in density on wild-type neurons from six- to 20-weeks.

3.2.3 Reduced densities of dendritic spines across multiple morphologies on MPS IIIA neurons

To characterise dendritic spines throughout MPS IIIA disease progression to 20-weeks of age, the spines were divided into categories based on synaptic maturity/morphology. These ranged from filopodia and stubby (immature) to thin and mushroom (mature). No significant differences between the morphologies in MPS IIIA mice were observed at three-weeks of age, although trends were evident (Fig 3.6). The six-week MPS IIIA cohort showed the most significant reduction in density of the more mature thin and mushroom sub-types when compared to six-week wild-type mice. Consistent with total density, no difference was observed in any morphology at 12-weeks, whilst at 20-weeks there was a significant reduction in both immature ($p<0.0001$; Fig 3.6B) and mature ($p<0.0001$; Fig 3.6D) dendritic spine densities.

Filopodial densities trended downwards across ages and genotypes until 20-weeks of age (Fig 3.6A). Stubby spine densities decreased significantly over time in both genotypes until 20-weeks ($p<0.0001$; Fig 3.6B), when the wild-type density plateaued and MPS IIIA decreased further. The inverse was observed for the more mature mushroom spines where densities increased significantly over time in both genotypes ($p<0.0001$; Fig 3.6D). Thin spine density was higher in 12-week MPS IIIA than both six- and 20-week MPS IIIA densities, a difference reflected in total spine density.

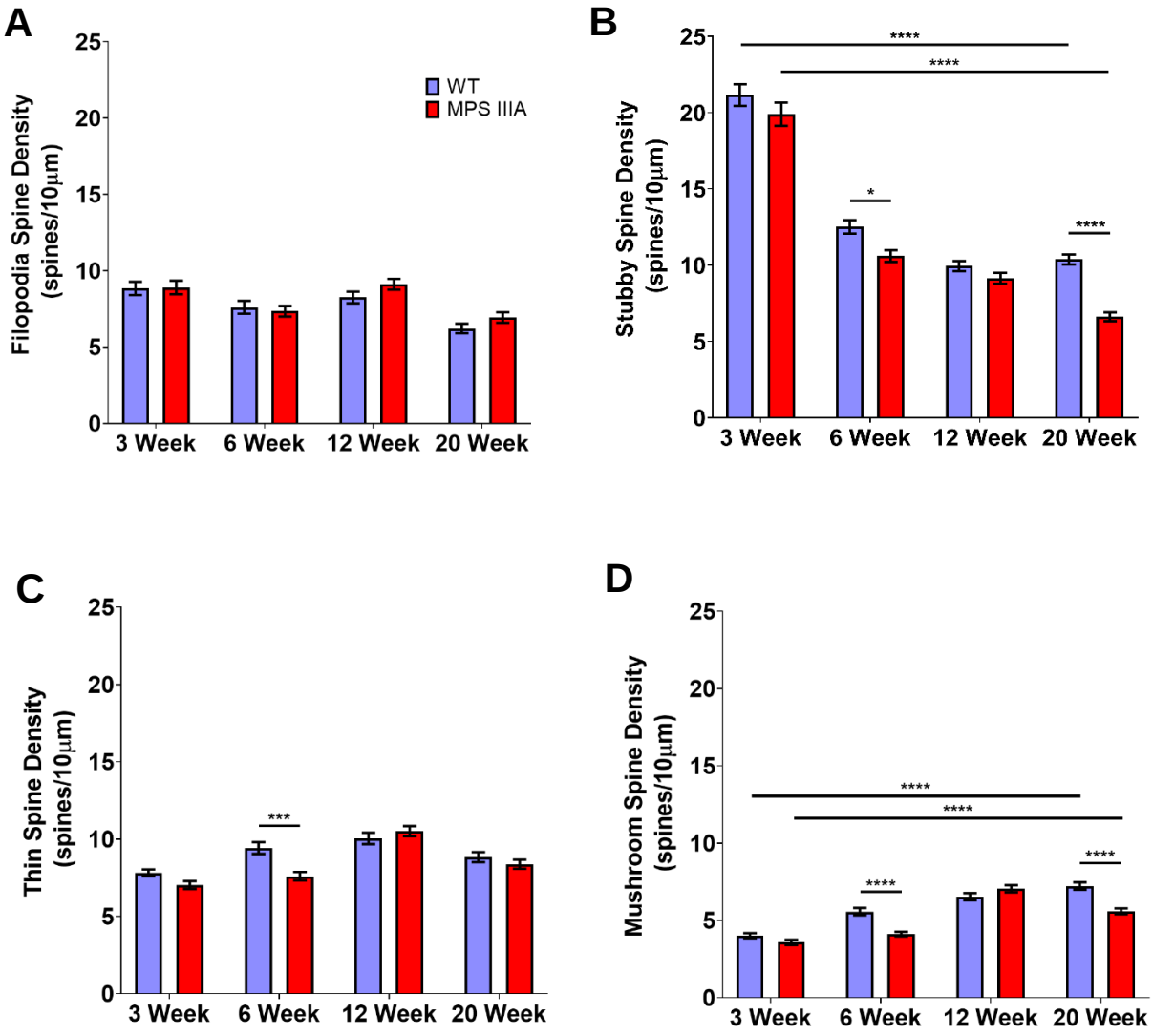


Figure 3.6 – Densities of dendritic spine sub-types in MPS IIIA. Dendritic spine densities on layer 5 motor cortical neurons of wild-type (WT) and MPS IIIA mice at three-, six-, 12-, and 20-weeks of age. Spine sub-types were categorised into filopodia (A), stubby (B), thin (C), and mushroom (D). N=6 dendritic segments per cell; six cells per animal; six animals per genotype per age. ***p<0.001; ****p<0.0001; two-way ANOVA with Bonferroni's multiple comparisons. Data are mean ± SEM. Experimenter blinded to genotype and age.

The more mature and stable mushroom spines had the lowest densities compared to all other morphologies (Fig 3.6D). In a pattern similar with the thin spine data, the wild-type mushroom density significantly increased over time until 20-weeks ($p<0.0001$; Fig 3.6D); the 12-week MPS IIIA mushroom spine density was higher than the six- and 20-week densities ($p<0.0001$) in these mice. In a pattern similar with the stubby and thin spine data from 12- to 20-weeks of age, wild-type mushroom spine density plateaued, whereas MPS IIIA mushroom spine density trended downwards.

3.3 Discussion

There is currently no explanation for the clinical neurological changes associated with MPS IIIA. Reports of negligible cell loss in the brain (Wilkinson et al., 2012; Beard et al., 2017) suggest that subtle changes downstream of HS storage underlie the phenotype, which is important to understand to maximise treatment efficacy. As the neurological basis for symptom generation in MPS IIIA is unknown, this study sought to characterise dendritic spine properties over the time course of MPS IIIA disease progression to a late-symptomatic stage. Within the MPS IIIA mouse motor cerebral cortex, a reduction in dendritic spine number was observed from a pre-symptomatic age which persisted to late-stage disease. To our knowledge, this is the first evaluation of dendritic spine morphological densities across multiple time-points in any model of a mucopolysaccharide disorder, and indeed LSDs more broadly.

The finding of a total dendritic spine deficiency in MPS IIIA mice occurring from a pre-symptomatic age is consistent with the spine defects observed in hippocampal neurons derived from pre-symptomatic MPS IIIC mice (de Aragao et al., 2020). The observation of these changes occurring at an early time-point suggests the deficiency in spine density precedes, and may contribute to, the onset of motor symptoms in MPS IIIA. Additionally, the lack of a strong synaptic difference at an even earlier age suggests that synapses form normally during the developmental stage of the MPS IIIA mouse brain but are subsequently lost as the disease progresses. Verifiably, no difference in total spine number was recorded at three-weeks of age in the same MPS IIIA mouse model, although this was within the somatosensory region of the cortex (Dwyer et al., 2017). However, de Aragao and colleagues (2020) observed highly significant reductions in spine densities in MPS IIIC mouse hippocampal neurons from 20-days of age. Their data suggest that dendritic

spine changes are occurring even earlier before symptom onset in MPS IIIC compared with MPS IIIA, but it should be noted their investigation was outside the cortex and focused on the hippocampal region. Interestingly, the same study assessed dendritic spine properties of cultured MPS IIIC mouse hippocampal neurons after 21-days *in vitro* and recorded ~50% fewer spines for both genotypes compared with the mouse brain slice assessments (de Aragao et al., 2020). In contrast with the slice assessments, they observed no overall deficiency in MPS IIIC spine density but did record significantly higher filopodia and stubby spines with reduced mushroom spines. This was the only time-point and model at which a morphological assessment has been conducted on MPS IIIC dendritic spines. Moreover, the differences in *in vitro* and *ex vivo* assessments may produce different outcomes. *In vitro* evaluations may be compromised by the artificial nature of the environment, compared with whole brain and slice analysis. Thus, the model of assessment should be kept consistent for accurate correlations between studies.

3.3.1 Potential mechanistic basis of synaptic defects

Consistent with human MPS IIIA, HS accumulates from birth in MPS IIIA mice and steadily increases with age (Crawley et al., 2006). As HS levels are higher at six-weeks than three-weeks, there is possibly a greater impact of storage on lysosomal function which may affect dendritic spine plasticity. Potentially, there could be a threshold of primary substrate accumulation impeding lysosomal function, from which dendritic spine defects occur. Lysosomes have been shown to degrade synaptic membrane proteins, including AMPARs, in neuronal processes by traveling bidirectionally on microtubules (Hendricks et al., 2010; Moughamian and Holzbaur, 2012; Maday et al., 2014). Incidentally, acute chemical inhibition of lysosomal function and motility has been shown to reduce dendritic spine growth and number (Goo et al, 2017; Padamsey et al, 2017a). Utilising leupeptin to chemically inhibit proteases contained within the lysosome, lysosomal motility was

reduced along the length of dendritic processes and did not traverse to the dendritic spine head. Simultaneously, the event frequency of spontaneous excitatory post-synaptic currents (EPSC) decreased, suggesting that impaired lysosomal recruitment to the synapse to recycle synaptic membrane proteins has a functional impact (Goo et al., 2017).

Translated to an MPS model, de Aragao et al. (2020) assessed transport of synapsin-1 vesicles in cultured MPS IIIC mouse hippocampal neurons at 21-days. They observed abnormal and reduced motility of vesicles along processes of MPS IIIC neurons compared with age-matched controls, indicating substrate storage may affect lysosomal transport of synaptic vesicles in neurons (de Aragao et al., 2020). Additionally, inhibiting the fusion of the lysosome with the plasma membrane by blocking Ca^{2+} release from the lysosome and specifically preventing the release of cathepsin B (utilising CA-074 cathepsin B inhibitor) into the extracellular matrix led to an observable decrease in dendritic spine density (Padamsey et al., 2017b). Therefore, as HS storage builds, it is possible that a deficiency in lysosomal function within neurons of the MPS IIIA mouse could be impacting on dendritic spine structure.

Moreover, it was reported that lysosomes also traffic to dendritic spines in response to synaptic activity (Goo et al., 2017; Padamsey et al., 2017a). When stimulated with the excitatory neurotransmitters AMPA and glutamate, lysosomes were recruited to the active spines where they were involved in recycling synaptic receptors to maintain synaptic plasticity. Mechanistically, generated action potentials move down axons, stimulating neurotransmitter release from pre-synaptic vesicles into the synaptic cleft (between the pre- and post-synapse), which activate ionotropic receptors in the post-synapse, and revert back to an electrical signal to depolarise the post-synaptic neuron and carry the action potential onwards (reviewed in Lepeta et al, 2016). If dendritic spines are not receiving appropriate

stimulation from the neighbouring pre-synapse, lysosomal recruitment to the synapse may be lacking and thus lead to a decline in maintenance of synaptic plasticity. Therefore, it is possible that dendritic spine loss due to insufficient pre-synaptic excitation or extracellular mechanisms prevents effective communication between the pre- and post-synapse.

As discussed in Chapter 1, the pre-synapse has been previously evaluated in MPS III mouse models. The pre-synaptic protein marker, synaptophysin, was reduced in the frontal cortex of MPS IIIB mice from 10-days through to eight-months of age but synaptic density was not affected, as detected using immunofluorescence for synaptobrevin (Vitry et al., 2009). Similarly, no difference in pre-synaptic density was observed at four- and nine-months of age in the MPS IIIA mouse somatosensory, motor and parietal cortex, despite decreases in the pre-synaptic vesicle proteins VAMP2 and synaptophysin (Wilkinson et al., 2012). Together, these findings suggest that the methods of assessment were potentially insensitive to the post-synapse changes, and that post-synapse characteristics may differ across the cortical regions.

Furthermore, as discussed in Chapter 1, reduced frequencies of vesicular catecholamine synaptic release have been reported in the peripheral nervous system of MPS IIIA mice (Keating et al., 2012), as well as decreases in MPS IIIA mouse CNS synaptic vesicle number (Sambri et al., 2017). Together, those reports suggest pre-synaptic alterations are impacting the neuropathology in MPS III, which, coupled with the findings in this study, suggest that alterations at the post-synapse could be underlying symptom development and progression.

The MPS IIIA mouse data generated in this study also showed changes in spine density when symptoms are well established, a trend also observed in the MPS IIIC mouse model

(de Aragao et al., 2020). A deficiency in MPS IIIA mouse synaptic head size has also been found at an advanced age and, as 2D electron micrographs were used, this further supports the observations of altered dendritic spine number and maturity in the MPS IIIA mouse.

In this study, the recorded average spine densities in wild-type mice of approximately 3.5-4.5 spines/µm is slightly lower than a separate report of 4-6 spines/µm on layer 5 pyramidal neurons in the motor cortex of three-month-old wild-type mice from the *Thy1*-EGFP-M line (Davidson et al., 2020). Their study also examined spine density in significantly aged mice (20-months) and noted an increase to approximately 6.5 spines/µm, which they attributed to the aged dendrites struggling to maintain previously stabilised and active spines. However, the cells analysed were a different subset from a different transgenic line. Conversely, an earlier study assessing the spine dynamics on layer 5 pyramidal neurons of the wild-type mouse motor cortex from the *Thy1*-YFP-H line showed spine densities of nearly six spines/µm at two-weeks of age which decreased to less than four spines/µm at 15-weeks of age (Tija et al., 2017), consistent with findings in this study. Importantly, and of more relevance, the study by Tija et al. (2017) utilised the same *Thy1*-YFP-H line as this study.

Turnover of dendritic spines is a normal process which occurs at a greater rate during development (Lendvai et al., 2000), and decreases with age to reach its peak level after pruning during adolescence (Zuo et al., 2005). The number of dendritic spines therefore decreases to a stable level over time due to similar rates of formation and elimination **(**Hofer et al, 2009; Chidambaram et al., 2019). Indeed, dendritic spines in layer 5 pyramidal neurons have been shown to become more stable over time with lower levels of synaptic pruning in the barrel, motor, and frontal cortices of adult mice (Zuo et al., 2005). In wild-type mice, results from this study are consistent with these statements, since after

six-weeks of age, the total spine density plateaued and remained stable for the remainder of the time course.

However, the MPS IIIA group did not plateau after six-weeks of age, and instead rose to a similar density level of the wild-type group before decreasing to the lowest level at 20-weeks. Characteristics of the 12-week group were detailed to investigate potential contributing factors to the discrepancy, and it was discovered a potential factor impacting on the neurophysiology could have included sex. Sex was not accounted for in this part of the study, and sex imbalances were indeed evident in the 12-week group: there were four female and two male mice in the MPS IIIA group, compared with three female and three male mice in the control group. Future studies investigating dendritic spine dynamics should account for hormonal effects and be sex-matched accordingly. Furthermore, we did not control for intra-cage environment, thus environmental factors may have also elicited an effect on synaptogenesis at 12-weeks. Environmental enrichment such as housing, exploratory chambers, blocks and balls, have indeed been investigated for their effect on the normal animal brain, including dendritic arborisation, neurogenesis and improved learning (van Praag et al., 2000). Enrichment, which included chambers and toys to enhance motor and cognitive stimulation, promotes synaptogenesis and neurogenesis in mouse models of CNS disorders (Nithianantharajah and Hannan, 2006; Burrows and Hannan, 2013). Whilst this study did not strictly regulate consistent enrichment across mouse cages, these reports of environmental enrichment and its impact on improving symptoms in CNS disorders suggests future studies on MPS III synaptic dynamics should account for environmental and housing conditions.

In the absence of newborn screening, MPS IIIA is presently diagnosed when symptoms are apparent or there is a family history. Recent assessments on human post-mortem cortical

tissue taken from end-stage MPS III patients showed reductions in PSD95-positive puncta (de Aragao et al., 2020), findings that support earlier studies by Takashima et al. (1985). Moreover, gene therapy-based treatment of MPS IIIC mice at eight-weeks of age revealed a slight improvement, but not complete restoration, of hippocampal PSD95-positive puncta six-months later (de Aragao et al., 2020). Therefore, if our observations of pre-symptomatic deficits in dendritic spines in the MPS IIIA mouse motor cortex extend to humans with MPS III, it is important to establish whether the loss of spines is preventable/reversible from therapies administered prior to and during symptom development.

3.4 Conclusion

In summary, for the first time, the densities and morphologies of dendritic spines were profiled in the MPS IIIA mouse motor cortex from pre- to late-symptomatic disease. Dendritic spine deficiencies were found to develop from a pre-symptomatic age and to persist with disease progression to 20-weeks of age. If they result in a functional change of the pyramidal neurons in the motor cortex, these changes may be contributing to symptom onset and this could help to explain the neurological decline associated with MPS IIIA. Future testing of therapeutic efficacy may therefore require closer examination of discrete changes to the brain architecture. Furthermore, investigation into potential mechanisms causing this observed spine loss is required.

– CHAPTER 4 –

ELECTROPHYSIOLOGICAL PROPERTIES OF LAYER 5 PYRAMIDAL NEURONS IN THE MPS IIIA MOUSE MOTOR CORTEX

4.1 Introduction

Assessments of synaptic electrical characteristics in MPS III commenced with a study on MPS IIIA chromaffin cells extracted from the adrenal glands of mice by Keating and colleagues (2012), who reported a reduction in the total number of secretory vesicle exocytotic events; further analysis of the amperometric recordings, however, showed no difference in the kinetics of these events.

Subsequently, Dwyer et al. (2017) utilised whole-cell patch clamping to evaluate EPSCs in the MPS IIIA mouse somatosensory cortex. At three-weeks of age, there was no change in inter-event interval in MPS IIIA tissue, but a decrease in EPSC amplitude was noted. Interestingly, this was despite no overall change in dendritic spine number or pre-synaptic neurotransmitter vesicle release. Sambri et al. (2017) utilised electrophysiological field recordings to measure the excitatory post-synaptic potential (EPSP) of the MPS IIIA mouse hippocampus in older (six-month old) MPS IIIA mice. They observed significant reductions in the EPSP amplitude in MPS IIIA brain slices compared with those from age-matched controls. Most recently, a more complete characterisation of post-synaptic events in the hippocampus of MPS IIIC mice was conducted by de Aragao et al. (2020). Significant reductions in both EPSC frequency and amplitude were observed in eight-week

old MPS IIIC mouse neurons, coinciding with significant dendritic spine loss (de Aragao et al., 2020). Collectively, these findings suggest that altered electrophysiological synaptic properties could potentially contribute to the functional deficits and symptomatic changes in MPS III.

Electrophysiological properties of the synapse include EPSCs, which are a measure of neurotransmitters released from the pre-synapse that bind to ligand-gated post-synaptic receptors of an excitatory synapse. These ionotropic receptors subsequently open and transduce the chemical signal into an electrical signal via an influx of ions to alter the polarity of the cell. The signal may be either excitatory or inhibitory, thus increasing or decreasing (respectively) the potential for an action potential to be generated. In the instance of an excitatory response, once the influx of ions reaches the positive threshold for the post-synaptic cell, significantly more post-synaptic channels open and rapidly increase the flow of ions, which increases the probability for an action potential to be generated. Action potentials then propagate along the post-synaptic cell to elicit a functional output (Lepeta et al, 2016; Alcami and Pereda, 2019).

Disruption to synaptic signalling can therefore affect the propagation of excitatory responses and hinder the functional output of neurons. Indeed, alterations to intrinsic synaptic molecular mechanisms, or loss of the synapses themselves, are implicated in several neurological disorders (reviewed in Lepeta et al., 2016). As shown in Figure 4.1, neurotransmitters released from a pre-synaptic bouton may fail to generate post-synaptic events, and therefore subsequent action potentials, with defective or absent post-synapses (Lacagnina et al., 2017). Therefore, it is possible that the post-synaptic deficits reported in Chapter 3 may be impacting on the functional output of neurons in the MPS IIIA mouse motor cortex, which could be underlying symptom onset.

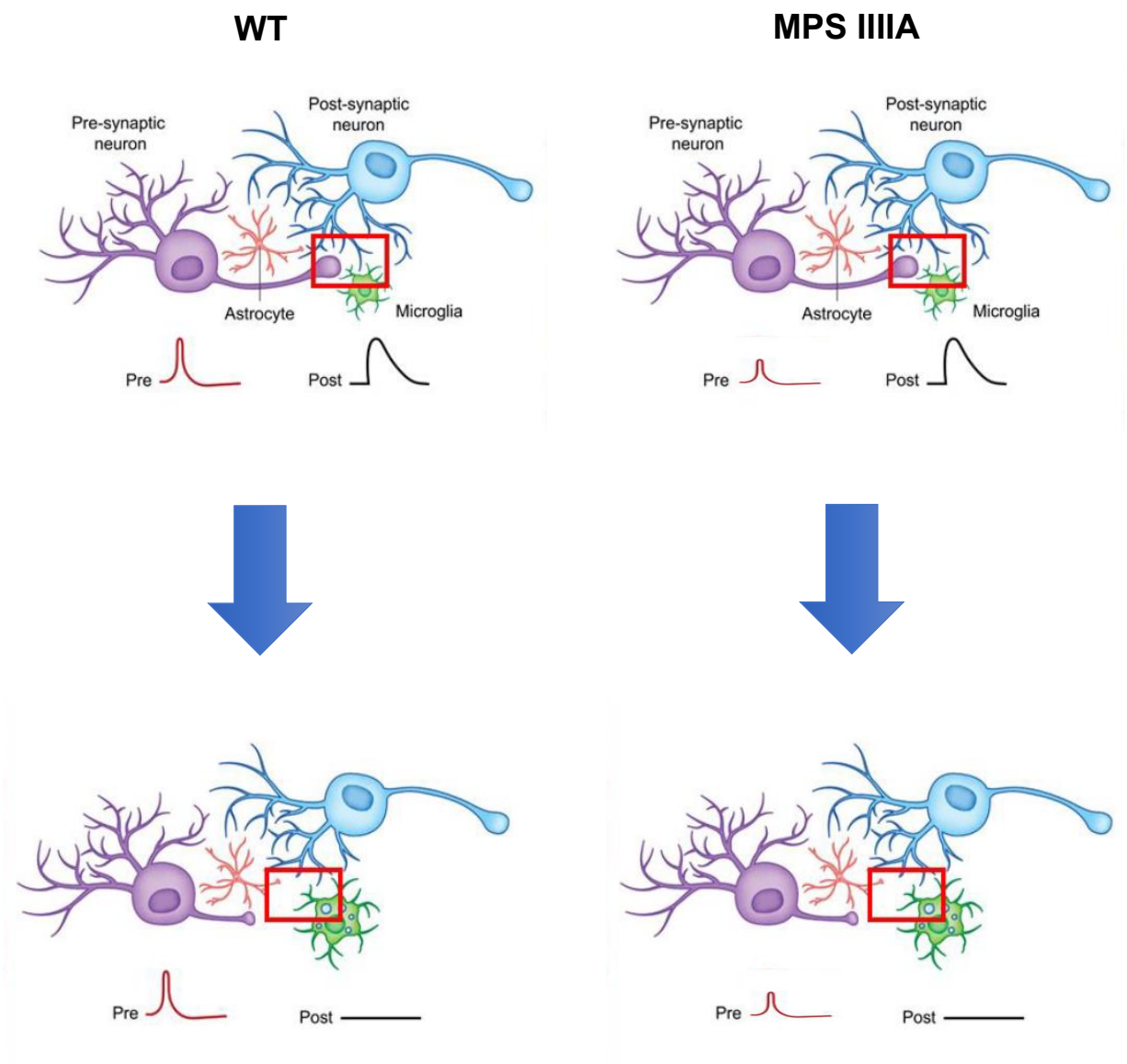


Figure 4.1 – Dendritic spine defects affecting neurotransmission. A diagram highlighting the effect of deficient post-synapses on transmitting pre-synaptic signals, with weaker pre-synaptic signals reported in MPS IIIA. (Adapted from Lacagnina et al., 2017).

To ensure consistent correlations with the findings in Chapter 3, the same $YFP^{+/-}$-MPS IIIA mice were utilised. As detailed in Methods (2.2.7), fresh brain slices were acquired for the electrophysiological experiments, and the expression of YFP ensured the same subset of neurons were tested.

To date, to the best of our knowledge, here has been no electrophysiological evaluation of pyramidal neurons in the MPS IIIA motor cortex. The experiments in this Chapter therefore aimed to utilise patch-clamp electrophysiology to elucidate the biological impact of dendritic spine loss (as described in Chapter 3) on the neuronal activity of layer 5 pyramidal neurons in the motor cortex of MPS IIIA mice at pre- and early-symptomatic ages.

4.2 Results

4.2.1 Electrophysiological properties of layer 5 pyramidal neurons in the MPS IIIA mouse motor cortex

Following the observations in Chapter 3, it was important to establish whether the dendritic spine deficits in MPS IIIA mice affected the electrophysiological properties of the motor cortical neurons. Six-week-old mice were initially evaluated, as this was the age at which spine deficits were first recorded. Brain slices (300µm-thick) encompassing the same motor cortical region of spine loss and the same subset of YFP-positive pyramidal cortical neurons were also utilised. Using a combination of fluorescent and Differential Interference Contrast live imaging, it was possible to ensure that the same neuronal subset was tested (Fig 4.2A) and they were also in physically good shape (Fig 4.2B) following the trauma of *ex vivo* slice preparation. Round and plump cells were identified as healthy cells, whereas shrunken and high-contrast cells were identified as lysed or dying cells (arrow, Fig 4.2B). The technique of somatic whole-cell patch-clamp recording was employed to gather readings, with the micropipette sealed to a typical healthy cell, as shown in Figure 4.2B.

The most likely electrophysiological property affected by dendritic spine loss would be spontaneous synaptic activity recordings, as these measure the direct ionic input via dendritic spines on the patched cell. Using a protocol without added stimulation, traces of miniature EPSCs (mEPSCs) were obtained for analysis of single post-synaptic event kinetics. Typical traces from six-week old wild-type (Fig 4.3A) and MPS IIIA neurons (Fig 4.3B) are shown. As evident in the traces, the frequency of mEPSCs in the motor cortex of MPS IIIA mice was significantly reduced compared with wild-type controls

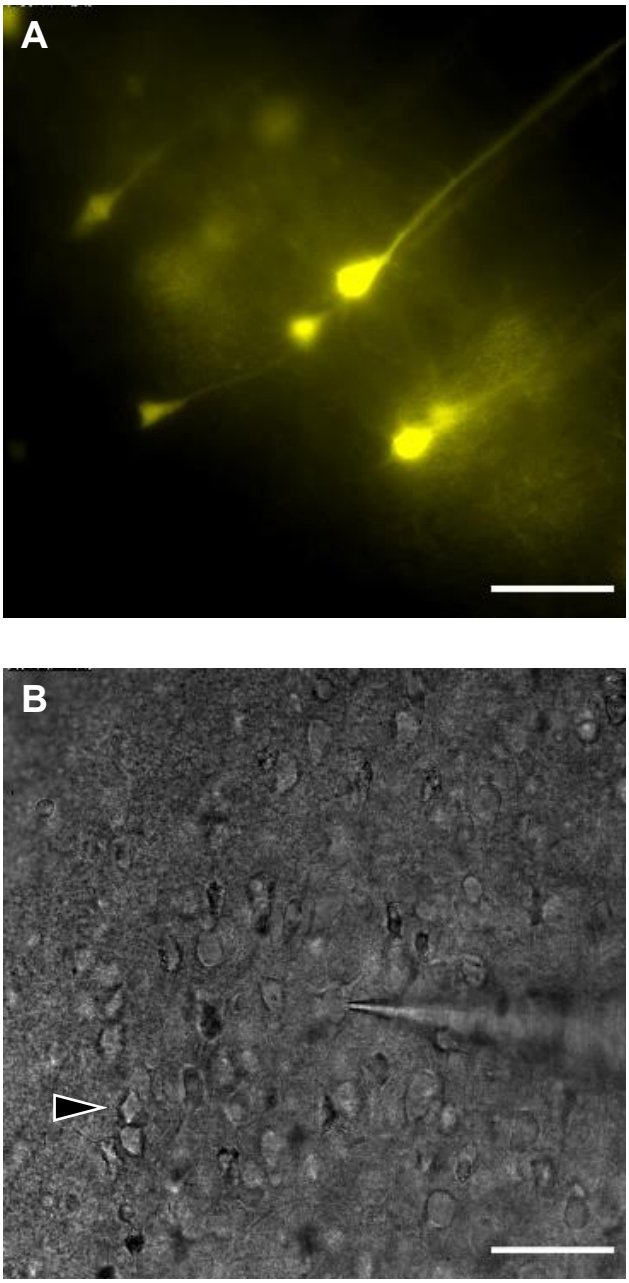


Figure 4.2 – Representative images of YFP-positive neurons patched in the mouse motor cortex. A typical YFP-positive neuron in layer 5 of the motor cerebral cortex (A) in an *ex vivo* slice patched with a micro-pipette (B) for electrophysiological recordings, with the arrow denoting an unhealthy cell. Scale bar is 100µm.

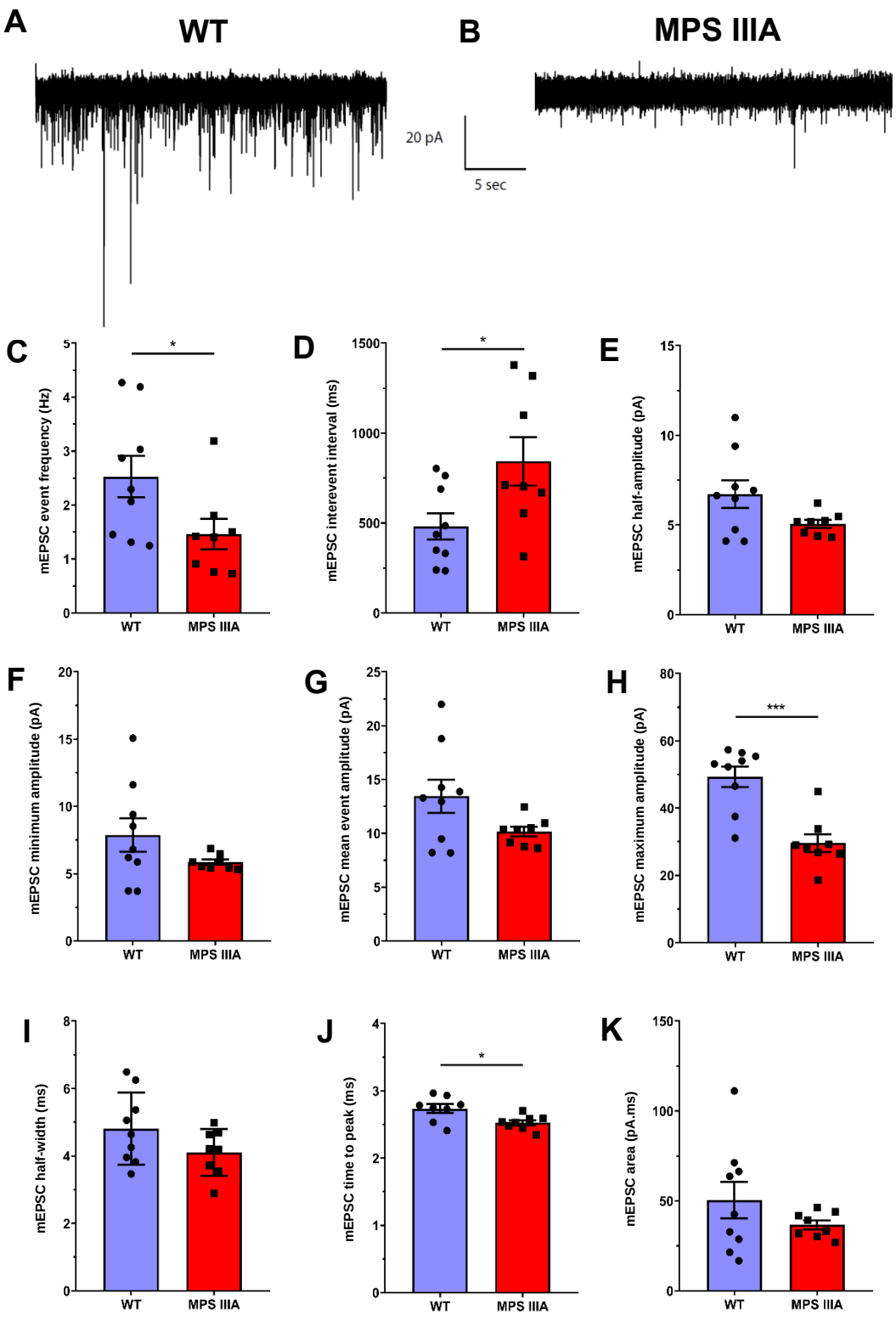

A
WT
B
MPS IIIA
20 pA
5 sec
C
mEPSC event frequency (Hz)
*
WT
MPS IIIA
D
mEPSC interevent interval (ms)
*
E
mEPSC half-amplitude (pA)
F
mEPSC minimum amplitude (pA)
G
mEPSC mean event amplitude (pA)
H
mEPSC maximum amplitude (pA)
***
I
mEPSC half-width (ms)
J
mEPSC time to peak (ms)
*
K
mEPSC area (pA.ms)

Figure 4.3 – Excitatory post-synaptic current kinetics at six-weeks. Representative traces of miniature excitatory post-synaptic current (mEPSC) events recorded in slices taken from six-week old wild-type (WT; A) and MPS IIIA (B) mice. The kinetics of mEPSC events show frequency (C), inter-event interval (D), half-amplitude (E), minimum amplitude (F), mean amplitude (G), maximum amplitude (H), half-width (I), time to peak (J), and area (K). N=3851 WT events; 1989 MPS IIIA events; 9 WT cells; 8 MPS IIIA cells; 1-4 cells per animal; 4 animals per genotype. *$p<0.05$; ***$p<0.001$; parametric unpaired t tests. Data are mean ± SEM.

($p<0.05$; Fig 4.3C). Consequently, the mEPSC inter-event interval increased in MPS IIIA ($p<0.05$; Fig 4.3D). Inter-event interval refers to the average period of time between events, which increases when there are fewer events over a given time period. The strength of the events could also be determined by analysing mEPSC amplitude. Whilst there appeared to be a trend towards lower half-amplitude in MPS IIIA cells (Fig 4.3E), along with minimum amplitude (Fig 4.3F) and mean amplitude (Fig 4.3G), it was not statistically significant. However, there was a significantly lower maximum amplitude for mEPSC events in MPS IIIA cells ($p<0.001$; Fig 4.3H). The duration of these events did not differ between genotypes (Fig 4.3I) but the time to peak did, with a shorter peak time for MPS IIIA cells ($p<0.05$; Fig 4.3J). Despite the differences in amplitude size and time to peak, there was no statistically significant difference regarding the area (under the curve) for the mEPSCs ($p>0.05$; Fig 4.3K).

Following the characterisation of electrophysiological post-synaptic kinetics, the effects of altered synaptic properties on action potential kinetics were examined. As action potentials are naturally generated by a summation of inputs via dendritic spines, it was important to assess the impact of the decreased MPS IIIA mEPSC event frequencies and amplitudes on MPS IIIA action potentials. Initially, a protocol was administered to stimulate the neuron via the electrode within the patched pipette. This protocol contained increasing stimulations in a step-wise manner to depolarise the cell further with each step, and thus increasingly force the neuron to evoke action potentials. These steps were applied for short durations before returning to rest, to allow the neuron to recover. A typically evoked train of action potentials is shown in the wild-type and MPS IIIA neuron traces in Figure 4.4A. By evoking action potentials, it could be determined whether the neurons could function sufficiently, regardless of the nature of synaptic input that was occurring spontaneously. Assessment of the kinetics of the evoked action potentials showed no significant difference

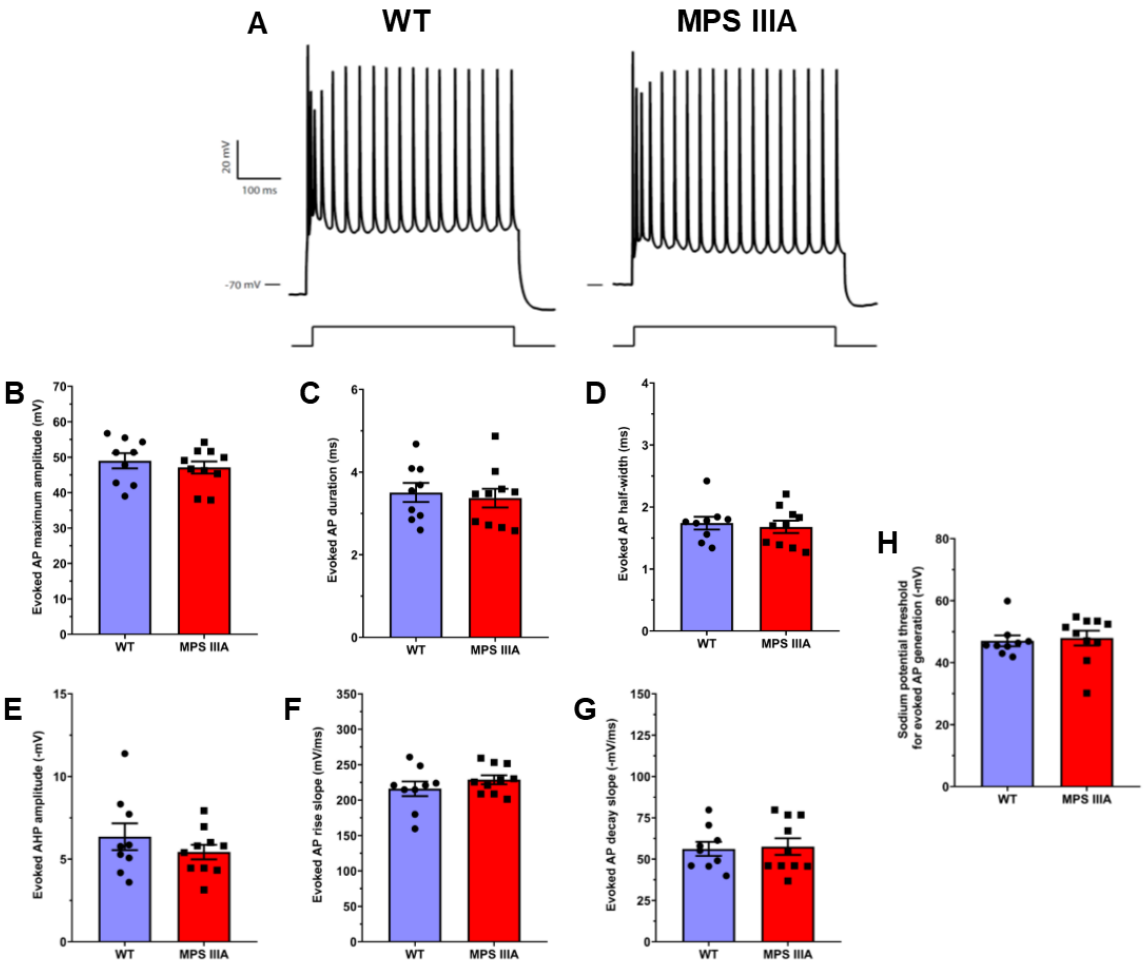


Figure 4.4 – Evoked action potential kinetics at six-weeks. Representative traces of evoked action potentials with the evoked step recorded in slices taken from six-week-old wild-type (WT) and MPS IIIA mice (A). The kinetics of evoked action potentials show maximum amplitude (B), duration (C), half-width (D), afterhyperpolarisation amplitude (E), rise slope (F), decay slope (G), and sodium potential threshold for action potential generation (H). AP, action potential; AHP, afterhyperpolarisation; N=9 WT cells; 10 MPS IIIA cells; 1-4 cells per animal; 4 animals per genotype. Parametric unpaired t tests. Data are mean ± SEM.

between genotypes at six-weeks of age. This included the maximum amplitude of an action potential (Fig 4.4B), action potential duration (Fig 4.4C), half-width (Fig 4.4D), and the amplitude of the afterhyperpolarisation, which is a measure of the cell's ability to restore itself to its resting membrane potential (Fig 4.4E). No differences between groups were observed in the velocities around the action potential peak, including rise (Fig 4.4F) and decay (Fig 4.4G), or in the voltage threshold at which action potentials were generated (Fig 4.4H).

In addition to assessing evoked action potential kinetics, the kinetics of spontaneously firing action potentials was also assessed. Trace examples of sustained firings of action potentials are shown in Figure 4.5A. No differences were observed between wild-type and MPS IIIA for any parameter: maximum amplitude (Fig 4.5B), half-width (Fig 4.5C), rise slope (Fig 4.5D), and decay slope (Fig 4.5E) ($p>0.05$).

Once the characterisation of electrophysiological kinetics had been conducted at six-weeks of age, the findings were validated in an older cohort of 12-week old $YFP^{+/-}$-MPS IIIA mice. Due to time constraints, fewer mice were analysed. The same methods were applied, and trace examples for spontaneous mEPSC are illustrated in Figure 4.6 for wild-type (Fig 4.6A) and MPS IIIA (Fig 4.6B) neurons. As seen at six-weeks, significantly lower mEPSC event frequency was evident at 12-weeks in the MPS IIIA group ($p<0.05$; Fig 4.6C), which correlated with a significantly higher inter-event interval for MPS IIIA neurons ($p<0.01$; Fig 4.6D). Similarly, mEPSC half-amplitude (Fig 4.6E), minimum event amplitude (Fig 4.6F), and mean event amplitude (Fig 4.6G) were not significantly different between genotypes. However, a statistically significant decrease in the maximum amplitude of mEPSC events in the MPS IIIA group was reproduced ($p<0.01$; Fig 4.6H). Lastly, the

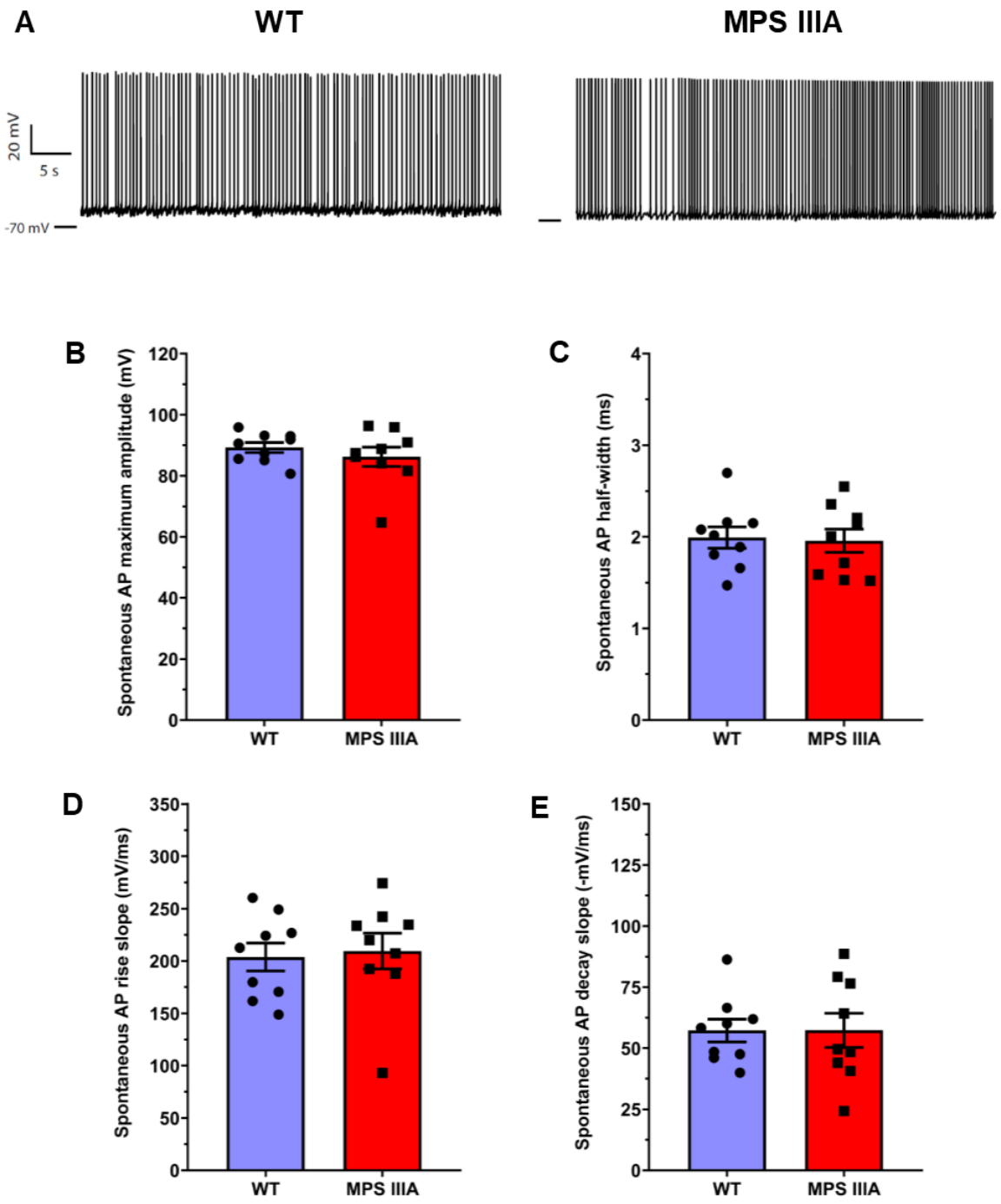


Figure 4.5 – Spontaneous action potential kinetics at six-weeks. Representative traces of spontaneous action potentials recorded in slices taken from six-week-old wild-type (WT) and MPS IIIA mice (A). The kinetics of spontaneous action potentials show maximum amplitude (B), half-width (C), rise slope (D), and decay slope (E). AP, action potential. N=9 WT cells; 10 MPS IIIA cells; 1-4 cells per animal; 4 animals per genotype. Parametric unpaired t tests. Data are mean ± SEM.

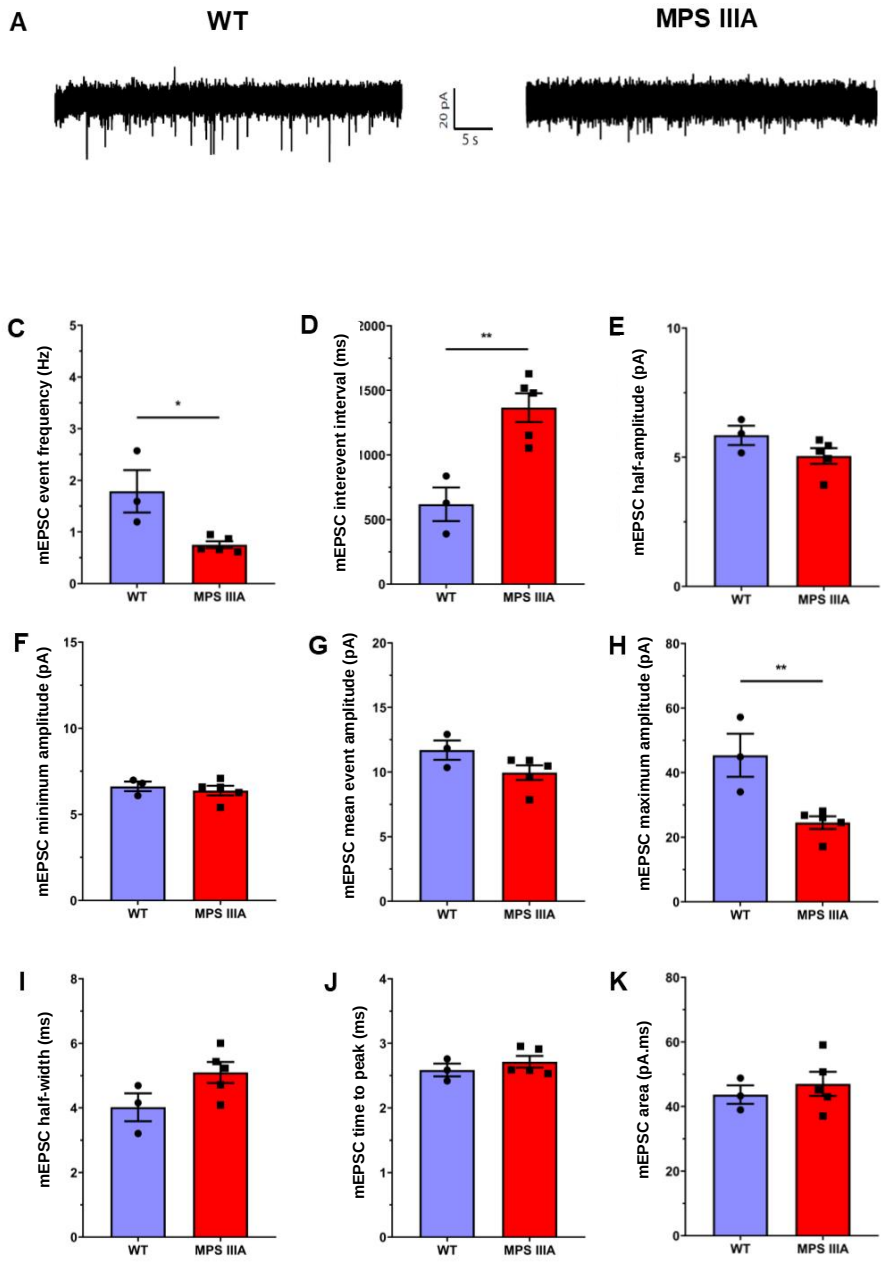


Figure 4.6 – Excitatory post-synaptic current kinetics at 12-weeks. Representative traces of miniature excitatory post-synaptic current (mEPSC) events recorded in slices taken from 12-week-old wild-type (WT) (A) and MPS IIIA (B) mice. The kinetics of mEPSC events show frequency (C), inter-event interval (D), half-amplitude (E), minimum amplitude (F), mean amplitude (G), maximum amplitude (H), half-width (I), time to peak (J), and area (K). N=959 WT events; 938 MPS IIIA events; 3 WT cells; 5 MPS IIIA cells; 1-2 cells per animal; 2 animals per genotype. *p<0.05; **p<0.01; parametric unpaired t tests. Data are mean ± SEM.

duration of these events did not differ between genotypes, as shown by the half-width (Fig 4.6I), time to peak (Fig 4.6J), and average area covered by an event (Fig 4.6K). The effects of altered synaptic properties on action potential kinetics were then assessed at the early-symptomatic age of 12-weeks. Trace examples of a typical train of evoked action potentials captured for analysis from both wild-type control and MPS IIIA motor cortical neurons are illustrated in Figure 4.7A. Although there was a smaller spread of data for each group at 12-weeks, the differences in action potential kinetics were similar with those observed at six-weeks. No significant difference was observed between genotypes, including the maximum amplitude of an action potential (Fig 4.7B), action potential duration (Fig 4.7C), half-width (Fig 4.7D), and the amplitude of the afterhyperpolarisation (Fig 4.7E). Furthermore, no differences were observed in the velocities around the action potential peak, including rise (Fig 4.7F) and decay (Fig 4.7G), or in the voltage threshold at which action potentials were generated (Fig 4.7H).

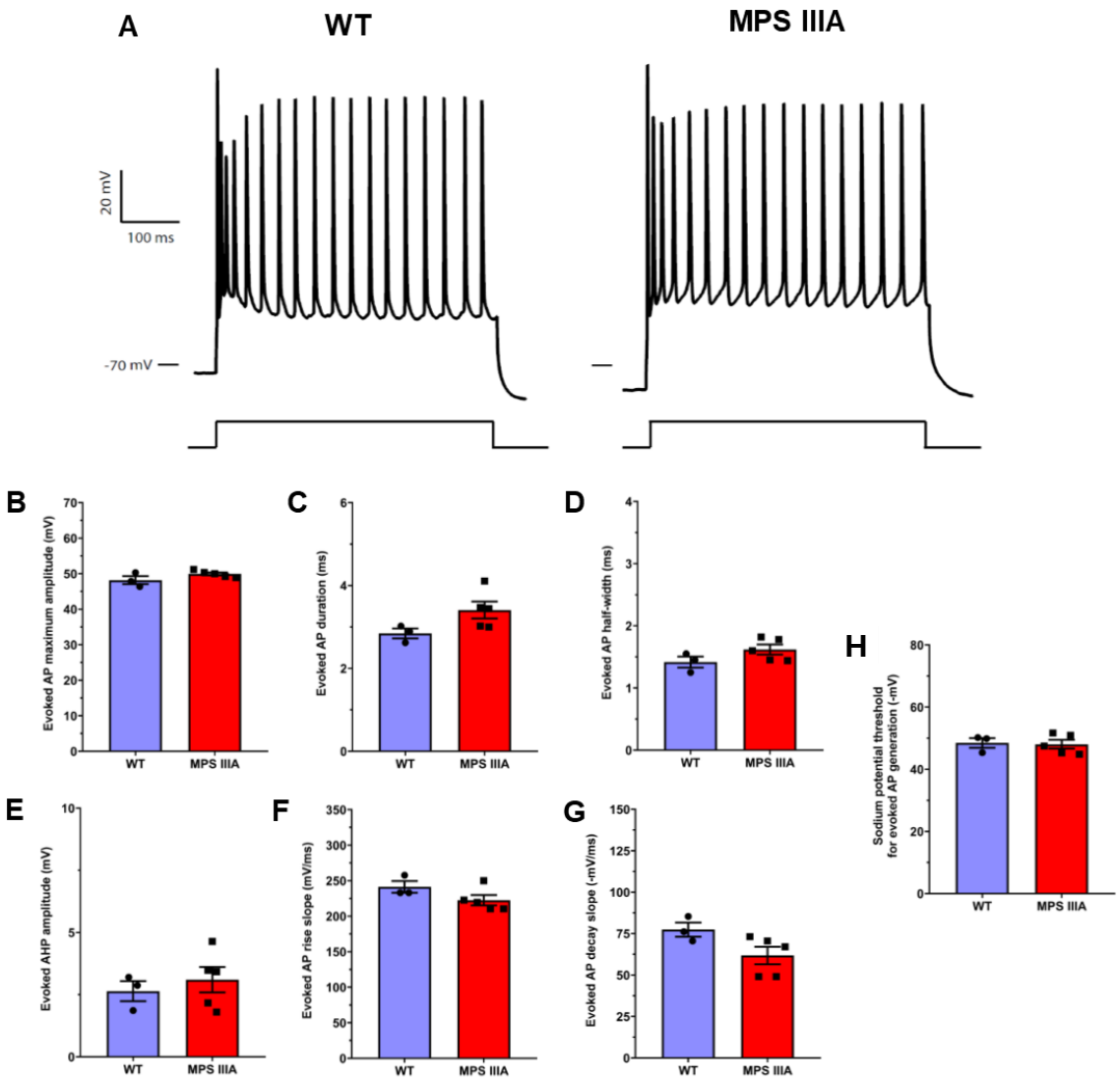


Figure 4.7 – Evoked action potential kinetics at 12-weeks. Representative traces of evoked action potentials with the evoked step recorded in slices taken from 12-week-old wild-type (WT) and MPS IIIA mice (A). The kinetics of evoked action potentials show maximum amplitude (B), duration (C), half-width (D), afterhyperpolarisation amplitude (E), rise slope (F), decay slope (G), and sodium potential threshold for action potential generation (H). AP, action potential; AHP, afterhyperpolarisation. N=3 WT cells; 5 MPS IIIA cells; 1-2 cells per animal; 2 animals per genotype. Parametric unpaired t tests. Data are mean ± SEM.

4.2.2 Sex may have an impact on electrophysiological properties

Following characterisation of the electrophysiological properties in the six-week old mice, a large variation was noted in the data obtained from the wild-type and MPS IIIA groups, the cause of which was then examined. With several reports indicating the impact of sex hormones on synaptic plasticity in neurological disease (McCarthy et al., 2017; McCarthy and Wright, 2017; Nicholson et al., 2020), electrophysiological data were stratified according to sex. Whilst not statistically significant, mEPSC event frequency differed between sex in mice of both genotypes (Fig 4.8A). There was a higher mEPSC inter-event interval in male MPS IIIA mice compared with female MPS IIIA mice but not the wild-type mice (Fig 4.8B). The MPS IIIA males showed the highest inter-event interval of any sub-group.

Whilst not statistically significant, the mean half-amplitude (Fig 4.8C) and mean event amplitude (Fig 4.8E) were higher in the wild-type female sub-group than any other sub-group. The wild-type female sub-group did, however, show a significantly higher minimum mEPSC event amplitude than any other sub-group ($p<0.05$; Fig 4.8D). Assessment of the maximum amplitude of mEPSC events (Fig 4.8F) did not reveal any differences between sex. Whilst mEPSC half-width (Fig 4.8G) and time to peak (Fig 4.8H) presented no sex differences, wild-type female neurons had the largest mEPSC area compared to other sub-groups ($p<0.05$; Fig 4.8I).

Action potential kinetics of the six-week old mice were also further analysed. No statistically significant difference was found between wild-type or MPS IIIA mice of different sex for the maximum amplitude of evoked action potentials (Fig 4.9A). Similarly, no difference in duration of the evoked action potentials was observed, however, MPS IIIA males did show a non-significant higher mean than the MPS IIIA females

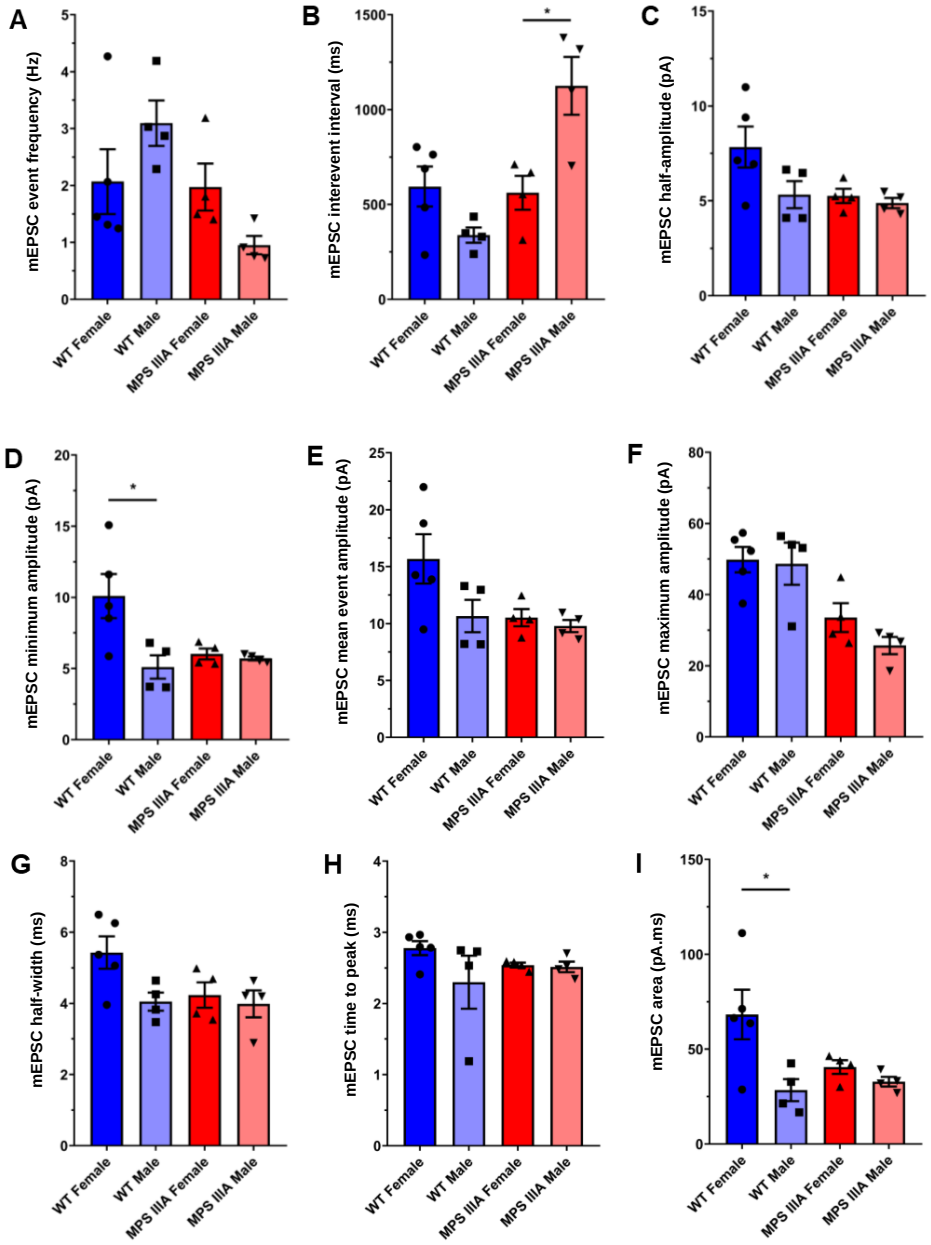


Figure 4.8 – Effect of sex on excitatory post-synaptic current kinetics at six-weeks.

The kinetics of miniature excitatory post-synaptic current (mEPSC) events across mice with different genotypes and sex at six-weeks of age are shown. Frequency (A), inter-event interval (B), half-amplitude (C), minimum amplitude (D), mean amplitude (E), maximum amplitude (F), half-width (G), time to peak (H), and area (I). WT, wild-type. N=959 WT events; 938 MPS IIIA events; 5 female WT cells; 4 male WT cells; 4 female MPS IIIA cells; 4 male MPS IIIA cells; 2 animals/sex/genotype. *$p<0.05$; one-way ANOVA with Bonferroni's multiple comparisons. Data are mean ± SEM.

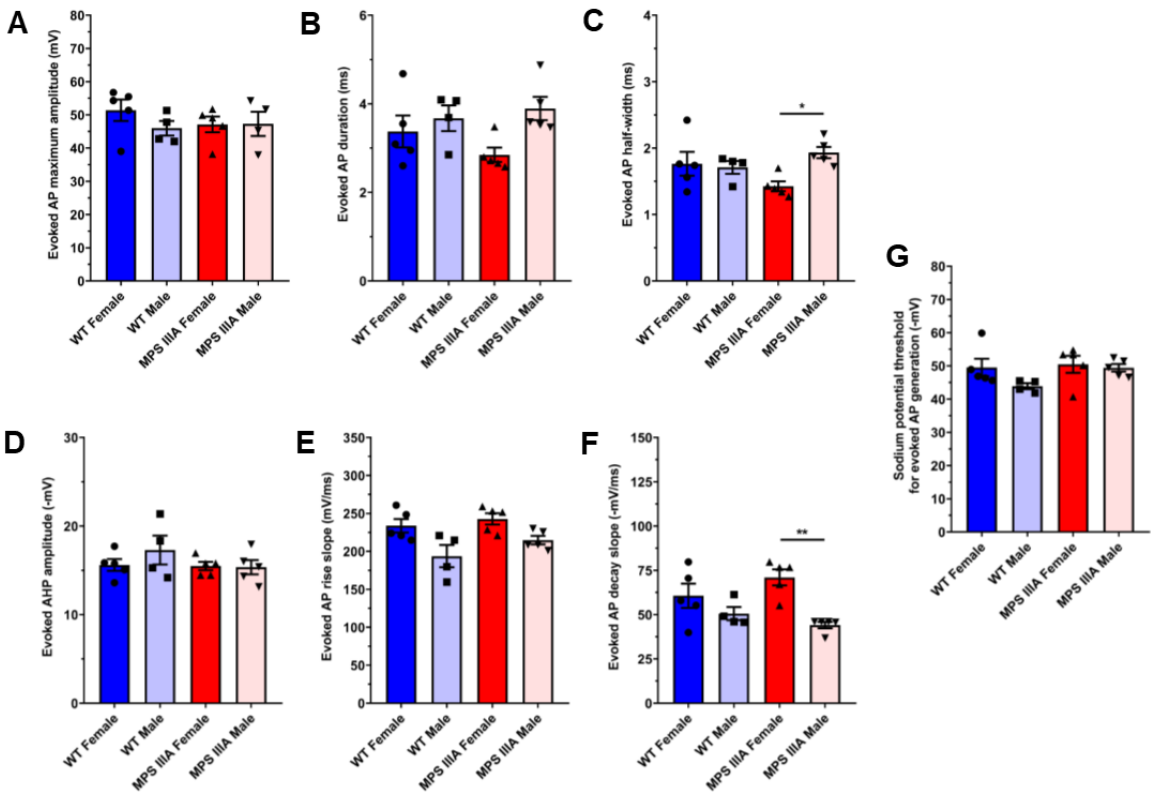


Figure 4.9 – Effects of sex on evoked action potential kinetics at six-weeks. The kinetics of evoked action potentials across mice of different sex and genotypes at six-weeks of age are shown. Maximum amplitude (A), duration (B), half-width (C), afterhyperpolarisation amplitude (D), rise slope (E), decay slope (F), and sodium potential threshold for action potential generation (G). AP, action potential; AHP, after-hyperpolarisation; WT; wild-type. N=5 female WT cells; 4 male WT cells; 5 female MPS IIIA cells; 5 male MPS IIIA cells; 2 animals/sex/genotype. *p<0.05; **p<0.01; one-way ANOVA with Bonferroni's multiple comparisons. Data are mean ± SEM.

(Fig 4.9B). This difference was revealed to be statistically significant after analysis of the half-width of the action potentials (Fig 4.9C). Afterhyperpolarisation amplitude (Fig 4.9D) and rise slopes of action potentials (Fig 4.9E) were not significantly different amongst sub-groups, however, MPS IIIA males had a significantly slower decay slope compared to MPS IIIA females ($p<0.01$; Fig 4.9F). No differences were observed in the sodium potential threshold for action potential generation between males and females (Fig 4.9G).

The maximum amplitude of the action potentials generated through sustained spontaneous firing did not differ between sexes (Fig 4.10A). When assessing the half-width of these action potentials, it was observed that MPS IIIA females generated the briefest individual action potentials, which was significant when compared with the MPS IIIA males ($p<0.05$; Fig 4.10B). Although the males in both genotype groups yielded lower means than the females for the rising slope of action potentials, it was not significant (Fig 4.10C). There was, however, a major difference amongst MPS IIIA neurons, with the decaying slope of MPS IIIA males being much lower than MPS IIIA females ($p<0.01$; Fig 4.10D). The MPS IIIA females had the highest mean value for decaying slope, and lowest mean value for half-width, indicating they were the fastest at returning to resting potential than any other sub-group, although this was not significant across genotypes.

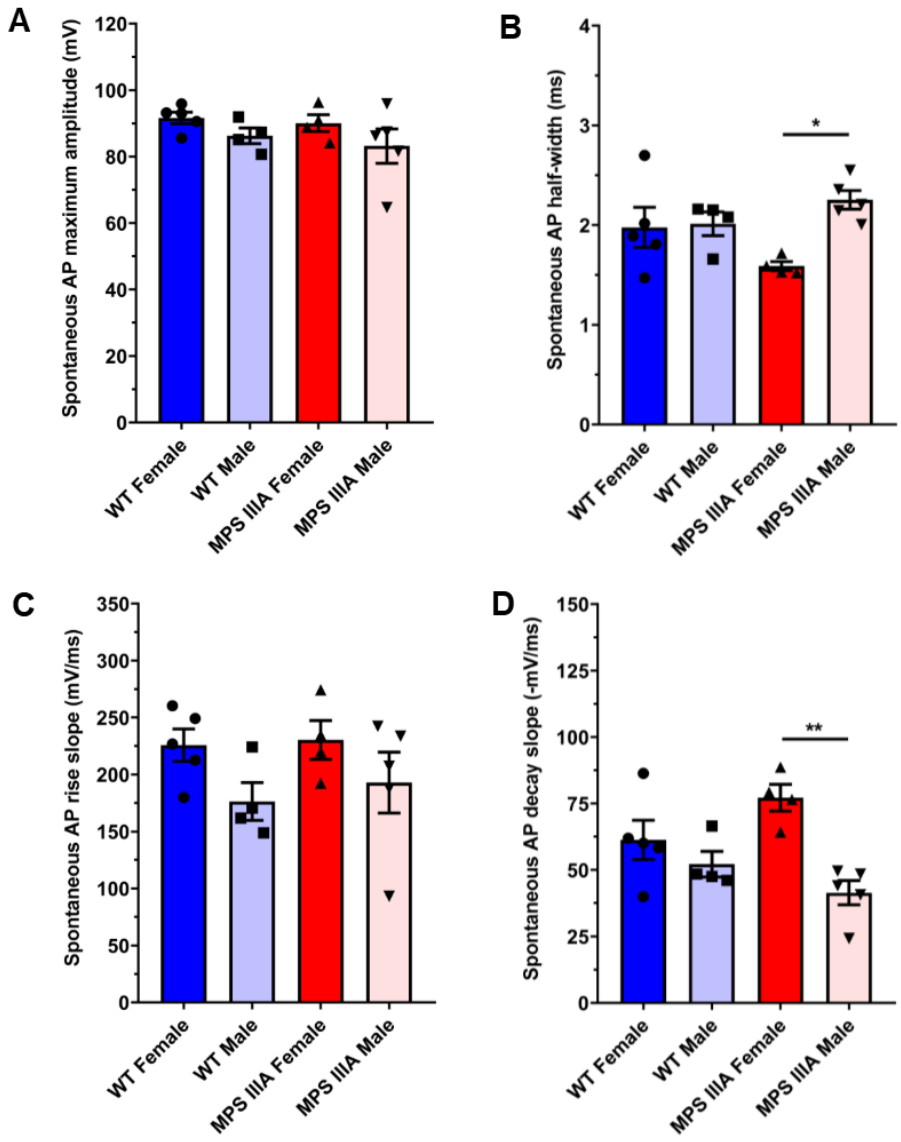


Figure 4.10 – Spontaneous action potential kinetics in six-week-old male and female mouse neurons. The kinetics of spontaneous action potentials across mice with different sex and genotypes at six-weeks of age are shown. Maximum amplitude (A), half-width (B), rise slope (C), and decay slope (D). AP, action potential; WT, wild-type. N=5 female WT cells; 4 male WT cells; 4 female MPS IIIA cells; 5 male MPS IIIA cells; 2 animals per sex per genotype. *p<0.05; **p<0.01; one-way ANOVA with Bonferroni's multiple comparisons. Data are mean ± SEM.

4.3 Discussion

Chapter 3 reported the loss of dendritic spines from layer 5 pyramidal neurons in the motor cortex of pre-symptomatic MPS IIIA mice. It was therefore important to elucidate the biological impact of post-synaptic loss on pyramidal neuron function. To our knowledge, this is the first-time MPS III mouse motor cortical neurons have been examined for the presence of aberrant electrophysiological properties.

The experiments identified reductions in post-synaptic function in spine-deficient MPS IIIA motor cortical neurons from a pre-symptomatic age. Significant reductions in mEPSC event frequency were observed at each of six- and 12-weeks of age in MPS IIIA mice, and a corresponding increase in inter-event interval. Reduced maximum amplitudes in MPS IIIA mEPSC events (compared to wild-type) at both ages was recorded, indicating that dendritic spines remaining on MPS IIIA neurons are not as functionally strong compared to wild-type.

The pioneering work by Keating and colleagues (2012) first assessed synaptic function in MPS IIIA mouse chromaffin cells of the adrenal gland. Using amperometric recordings, they reported an impairment in vesicle secretion at the pre-synapse. There were significant reductions in the frequency of events, and whilst not significant, there were decreases in the mean amplitude kinetics, which is collectively consistent with findings reported in this study.

The findings reported here also support those in a recent study which showed changes to excitatory post-synaptic function in the somatosensory cortex of MPS IIIA mice (Dwyer et al., 2017). They conducted whole-cell patch-clamping in 21-day-old mice and whilst they

found no change to inter-event interval in mEPSC events, they did report a decrease in the average amplitude of mEPSCs in MPS IIIA mice, indicating a reduction in synaptic strength. Dwyer and colleagues (2017) suggest that these changes at 21-days correlated temporally with behavioural changes observed in MPS IIIA mice at three-weeks (Hemsley and Hopwood, 2005; Crawley et al., 2006). Dwyer and colleagues (2017) also reported that HS accumulation increased the levels of selected AMPAR subunits, hypothesising that substrate storage potentially contributes to synaptic neurotransmission defects.

Reduced excitatory function has also been reported in six-month-old MPS IIIA mice, with decreases in the strength of hippocampal field recordings of excitatory potentials (Sambri et al., 2017). Reductions in pre-synaptic vesicle numbers were also noted, suggesting a loss in pre-synaptic function downstream of lysosomal impairment, which impacts post-synaptic function. Indeed, the pre-synapse functions as the release site for neurotransmitters packaged into vesicles that are released at the synaptic terminal, allowing uptake by the post-synaptic dendritic spines (Alberts et al., 2006). There are multiple "pools" of vesicles available for release by the pre-synapse: the reserve (resting/non-recycling) pool which constitutes 85% of vesicles; the recycling pool which constitutes 10% of vesicles; and the readily releasable pool (RRP) which constitutes 5% of vesicles (Rizzoli and Betz, 2005). Vesicles within the RRP are directly released into the synaptic cleft, and in excitatory synapses primarily contain glutamine. Released glutamine binds to the post-synaptic NMDA and AMPAR to allow calcium influx and trigger EPSCs. It is the summation of these EPSCs that triggers an action potential (Sudhof, 2012). Used glutamate leaves the synaptic cleft and is taken up by adjacent glial cells, where glutamine synthase converts glutamate to glutamine. Glutamine is passed back to the pre-synaptic neuron where it is packaged back into vesicles and returned to the pools.

Lysosomal storage of accumulated and undegraded substrate reportedly influences the machinery facilitating synaptic vesicle recycling and trafficking and affects the storage of vesicles in all pools (Parton et al., 1992; Para et al., 2020). This altered recycling process could potentially occur as a result of dysfunctional endocytosis of neurotransmitters at the synaptic cleft, and impaired retrograde transport of the vesicles resulting from reduced microtubule stability (Teixeira et al., 2014). Further investigation into lysosomal function at the synapse by inducing lysosomal inhibition with the chemical leupeptin in cultured rat hippocampal neurons reduced mEPSC frequency, yet did not have a significant effect on mEPSC amplitude (Goo et al., 2017); in addition to altered mEPSC frequency, the same study also reported a reduction in dendritic spines on the hippocampal neurons. Indeed, a recent assessment of MPS IIIC hippocampal neurons recorded partially impaired mobility of synaptic vesicles, with storage bodies identified between microtubule filaments impacting upon trafficking by disorganising the majority of microtubules and coinciding with reduced dendritic spines (de Aragao et al., 2020).

Despite decreases in the number and strength of post-synaptic events in MPS IIIA motor cortical pyramidal neurons, when neurons were stimulated to forcibly generate action potentials, no difference was observed in strength, frequency or kinetics. This suggests that MPS IIIA neurons have the capacity to elicit an excitatory response to 12-weeks of age, but when sufficiently stimulated. Consistent with the findings reported here, no difference in action potential amplitude was recorded in an NPC1 mouse model (Deisz et al., 2005). Conflicting findings were, however, noted in a separate study on cerebellar slices from $NPC1^{-/-}$ mice, with increased frequency of GABAergic IPSCs of $NPC1^{-/-}$ Purkinje cells preceding neuronal loss (Rabenstein et al., 2019). Whilst this was still the result of dysfunctional neurons, impaired exchange of post-synaptic AMPAR was suggested to

cause the increased release of pre-synaptic vesicles to reach the post-synaptic receptors (Rabenstein et al., 2019).

Conversely, components of pre-synaptic vesicles within the RRP were reportedly reduced at both excitatory and inhibitory synapses in a separate study on NPC1 mice (Xu et al., 2010). Moreover, a murine model of the neurological lysosomal disorder Sandhoff disease showed GM2-ganglioside accumulation in the hippocampus reduced the amplitude of AMPAR-mediated currents, despite no difference in overall number of GluR1 receptors (Hooper and Igdoura, 2016). Additionally, inactivation of cathepsin D (located in GABAergic pre-synaptic endosomes and associated with CLN10 Batten disease) was found to result in enlarged pre-synaptic endosomes, reducing the RRP and impairing synaptic transmission (Li et al., 2019). Collectively, these data suggest that sub-cellular receptor trafficking rather than actual protein levels could be directly influencing neuronal function (along with the impact of storage material within neuronal lysosomes) on the regulation of synaptic proteins and neurotransmission.

Expanding on these data, a more extensive assessment of electrophysiological parameters has been conducted in LSD mouse models (listed in Table 4.1). In addition to the described studies, Niemann-Pick disease type C models have shown fluctuating electrophysiological kinetics in Purkinje cells, with no change in EPSC amplitude but an increase in frequency (Sun et al., 2011). EPSP is a measure of membrane voltage changes as a result of positively charged ions moving into a post-synaptic cell. It was assessed at six-weeks of age in the striatum and hippocampus of NPC1 mouse brain slices: no differences were recorded but it did present with an increased amplitude in the somatosensory cortex compared with age-matched controls (Avchalumov et al., 2012). Despite the change in amplitude, there was no recorded difference in paired-pulse ratio (ratio of second signal

amplitude strength to first), which indicated no difference in release probability of the pre-synaptic terminals. Conflictingly, at the same age and within the hippocampus, there was an earlier finding of increased EPSP amplitude and decreased paired-pulse ratio in NPC1 mice compared with controls (Zhou et al., 2011). A decreased paired-pulse ratio in NPC1 mice indicated an increased release probability of the pre-synaptic terminals (Zhang et al., 2003).

Assessments of a CLN1 mouse model at six-weeks of age found an increased EPSC rise time but decreased EPSC amplitude within the visual cortex (Koster et al., 2019). Assessment of brain slices containing the amygdala and hippocampus from the CLN3 Batten disease mouse at the advanced age of 14-months recorded significant functional impairment with decreases in EPSC and IPSC frequency and amplitude (Grunewald et al., 2017). IPSC refers to the events of chloride channels opening on the post-synaptic inhibitory synapse, which hyperpolarises the cell and makes it less likely to generate an action potential. Within the cerebellum of the same model, whilst post-synaptic currents were not assessed, reductions in action potential frequency were recorded (Grunewald et al., 2017). Time course electrophysiological assessments in hippocampal and visual cortical slices at one-, four-, eight-, and 12-months showed no difference in CLN3 EPSP amplitude compared with age-matched controls, however, deficits in axonal excitability were recorded (Burkovetskaya et al., 2017). Interestingly, an *in vivo* time course assessment of the hippocampus in the same model found functional deficits from two-months of age (Ahrens-Nicklas et al., 2019). Lastly, investigation into the electrophysiological properties of the neurodegenerative LSD alpha-mannosidosis found a decrease in post-synaptic strength in the hippocampus at 10-months of age (Stroobants et al., 2017).

Table 4.1 – Summary of current electrophysiological knowledge in LSD mouse models. A summary of the current knowledge for electrophysiological parameters in the brain of LSD mouse models. The arrows denote a difference in the MPS genotype of 'increase', 'decrease', or 'no change'. AP, action potential; EPSC, excitatory post-synaptic current; EPSP, excitatory post-synaptic potential; IPSC, inhibitory post-synaptic current; NCL, neuronal ceroid lipofuscinosis; NPC, Niemann-Pick C; VSDI, voltage-sensitive dye imaging.

Disease Model	Age	Model	Region	Recording	Difference	Reference
MPS IIIA	20-week	*In vitro*	Chromaffin cells (adrenal glands)	Pre-synaptic vesicle exocytosis frequency	↓	Keating et al., 2012
				Pre-synaptic vesicle exocytosis kinetics	↔	
	3-week	*Ex vivo*	Somatosensory cortex	EPSC frequency	↔	Dwyer et al., 2017
				EPSC amplitude	↓	
			Hippocampus	EPSP amplitude	↔	
	6-month	*Ex vivo*	Hippocampus	EPSP amplitude	↓	Sambri et al., 2017
MPS IIIC	3-week	*In vitro*	Hippocampus	EPSC frequency	↑	Aragao et al., 2020
				EPSC amplitude	↑	
				IPSC frequency	↔	
				IPSC amplitude	↔	
	8-week	*Ex vivo*	Hippocampus	EPSC frequency	↓	
				EPSC amplitude	↓	
				EPSC kinetics	↔	
				IPSC frequency	↓	
				IPSC amplitude	↓	
Niemann-Pick C1	3-week	*Ex vivo*	Hippocampus	EPSC amplitude	↔	Xu et al., 2010
				EPSC depression	↓	
				EPSC area	↓	
				IPSC amplitude	↔	
				IPSC depression	↓	
				IPSC area	↓	
	3-week	*Ex vivo*	Cerebellum	EPSC frequency	↑	Sun et al., 2011
				EPSC amplitude	↔	
	3-week	*Ex vivo*	Cerebellum	IPSC frequency	↑	Rabenstein et al., 2019
	6-week	*Ex vivo*	Hippocampus	EPSP amplitude	↑	Zhou et al., 2011
				Paired-pulse ratio	↓	
	6-week	*Ex vivo*	Striatum	EPSP amplitude	↔	Avchalumov et al., 2012
			Hippocampus	EPSP amplitude	↔	
			Somatosensory cortex	EPSP amplitude	↑	
				Paired-pulse ration	↔	
	10-week	*Ex vivo*	Sensory-motor cortex	AP amplitude	↔	Deisz et al., 2005

Table 4.1 – Summary of current electrophysiological knowledge in LSD mouse models (continued).

Disease Model	Age	Model	Region	Recording	Difference	Reference
Batten (CLN1)	6-week	*Ex vivo*	Visual cortex	EPSC amplitude	↓	Koster et al., 2019
				EPSC rise time	↑	
Batten (CLN3)	14-month	*Ex vivo*	Amygdala	IPSC amplitude	↓	Grunewald et al., 2017
				IPSC frequency	↓	
				EPSC amplitude	↓	
				EPSC frequency	↓	
			Hippocampus	IPSC amplitude	↓	
				IPSC frequency	↓	
				EPSC amplitude	↓	
				EPSC frequency	↓	
			Cerebellum	AP frequency	↓	
	2-month	*In vivo*	Hippocampus	VSDI area	↓	Ahrens-Nicklas et al., 2019
	7-month	*In vivo*	Hippocampus	VSDI area	↓	
	21-month	*In vivo*	Hippocampus	VSDI area	↓	
	1-month	*Ex vivo*	Hippocampus	EPSP amplitude	↑	Burkovetskaya et al., 2017
	4-month	*Ex vivo*	Hippocampus	EPSP amplitude	↔	
	8-month	*Ex vivo*	Hippocampus	EPSP amplitude	↔	
	12-month	*Ex vivo*	Hippocampus	EPSP amplitude	↔	
	1-month	*Ex vivo*	Visual cortex	EPSP amplitude	↔	
	4-month	*Ex vivo*	Visual cortex	EPSP amplitude	↔	
	12-month	*Ex vivo*	Visual cortex	EPSP amplitude	↔	
α-mannosidosis	10-month	*Ex vivo*	Hippocampus	EPSP amplitude	↓	Stroobants et al., 2017

Collectively, these studies provide a baseline for electrophysiological assessment and comparison amongst the LSDs. However, there was minimal data characterising the functional properties of MPS IIIA neurons, and a lack of assessment of the motor cortex for any of the other LSD models tested. Additionally, whilst time courses have been conducted, they are limited to Batten disease, and morphometric analyses of dendritic spines were not included in those studies. The findings reported here suggest motor cortical neurons in MPS IIIA mice have functionally impaired post-synapses from a pre-symptomatic age, which persist to an early-symptomatic age and could thus contribute to symptom development and progression due to insufficient post-synapses and ionic flow into the post-synaptic neuron.

Secondary to these findings, some differences between females and males were found in both the wild-type and MPS IIIA groups, which had not been previously addressed for any brain region in MPS IIIA or any other LSD model. Indeed, the observations reported here were not limited to post-synaptic kinetics where initial genotypic differences were observed. Differences in action potential kinetics were also found, which was particularly interesting given that significant differences in action potential kinetics were not observed between genotypes when sex was not accounted for. Whilst similar trends were observed for mEPSC characteristics within genotypes (e.g. same observed trends for rise and decay slopes between females and males in both wild-type and MPS IIIA groups), only the single sub-group of wild-type females showed strong differences in mEPSC amplitude characteristics compared to any other sub-group. Therefore, sex appears to have an impact on dendritic spine function in the cerebral motor cortex regardless of disease phenotype. However, these findings should be taken with caution, as group sizes for each sex and genotype following sub-categorisation were small.

Whilst this was a preliminary evaluation of sex impact on electrophysiological parameters for any brain region in any LSD model, the effects of gonadal hormones on brain structure and function have in fact been previously investigated throughout both the developing and adult normal mouse and human brains (Luine and Rodriguez, 1994; McEwen and Alves, 1999; Brinton, 2009; Srivastava et al., 2013). Female mice can reportedly express double the density of dendritic spines compared with males but show no difference following removal of the ovaries, heavily suggestive of the impact of sex on synaptic plasticity (Gould et al., 1990; Shors et al., 2001). The hippocampal region has been extensively investigated in mice, with multiple studies conclusively reporting higher levels of oestrogen during the proestrus phase of the oestrus cycle correlating to higher densities of dendritic spines (Woolley et al., 1990; Woolley and McEwen, 1992; Kato et al., 2013). This was translated to humans where there was a reported significant increase in hippocampal volume in females when oestrogen levels peaked (Protopopescu et al., 2008). In addition to the hippocampus, chronic changes to dendritic spine density due to oestradiol have also been reported in the rat hypothalamus (Frankfurt et al., 1990) and amygdala (de Castilhos et al., 2008; Rasia-Filho et al., 2012).

Studies of the cerebral cortex are fewer and less conclusive, with some reports of the female cortex presenting higher densities of dendritic spines during the proestrus phase in the rat primary somatosensory cortex (Chen et al., 2009), while others report no differences in density at different stages of the oestrus cycle. These include the neocortex in rats (Prange-Kiel et al., 2008), and the prefrontal cortex in rats (Markham and Juraska, 2002). A more recent *in vivo* study assessed mouse layer 5 cortical pyramidal neurons (comparable to this study) but within the primary somatosensory cortex **(**Alexander et al., 2018): no differences in spine density were found in females across the oestrus cycle, and the density was similar with males. They did, however, report a higher level of induced

synaptic plasticity in female mice when stimulating during the proestrus and oestrus phases compared with the metestrus/diestrus phases, suggesting certain stages of the oestrus cycle could favour the formation and elimination of synaptic connections.

Our laboratory generally utilises male mice for MPS IIIA behavioural testing, as female MPS IIIA mice reportedly show an absence or delay in phenotypic changes, which was initially hypothesised to be due to hormonal effects (Hemsley and Hopwood, 2005; Crawley et al., 2006). In another neurodegenerative disorder, clinical data suggest the risk for females to develop Alzheimer's disease increases after menopause, when levels of oestradiol decrease (Lan et al., 2015). However, there are no reports of increased prevalence of MPS IIIA in males compared with females. The electrophysiological findings in this study are supported by the literature and suggest that sex may have some impact on dendritic spine functionality and potentially phenotypic expression in the MPS IIIA mouse motor cortex. Unfortunately, earlier electrophysiological studies in MPS IIIA mice did not report sex (Dwyer et al., 2017; Sambri et al., 2017) so it is not possible to extrapolate. However, the recent report by de Aragao and colleagues (2020) in MPS IIIC mouse neurons did report sex. Interestingly, they combined sexes for their *in vitro* experiments, and showed no difference between sexes in their neuronal cultures. This may potentially be due to the absence of gonadal hormones in the culture media, which would normally impact synaptic development in an *in vivo* setting. Future studies assessing synaptic properties in animal models of neurological disease should therefore account for and report sex.

When assessing neuronal function, it is important to consider all components of the neuronal synapse. As discussed, extensive evaluation of the pre-synapse has been reported in models of MPS III. This study contributes to our understanding of the role and impact of

the post-synapse in MPS IIIA. Collectively, these data and reports suggest multiple factors could be contributing to MPS IIIA symptom onset and disease progression. The reduced pre-synaptic vesicle density and release in MPS IIIA could be contributing to a reduction in the number and strength of post-synaptic events. As these changes are observed from pre-symptomatic ages and persist throughout the MPS IIIA disease course up to 20-weeks, these could be the changes to the neurons that trigger symptom onset. Interestingly, despite suffering weakened and fewer post-synapses, the MPS IIIA neurons were still able to function effectively with evoked wild-type level action potentials at both six- and 12-weeks of age, suggesting biological function has not completely deteriorated and could potentially be restored with sufficient stimulation of the post-synapse.

These factors highlight additional avenues for future investigation and treatment. As deficient electrophysiological properties in MPS IIIA motor cortical neurons corresponded to reduced dendritic spines, it will be interesting to investigate therapeutic approaches on post-synaptic function. Indeed, a gene therapy supplied to MPS IIIC mice at eight-weeks of age led to partial restoration of the PSD six-months post-treatment (de Aragao et al., 2020). However, earlier intervention is likely to yield more effective results. The use of gene therapy and its ability to prevent dendritic spine loss will be discussed further in Chapter 6. Until proven otherwise, future studies should involve the animals/subjects of both sexes in MPS IIIA phenotypic or therapeutic evaluations.

4.4 Conclusion

In summary, this study observed reduced electrophysiological activity in dendritic spine-deficient layer 5 pyramidal neurons in the MPS IIIA mouse motor cortex from a pre-symptomatic age. This suggests that the spine defects exert a biological impact on the functionality of neurons in the motor cortex of MPS IIIA mice, and thus may be the source of symptom onset. Some sex-based differences in electrophysiological parameters were identified and should be considered in future investigations. Based on these findings, future testing of therapeutic interventions could include post-synaptic proteins as novel biomarkers to measure the presence of disease lesions and their amelioration compared with treatment.

– CHAPTER 5 –

NEUROIMMUNE PROPERTIES OF THE MPS IIIA MOUSE BRAIN AND THEIR RELATION TO DENDRITIC SPINE DEFECTS

5.1 Introduction

Astro- and microgliosis have been well documented to occur in MPS III brain tissue. Neuroinflammation is suggested to be triggered by the increase in and accumulation of HS and secondary lipids present in both neurons and glial cells (Ohmi et al., 2003). Furthermore, priming of microglia was postulated to occur due to elevated pro-inflammatory cytokine levels in MPS IIIB mice, including IL-1β and TNF-α, by 12-weeks of age (Ausseil et al., 2008). Elevated mRNA for inflammatory C1q and C4 were also identified in MPS IIIB and MPS II mouse brain (Ohmi et al., 2003; Motas et al., 2016). Collectively, these data indicate that pro-inflammatory activation of both microglia and astrocytes may contribute to disease onset in MPS III, but the precise mechanism of action is unknown (Fig 5.1).

Complement cascade components released from astrocytes localise to developing synapses and mediate phagocytosis of the synapse by microglia, refining and strengthening the remaining synaptic connections in the CNS through a process termed “synaptic pruning”, which removes unnecessary dendritic spines (Fig 5.2; Pfrieger and Barres, 1997; Schafer et al., 2012). However, an elevated and sustained pruning process has been implicated in neurodegenerative diseases, including Alzheimer’s, Parkinson’s, and Huntington’s diseases (Stevens et al., 2007; Liddelow et al., 2017; Sellgren et al., 2019; Hammond et al., 2020).

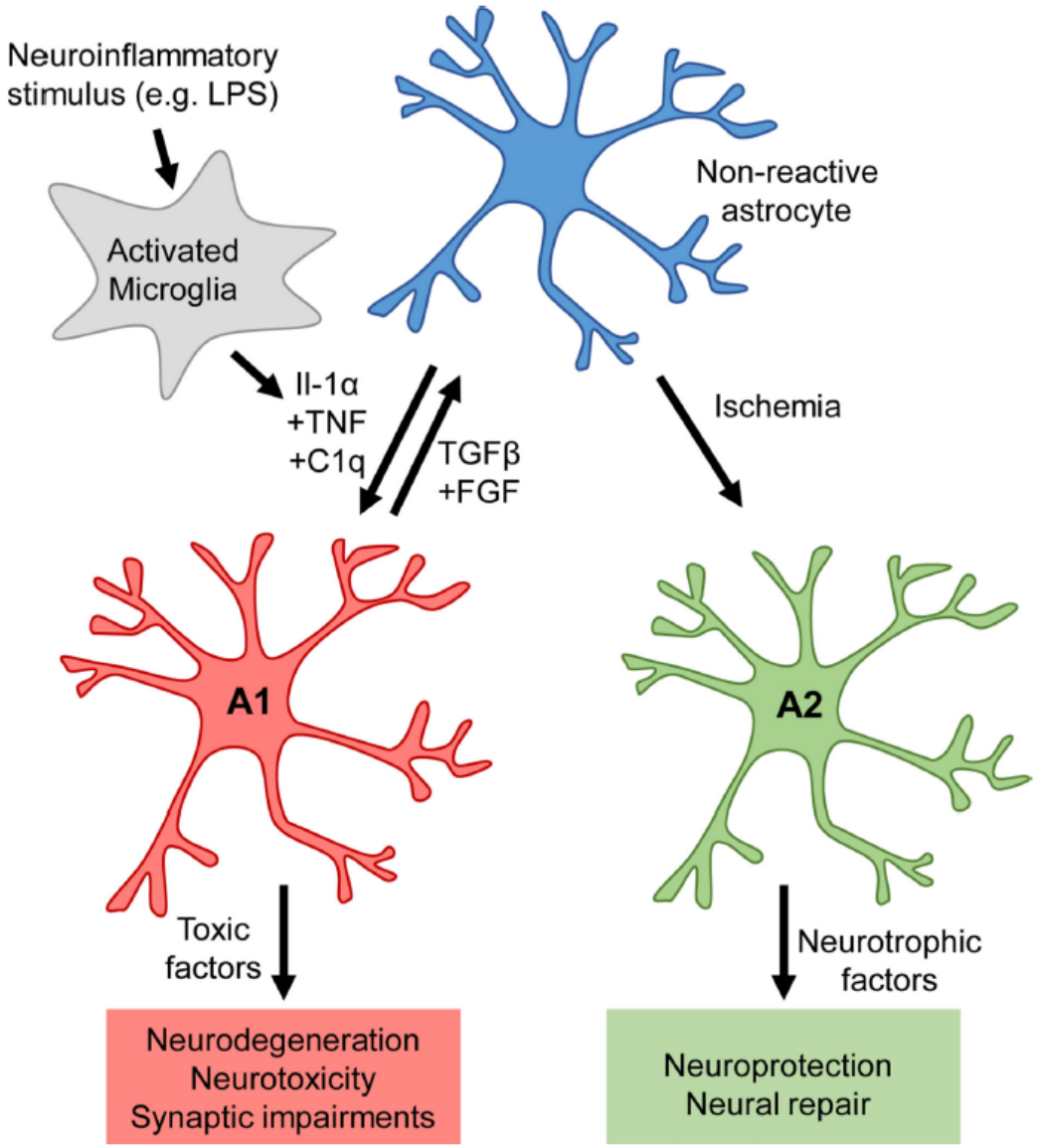


Figure 5.1 – Mediation of astrocyte activation. A diagram highlighting the activation of multiple astrocyte phenotypes by neuroinflammatory stimuli and cytokine release by microglia. C1q, complement component 1 subcomponent q; TNF, tumour necrosis factor; FGF, fibroblast growth factor; IL-1α, interleukin 1-alpha; TGFβ, transforming growth factor beta**.** (Baldwin and Eroglu, 2017).

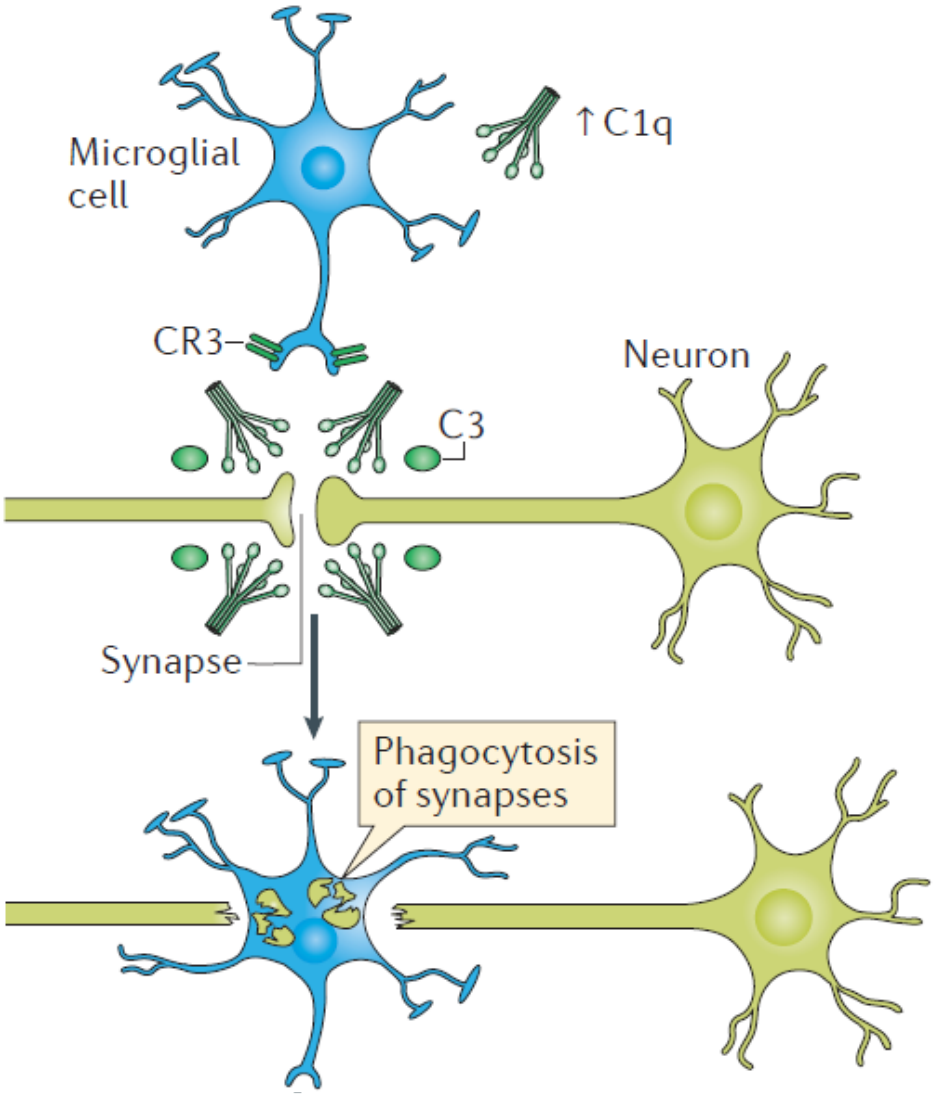


Figure 5.2 –Complement-mediated synaptic pruning. A diagram highlighting the pruning of synapses through the binding of complement components C1q and C3, and recruitment of microglia. C1q, complement component 1 subcomponent q; C3, complement component 3; CR3, complement receptor 3. (Li and Barres, 2018).

The induction of reactive astrocytes by microglia, particularly through the complement cascade, may therefore play a significant role via neuroinflammation in the mucopolysaccharide disorders. However, the types of reactive astrocytes activated in the mucopolysaccharidoses, and indeed in any of the LSDs, is presently unknown. Furthermore, it is not known whether reactive glial cells are directly harmful to synapses or if they have any possible impact on symptom development as a result of lysosomal dysfunction.

Overall, the experiments in this Chapter aimed to expand our understanding about whether complement-based mechanisms contribute to neurological dysfunction in MPS IIIA, and thus potentially provide therapeutic targets for this currently untreated disease.

5.2 Results

5.2.1 Glial cell activation and complement component levels are higher in the MPS IIIA motor cortex

To address the third aim of the study, these experiments sought to quantify complement C1q and C3 expression and associate microglial and astrocyte activation over the disease time course up to 20-weeks of age in MPS IIIA mice. Subsequently, changes in innate immune activity were then related to synaptic changes noted on pyramidal neurons in the MPS IIIA mouse motor cortex.

The same brain samples from the $YFP^{+/-}$-MPS IIIA and wild-type mice examined in Chapter 3 were utilised, which were bred and aged to three- and six-weeks (pre-symptomatic), 12-weeks (early-symptomatic), and 20-weeks (late-symptomatic). Immunofluorescence staining was carried out on free-floating 20µm-thick slices encompassing the same motor cortical region where differences in dendritic spine density were observed (Chapter 3). The first assay analysed C1q (the initiating component of the complement cascade) expression levels and microglial activation. Microglia were identified by the ionised calcium-binding adaptor molecule 1 (Iba1) antibody, which detects the protein exclusively expressed in microglia. Representative images of this assay over the disease time course to 20-weeks are shown in Figure 5.3.

A significant increase in the level of C1q was observed in MPS IIIA mice at the pre-symptomatic age of six-weeks ($p<0.05$; Fig 5.4A), coinciding with the observed loss of dendritic spines. Whilst not statistically significant, C1q expression trended upwards compared with age-matched controls for the remaining ages studied ($p>0.05$) and separated into two distinct sub-groups by 20-weeks of age. The 20-week-old MPS IIIA mice with

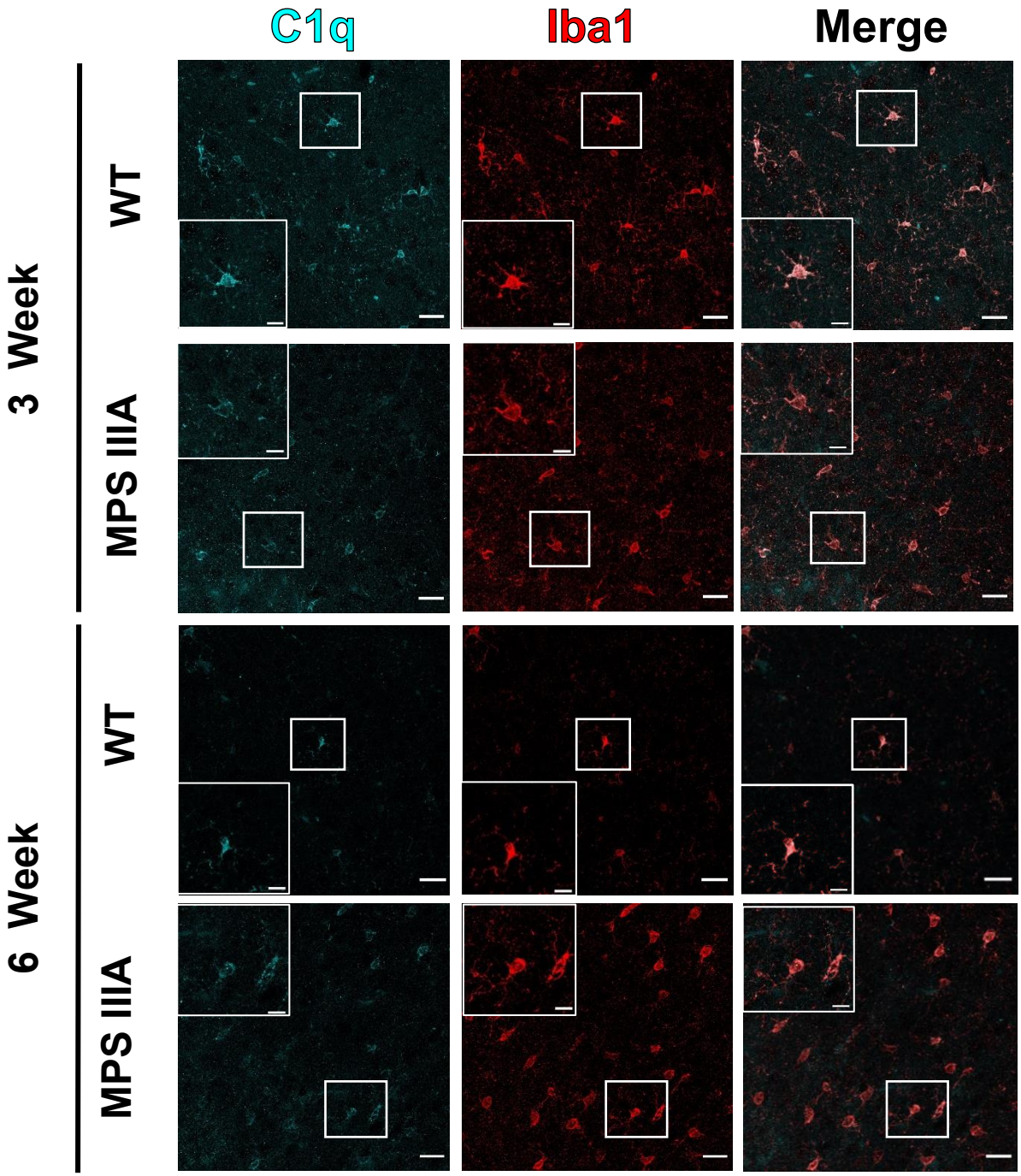


Figure 5.3 – Representative images of C1q and Iba1 immunofluorescence assay. Visualisation of complement component C1q and Iba1 (microglia) in layer 5 of the cerebral motor cortex in wild-type (WT) and MPS IIIA mice at three-, six-, 12-, and 20-weeks of age. Scale bar is 25µm; magnified inset scale bar is 10µm.

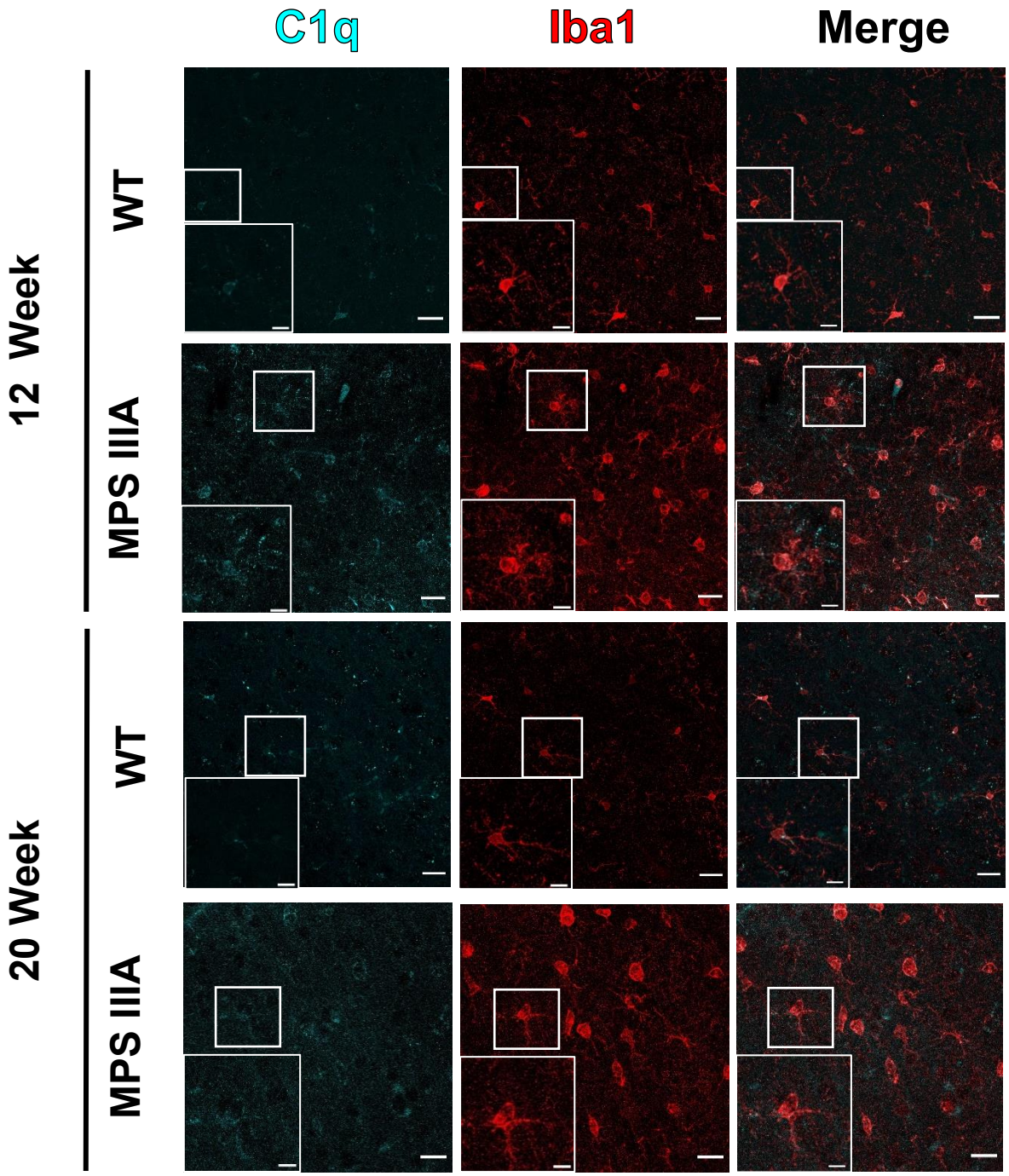


Figure 5.3 – Representative images of C1q and Iba1 immunofluorescence assay (continued).

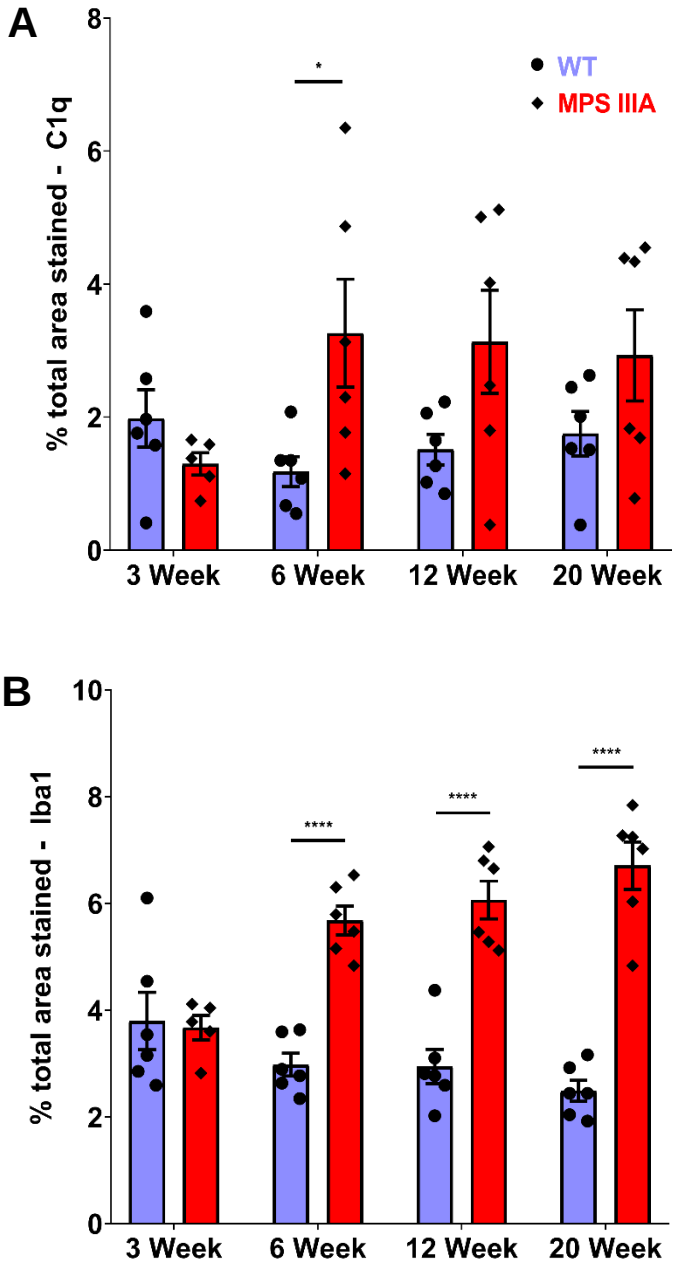


Figure 5.4 – Levels of C1q and Iba1 in the mouse motor cortex. Complement component C1q (A) and Iba1 (microglial) (B) levels localised in layer 5 motor cortex of wild-type (WT) and MPS IIIA mice at three-, six-, 12-, and 20-weeks of age. N=6 animals per genotype per age. $p<0.05$; ****$p<0.0001$; two-way ANOVA, with Bonferroni's multiple comparisons. Data are mean ± SEM. Experimenter blinded to genotype and age.

higher C1q expression were male, and the 20-week MPS IIIA mice expressing lower C1q levels were female. The percent of Iba1 staining within the motor cortex was also higher in MPS IIIA mice from six-weeks of age ($p<0.0001$; Fig 5.4B). The area of microglial activation remained elevated in MPS IIIA mice throughout the ages studied, and in fact trended further upwards with age with a distinct separation into two sub-groups at 12-weeks of age, and the highest number and greatest difference compared with the controls occurring at 20-weeks of age ($p<0.0001$).

The next immunofluorescence assay determined expression levels of C3 and astrocyte activation, as determined by increased GFAP staining. Representative images of the staining throughout the ages studied are shown in Figure 5.5. Subsequent analysis revealed that C3 expression in the MPS IIIA mice trended upwards from three-weeks of age but was not statistically significant from wild-type mice at any time-point ($p>0.05$; Fig 5.6A). C3 expression in MPS IIIA mice separated into two sub-groups by 20-weeks of age, with males expressing higher complement levels than females. The highest datapoint in the 12-week MPS IIIA group was determined to be a statistical outlier, and was thus excluded from analysis but has been included here for illustration. GFAP expression, however, was significantly elevated in MPS IIIA mice compared with wild-type mice from three-weeks of age ($p<0.01$; Fig 5.6B). GFAP expression remained elevated at six-weeks ($p<0.05$) and increased further through to 12- and 20-weeks ($p<0.0001$).

With emerging evidence of multiple states of activation amongst astrocytes, the level of reactive astrocytes expressing C3 was quantified to determine the populations of A1 astrocytes in the MPS IIIA mouse motor cortex. Astrocytes devoid of C3 were designated as A2 astrocytes. A1 astrocytes were significantly more prevalent in MPS IIIA within areas of dendritic spine loss from three-weeks of age and this was maintained through to 20-

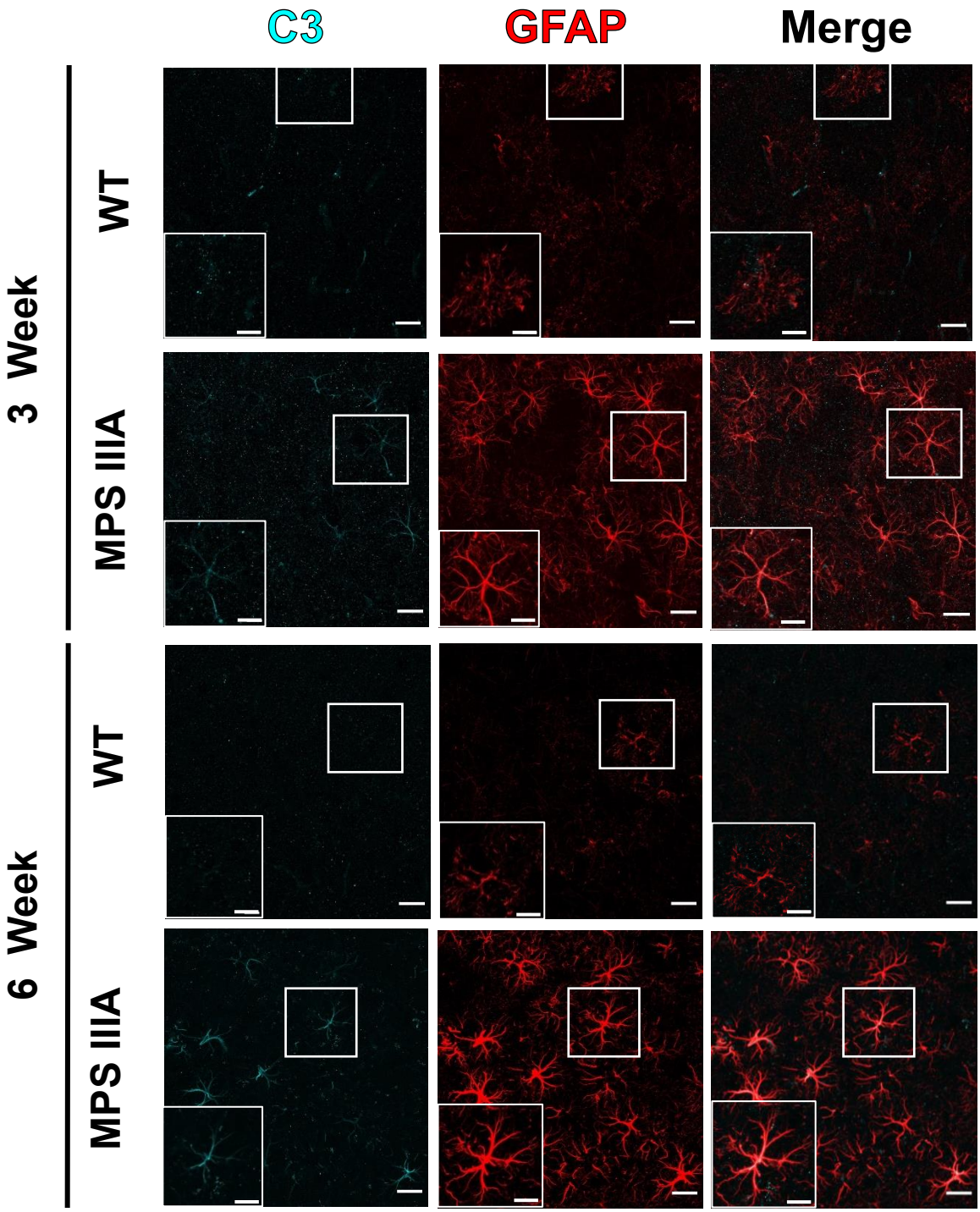


Figure 5.5 – Representative images of C3 and GFAP immunofluorescence assay.

Visualisation of astrocytes and complement component C3 in layer 5 of the cerebral motor cortex in wild-type (WT) and MPS IIIA mice at three-, six-, 12-, and 20-weeks of age. Scale bar is 25µm; magnified inset scale bar is 10µm.

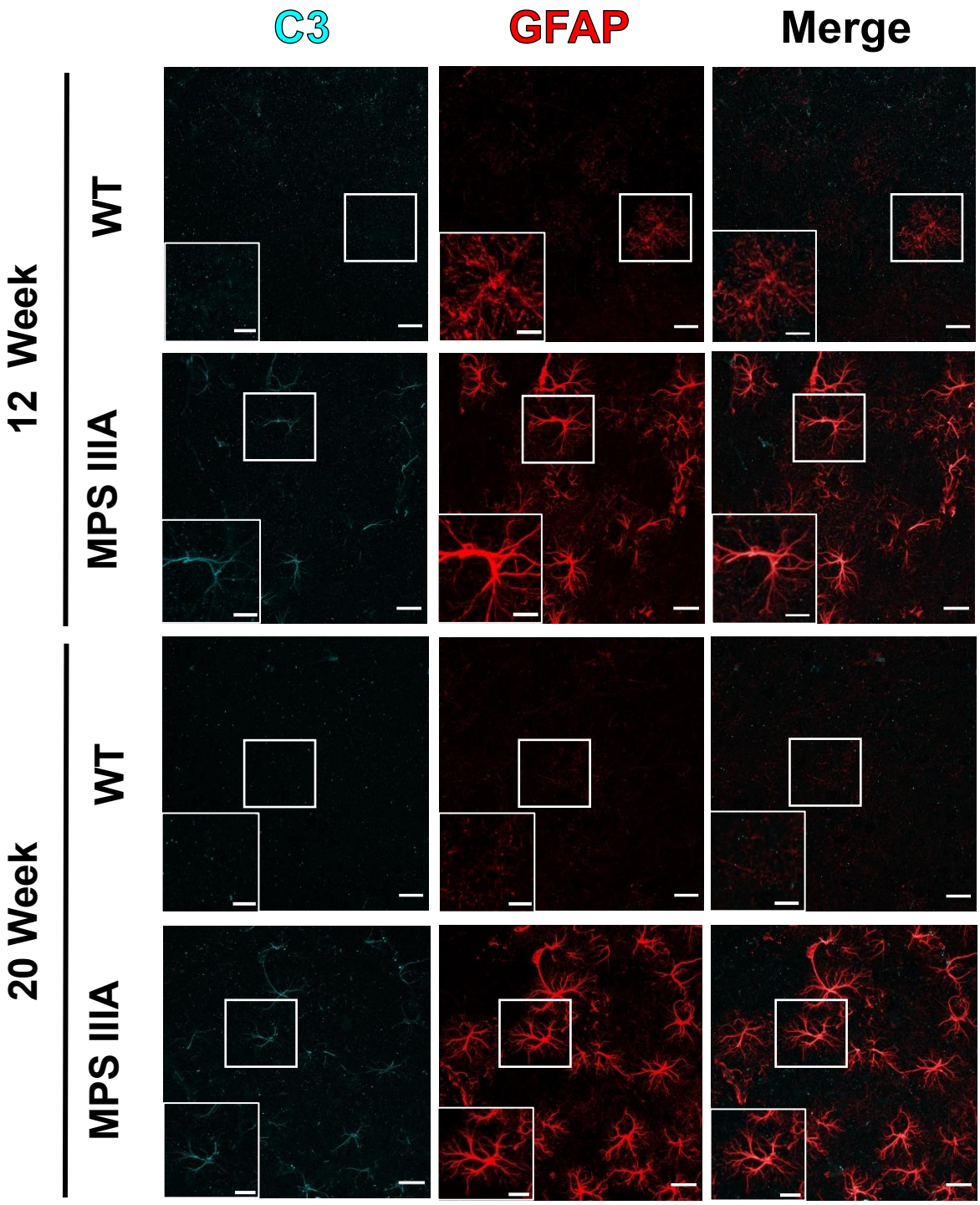


Figure 5.5 – Representative images of C3 and GFAP immunofluorescence assay (continued).

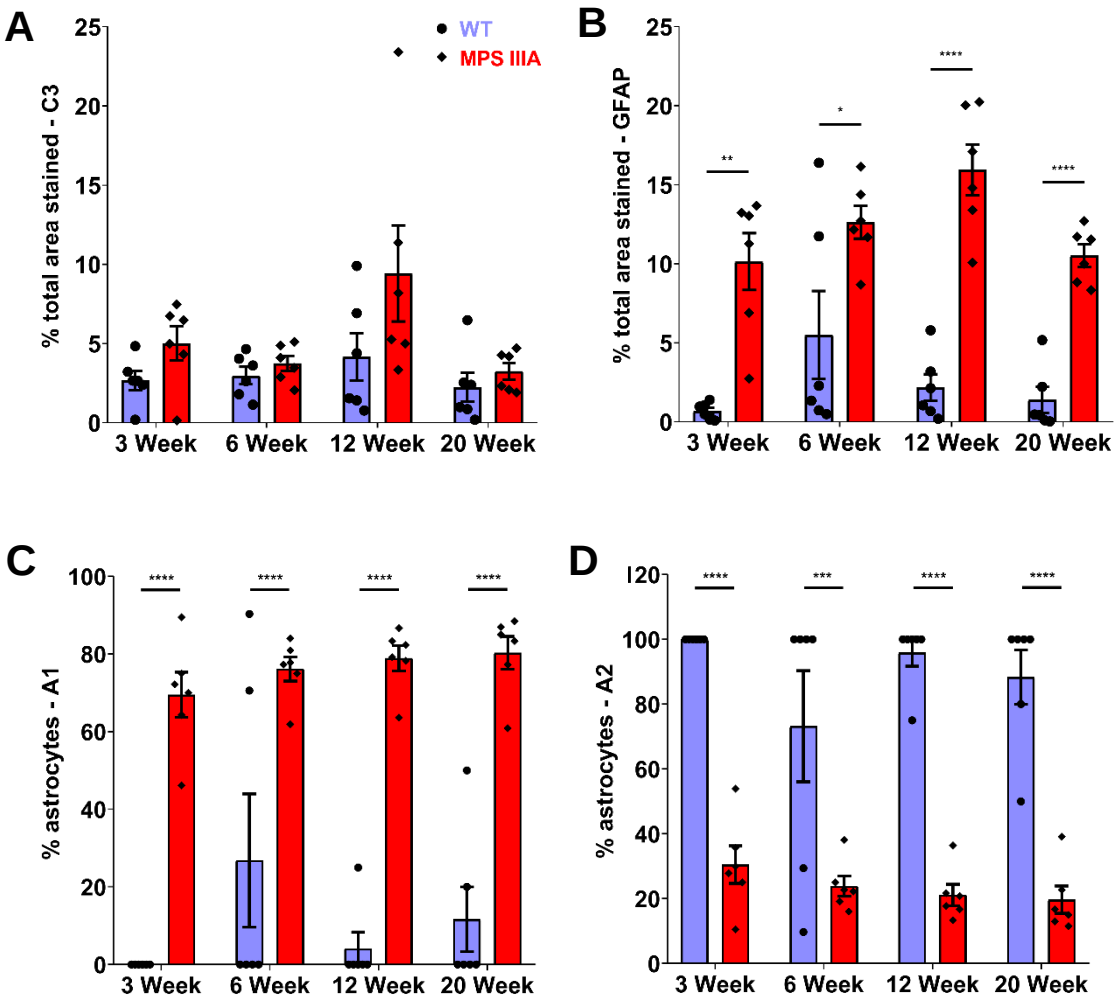


Figure 5.6 – Levels of C3, activated astrocytes, and astrocyte type in the mouse motor cortex. Complement component C3 (A) and GFAP (B) levels, and percentage of A1-type (C) and A2-type (D) astrocytes in the layer 5 motor cortex of wild-type (WT) and MPS IIIA mice at three-, six-, 12-, and 20-weeks of age. N=6 animals per genotype per age. *p<0.05; **p<0.01; ***p<0.001; ****p<0.0001; two-way ANOVA, with Bonferroni's multiple comparisons. Data are mean ± SEM; MPS IIIA outlier at 12-weeks (A). Experimenter blinded to genotype and age.

weeks ($p<0.0001$; Fig 5.6C). Conversely, the neuroprotective A2 astrocytes were significantly less prevalent in the MPS IIIA mouse brain from three-weeks of age ($p<0.0001$; Fig 5.6D), with a decreasing trend observed to 20-weeks of age. This suggests that not only is there increased expression of reactive astrocytes within the motor cortical region of the MPS IIIA mouse brain, but they are also of the newly identified proinflammatory/neurotoxic population.

5.2.2 Activated glia are apposed to sites of synaptic loss in the MPS IIIA motor cortex

To expand on the hypothesis that glial cells contribute to reduced dendritic spine densities in MPS IIIA, the localisation of these cells directly to the sites of synaptic loss was assessed. Utilising the slices from the immunofluorescence assays (5.2.1), Iba1-positive microglia and YFP-positive neurons were rendered into three-dimensional models using Imaris software. The same subset of layer 5 pyramidal neurons within the motor cortex that were analysed in Chapter 3 were also analysed here. Representative images of the Iba1-positive microglia and YFP-positive neurons examined across all timepoints are demonstrated in Figure 5.7.

Using the 'distance-between-surfaces' feature in the Imaris software, the distance between a microglial voxel and the closest YFP-positive neuronal voxel was measured. The volume of all microglial voxels was accumulated at incremental micrometre distances from the nearest neuron and averaged for each mouse (Fig 5.8). The raw outputs showed no difference between genotypes at three-weeks of age (Fig 5.8A). However, there was a higher frequency of microglia proximal ($\leq 2\mu m$) to YFP-positive neurons in MPS IIIA mouse motor cortex at six-weeks (Fig 5.8B), 12-weeks (Fig 5.8C), and 20-weeks of age (Fig 5.8D).

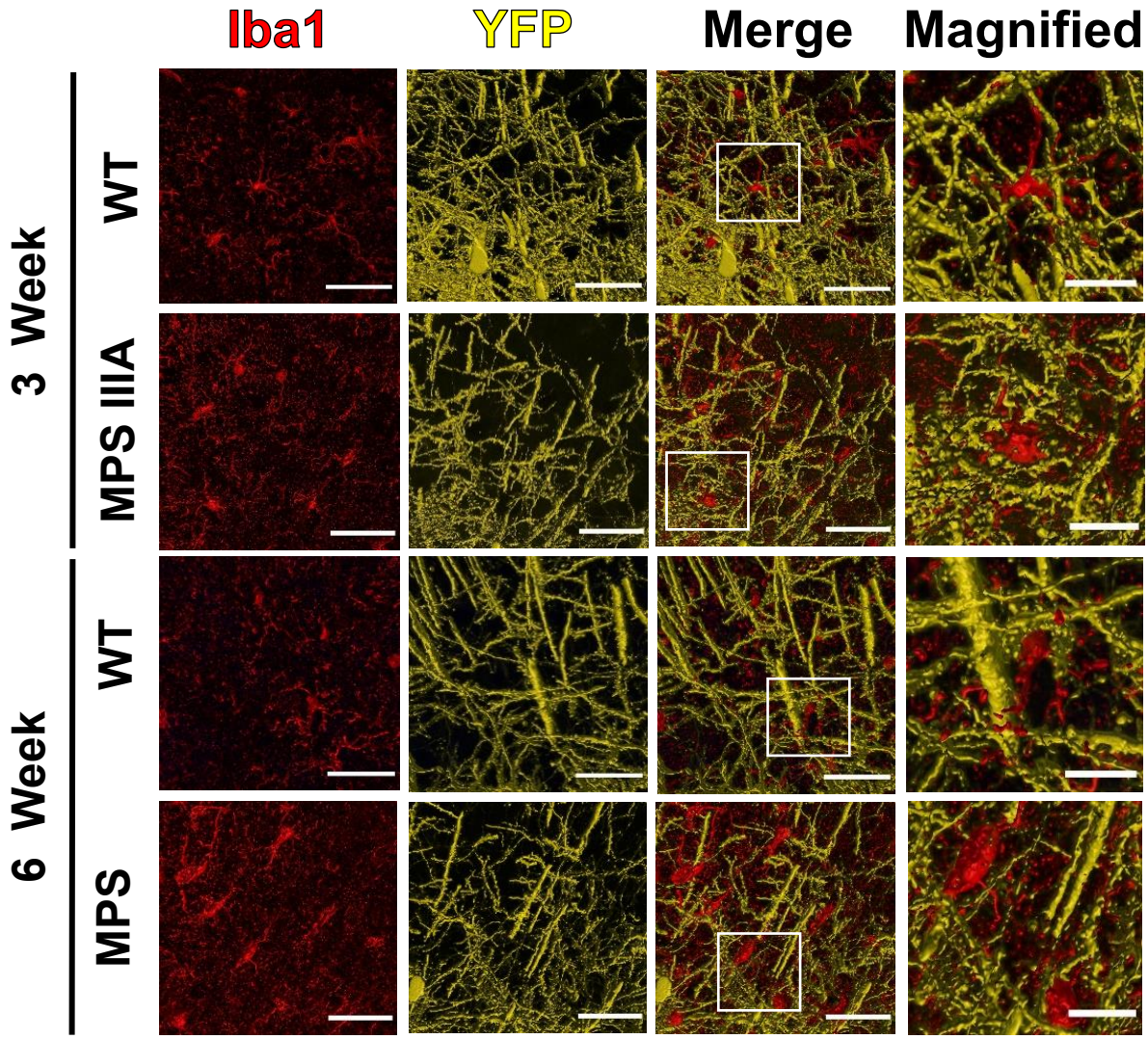


Figure 5.7 – Representative images of microglia apposed to YFP neurons.

Visualisation of microglia apposed to the sites of dendritic spine loss on YFP-positive pyramidal neurons in the cerebral motor cortex of wild-type (WT) and MPS IIIA mice at three-, six-, 12-, and 20-weeks of age. Scale bar is 50µm; magnified scale bar is 20µm.

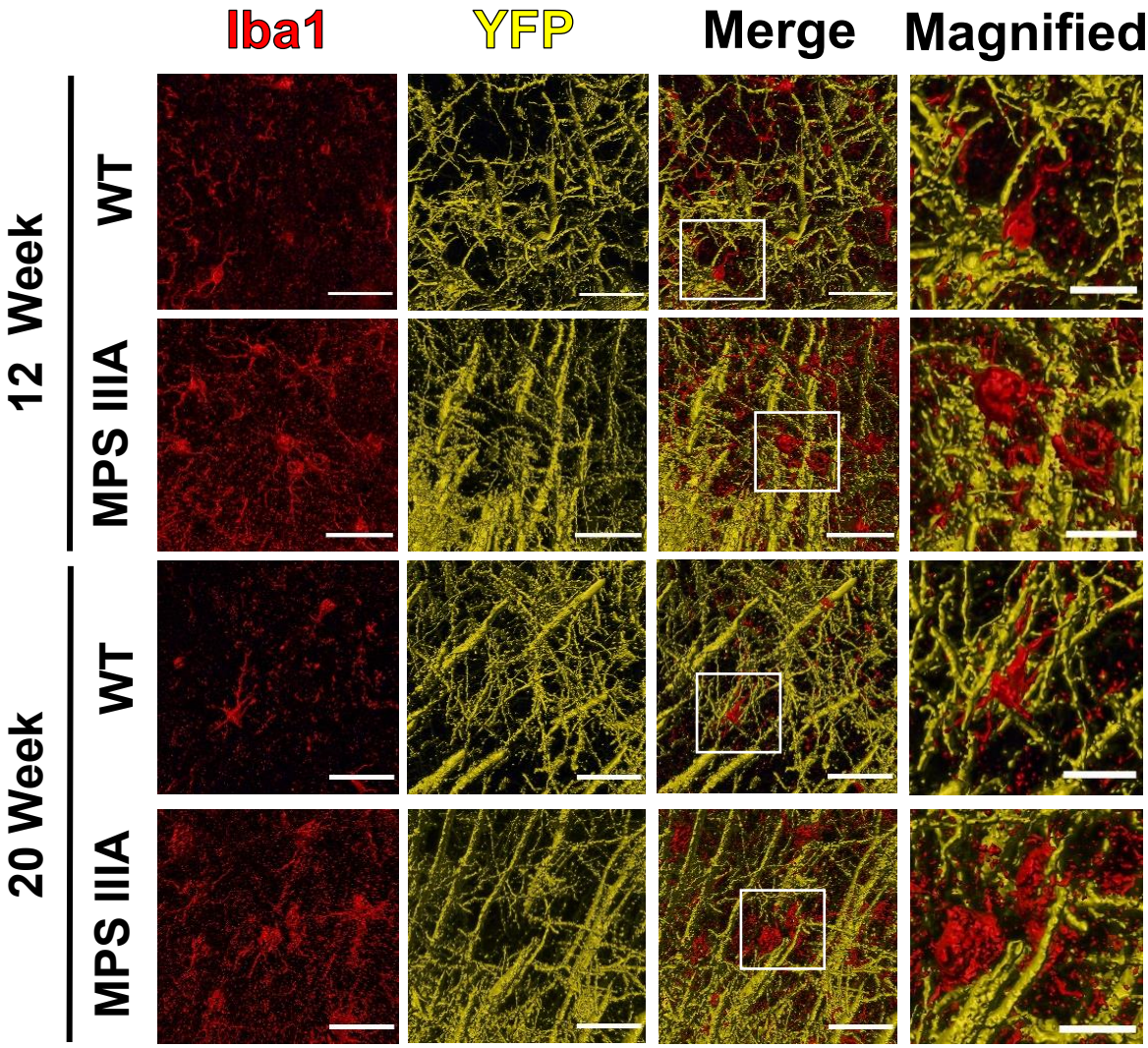


Figure 5.7 – Representative images of microglia apposed to YFP neurons (continued).

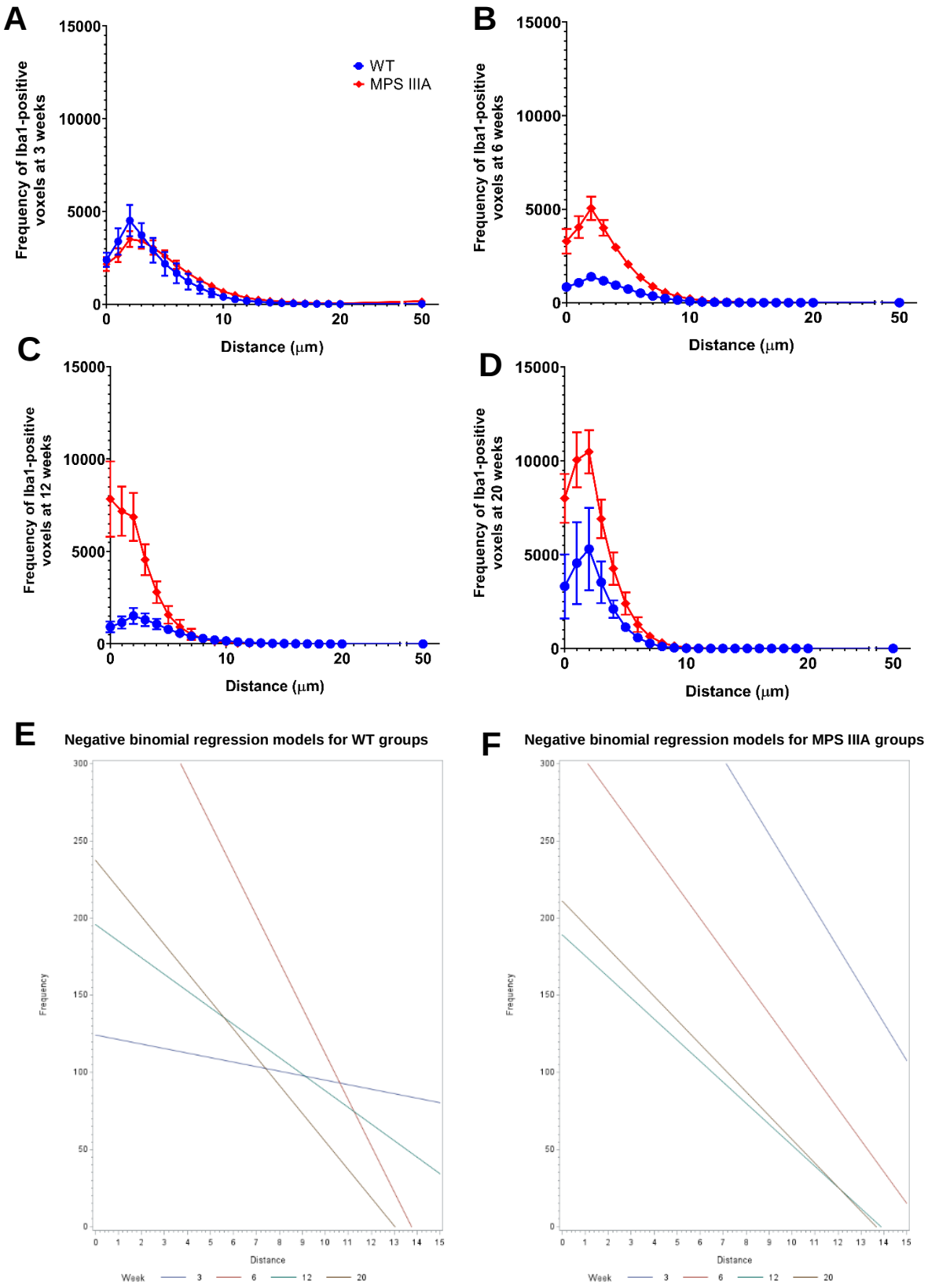

A
Frequency of Iba1-positive voxels at 3 weeks
WT
MPS IIIA
Distance (μm)
B
Frequency of Iba1-positive voxels at 6 weeks
Distance (μm)
C
Frequency of Iba1-positive voxels at 12 weeks
Distance (μm)
D
Frequency of Iba1-positive voxels at 20 weeks
Distance (μm)
E
Negative binomial regression models for WT groups
Frequency
Distance
Week 3 6 12 20
F
Negative binomial regression models for MPS IIIA groups
Frequency
Distance
Week 3 6 12 20

Figure 5.8 –Apposition of microglia to YFP neurons over time. The abundance and proximity of Iba1-positive voxels to sites of dendritic spine loss on YFP-positive pyramidal neurons in the cerebral motor cortex of wild-type (WT) and MPS IIIA mice at three- (A), six- (B), 12- (C), and 20-weeks (D) of age. For statistical analysis, the data were transformed to negative binomial regression models for WT (E) and MPS IIIA (F) groups. N=6 animals per genotype per age. Data are mean ± SEM. Experimenter blinded to genotype and age.

To conduct statistical analysis, the data were transformed into negative binomial regression models, showing all ages for either wild-type (Fig 5.8E) or MPS IIIA groups (Fig 5.8F). Statistical outputs are provided in Appendix 1. The association between frequency and distance for each genotype at a given age was assessed, and interaction p-values were generated.

At three-weeks of age, there was no difference in the decreasing rate of frequency of microglia apposition to neurons, with both wild-type and MPS IIIA groups showing an 11% decrease for every micrometre increment ($p>0.05$). At six-weeks, MPS IIIA microglial apposition decreased in frequency by 29% with every micrometre increment compared with wild-type (35% decrease in wild-type compared with a 6% decrease in MPS IIIA), which was statistically significant ($p<0.0001$), and due to a higher mean in MPS IIIA microglial frequency at any distance $\leq 2\mu m$ from the nearest neuron (Fig 5.8B). At 12-weeks, MPS IIIA astrocyte apposition decreased in frequency at a lower rate, by 6% with every incremental micrometre (43% decrease in wild-type compared with a 37% decrease in MPS IIIA), which was statistically significant ($p<0.05$). This could also be due to a higher mean number of reactive microglia juxtaposed to neurons in MPS IIIA over a greater distance range, as shown in Figure 5.8C. At 12-weeks, MPS IIIA microglial apposition decreased in frequency at a lower rate, by 6% with every incremental micrometre (43% decrease in wild-type compared with a 37% decrease in MPS IIIA), which was statistically significant ($p<0.05$). This could also be due to a higher mean number of microglia juxtaposed to neurons in MPS IIIA over a greater distance range, as shown in Figure 5.8C. However, at 20-weeks, the rates were reversed, with MPS IIIA presenting a greater decrease in microglial frequency by 36% with every micrometre increment (7% decrease in wild-type compared with a 43% decrease in MPS IIIA), which was statistically significant ($p<0.0001$). This was most likely due to the high mean number

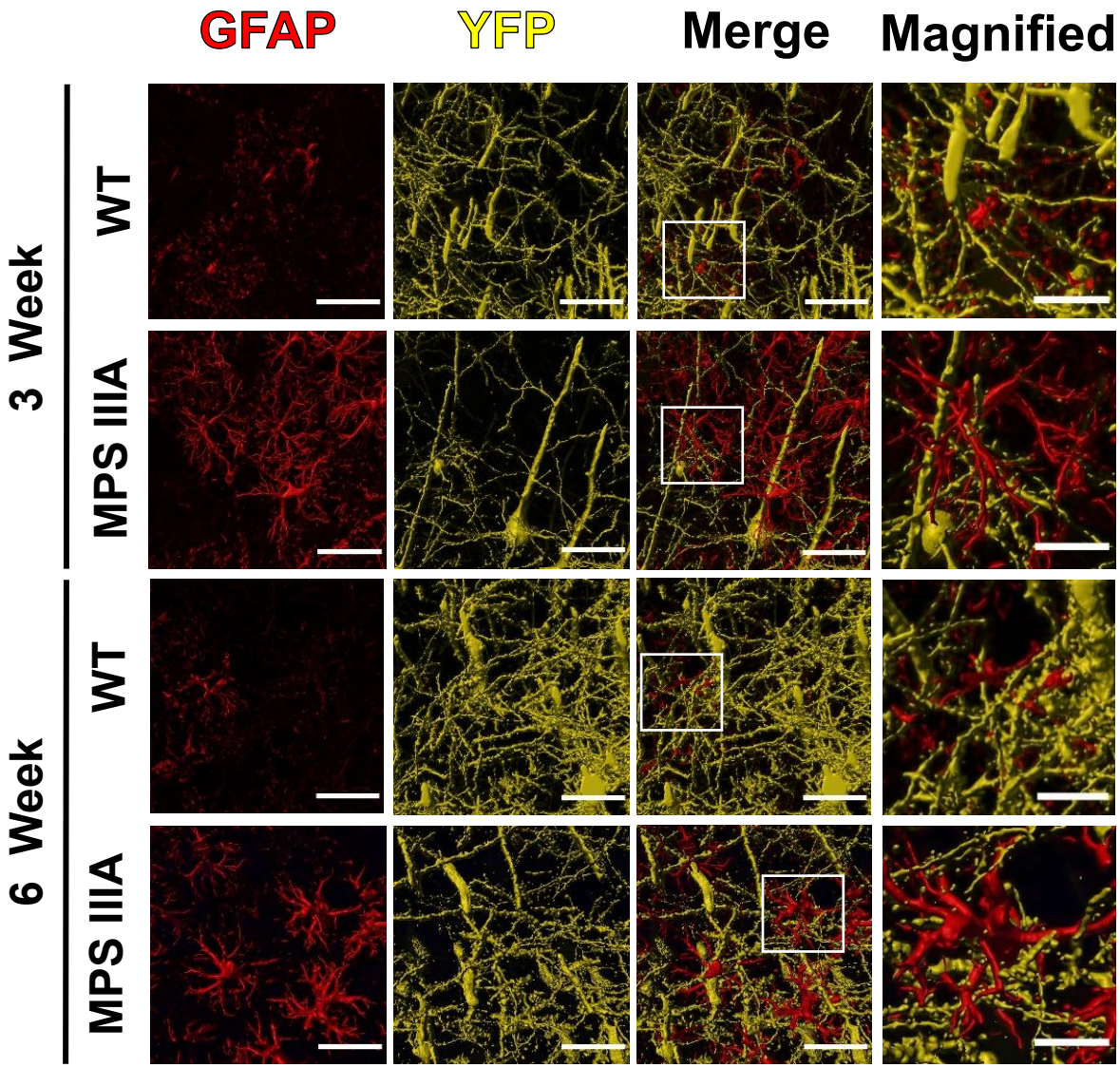


Figure 5.9 – Representative images of astrocytes apposed to YFP neurons.

Visualisation of astrocytes apposed to the sites of dendritic spine loss on YFP-positive pyramidal neurons in the cerebral motor cortex of wild-type (WT) and MPS IIIA mice at three-, six-, 12-, and 20-weeks of age. Scale bar is 50µm; magnified scale bar is 20µm.

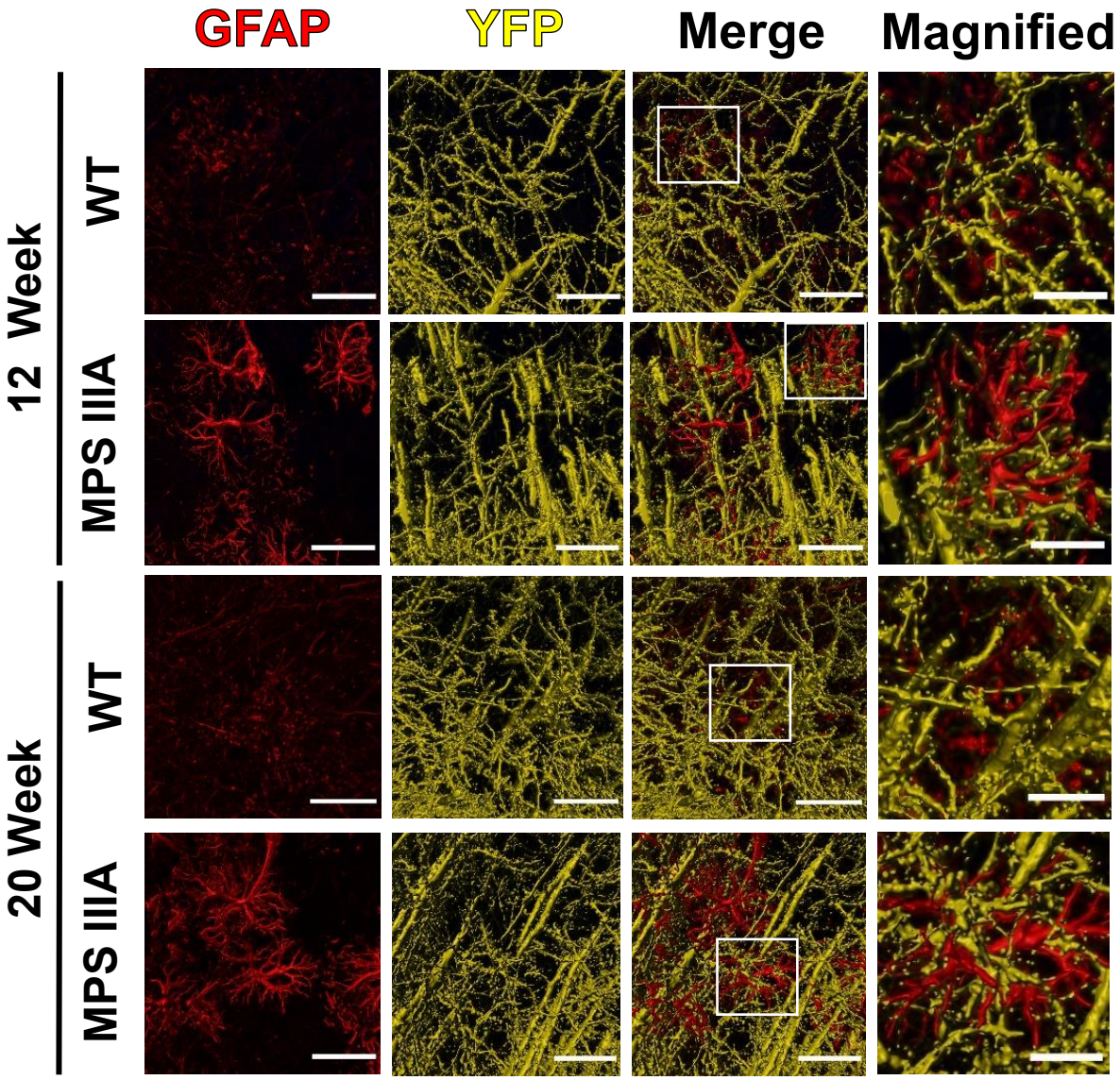


Figure 5.9 – Representative images of astrocytes apposed to YFP neurons (continued).

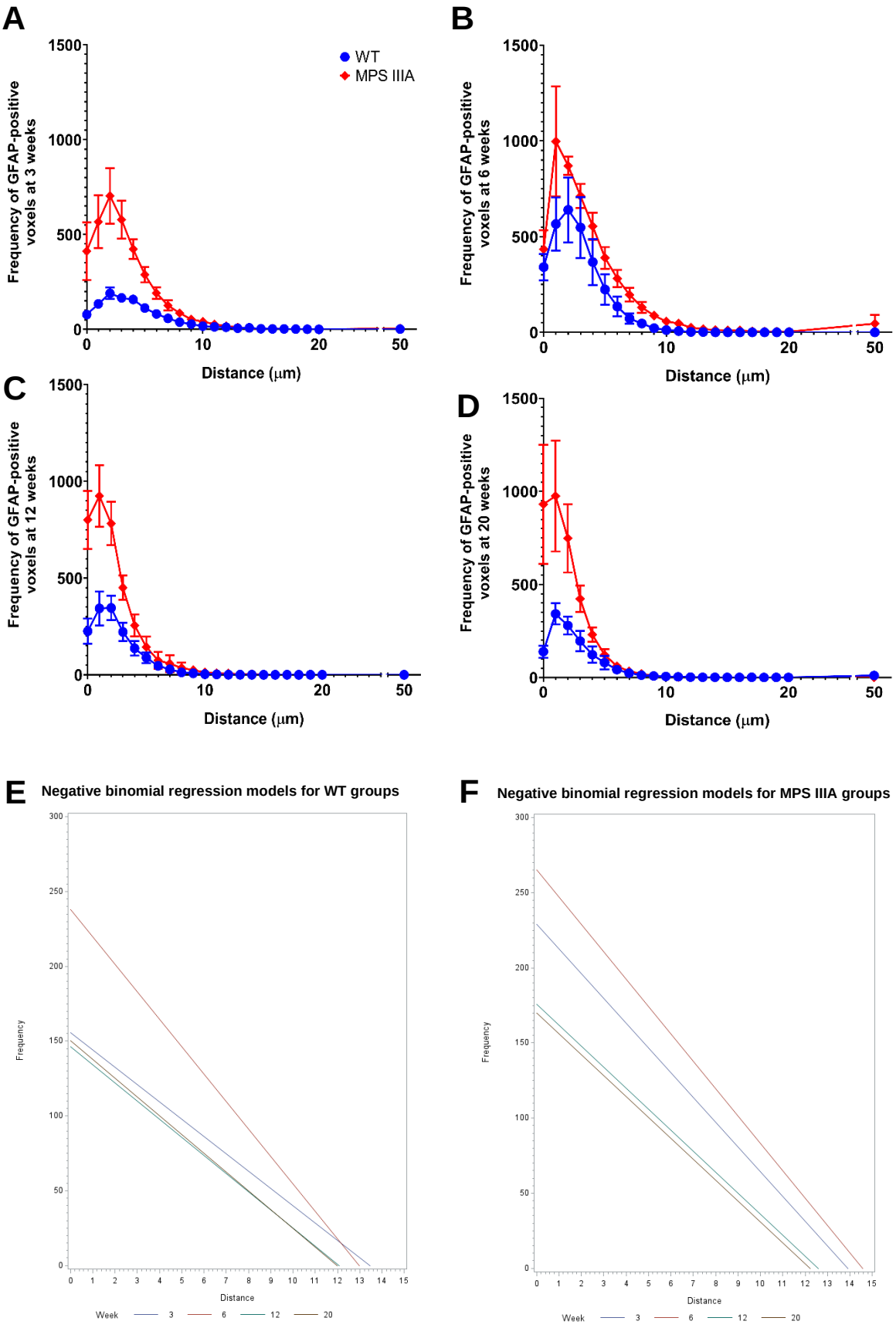

A
B
C
D
E
F
WT
MPS IIIA
Frequency of GFAP-positive voxels at 3 weeks
Frequency of GFAP-positive voxels at 6 weeks
Frequency of GFAP-positive voxels at 12 weeks
Frequency of GFAP-positive voxels at 20 weeks
Distance (μm)
Negative binomial regression models for WT groups
Negative binomial regression models for MPS IIIA groups
Frequency
Distance
Week 3 6 12 20

Figure 5.10 – Apposition of astrocytes to YFP neurons over time. The abundance and proximity of GFAP-positive voxels to sites of dendritic spine loss on YFP-positive pyramidal neurons in the cerebral motor cortex of wild-type (WT) and MPS IIIA mice at three- (A), six- (B), 12- (C), and 20-weeks (D) of age. For statistical analysis, the data were transformed to negative binomial regression models for WT (E) and MPS IIIA (F) groups. N=6 animals per genotype per age. Data are mean ± SEM. Experimenter blinded to genotype and age.

of microglia present in MPS IIIA at the distance of 0-2µm, which resulted in the sharply declining slope (Fig 5.8D). Overall, there was a combined and statistically significant association between frequency and genotype, with MPS IIIA microglia apposed to neurons in the motor cortex 57% more frequently than wild-type microglia ($p<0.0001$).

The same method of rendering was applied to the GFAP-positive astrocytes to determine their level of recruitment to YFP neurons suffering synaptic loss in the mouse motor cortex. Representative images of the astrocytic and neuronal models generated across all time-points and genotypes are demonstrated in Figure 5.9. Using the 'distance-between-surfaces' feature of the Imaris software, the proximity between an astrocytic voxel and the closest neuronal voxel was measured. The frequency of all reactive astrocytic voxels was accumulated and recorded for each mouse, with the mean of all mice for each micrometre increment shown (Fig 5.10). The raw outputs show differences between genotypes across all ages, with higher mean frequencies in MPS IIIA at distances less than or equal to 2µm starting from three-weeks (Fig 5.10A) through to six-weeks (Fig 5.10B), 12-weeks (Fig 5.10C), and 20-weeks (Fig 5.10D).

The astrocyte data were transformed into negative binomial regression models, showing all ages for either wild-type (Fig 5.10E) or MPS IIIA (Fig 5.10F). Statistical outputs are provided in Appendix 2. The association between frequency and distance for each genotype at a given age was assessed, and interaction p-values were generated. At three-weeks of age, there was a decreased frequency of 5% in MPS IIIA mice with every unit increase in distance compared with the wild-type group (12% decrease in wild-type compared with a 7% decrease in MPS IIIA), which was statistically significant ($p<0.0001$). This is shown by the sharper slope occurring due to a higher mean in MPS IIIA astrocyte frequency at 2µm (Fig 5.10A). At six-weeks, MPS IIIA astrocyte apposition decreased in

frequency by 4% with every micrometre increment compared with wild-type (39% decrease in wild-type compared with a 35% decrease in MPS IIIA), which was statistically significant ($p<0.05$). This difference could be due to the greater variance observed in the wild-type group with high numbers of reactive astrocytes observed in some mice (Fig 5.6B), as well as a higher mean number of reactive astrocytes observed in MPS IIIA mice across a greater distance range up to and including 10µm from any neuron (Fig 5.10B). At 12-weeks, the greatest difference in decreasing frequency occurred between groups, with MPS IIIA astrocytes decreasing in frequency by 31% with every micrometre increment compared with the wild-type, which was statistically significant ($p<0.0001$). This was observed by the highest occurrence of astrocytes within 0-1µm from the nearest neuron (Fig 5.10C). At 20-weeks, however, there was only a difference of 1% in decreasing frequency over distance (MPS IIIA 1% lower), which was not significant ($p>0.05$). This could be due to the higher variance and presence of astrocytes adjacent to neurons in the older MPS IIIA mice (Fig 5.10D); 20-weeks of age was also the time-point at which the highest number of astrocytes were recruited to YFP-positive neurons for any of the ages studied. There was a decreasing frequency of 54% for every micrometre increment away from a wild-type neuron, and a decreasing frequency of 53% from an MPS IIIA neuron. Overall, there was a combined and statistically significant association between frequency and genotype, with MPS IIIA reactive astrocytes apposed to neurons in the motor cortex 56% more frequently than wild-type astrocytes ($p<0.0001$).

5.3 Discussion

The mechanism(s) causing neuronal functional changes associated with neurodegenerative and subsequent behavioural symptom onset in MPS IIIA is currently unknown. In Chapter 3, a loss of dendritic spines in MPS IIIA mice from a pre-symptomatic age was observed. As neuroinflammatory changes characterise MPS III and other LSDs, and complement-dependent pruning occurs throughout development and is repeatedly overactive in some disease states, it was therefore important to determine whether over-enthusiastic pruning of dendritic spines was occurring by activated glia in the MPS IIIA mouse cerebral cortex. Expression of complement C1q and C3 proteins was increased, and activation of pro-inflammatory astrocytic and microglial cells temporally correlated with synaptic loss. To our knowledge, this is the first test of the hypothesis that activated astrocytes and microglia are responsible for deficits in neuronal structure, and potentially function, in MPS III.

Whilst it is well documented that microglial and astrocyte activation is an early phenomenon in the MPS III mouse brain, to date their toxic phenotype has not been investigated. The data presented in this Chapter identified the presence of neurotoxic A1 astrocytes in the young MPS IIIA mouse brain, and provided evidence of the increased proximity of both activated microglia and astrocytes to diseased pyramidal neurons in the MPS IIIA mouse motor cortex, the first time such observations have been made in a model of MPS III.

Visualisation of microglia traditionally occurs via Iba1 expression. Whilst Iba1 expression is reported to increase with microglial activation and be involved with phagocytosis, it is generally regarded as a marker of all types of microglia rather than a specific activated sub-type (Hopperton et al., 2018). Indeed, elevated expression of inflammatory mediators,

including IL1β and chitinase-like 3, are more indicative of the polarised microglial phenotypes (Block et al., 2007; Boche et al., 2013). GFAP, however, is the traditional marker for visualising astrocytes and expresses increases in activated astrocytes. Since its first use in human Alzheimer tissue (Bignami et al., 1972), changes in GFAP expression have been the standard marker for assessing astrocyte reactivity in both animal models and human neurological disease tissues. More recent evidence, however, highlights that different types of injury and disease induce different states of reactive astrocytes: inflammatory insult induces A1-type; and ischaemic injury induces A2-type reactive astrocytes, which have either a toxic or protective effect, respectively, towards neurons (Zamanian et al., 2012; Liddelow and Barres, 2017).

The findings in this study highlighted the significantly increased expression of C1q in the MPS IIIA motor cortex from six-weeks of age. At subsequent ages, whilst trending upwards, the elevated expression of C1q in MPS IIIA was not significant, and in fact separated into two distinct sub-groups by 20-weeks of age. Interestingly, the 20-week-old MPS IIIA mice with higher C1q expression were male, and the 20-week MPS IIIA mice expressing lower C1q levels were female. Comparably, within the MPS IIIA 12-week group for Iba1, only female mice were in the lower sub-group, while male mice comprised the other sub-group and expressed higher Iba1 (microglial) levels. Furthermore, whilst not statistically significant, C3 expression trended upwards in MPS IIIA mice, and separated into two sub-groups by 20-weeks of age, again with males expressing higher complement levels than females. Whilst the influence of gonadal hormones on the complete complement cascade in the brain remains unclear, oestrogen has been reported to reduce conversion of the M1-like microglia, promote non-reactive astrocytes and subsequent synaptogenesis (McCarthy et al., 2017; Larson, 2018; Bollinger et al., 2019). In fact, oestrogen has been shown to prevent M1-like microglial activation in lipopolysaccharide-

induced inflammation by preventing C3 receptor expression on the microglia (Vegeto et al., 2001). Furthermore, oestrogen has also been shown to stimulate expression of glutamate transporters and post-synaptic NMDA receptors at excitatory synapses, improving excitatory function (Jelks et al., 2007). Further to the discussions in Chapter 4, gonadal hormones may therefore be mediating synaptic function and loss by affecting the reactive state and function of glial cells in the mouse brain. Regardless of the compounding effect of sex, as Iba1 is a marker for total microglia and did not differentiate between polarised states, future experiments should therefore consider identifying the state of microglia (for example, through mediators of isolectin B4, TNF for M1 (Block et al., 2007), and arginase 1 for M2 (Boche et al., 2013)) to elucidate the role of microglia at the synapse more accurately.

Moreover, A1-type astrocytes were significantly more prevalent from three-weeks of age in MPS IIIA mice. This suggests the early and elevated astrocytic activation previously reported in MPS IIIA mice could be of the A1-type phenotype, and could be contributing to disease progression, at least within the motor cortex. Similar with the observations of Liddelow and colleagues (2017), our observation that A1 astrocytes constitute the majority of astrocytes in this MPS IIIA brain region affected by neurodegeneration suggests gliosis may be important to disease onset and progression.

However, the strong difference in A1-type astrocyte expression between genotypes did not correlate with significant differences in the C3-positive stained area at any age. In fact, further evaluation showed the area was predominantly occupied by GFAP-positive astrocytes in MPS IIIA mice, with C3 mostly localised to astrocytes in addition to diffuse staining externally. Conversely, wild-type mice were devoid of A1 astrocytes, and C3 expression was widespread throughout the motor cortex. Therefore, C3 expression alone

may not be a reliable indicator of synaptic pruning activity but should be used in conjunction with other markers. Indeed, engulfment of processes by microglia was shown to be highly dependent on the C3 receptor expressed on activated microglia (Linnartz et al., 2012). Additionally, a C3 knock-out mouse model only partially reduced engulfment of synaptic processes, which suggested alternative phagocytic pathways could be influencing synaptic pruning (Schafer et al., 2012). These pathways could reportedly involve "find-me", "eat-me", and "don't-eat-me" signalling pathways (Schafer et al., 2013; Gabande-Rodriguez et al., 2020). "Find-me" signals include chemoattractant CX3CL1 (fractalkine), with receptors also expressed on microglia (Truman et al., 2008; Arnoux and Audinat, 2015). The "eat-me" phase involves tethering and engulfment of material by microglia and, in addition to C3, includes identification by phosphatidylserine (Martin et al., 1995; Marino and Kroemer, 2013). The predominant "don't-eat-me" signal is CD47, which has incidentally been shown to prevent excessive synaptic pruning during neurodevelopment (Lehrman et al., 2018; Gabande-Rodriguez et al., 2019). Therefore, whilst over-enthusiastic synaptic pruning may be implicated in MPS IIIA, pathways in addition to the complement cascade, and comparisons of visualised phagocytosis by microglia may definitively show the mechanistic role of glia in MPS IIIA disease progression through synaptic removal.

Elevated glial expression has been reported across multiple brain regions in mouse models of MPS I, MPS II, and MPS III (Ohmi et al., 2003; Savas et al., 2004; Villani et al., 2007; Hemsley et al., 2008; Arfi et al., 2011; Wilkinson et al., 2012; Martins et al., 2015; Roca et al., 2017; Gleitz et al., 2018; Tordo et al., 2018). However, this study showed confocal imaging of tissues and three-dimensional models of glial cells and affected neurons, for the first time, a significantly higher level of glial activity and apposition to sites of synaptic loss in MPS IIIA mice. This was also recently reported in Niemann Pick disease disease

type C, where microglia were in close contact to the dendrites of Purkinje neurons (the degeneration of which is responsible for symptom onset) prior to cellular loss (Kavetsky et al., 2019). Therefore, these data suggest over-active glial cells potentially have a negative impact on MPS IIIA neurons due to their greater apposition from a pre-symptomatic age.

Recently, a gene therapy approach was trialled to inhibit the actions of C3 at the synapse in an Alzheimer's mouse model in which C3 was ablated, resulting in preserved synaptic structures and improved cognitive performance (Shi et al., 2017). These findings were recently verified in a mouse model of multiple sclerosis, in which C3 inhibition prior to symptom onset showed decreased microglial engulfment of synapses which protected neuronal function (Werneburg et al., 2020). Additionally, another phagocytic triggering receptor expressed on myeloid cells 2 has been shown to promote the engulfment of synaptic proteins, and to alter lysosomal proteins and trigger abnormal cell morphologies (Filipello et al., 2018). Moreover, increased engulfment of synaptic material by astrocytes has been observed in the visual cortex, resulting in weaker functional synapses (Chung et al., 2013). Coupled with the literature and discussion above, the findings reported here suggest a potentially elevated and sustained mechanism of synaptic pruning of neurons in the motor cortex of MPS IIIA mice that commences prior to symptom onset and thus could be contributing to symptom development. Therefore, regulation of pro-inflammatory markers should be carefully considered in association with therapeutic interventions. However, further evaluation with additional markers, recordings of phagocytosis, and investigation into complement-independent pathways are required to confirm the mechanistic role of glia and synaptic pruning in MPS IIIA.

5.4 Conclusion

In summary, this study has identified a closer apposition of glial cells to the sites of synaptic loss within the MPS IIIA mouse motor cortex from a pre-symptomatic age, coinciding with synaptic loss and electrophysiological deficiency. Additionally, we have shown that the recently identified A1-type reactive astrocyte is highly prevalent in the MPS IIIA mouse cerebral motor cortex. Together, this suggests an over-active synaptic pruning mechanism could potentially be contributing to the observed synaptic loss in MPS IIIA through pro-inflammatory marker expression and glial activation.

– CHAPTER 6 –

ASSESSING THE EFFECTS OF AAV9-*SGSH* GENE THERAPY ON THE MPS IIIA MOUSE MOTOR CORTEX

6.1 Introduction

Due to the monogenic nature of LSDs, viral and non-viral gene-based therapies have emerged as an attractive therapeutic strategy, especially serotypes shown to cross the blood-brain barrier and transduce cells in the brain (Aronovich et al., 2017; Platt et al., 2018).

AAVs have been identified as an advantageous and promising gene delivery method since they do not present pathogenicity in humans, and they provide a less transient and more permanent therapeutic strategy than other vectors (Sands & Davidson, 2006; Leal et al., 2020). There are over 100 natural AAV variants, and 11 identified AAV serotypes, which are non-enveloped, single-stranded DNA parvoviruses (within the *Dependoparvovirus* genus) with a diameter of ~25nm (Zincarelli et al, 2008; Zhang et al, 2019). The viral genome is approximately 4.8 kilobases and contains three genes: *Rep* (Replication), *Cap* (Capsid), and *aap* (Assembly). Within the sequence of recombinant (designed) vectors is generally a mammalian promoter, the gene of interest, and a terminator (Naso et al, 2017). AAVs generally enter target cells through interactions with cell-surface N-linked glycan residues, including sialylated and desialylated β-galactosyl residues (Asokan et al, 2012; Zhu et al., 2018), and secondary receptors provide downstream roles in viral transduction leading to cell and tissue selectivity. The variations across serotypes in receptor

interactions permit targeting of specific cells or tissues over others, and therefore exhibit different profiles that are most beneficial to a wide range of diseases. Table 6.1 provides a list of the different tissues known to be directly affected by the AAV variants via known receptors.

A study of AAV transgene expression and biodistribution following tail vein injection in mice showed that AAV9 resulted in the highest level of genome infectivity and protein translation, expressed a kinetically rapid onset, and presented the best viral genome distribution (Zincarelli et al, 2008). The AAV9 serotype can also cross the blood-brain barrier and transduce CNS cells following intravenous infusion, including neurons and astrocytes (Bevan et al, 2011; Green et al, 2016). Its ability to transduce CNS cells was particularly evident in a study on non-human primate brains where the genome copy levels of AAV9 were three-fold higher post-injection when compared with the genome copy levels at delivery (Green et al, 2016). In the same study, an effective transport mechanism was observed where the vector was shown to be transported along axons in both a retrograde and anterograde manner. This was crucial to the success of AAV9, as it can be transported over long distances through neuronal projections, and thus reach and transduce extensive and distal regions of the brain (Green et al., 2016). This bi-directional trafficking of AAV9 coupled with the preferential galactose binding and subsequent transduction of multiple CNS cells could therefore have strong implications for CNS diseases.

The monogenic nature and CNS pathology of LSDs has led to significant development of AAV genetic therapies, in turn leading to clinical trials (reviewed in Nagree et al., 2019). These investigations into the amelioration of CNS pathology combined with the multiple tropisms and safety of AAVs has opened the door to the possibility of treatment for idiopathic and age-related neurodegenerative diseases (Deverman et al., 2018; Hudry

Table 6.1 – Known AAV serotype targets. The AAV variants with known tissue tropisms and known receptor interactions. (Adapted from Asokan et al., (2012); Naso et al., (2017); Zhang et al., 2019).

AAV Serotype	Affecting Tissue Type	Binding Receptor
1	Neuronal, Skeletal, Heart, Retinal pigment epithelium	Sialic acid
2	Neuronal, Kidney, Photoreceptor cells, Retinal pigment epithelium	Heparan sulphate, Fibroblast growth factor receptor, Hepatocyte growth factor receptor, Laminin receptor
3	Liver	Heparan sulphate, Fibroblast growth factor receptor, Hepatocyte growth factor receptor, Laminin receptor
4	Neuronal, Lung, Retinal pigment epithelium	Sialic acid
5	Neuronal, Retinal pigment epithelium, Lung, Photoreceptor cells	Sialic acid, Platelet-derived growth factor receptor
6	Skeletal, Lung	Sialic acid, Heparan sulphate, Epidermal growth factor receptor
7	Skeletal, Liver	Sialic acid
8	Neuronal, Liver, Skeletal, Heart, Pancreas, Photoreceptor cells, Retinal pigment epithelium	Laminin receptor
9	Neuronal, Liver, Skeletal, Heart, Lung	Galactose, Laminin receptor
10	Neuronal, Liver, Heart, Muscle, Lung, Kidney,	Laminin receptor

and Vandenberghe, 2019). Despite the complex nature of CNS diseases and the difficulty in identifying a clear genetic marker, the increased prevalence of diseases such as Alzheimer's disease, permits the design of larger cohorts to trial possible disease modifiers, which is not often feasible for the LSDs (Hudry and Vandenberghe, 2019). A list of recent clinical trials testing AAV-based gene therapies in LSDs and more complex neurological disorders is provided in Table 6.2. Findings from pre-clinical genetic therapy studies, particularly in the mucopolysaccharidoses can have secondary effects by benefiting the more complex idiopathic and age-related neurodegenerative diseases which are more common within the community.

However, whilst the impact of AAV gene therapy on overall lysosomal function and general glial activation in select brain regions has been investigated, assessments on neuronal architecture or the impact on emerging inflammatory mechanisms have not, both of which could be contributing to symptom development. Moreover, these studies did not assess the motor cortical region, which is in part responsible for the motor behavioural phenotypes. Thus, the overall aim of this Chapter was to determine whether pre-symptomatic treatment with AAV9-*SGSH* could prevent dendritic spine deficits in the MPS IIIA mouse motor cortex. We used a modified gene therapy based on the AAV9-*SGSH* vector which is currently being evaluated in a Phase I/II clinical trial (NCT02716246) to improve the clinical relevance of findings. These experiments aimed to assess the impact of pre-symptomatic administration of AAV9-*SGSH* at preventing inflammatory-mediated synaptic pruning of dendritic spines on pyramidal neurons in the MPS IIIA mouse motor cortex, and thus determine whether these disease lesions can be delayed or are preventable.

Table 6.2 – Recent clinical trials for LSDs and CNS diseases using AAV. The ongoing or recently terminated (2018-2020) clinical programs testing AAV-based gene therapy in LSDs and other neurological disorders (adapted from ClinicalTrials.gov; ClinicalTrialsRegister.eu; Deverman et al., 2018; Hudry and Vandenberghe, 2019; Nagree et al., 2019). Abbreviations: AADC, aromatic L-amino-acid decarboxylase; APOE2, apolipoprotein 2; ARSA, arylsulphatase A; ARSB, arylsulphatase B; CLN2, protein tripeptidyl peptidase-I; GAA, α-glucosidase; GAN, giant axonal neuropathy; GDNF, glial-cell-derived neurotrophic factor; IDS, iduronate-2-sulphatase; IDUA, alpha-L-iduronidase; LINCL, late infantile neuronal ceroid lipofuscinosis; MLD, metachromatic leukodystrophy; MPS, mucopolysaccharidosis; NAGLU, alpha-N-acetylglucosaminidase; NGF, nerve growth factor; NINDS, National Institute of Neurological Disorders and Stroke; NTN, neurturin; SGSH, N-sulphoglucosamine sulphohydrolase; SMA1, spinal muscular atrophy type 1; SMN1, survival motor neuron 1.

Disease	Serotype	Transgene	Delivery	PI or Sponsor	ID
MPS I	AAV6	hIDUA	Intravenous	Sangamo	NCT02702115
	AAV9	hIDUA	Intracisternal	Regenxbio	NCT03580083
MPS II	AAV6	hIDS	Intravenous	Sangamo	NCT03041324
	AAV9	hIDS	Intracisternal	Regenxbio	NCT03566043
MPS IIIA	AAV9	hSGSH	Intravenous	Abeona	NCT02716246
	AAVrh.10	hSGSH	Intracerebral	Lysogene	NCT03612869
	AAV9	hSGSH	Intracerebro-ventricular	Esteve	2015–000359-26
MPS IIIB	AAV5	hNAGLU	Intracerebral	UniQure	NCT03300453
	AAV9	hNAGLU	Intravenous	Abeona	NCT03315182
MPS VI	AAV2/8	hARSB	Intravenous	Brunetti-Pieri	NCT03173521
Pompe	AAV2/8	hGAA	Intravenous	Asklepios	NCT03533673
	AAV9	hGAA	Intramuscular	Lacerta	NCT02240407
LINCL (Batten disease)	AAV2	hCLN2	Intra-parenchymal	Crystal	NCT00151216
	AAVrh.10	hCLN2	Intra-parenchymal	Crystal	NCT01161576 NCT01414985
	AAV9	hCLN3	Intrathecal	Amicus	NCT03770572
	AAV9	hCLN6	Intrathecal	Mendell	NCT02725580
MLD	AAVrh.10	hARSA	Intra-parenchymal	Aubourg	NCT01801709
GAN	AAV9	hGAN	Intrathecal	NINDS	NCT02362438
Canavan disease	AAV2	hASPA	Intra-parenchymal	NINDS	N/A
AADC deficiency	AAV2	hAADC	Intra-parenchymal	Hwu	NCT01395641
	AAV2	hAADC	Intra-parenchymal	Chien	NCT02926066
	AAV2	hAADC	Intra-parenchymal	Bankiewicz	NCT02852213
Parkinson's disease	AAV2	hNTN	Intra-parenchymal	Sangamo	NCT00985517
	AAV2	hGDNF	Intra-parenchymal	NINDS	NCT01621581
	AAV2	hAADC	Intra-parenchymal	Voyager	NCT01973543
	AAV2	hAADC	Intra-parenchymal	Voyager	NCT03562494
	AAV2	hAADC	Intra-parenchymal	Voyager	NCT03065192
	AAV2	hAADC	Intra-parenchymal	Muramatsu	NCT02418598
Alzheimer's disease	AAV2	hNGF	Intra-parenchymal	Ceregene	NCT00087789
	AAVrh.10	hAPOE2	Intra-cisternal	Crystal	NCT03634007
SMA1	AAV9	hSMN	Intrathecal	AveXis	NCT03381729
	AAV9	hSMN	Intravenous	AveXis	NCT03505099
SMA1	AAV9	hSMN	Intravenous	AveXis	NCT03306277
	AAV9	hSMN	Intravenous	AveXis	NCT03461289

6.2 Results

To address the final aim of the study a gene therapy approach was administered to YFP$^{+/-}$-MPS IIIA mice (described in the previous Chapters) to determine the therapeutic effect on discrete brain changes. As described in Methods (2.2.8), 30 wild-type mice and 60 MPS IIIA mice (comprising equal female and male mice) received an intraventricular injection (1µL/ventricle) of either sterile saline or AAV9-*SGSH* (2.5x10^{10} gc/µL), respectively, at birth (Day 0). This generated the necessary n=15 male mice per treatment group, which, based on the preliminary power calculations, was enough to achieve a statistically relevant outcome in the behavioural tests. The mice were then aged up to 20-weeks. Female mice (n=6/group/age) from all three groups were euthanised and had tissue collected at six-weeks of age, temporally corresponding with the pre-symptomatic findings discussed previously. Female mice were also euthanised at 15-weeks of age, temporally correlating with the open-field behavioural testing of the male mice. The male mice were euthanised at 20-weeks of age following the final behavioural testing.

As seen in the individual plots for the behavioural data (Fig 6.1; 6.2), 15 male mice were not tested at either the 15- or 20-week time-points from either group. What occurred following the injections at birth was a high level of cannibalisation of mouse pups by the mother from Day 0 up to weaning (Day 21), which resulted in reduced group sizes for behavioural testing. Observations within our mouse colony suggest that MPS IIIA parents, particularly within the YFP$^{+/-}$-MPS IIIA colony, have a tendency (over wild-type) to cannibalise their young. In fact, primiparous (first-time pregnant) MPS IIIA mice have an even greater tendency to cannibalise their young (Lau et al., 2007). The mice bred for this study were primiparous for all genotypes, as it was unethical to breed a generation of 90 mice for surplus purposes. The vehicle-treated controls retained the highest number of

mice, with 13 tested for all tests. The vehicle-treated MPS IIIA group was heavily reduced to a size of six, and the AAV9-*SGSH* MPS IIIA group was the lowest with five. Due to time constraints, histological assessments were predominantly conducted at 20-weeks of age, thus capturing the effect of treatment in late-stage disease.

Additionally, following treatment with AAV9-*SGSH*, the mice could not be returned to their standard and pre-treatment quiet holding/breeding room and were required to be transported to a PC2-compliant holding area. Due to physical limitations in the Animal Care Facility at the Women's and Children's Hospital Health Network, only one PC2-holding area was available for the mice, which experienced a high volume of activity by other researchers housing mice in the same area for other studies. The increased noise, activity, and aromas of foreign researchers in the vicinity potentially stressed the mice, more so impacting the MPS IIIA mice. In turn, this may have exacerbated the level of pup cannibalisation, especially by the MPS IIIA mothers, profoundly impacting group sizes and robust assessment of AAV9-*SGSH* on MPS IIIA behavioural motor function.

6.2.1 Open-field behavioural testing

To assess the effects of AAV9-*SGSH* on the motor phenotype in MPS IIIA, the open-field behaviour test was conducted at 15-weeks of age to measure differences in general activity and exploration over five-minutes. Identifications for each mouse are shown in Appendix 5. On average, wild-type mice recorded the greatest distance travelled throughout the course (Fig 6.1A). The MPS IIIA (saline) mice recorded the lowest average distance: only mice 728 and 729 (represented as half-empty and empty squares, respectively) were lower than the minimum score in the wild-type mice, which resulted in a non-significant difference. The AAV9-*SGSH* MPS IIIA mice recorded a similar travelling distance to the MPS IIIA (saline) mice, with only mouse 743 (solid circle) falling outside the MPS IIIA

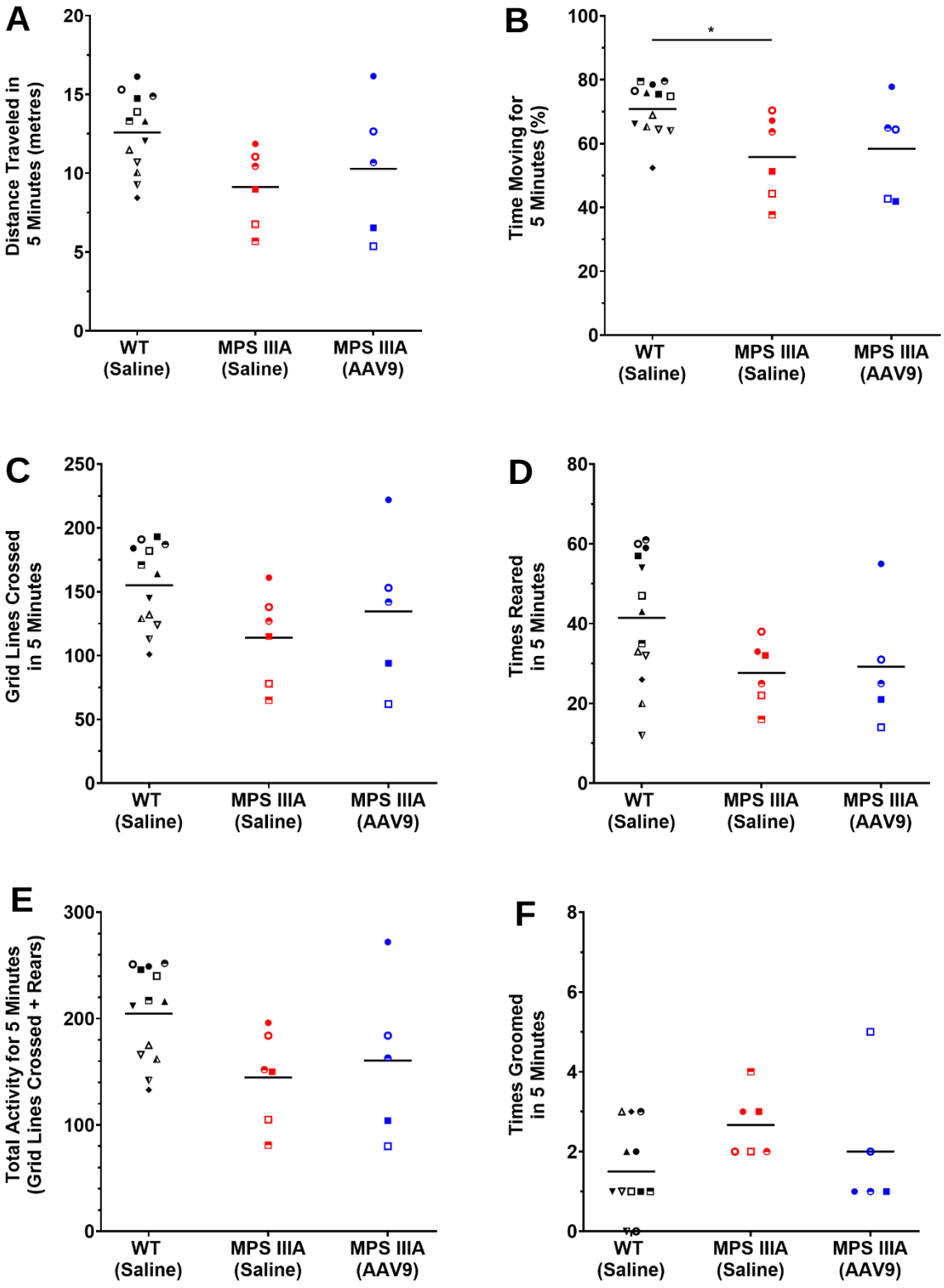

A
Distance Traveled in 5 Minutes (metres)
20
15
10
5
0
WT (Saline)
MPS IIIA (Saline)
MPS IIIA (AAV9)
B
Time Moving for 5 Minutes (%)
100
80
60
40
20
0
*
WT (Saline)
MPS IIIA (Saline)
MPS IIIA (AAV9)
C
Grid Lines Crossed in 5 Minutes
250
200
150
100
50
0
WT (Saline)
MPS IIIA (Saline)
MPS IIIA (AAV9)
D
Times Reared in 5 Minutes
80
60
40
20
0
WT (Saline)
MPS IIIA (Saline)
MPS IIIA (AAV9)
E
Total Activity for 5 Minutes (Grid Lines Crossed + Rears)
300
200
100
0
WT (Saline)
MPS IIIA (Saline)
MPS IIIA (AAV9)
F
Times Groomed in 5 Minutes
8
6
4
2
0
WT (Saline)
MPS IIIA (Saline)
MPS IIIA (AAV9)

Figure 6.1 – Open-field behavioural testing. Testing of motor function utilising the open-field test on wild-type (WT) (saline), MPS IIIA (saline), and MPS IIIA (AAV9-*SGSH*) mice at 15-weeks of age. The test measured, over five-minutes, total distance travelled (A), duration moving during the test (B), grid lines crossed (C), rears (D), total horizontal and vertical activity (E), and grooms (F). N=5 to13 animals per genotype per age. *$p<0.05$; one-way ANOVA, with Bonferroni's multiple comparisons. Data are individual mice with statistical mean.

(saline) scores yet within the wild-type scores. AAV9-*SGSH* did not appear to affect mice 741 (solid square) and 742 (empty square), as they travelled less than the wild-type mice. While most of these observations were repeated when moving time was calculated (Fig 6.1B), on average, MPS IIIA (saline) mice were less active and less exploratory compared with wild-type mice, which reached statistical significance ($p<0.05$). There was no significant difference between AAV9-*SGSH* MPS IIIA mice and any of the vehicle-treated mice ($p>0.05$).

Similar with the observations of "horizontal" movement, the number of grid lines crossed within the open-field test was not statistically significant between any of the groups (Fig 6.1C). The individual points also trended the same way, as shown in Figs 6.1A and 6.1B. "Vertical" behaviour not recorded by video was manually noted as times reared onto hind-limbs (Fig 6.1D). On average, wild-type mice reared more frequently than the other groups. However, they also showed the greatest variation, and thus calculated statistically non-significant differences with the other groups.

Combined behavioural traits did not show significant difference between any of the groups, and complemented the patterns observed in the other calculations (Fig 6.1E). Times groomed were not significant between groups (Fig 6.1F). Therefore, it appears that intraventricular AAV9-*SGSH* treatment had only subtle effects on performance in the open-field test in $YFP^{+/-}$-MPS IIIA mice in the timeframe of these experiments.

6.2.2 Motor function behavioural testing

To assess the effects of AAV9-*SGSH* when the MPS IIIA behavioural phenotype is more advanced (20-weeks of age), the pole-climb, negative geotaxis and grip strength behaviour tests were conducted to measure motor function. The pole-climb test was conducted five

times within the one session, with assessments made on all tests to determine whether mice improved with repetition. The wild-type mice and AAV9-*SGSH* MPS IIIA mice showed similar means of time taken to correct orientation and face down the pole in the first two tests (Fig 6.2A) and for all tests (Fig 6.2B). Once orientation was corrected, time taken to descend the pole was calculated and shown for the initial tests (Fig 6.2C) and for all tests (Fig 6.2D). Similar trends were observed in the descent for all groups. The averages for all groups did not improve after multiple tests. MPS IIIA (saline) mouse 728 (half-empty square) was determined to be a statistical outlier and was thus removed from statistical analysis.

The assessment of negative geotaxis revealed that MPS IIIA (saline) mice took a statistically significantly longer time to correct orientation compared with the wild-type mice ($p<0.05$; Fig 6.2E). Whilst the majority of AAV9-*SGSH* MPS IIIA mice showed a downwards trend by recording similar times with the wild-type mice (mouse 664 of the wild-type group was determined to be a statistical outlier), the group did not perform significantly better compared to the MPS IIIA (saline) mice. Differences in grip strength were not observed in MPS IIIA (saline) mice compared with wild-type (saline) mice or following treatment in AAV9-*SGSH* MPS IIIA mice (Fig 6.2F).

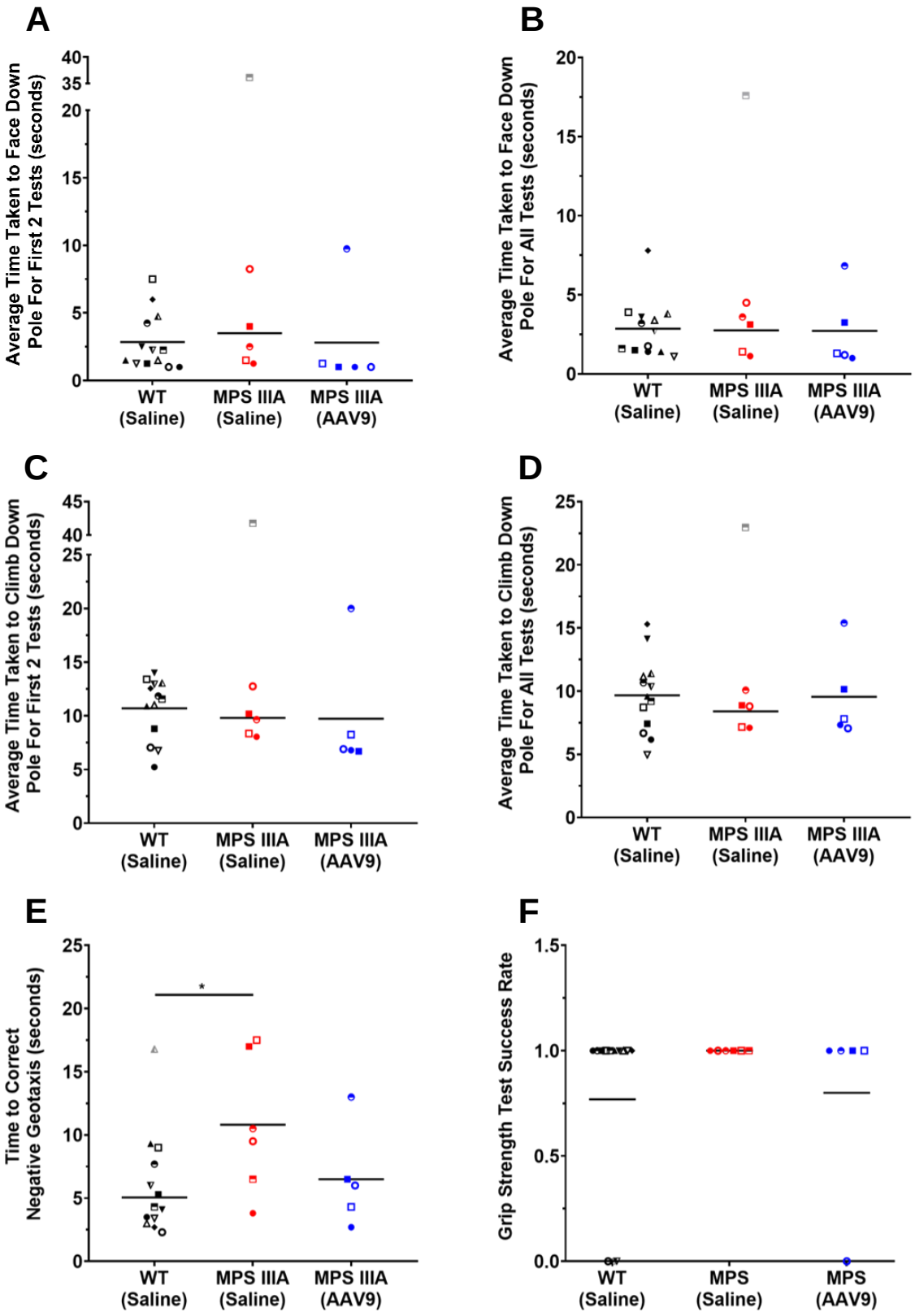

A
Average Time Taken to Face Down Pole For First 2 Tests (seconds)
40
35
20
15
10
5
0
WT (Saline)
MPS IIIA (Saline)
MPS IIIA (AAV9)
B
Average Time Taken to Face Down Pole For All Tests (seconds)
20
15
10
5
0
WT (Saline)
MPS IIIA (Saline)
MPS IIIA (AAV9)
C
Average Time Taken to Climb Down Pole For First 2 Tests (seconds)
45
40
25
20
15
10
5
0
WT (Saline)
MPS IIIA (Saline)
MPS IIIA (AAV9)
D
Average Time Taken to Climb Down Pole For All Tests (seconds)
25
20
15
10
5
0
WT (Saline)
MPS IIIA (Saline)
MPS IIIA (AAV9)
E
Time to Correct Negative Geotaxis (seconds)
*
25
20
15
10
5
0
WT (Saline)
MPS IIIA (Saline)
MPS IIIA (AAV9)
F
Grip Strength Test Success Rate
1.5
1.0
0.5
0.0
WT (Saline)
MPS (Saline)
MPS (AAV9)

Figure 6.2 – Motor function testing of mice. Behaviour testing of motor function utilising the pole-climb, negative geotaxis, and grip strength tests on wild-type (WT) (saline), MPS IIIA (saline), and MPS IIIA (AAV9-*SGSH*) mice at 20-weeks of age. The pole climb test measured average time to correct orientation for first two tests (A) and all tests (B), and duration to descend the pole for first two tests (C) and all tests (D). The negative geotaxis test measured time to correct orientation (E), and grip strength success was also recorded (F). N=5 to 13 animals per genotype per age. *$p<0.05$; one-way ANOVA, with Bonferroni's multiple comparisons. Data are individual mice with statistical mean. Outliers are greyed out.

*6.2.3 Lysosomal dysfunction is prevented following AAV9-*SGSH *administration to YFP$^{+/-}$-MPS IIIA mice*

The effect of AAV9-*SGSH* on lysosomal storage of HS in mice was determined up to 20-weeks of age by measuring HS levels in the cerebral cortex via LC-MS/MS. From six-weeks of age, MPS IIIA (saline) mice accumulated significantly higher levels of HS compared to wild-type (saline) mice ($p<0.0001$; Fig 6.3). The AAV9-*SGSH* MPS IIIA mice accumulated significantly lower levels of HS compared to the MPS IIIA (saline) mice ($p<0.0001$) and showed similar HS levels to the wild-type (saline) mice ($p>0.05$). These differences were replicated at 15- and 20-weeks of age.

The effect of AAV9-*SGSH* on the abundance of lysosomes in the brain was evaluated by measuring levels of lysosomal-associated membrane protein 1 (LAMP1) as a histological marker of lysosomes via immunofluorescence assays on 20µm-thick free-floating sections. Lysosomal compartments were observed as being localised around YFP-positive layer 5 neurons within the cerebral motor cortex, which were the same sites of previously described dendritic spine changes (Fig 6.4). At 20-weeks of age, consistent with the LC-MS/MS findings, MPS IIIA (saline) mice had significantly greater LAMP1 levels compared with wild-type (saline) mice ($p<0.0001$; Fig 6.5) and AAV9-*SGSH* MPS IIIA mice ($p<0.001$; Fig 6.5). There was no significant difference between the MPS IIIA (AAV9-*SGSH*) and the wild-type (saline) mice ($p>0.05$).

These data indicate that AAV9-*SGSH* administration to YFP$^{+/-}$-MPS IIIA mice restores lysosome function from an early-symptomatic disease stage and maintains reduced HS levels within the cerebral cortex, including areas of dendritic spine loss, at the late-symptomatic stage of 20-weeks.

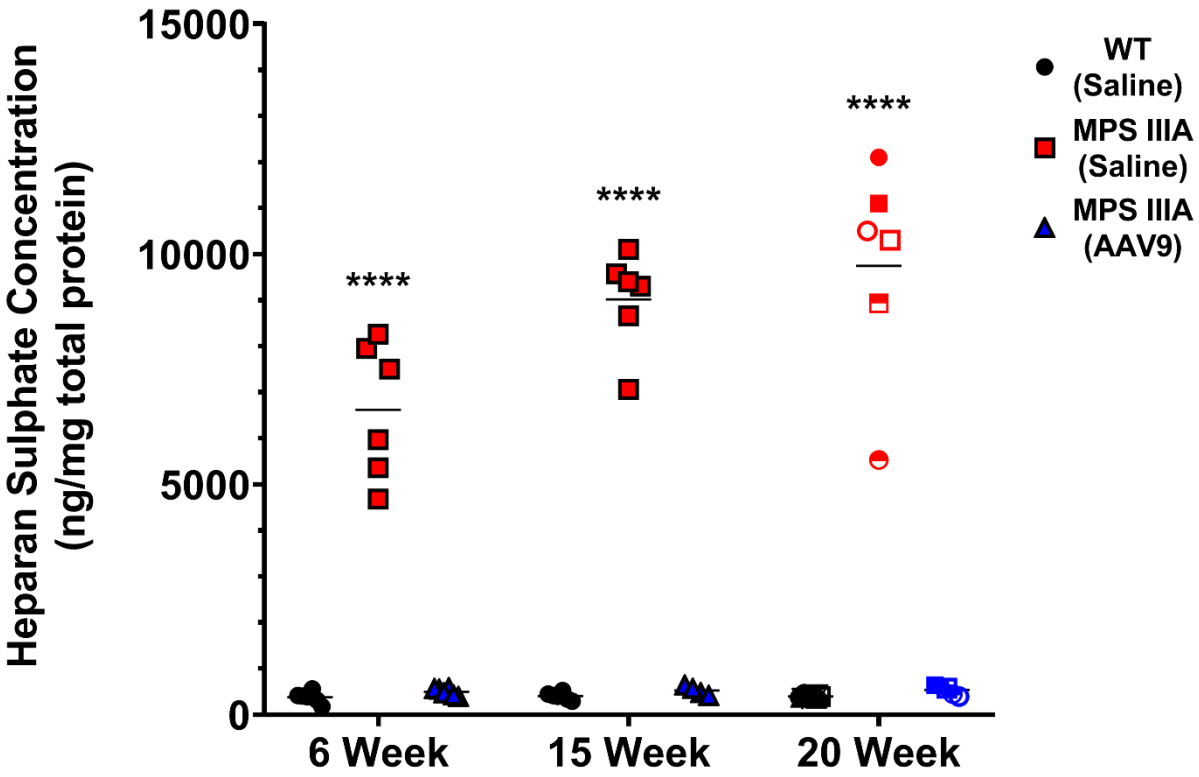


Figure 6.3 – Heparan sulphate levels in mice. Levels of HS in the cerebral cortex of wild-type (WT) (saline), MPS IIIA (saline), and MPS IIIA (AAV9-*SGSH*) mice at six-, 15- and 20-weeks of age. N=5 to 6 animals per genotype per age. ****p<0.0001; one-way ANOVA, with Bonferroni's multiple comparisons. Data are individual mice with statistical mean.

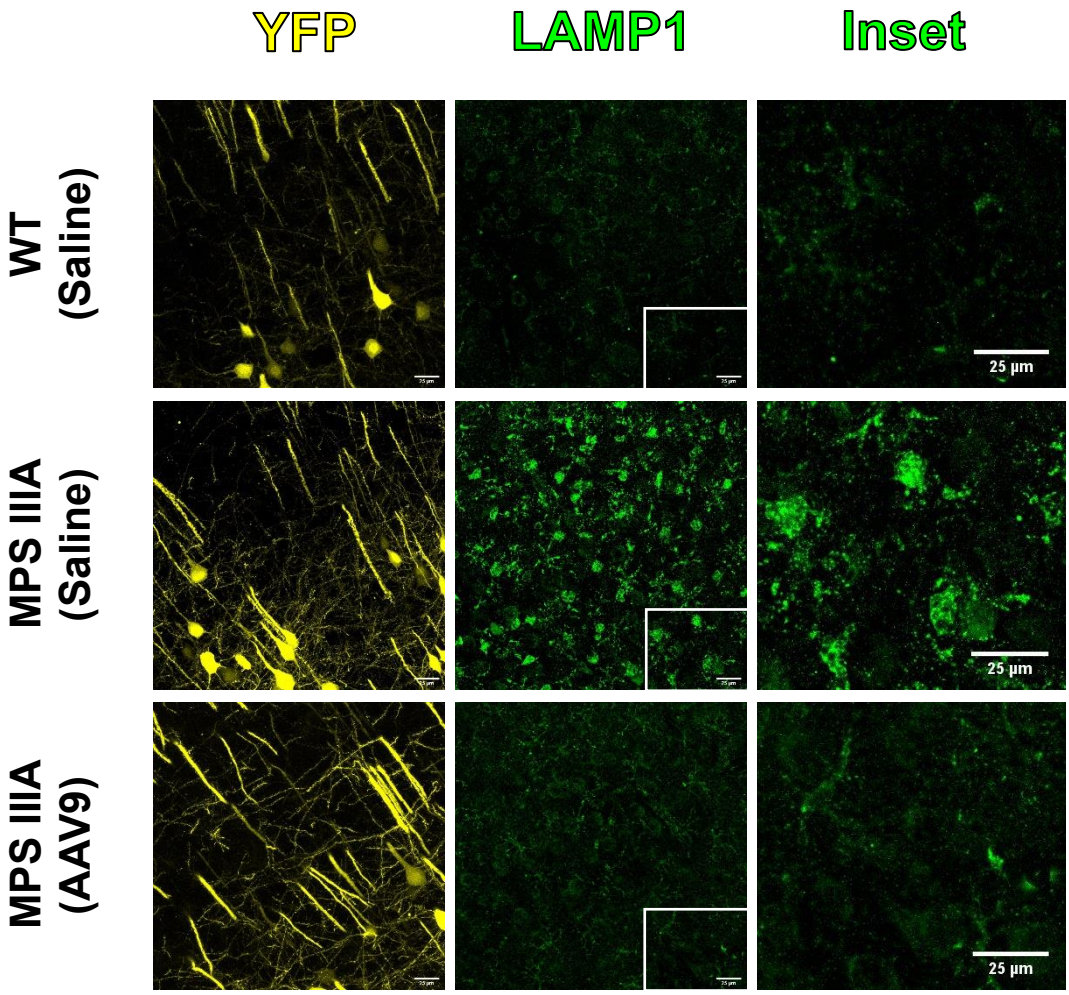


Figure 6.4 – Representative images of LAMP1 staining in mice. Visualisation of LAMP1-positive cells localised around dendrites of layer 5 YFP-positive pyramidal neurons in the cerebral motor cortex of wild-type (WT) (saline), MPS IIIA (saline), and MPS IIIA (AAV9-*SGSH*) mice at 20-weeks of age. LAMP1; lysosomal-associated membrane protein 1. Scale bar is 25µm.

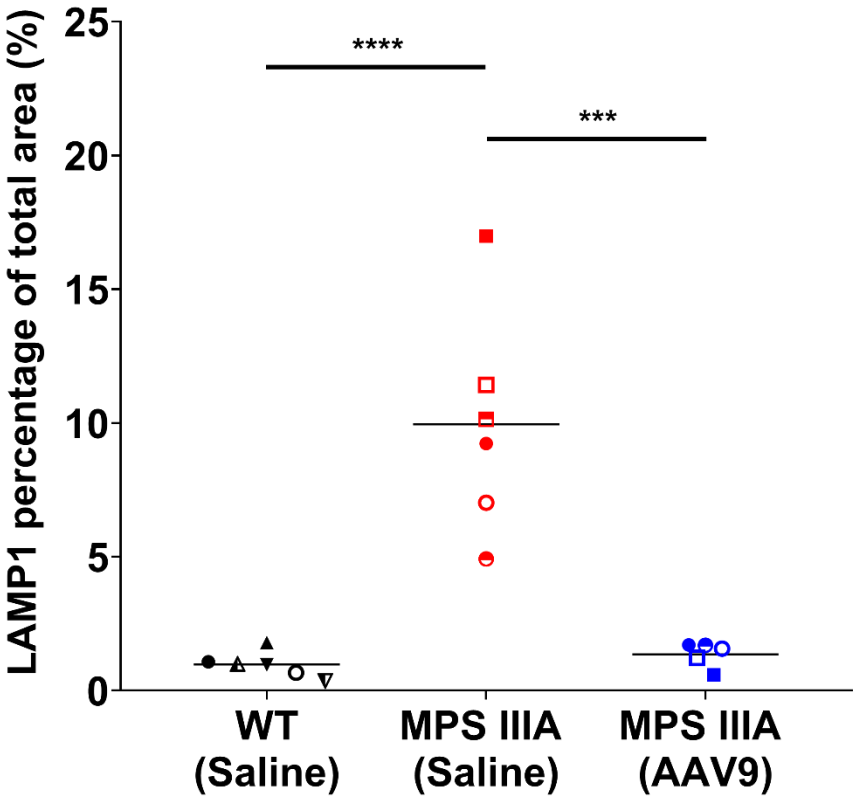


Figure 6.5 – Percentage of LAMP1-positive staining in the mouse motor cortex. The size of LAMP1-positive stain localised around YFP-positive layer 5 motor cortical neurons of wild-type (WT) (saline), MPS IIIA (saline), and MPS IIIA (AAV9-*SGSH*) mice at 20-weeks of age. N=5 to 6 animals per genotype per age. ***p<0.001; ****p<0.0001; one-way ANOVA, with Bonferroni's multiple comparisons. Data are individual mice with statistical mean.

*6.2.4 Reduction of dendritic spine loss across multiple morphologies in YFP$^{+/-}$-MPS IIIA mice following AAV9-*SGSH *treatment*

To determine whether AAV9-*SGSH* treatment could prevent the dendritic spine loss observed in YFP$^{+/-}$-MPS IIIA mice, assessments of dendritic spine morphology and density were conducted at pre- (six-weeks) and late-symptomatic (20-weeks) disease stages. Representative images of the spines on dendritic segments of layer 5 motor cortical neurons in vehicle-treated and AAV9-*SGSH* mice at 20-weeks of age are shown in Figure 6.6. At six-weeks, MPS IIIA (saline) mice exhibited fewer filopodia than both the wild-type (saline) ($p<0.05$) and the MPS IIIA (AAV9-*SGSH*) mice (Fig 6.7A). Whilst not statistically significant, the immature stubby spines were fewest in the MPS IIIA (saline) mice compared with wild-type and MPS IIIA (AAV9-*SGSH*) mice (Fig 6.7B).

The more mature thin spine densities were highest in the wild-type (saline) mice, but this was not statistically significant when compared with the MPS IIIA (saline) group (Fig 6.7C). The MPS IIIA (AAV9-*SGSH*) mice also presented a trend towards more thin spines than the MPS IIIA (saline) mice. The most mature mushroom spines exhibited the lowest average densities of any of the spine sub-types at six-weeks of age (Fig 6.7D). Whilst the MPS IIIA (saline) mice presented with the lowest mean of all treatment groups, it was not significantly lower than the wild-type (saline) group or the MPS IIIA (AAV9-*SGSH*) group (Fig 6.7D). Across all spine sub-types at the pre-symptomatic age of six-weeks, there were no significant differences between the wild-type (saline) and MPS IIIA (AAV9-*SGSH*) mice.

Late-symptomatic MPS IIIA (saline) mice exhibited fewer average spine densities compared with wild-type (saline), which was statistically significant for filopodia ($p<0.01$; Fig 6.8A), thin ($p<0.01$; Fig 6.8C), and mushroom ($p<0.05$; Fig 6.8D). Stubby spines,

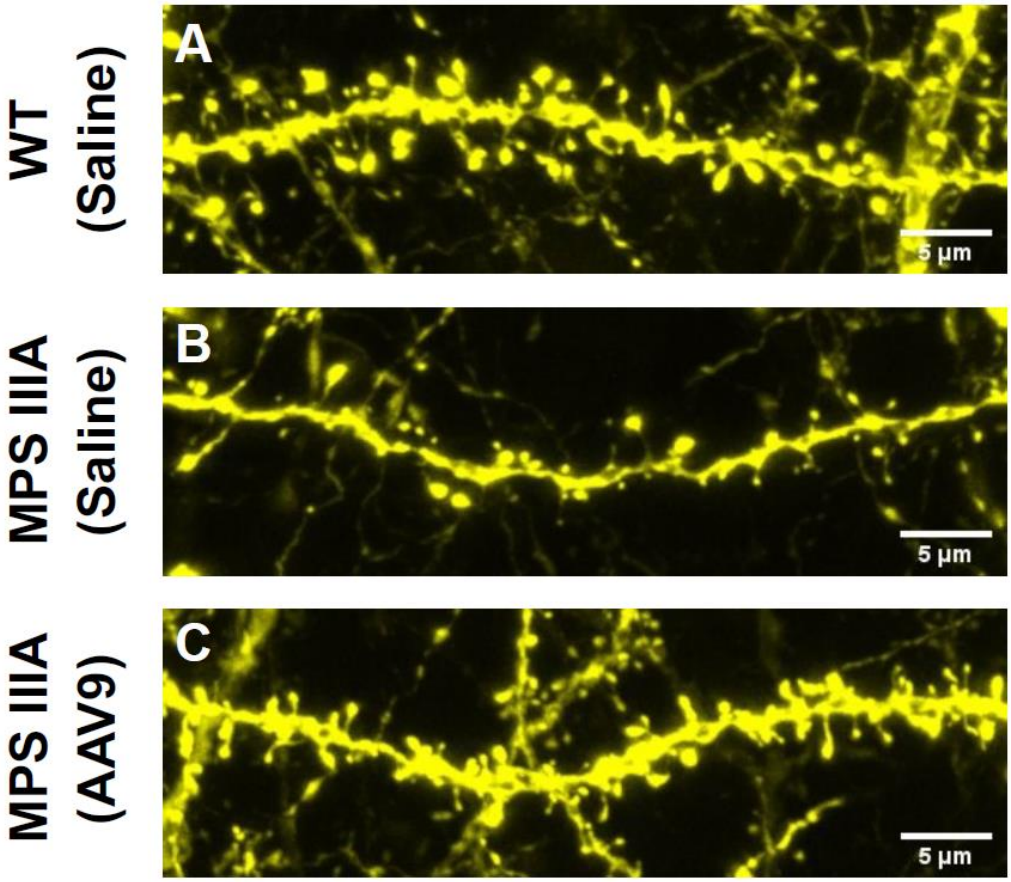


Figure 6.6 – Representative images of dendritic spines in 20-week old mice. Dendrites of layer 5 pyramidal neurons in the cerebral motor cortex of wild-type (WT) (saline; A), MPS IIIA (saline; B), and MPS IIIA (AAV9-*SGSH*; C) at 20-weeks of age. Scale bar is 5µm.

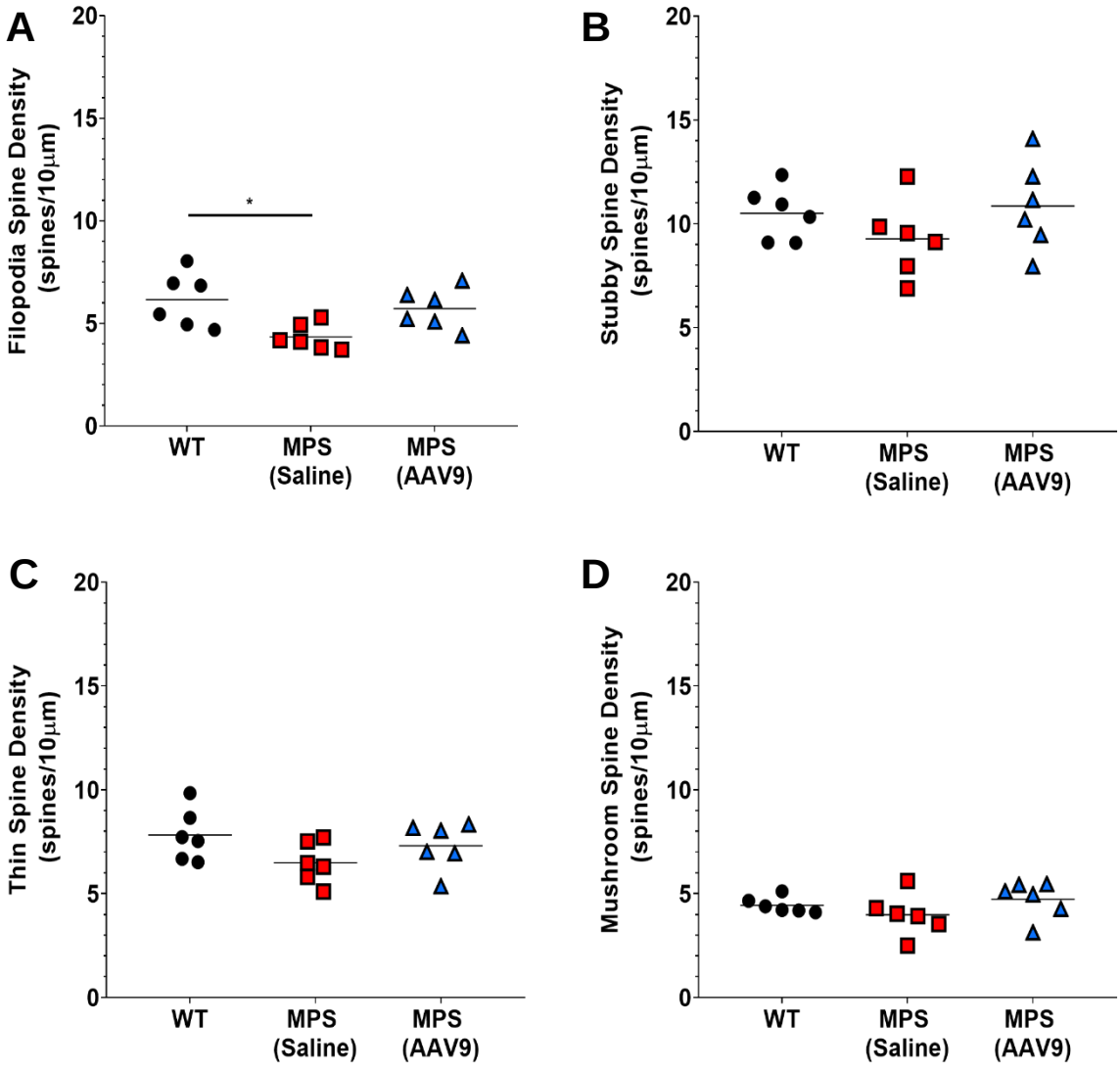


Figure 6.7 – Densities of dendritic spine sub-types in pre-symptomatic mice. Dendritic spine densities on layer 5 motor cortical neurons of wild-type (WT) (saline), MPS IIIA (saline), and MPS IIIA (AAV9-*SGSH*) mice at six-weeks of age. Spine sub-types were categorised into filopodia (A), stubby (B), thin (C), and mushroom (D). N=6 dendritic segments per cell; 6 cells per animal; 6 animals per genotype per age. *$p<0.05$; one-way ANOVA, with Bonferroni's multiple comparisons. Data are individual mice with statistical mean.

however, were not significant when compared with wild-type mice ($p>0.05$; Fig 6.8B). Compared with MPS IIIA (saline) mice, MPS IIIA (AAV9-*SGSH*) mice presented with filopodia and thin spine densities trending upwards but without statistical significance. The MPS IIIA (AAV9-*SGSH*) mice did, however, exhibit significantly higher stubby ($p<0.01$; Fig 6.8B) and mushroom ($p<0.05$; Fig 6.8D) densities compared with the MPS IIIA (saline) group. There was no significant difference between the wild-type (saline) and MPS IIIA (AAV9-*SGSH*) mice.

6.2.5 Glial cell activation and complement component levels are reduced in the AAV9-SGSH-treated YFP$^{+/-}$-MPS IIIA mice

We also sought to determine whether there were any changes in the expression of inflammatory markers and glial cell activation previously described around the YFP-positive layer 5 neurons that exhibited synaptic changes. Immunofluorescence assays were conducted on free-floating 20µm-thick slices encompassing the motor cortical region. C1q expression levels and microglial density (Iba1) were analysed at 20-weeks of age in mice following treatment with saline or AAV9-*SGSH*. Representative images are shown in Figure 6.9. C1q expression was significantly higher in MPS IIIA (saline) mice compared with wild-type (saline) mice ($p<0.001$; Fig 6.10A); C1q levels were significantly reduced in MPS IIIA (AAV9-*SGSH*) compared with MPS IIIA (saline) groups ($p<0.01$); and C1q expression did not significantly differ between the wild-type (saline) and MPS IIIA (AAV9-*SGSH*) groups.

The number of microglia was also significantly higher in the MPS IIIA (saline) group compared with the wild-type (saline) mice ($p<0.001$; Fig 6.10B). Comparatively, MPS IIIA (AAV9-*SGSH*) mice showed a significant reduction in microglial levels compared with MPS IIIA (saline) mice ($p<0.001$). The reduction resulted in a similar mean when

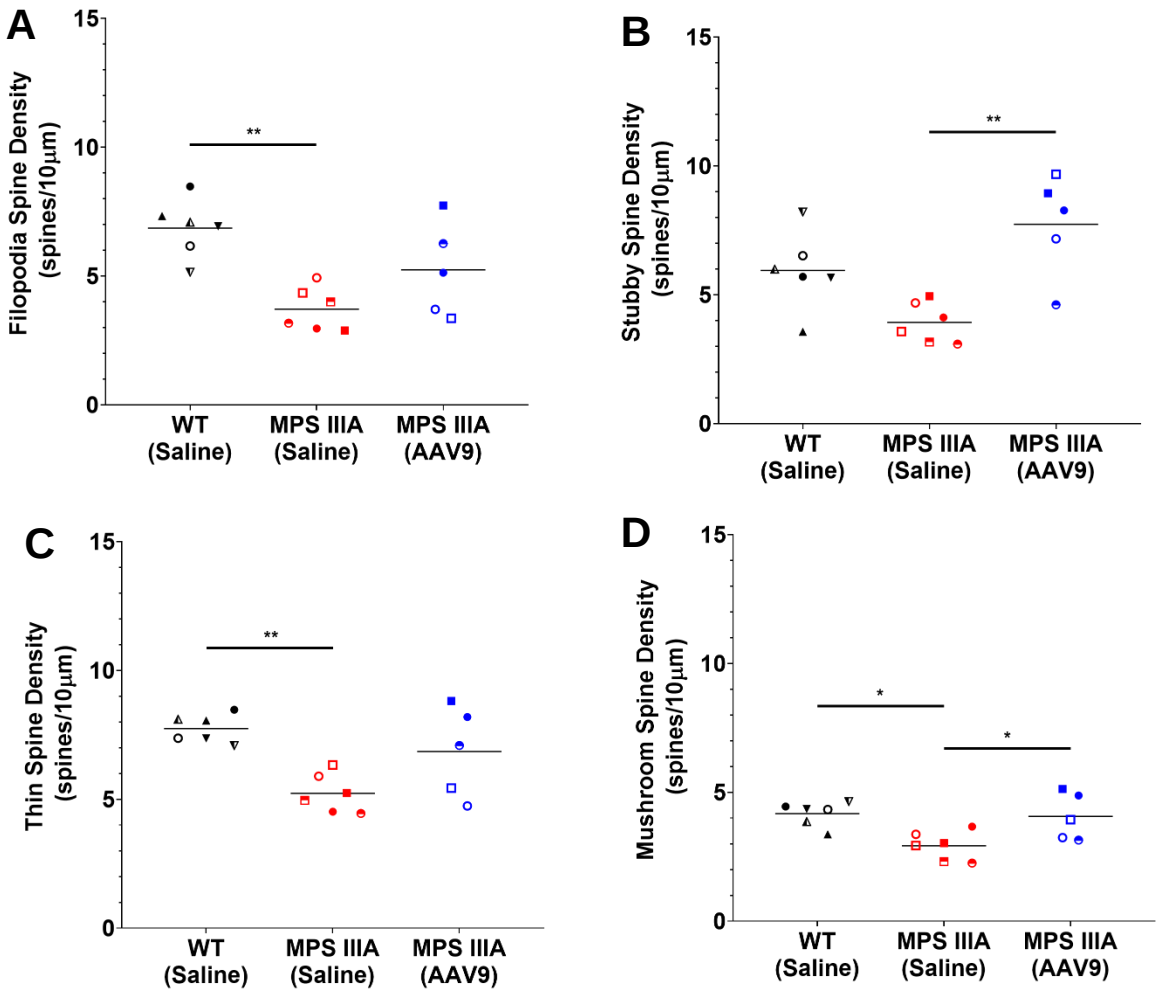


Figure 6.8 – Densities of dendritic spine sub-types in late-symptomatic mice. Densities of dendritic spines on layer 5 motor cortical neurons of wild-type (WT) (saline), MPS IIIA (saline), and MPS IIIA (AAV9-*SGSH*) mice at 20-weeks of age. Spine sub-types were categorised into filopodia (A), stubby (B), thin (C), and mushroom (D). N=6 dendritic segments per cell; 6 cells per animal; 5-6 animals per genotype per age. *p<0.05; **p<0.01; one-way ANOVA, with Bonferroni's multiple comparisons. Data are individual mice with statistical mean.

compared with the wild-type (saline) mice, but resulted in no statistically significant difference.

The second immunofluorescence assay analysed expression levels of the C3 inflammatory component, astrocytic activation, and the abundance of A1 neurotoxic astrocytes. Representative images are illustrated in Figure 6.11. C3 expression was significantly higher in MPS IIIA (saline) mice compared with wild-type (saline) mice ($p<0.05$; Fig 6.12A). C3 expression in the MPS IIIA (AAV9-*SGSH*) group was significantly reduced when compared with MPS IIIA (saline) mice ($p<0.01$). Mouse 729 (empty square) of the MPS IIIA (saline) group revealed particularly higher levels of C3 expression than the other mice within the sub-group and was determined to be a statistical outlier; it was thus excluded from statistical tests but included for illustrative purposes (Fig 6.12A). GFAP expression was also significantly higher in the MPS IIIA (saline) group compared with the wild-type (saline) mice ($p<0.0001$; Fig 6.12B) and was reduced in the MPS IIIA (AAV9-*SGSH*) mice following treatment ($p<0.0001$). Lastly, the population of A1 astrocytes was also significantly higher in the MPS IIIA (saline) group compared with the wild-type (saline) mice ($p<0.0001$; Fig 6.12C) and the MPS IIIA (AAV9-*SGSH*) mice following treatment ($p<0.0001$).

Through identification of individual mice within the graphical outputs (Appendix 5), some behavioural data could be salvaged and used to investigate any trends across datasets from behavioural through to the histological assessments, potentially correlating behavioural performance with spine and inflammatory changes. The variability between animals could also be observed. For example, mouse 728 (half-empty square) of the vehicle-treated MPS IIIA group was the most inactive within the sub-group in the open-field behavioural test (Fig 6.1). Five-weeks later, mouse 728 was also the worst performer

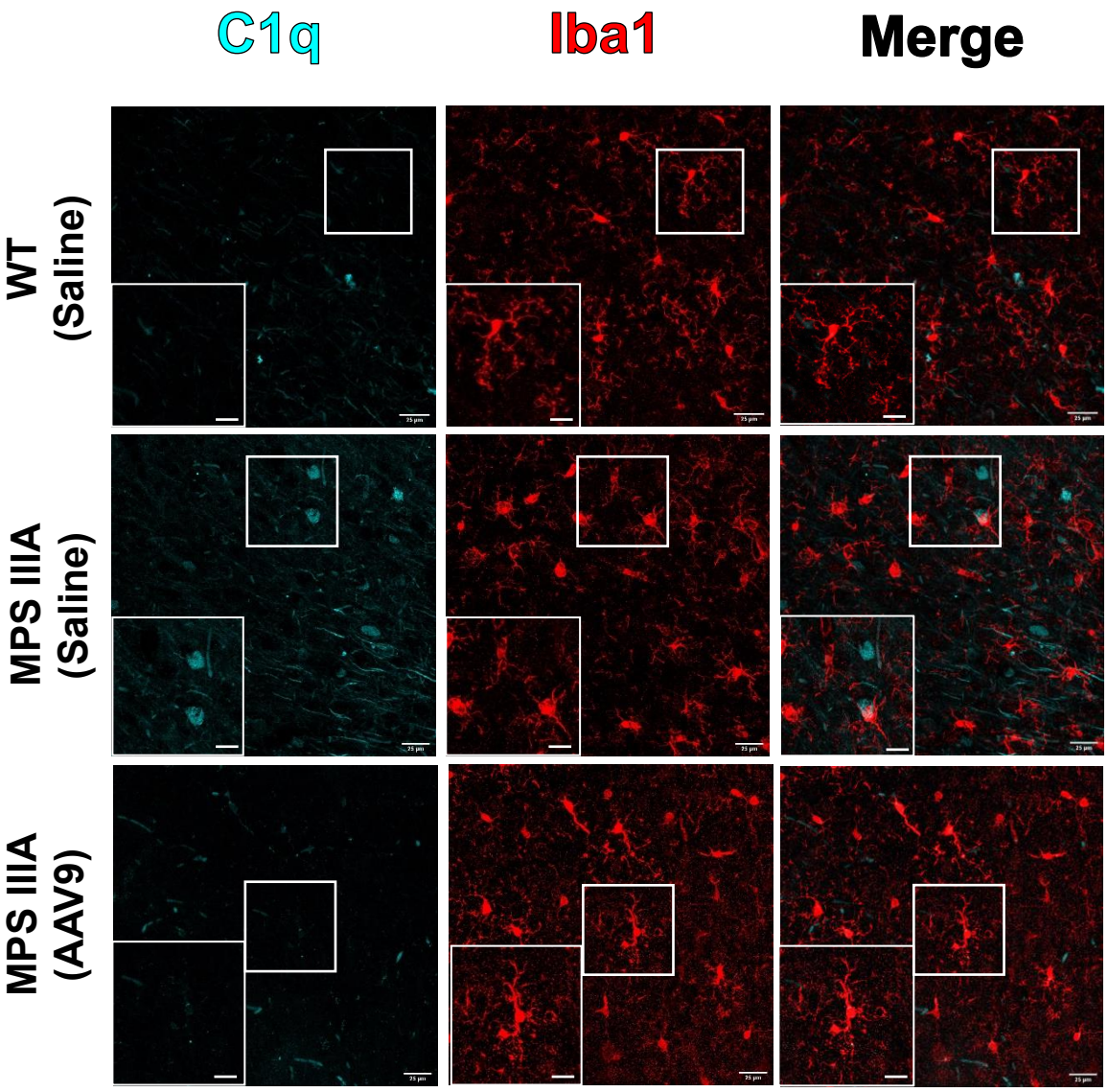


Figure 6.9 – Representative images of C1q and Iba1 immunofluorescence in layer 5 of the mouse motor cortex. Visualisation of complement component C1q and microglia in the cerebral motor cortex of wild-type (WT) (saline), MPS IIIA (saline), and MPS IIIA (AAV9-*SGSH*) treated mice at 20-weeks of age. Scale bar is 25µm; inset 15µm.

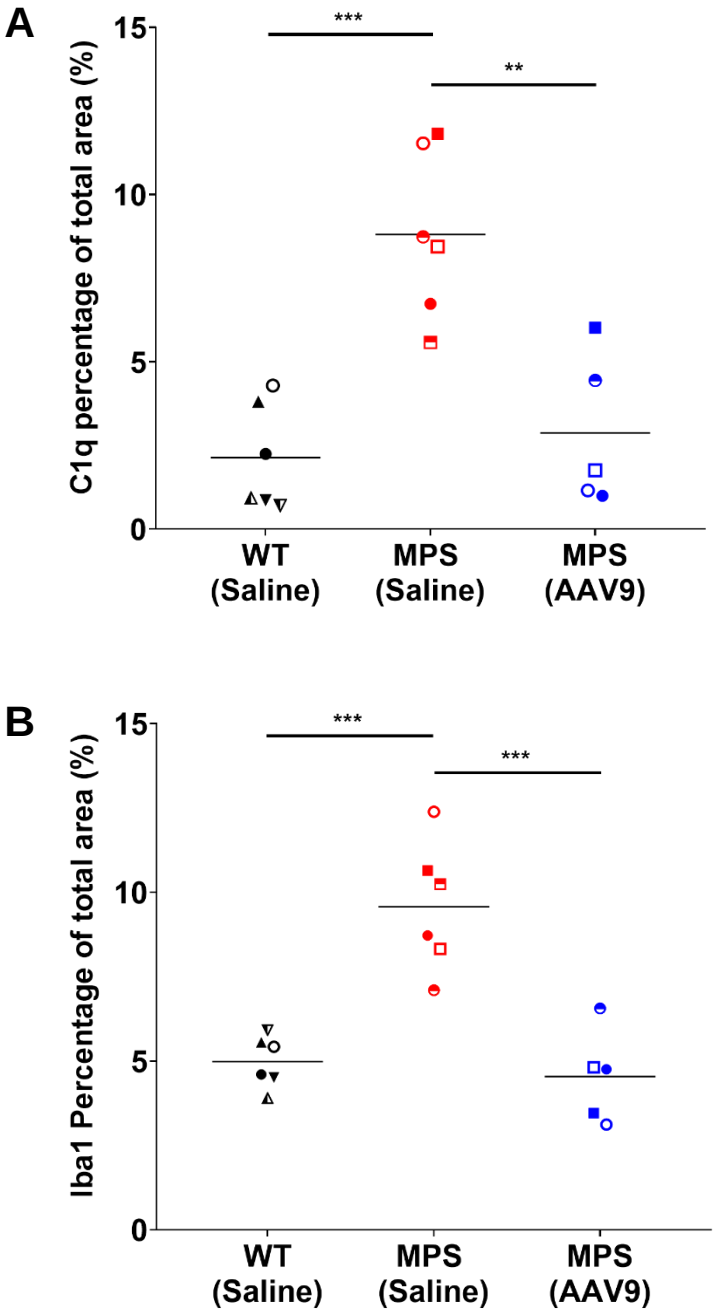


Figure 6.10 – Levels of C1q and microglia in the mouse motor cortex. Complement component C1q (A) and Iba1-positive (B) levels localised around YFP-positive layer 5 motor cortical neurons of wild-type (WT) (saline), MPS IIIA (saline), and MPS IIIA (AAV9-*SGSH*) treated mice at 20-weeks of age. N=5 to 6 animals per genotype per age. **p<0.01; ***p<0.001; one-way ANOVA, with Bonferroni's multiple comparisons. Data are individual mice with statistical mean.

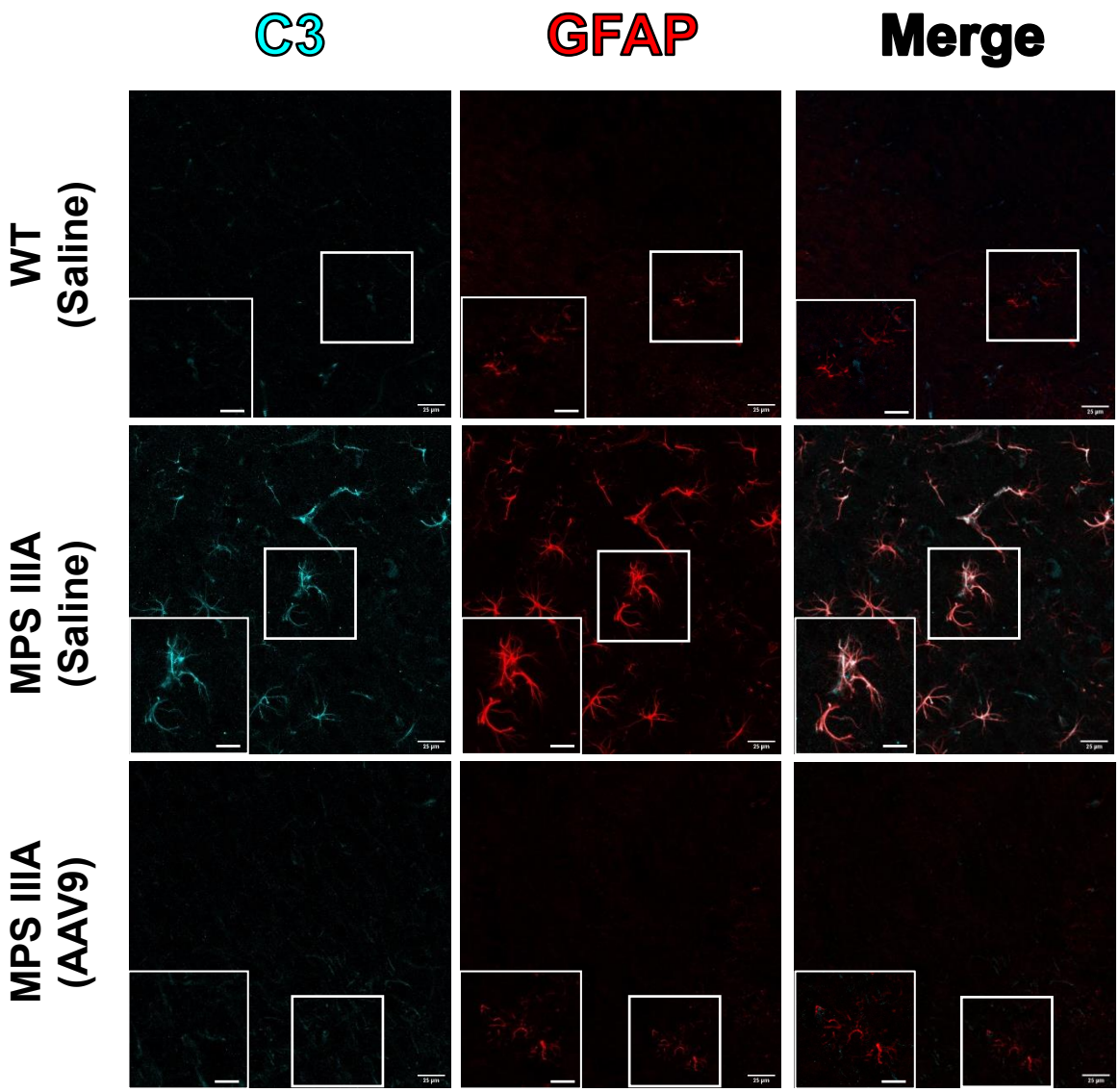


Figure 6.11 – Representative images of C3 and GFAP immunofluorescence in layer 5 of the mouse motor cortex. Visualisation of astrocytes and complement component C3 in the cerebral motor cortex of wild-type (WT) (saline), MPS IIIA (saline), and MPS IIIA (AAV9-*SGSH*) treated mice at 20-weeks of age. Scale bar is 25µm; inset 15µm.

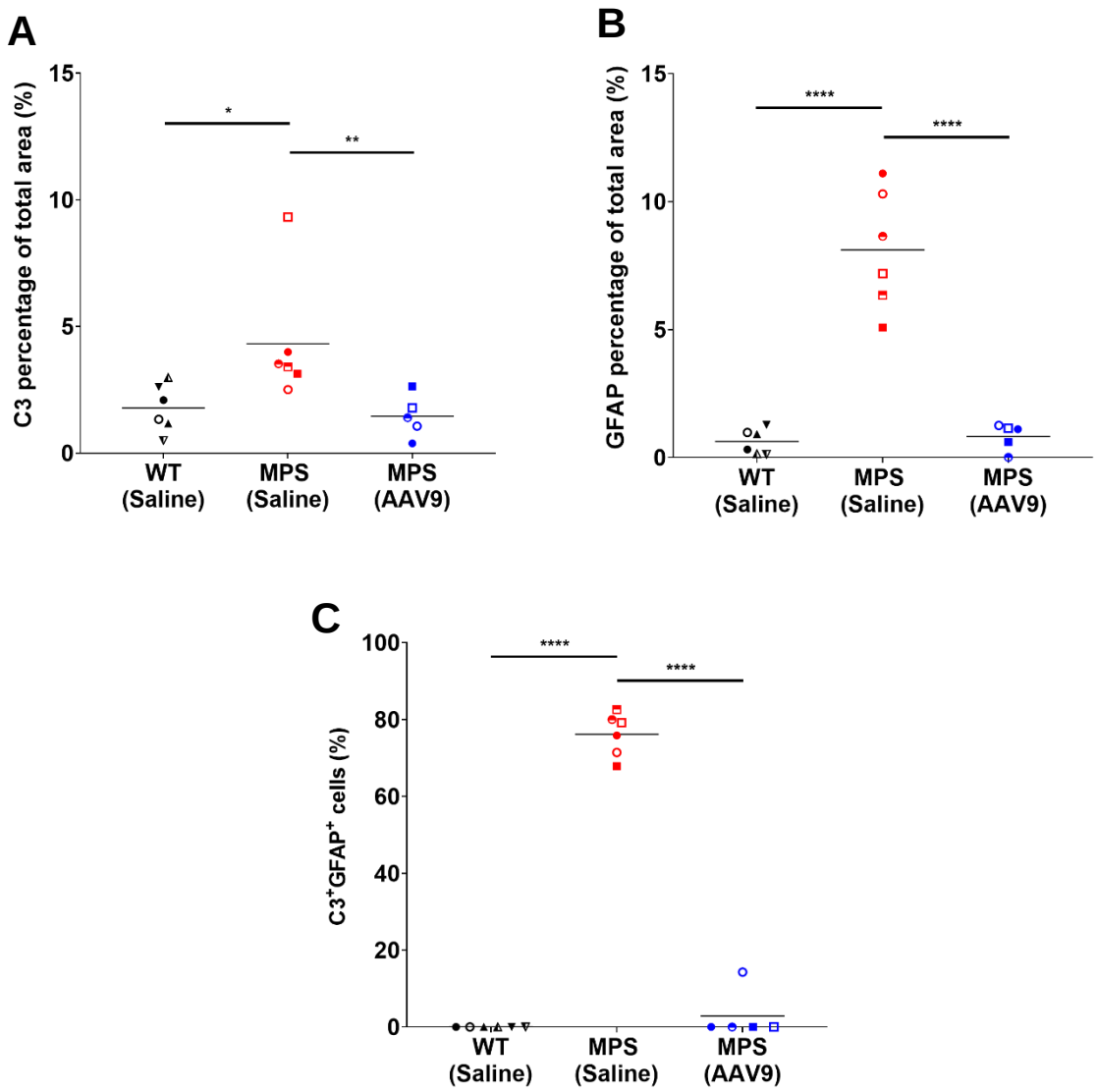


Figure 6.12 – Levels of C3, activated astrocytes, and A1 astrocytes in the mouse motor cortex. Complement component C3 (A) and GFAP (B) levels, and percentage of A1-type astrocytes (C) localised around YFP-positive layer 5 motor cortical neurons of wild-type (WT) (saline), MPS IIIA (saline), and MPS IIIA (AAV9-*SGSH*) mice at 20-weeks of age. N=5 to 6 animals per genotype per age. *p<0.05; **p<0.01; ****p<0.0001; one-way ANOVA, with Bonferroni's multiple comparisons. Data are individual mice with statistical mean.

in the pole climbing test to the point that it was calculated to be a statistical outlier (Fig 6.2). Whilst it did not have the highest level of HS storage (Fig 6.3), it was one of two mice (with mouse 727) with the lowest stubby and mushroom dendritic spine densities (Fig 6.8B, D). Mouse 728 also recorded the highest percentage of A1-type astrocytes (Fig 6.12C).

Meanwhile, mouse 743 (filled circle) of the MPS IIIA (AAV9-*SGSH*) group recorded the highest activity level in the open-field test (even compared with the vehicle-treated wild-type mice; Fig 6.1), and continued to be the fastest-reacting within the sub-group in the pole-climb and negative geotaxis motor function tests (Fig 6.2). Assessment of dendritic spine density showed mouse 743 was one of two mice in the AAV9-*SGSH* sub-group with the highest thin and mushroom spine densities (Fig 6.8C, D); mouse 743 also had the lowest C1q and C3 protein expression levels of any AAV9-*SGSH*-treated MPS IIIA mice (Fig 6.10A; 6.12A). Similarly, mouse 731 (empty circle) of the vehicle-treated MPS IIIA group recorded higher activity levels in the open-field test (Fig 6.1), synonymous with those observed in the control group. The histological data also revealed mouse 731 had the highest filopodial density (Fig 6.8A). Additionally, whilst not presenting with the highest densities, mouse 731 consistently presented as the only mouse in the top two mice with the highest spine density in the vehicle-treated MPS IIIA group (Fig 6.8). Interestingly, mouse 731 recorded amongst the highest levels of expression for C1q and microglia (Fig 6.10), yet C3 expression was the lowest of the group (Fig 6.12A), falling to levels observed in the wild-type mice and corrected AAV9-*SGSH* MPS IIIA mice.

*6.2.6 Activated glial cell apposition to dendritic spines is reduced in YFP$^{+/-}$-MPS IIIA mice following AAV9-*SGSH *treatment*

To build on the previous observation of greater glial cell apposition to sites of synaptic loss in MPS IIIA mice, the localisation of these cells to sites of synaptic loss with treatment of AAV9-*SGSH* was assessed. Representative images of the microglial and neuronal models generated for the vehicle-treated and AAV9-*SGSH*-treated mice are demonstrated in Figure 6.13.

Utilising the 'distance-between-surfaces' feature of the Imaris software, the proximity between a microglial voxel and the nearest neuronal voxel was measured. The frequency of all microglial voxels was accumulated and recorded for each mouse, with the mean of all mice for each micrometre increment within a sub-group shown (Fig. 6.14A). The raw output shows the highest occurrence of microglia apposed ≤ 2μm to a nearby neuron at 20-weeks of age in the MPS IIIA (saline) mice (Fig 6.14A). The wild-type (saline) mice were found to have the next highest level of microglial apposition, followed by MPS IIIA (AAV9-*SGSH*) with the lowest level of microglial apposition to the neurons at distances of ≤ 2μm (Fig 6.14A).

To conduct statistical analysis on these outputs, the data were transformed into negative binomial regression models for the wild-type (saline) (Fig 6.14B), MPS IIIA (saline) (Fig 6.14C), and MPS IIIA (AAV9-*SGSH*) groups (Fig 6.14D). Statistical outputs are provided in Appendix 3. The association between frequency and distance for each treatment and genotype group at 20-weeks of age was assessed, and interaction p-values were generated. The wild-type (saline) mice showed the greatest decrease in frequency (45%) with every unit increase in distance away from the nearest YFP-positive voxel. In comparison, the MPS IIIA (saline) mice showed a similar decrease in microglial frequency (43%) with

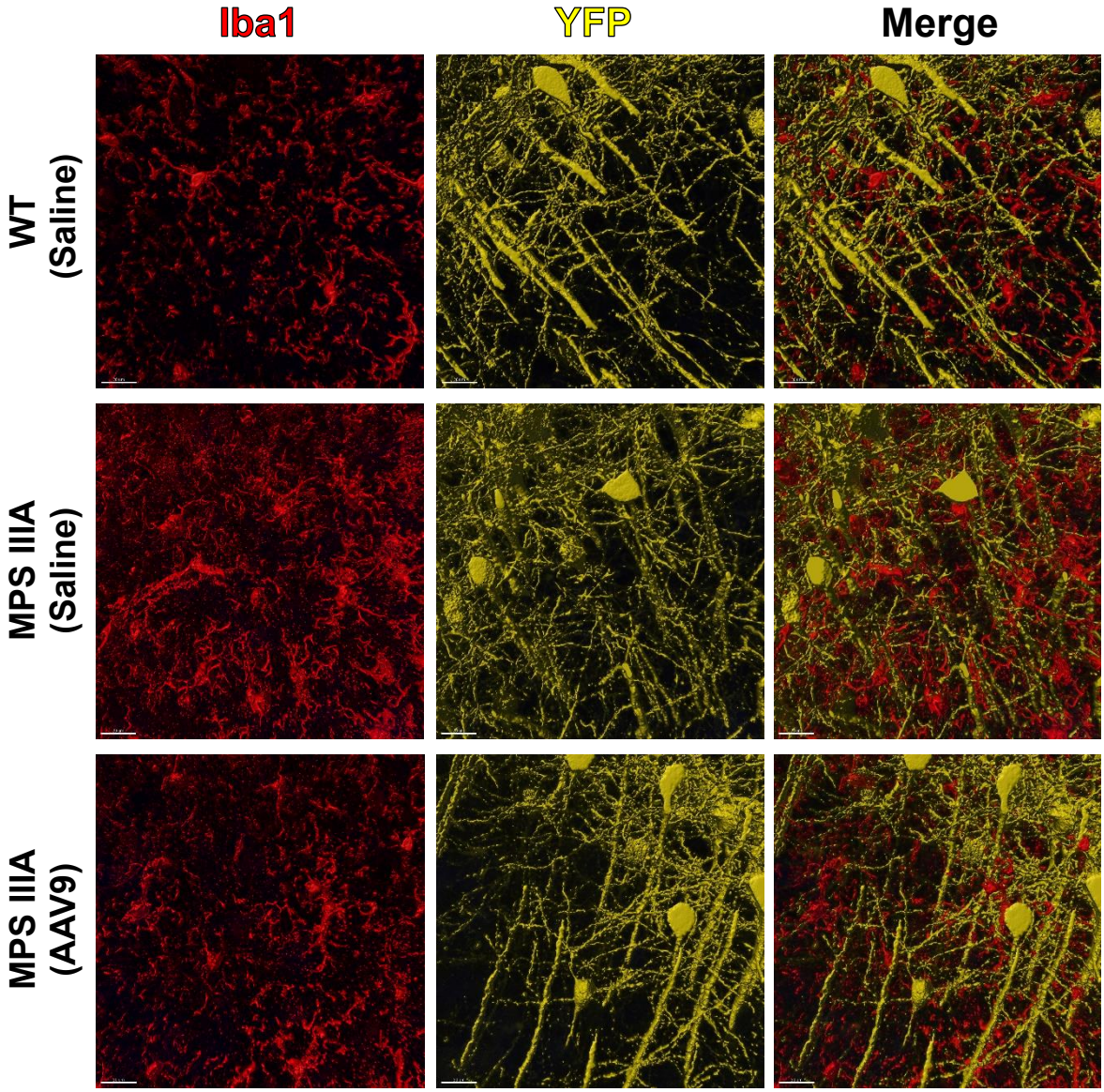


Figure 6.13 – Representative images of microglia apposed to YFP neurons.

Visualisation of microglia apposed to the sites of dendritic spine loss on YFP-positive pyramidal neurons in the cerebral motor cortex of wild-type (WT) (saline), MPS IIIA (saline), and MPS IIIA (AAV9-*SGSH*) mice at 20-weeks of age. Scale bar is 20µm.

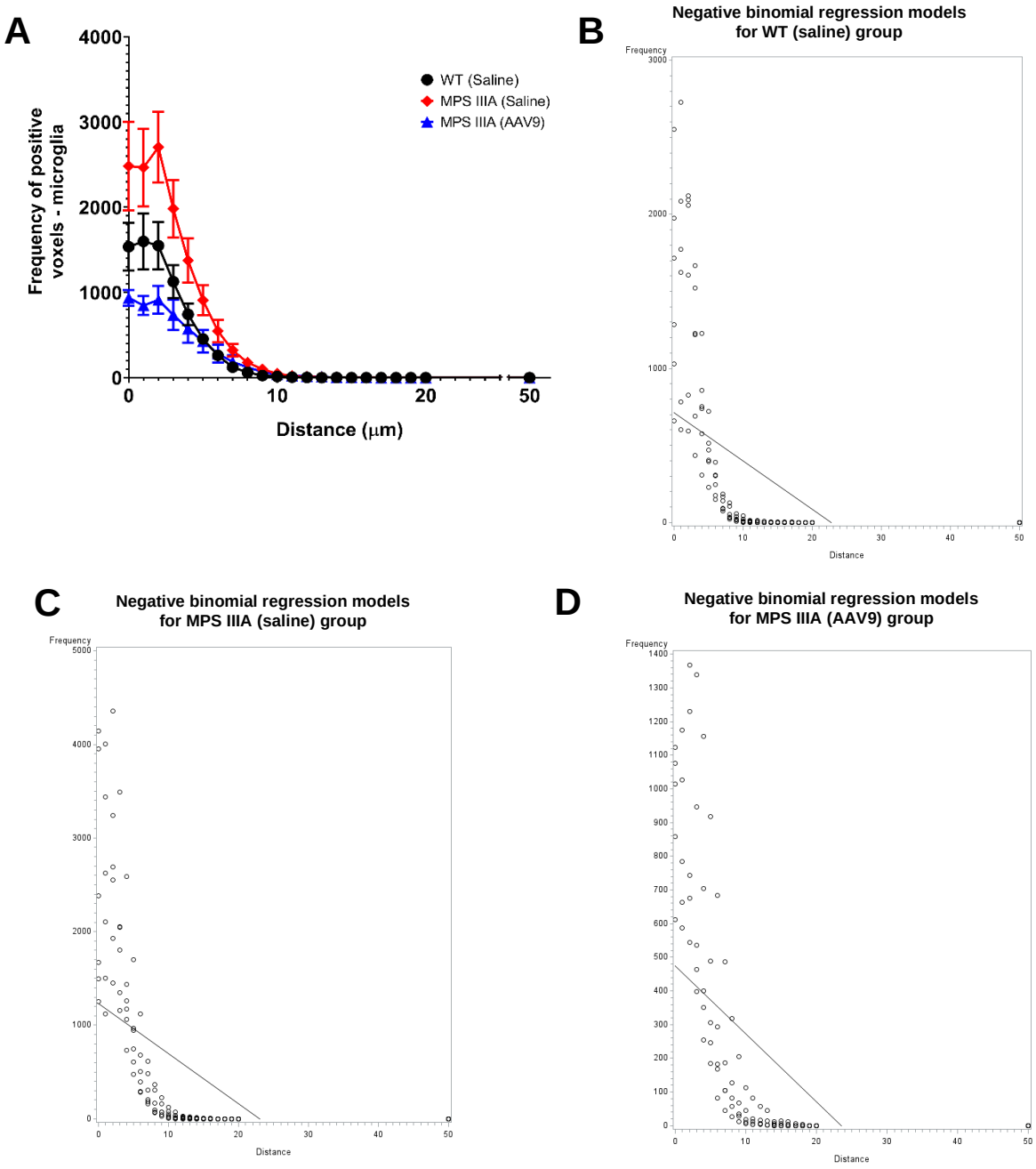


Figure 6.14 –Apposition of microglia to YFP neurons following treatment. The abundance and proximity of Iba1-positive cells apposed to sites of dendritic spine loss on YFP-positive pyramidal neurons in the cerebral motor cortex of wild-type (WT) (saline), MPS IIIA (saline), and MPS IIIA (AAV9-*SGSH*) mice at 20-weeks of age (A). For statistical analysis, the data were transformed to negative binomial regression models for WT (saline) (B), MPS IIIA (saline) (C) and MPS IIIA (AAV9-*SGSH*) (D) groups. N=5 to 6 animals per genotype per age. Data are mean ± SEM.

every unit increase in distance, whilst the MPS IIIA (AAV9-*SGSH*) mice showed the lowest decrease in frequency (36%) with every unit increase in distance away from the nearest YFP-positive voxel. The difference in decreasing frequency between wild-type and MPS IIIA (saline) mice was only 2% and not significant ($p>0.05$), indicating that although Iba1 levels were higher in MPS IIIA (saline), the number of Iba1-positive voxels declined in frequency at similar rates away from the nearest YFP-positive voxel. This suggests that the proportion of microglia apposed to neurons within each group was similar at this point, but there were more Iba1-positive microglia apposed to the YFP-positive neurons in MPS IIIA (saline) compared with the wild-type mice. The comparison between wild-type and MPS IIIA (AAV9-*SGSH*) mice was significantly different, however, with a decreasing frequency rate of 14% per micrometre in the MPS IIIA (AAV9-*SGSH*) mice ($p<0.0001$). This is illustrated in Figure 6.14A, which shows the wild-type group had a sharper declining slope due to the higher Iba1-positive voxel mean at 1-2µm distance from the nearest YFP-positive voxel. The AAV9-*SGSH*-treated MPS IIIA mice maintained the lower decreasing frequency rate, but by 11%, when compared to the MPS IIIA (saline) mice ($p<0.0001$). Similar with wild-type mice, this was due to the higher microglial mean at 2µm, and a subsequent sharply declining slope in the MPS IIIA (saline) group. Overall, the association between microglial frequency and YFP-positive distance was significantly different between treatment groups ($p<0.0001$).

The same method of rendering was applied to the activated astrocytes to determine their level of apposition to YFP-positive neurons suffering synaptic loss in the mouse motor cortex. Representative images of the astrocytic and neuronal models generated across the treatment groups are demonstrated in Figure 6.15. Using the ‘distance between surfaces’ feature of the Imaris software, proximity was measured between a GFAP-positive voxel and the closest YFP-positive voxel. The frequency of all GFAP-positive voxels was

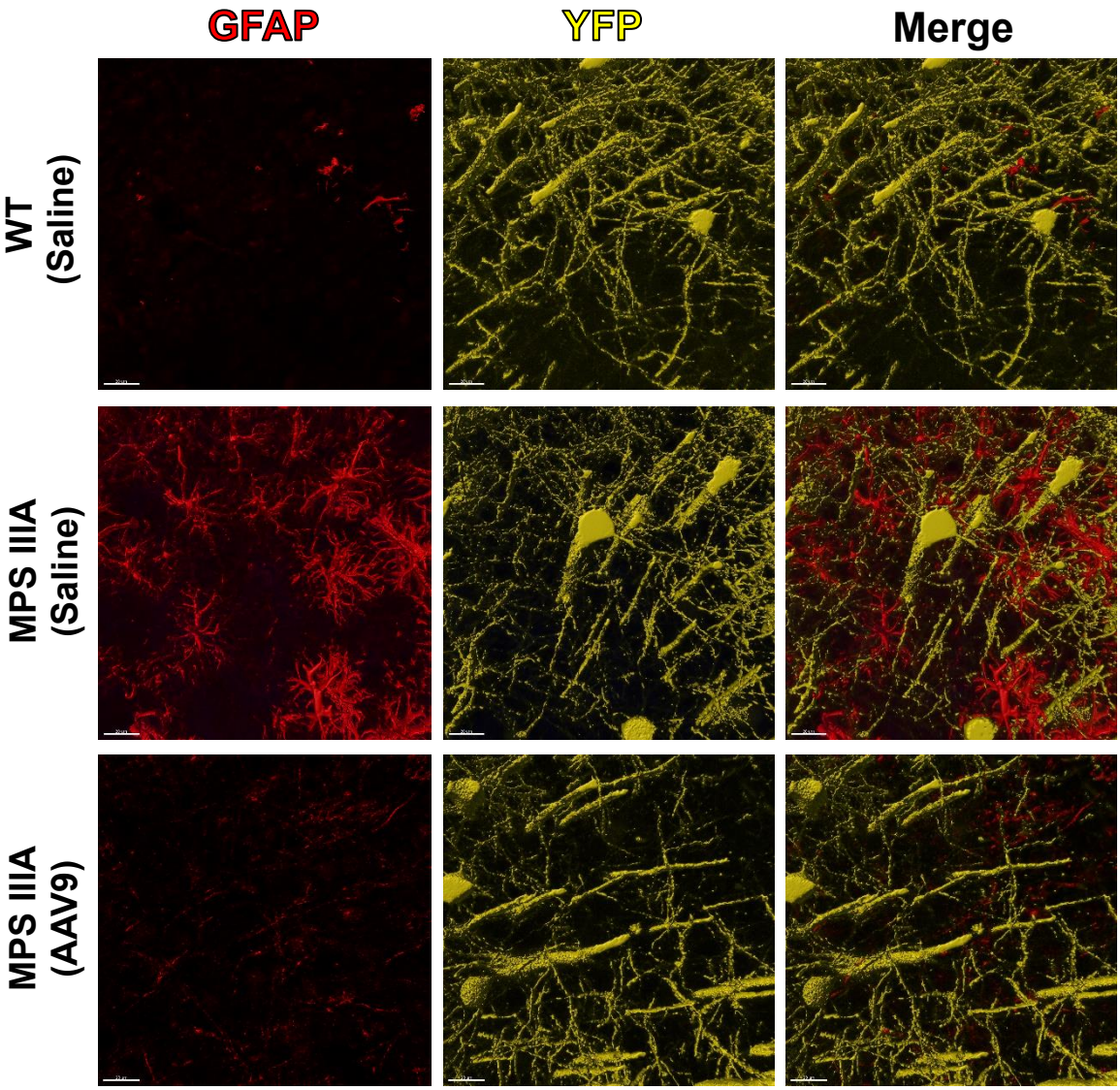


Figure 6.15 – Representative images of astrocytes apposed to YFP neurons.

Visualisation of astrocytes apposed to the sites of dendritic spine loss on YFP-positive pyramidal neurons in the cerebral motor cortex of wild-type (WT) (saline), MPS IIIA (saline), and MPS IIIA (AAV9-*SGSH*) mice at 20-weeks of age. Scale bar is 25µm.

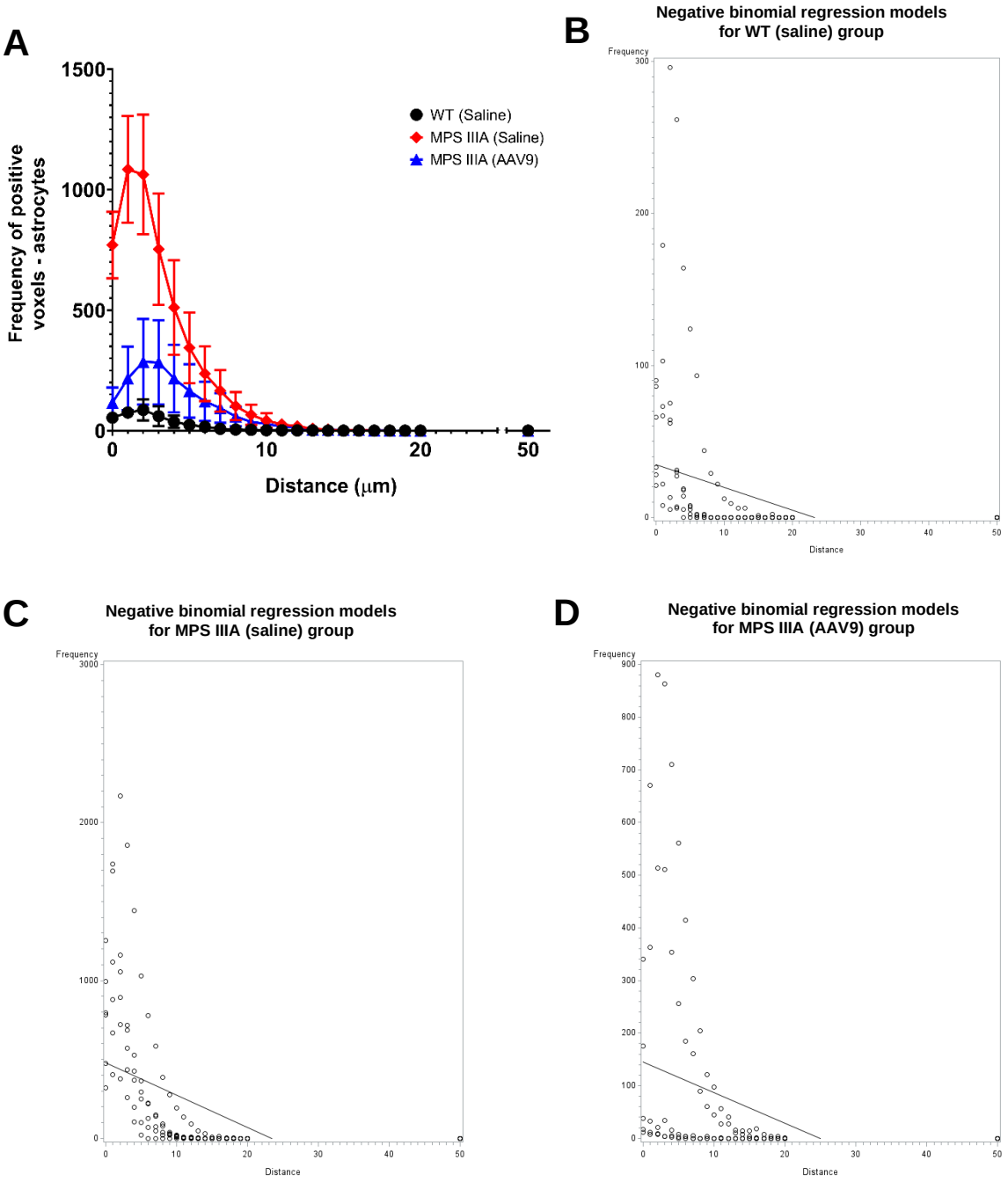


Figure 6.16 – Apposition of astrocytes to YFP neurons following treatment. The abundance and proximity of astrocytes apposed to sites of dendritic spine loss on YFP-positive pyramidal neurons in the cerebral motor cortex of wild-type (WT) (saline), MPS IIIA (saline), and MPS IIIA (AAV9-*SGSH*) mice at 20-weeks of age (A). For statistical analysis, the data were transformed to negative binomial regression models for WT (saline) (B), MPS IIIA (saline) (C) and MPS IIIA (AAV9-*SGSH*) (D) groups. N=5 to 6 animals per genotype per age. Data are mean ± SEM.

accumulated and recorded for each mouse across all groups, with the mean of all mice for each micrometre increment shown (Fig 6.16A). The raw output showed that the highest number of GFAP-positive voxels with the closest apposition to dendrites of ≤ 2μm was in the MPS IIIA (saline) mice at 20-weeks of age (Fig 6.16A). The MPS IIIA (AAV9-*SGSH*) mice were found to have the next highest level of astrocytic apposition to neurons, followed by the wild-type (saline) group with the lowest level of astrocytic apposition to the YFP neurons at distances of ≤ 2μm (Fig 6.16A).

Consistent with the microglial models, the astrocyte models were transformed into negative binomial regression models for the wild-type (saline) (Fig 6.16B), MPS IIIA (saline) (Fig 6.16C), and MPS IIIA (AAV9-*SGSH*) mice (Fig 6.16D). Statistical outputs are provided in Appendix 4. The association between frequency and distance for each treatment and genotype group was assessed at 20-weeks of age, and interaction p-values were generated. The initial interaction model determined the association between distance and treatment group for the outcome frequency and was found to be not statistically significant ($p>0.05$). This indicated that the rates of decreasing frequency for GFAP-positive voxels away from the nearest YFP-positive voxel were similar between groups. Therefore, a subsequent 'main effects only' model was performed to compare voxel frequency between treatment groups, which found a statistically significant association between frequency and distance when adjusting for treatment group ($p<0.0001$), and between frequency and group when adjusting for distance ($p<0.0001$). Collectively, these associations showed that for every one-micrometre increase in distance, the frequency rate decreased by 35%. Assessment of comparisons between the individual treatment groups showed that wild-type (saline) mice had the lowest astrocytic apposition to neurons; MPS IIIA (saline) mice had a comparatively higher frequency rate of 93% more than the wild-type (saline) mice, and the MPS IIIA (AAV9-*SGSH*) mice had a frequency rate of 90%

more (due to the relatively higher mean compared with the wild-type mice; Fig 6.16A). Thus, the proportion of reactive astrocytes apposed to neurons in the MPS IIIA sub-groups were similar but the number of reactive astrocytes in the MPS IIIA (saline) group was greater compared with the MPS IIIA (AAV9-*SGSH*) mice. This is further illustrated in Figure 6.16A, where the wild-type mice had the lowest frequency mean, particularly at distances of 0-2µm from the nearest neuron. Whilst the MPS IIIA (AAV9-*SGSH*) mice had a reduced frequency rate of 42% compared with the MPS IIIA (saline) mice, this comparison was not statistically significant ($p>0.05$).

6.3 Discussion

The mechanistic basis for neurodegenerative changes and symptom onset in MPS III is presently unknown; similarly, it is not known whether gene therapies that are currently in trial are effectively targeting potential mechanisms contributing to symptom onset. As previously described, gene therapy is an emerging strategy to combat CNS pathology in LSDs, with multiple AAV serotypes proving most effective at transducing CNS cells, including neurons and astrocytes (Bevan et al., 2011; Green et al., 2016). Whilst assessments of overall cognitive behavioural changes from AAV9 in MPS IIIA models have taken place (Ruzo et al., 2012; Haurigot et al., 2013; Fu et al., 2016), investigation into synaptic changes is lacking. Therefore, the experiments in this Chapter sought to assess the impact of a clinically relevant gene therapy on the observed synaptic and inflammatory changes in MPS IIIA mice and to determine its efficacy as a preventative measure. In this study, administration of AAV9-*SGSH* gene therapy at birth to MPS IIIA mice reduced the activation of pro-inflammatory glial cells, which may have prevented or delayed dendritic spine loss at a late-symptomatic stage of disease.

The primary finding of this study was a reduction in dendritic spine density loss for immature and mature sub-types in AAV9-*SGSH*-treated MPS IIIA mice at pre- and late-symptomatic disease stages. However, not all mice maintained the AAV9-*SGSH* treatment effect until 20-weeks of age. These mice presented with consistently lower dendritic spine densities across multiple morphologies, which may have occurred as a result of insufficient treatment. Studies with longer timeframes are required to determine whether these observations continue to trend down, and thus confirm the effect of AAV9-*SGSH* on preventing spine loss. Overall, however, the trends were repeated and differences in

dendritic spine densities were replicated between genotypes when comparing with the genotypes at ages of 20-weeks (discussed in Chapter 3).

To our knowledge, this is the first assessment of dendritic spine morphology combined with density following gene therapy in any of the mucopolysaccharide disorders. Most recently, the study by de Aragao and colleagues (2020) assessed the effect of AAV9-*HGSNAT* on PSD95-positive puncta following administration of gene therapy to MPS IIIC mice at eight-weeks of age. They reported a minor rescue in puncta levels compared with wild-type mice six-months post-treatment but did not assess morphological changes to dendritic spines over sequential timepoints.

Further to this *in vitro* work, a recent *in vivo* study assessed lysosomal dysfunction on dendritic spine density in another working mouse model of a lysosomal storage disorder – CLN6-Batten disease (Cain et al., 2019). Moreover, they assessed a gene therapy using self-complementary AAV9 expressing human *CLN6* with a chicken β-actin promoter (scAAV9-CB-*CLN6*) for its ability to prevent dendritic spine loss observed in that disorder. Similar with our study, intraventricular injections were administered to the mouse pups at birth, and subsequent quantification of dendritic spines occurred at two-months of age. Although limited to a Golgi stain of neurons, Cain et al. (2019) observed that total dendritic spine density in the cortex was normalised in the scAAV9-CB-*CLN6*-treated group at a time when CLN6 protein was normally expressed along with reduced levels of autofluorescent storage material – a hallmark of Batten disease. Taken together, these findings, in combination with this study, suggest that accumulation of substrate within the lysosomes of CNS neurons affects local synaptic plasticity, thus underlying the neurological symptoms of LSDs.

The other significant finding in this Chapter was the reduced levels of inflammatory markers and conversion of A1-type astrocytes, and the reduction of pro-inflammatory glial cell apposition to dendritic spines in the motor cortical region of AAV9-*SGSH*-treated MPS IIIA mice by late-symptomatic disease. As discussed in Chapter 4, the higher expression of inflammatory complement markers and A1 reactive astrocytes, in combination with the increased presence of glia at the synapse, leads to increased synaptic pruning and symptom progression in neurological disease (Stevens et al., 2007; Schafer et al., 2012; Liddelow et al., 2017; Kavetsky et al., 2019). Indeed, CNS inflammation is a hallmark of MPS III, amelioration of which is used as a measure of therapeutic efficacy. Intravenous injection of AAV9-*NAGLU* to MPS IIIB mice was shown to reduce the number of activated astrocytes (via anti-GFAP) in multiple brain areas, including the cortex, striatum, thalamus, and brainstem (Fu et al., 2011). These observations were recorded six-months after injection of AAV9-*NAGLU*, which was a similar post-injection time-point to this study. However, their injections were administered at four- to six-weeks of age, and not at Day 0, as it was done in this study. Regardless, their therapy was still administered pre-symptomatically and it showed the AAV9 vector was effective at producing NAGLU enzyme, which degraded the stored HS within CNS tissues of MPS IIIB mice and prevented astrocyte activation from occurring six-months later.

Assessment of corrected astrocyte activation in the cerebral cortex also occurred via intravenous injection of an AAV9 vector in the MPS IIIA mouse encoding for SGSH (Ruzo et al., 2012; Haurigot et al., 2013). AAV9-*SGSH* was administered at two-months of age in both studies, and assessments of astrocytosis occurred at four-months (Haurigot et al., 2013) or eight-months post-injection (Ruzo et al., 2012). More recently, AAV9-*SGSH* was intravenously injected into one-month-old MPS IIIA mice and assessed for astrocytosis correction seven-months later **(**Fu et al., 2016): correction of astrocytosis was

reported in the cerebral cortex in addition to the hippocampus, brainstem, and spinal cord. A recent study of AAV9-*IDS* treatment to the MPS II mouse via intra-CSF delivery delved into its ability to correct both astrocytosis and inflammatory cytokine levels (Motas et al., 2016). Treatment of the MPS II mice occurred at two-months of age, and measures of inflammatory response occurred at six-months of age. Assessment occurred via microarray expression, with genetic profiling for each treatment group showing a correction of multiple inflammatory genes. Whilst protein levels were not measured, gene expression was notably improved for *C1qa*, *C1qb, C1qc, C3ar1, Gfap,* and *C4b* (Motas et al., 2016).

This study's findings verify and expand on those data and indicate - for the first time - that altered complement genetic expression is translated to the protein level and is corrected via treatment with AAV9-*SGSH* in the MPS IIIA mouse. The complement cascade is possibly implicated in multiple mucopolysaccharide disorders, along with A1-type astrocytosis, and could be reduced with AAV9 treatment. As discussed previously, microglial apposition to neurons prior to cellular loss has also been observed in Niemann Pick disease type C mice (Kavetsky et al., 2019). Our data also indicate that highly activated A1 astrocytes and microglia reported in other brain regions and other models of the mucopolysaccharidoses trigger synaptic pruning. Therefore, pre-symptomatic AAV9-*SGSH* treatment appears to reduce over-active pruning that could potentially underlie symptom development and disease progression.

A notable finding from this study was its failure to find many conclusive corrections of behavioural phenotypes in the AAV9-*SGSH*-treated mice. Whilst there were greater differences between the means of AAV9-*SGSH*-treated MPS IIIA and vehicle-treated wild-type mice with vehicle-treated MPS IIIA mice in the 20-week motor behavioural tests compared with the 15-week open-field test, the only calculated statistical significance was

between the vehicle-treated wild-type and MPS IIIA groups. Despite no significant differences between the wild-type and the AAV9-*SGSH*-treated MPS IIIA mice in any of the behavioural tests, there were also no differences between the AAV9-*SGSH* and vehicle-treated MPS IIIA mice. AAV9 has been proven an effective tool for correcting behavioural phenotypes in MPS mice when administered pre-symptomatically (Fu et al., 2011, 2016; Ruzo et al., 2012; Haurigot et al., 2013; Motas et al., 2016), thus phenotype corrections were expected in this study. However, as the study was under-powered due to cannibalisation of the mouse pups, this outcome is not surprising.

Yet, by identifying the remaining individual mice within the graphical outputs, some behavioural data could be salvaged and used to investigate any trends across datasets from behavioural through to histological. The treated mice that underwent behavioural testing and subsequent histological assessment were identified, with their corresponding symbols provided in Appendix 5. Thus, whilst we did not retain the power to obtain statistically significant results for most of the behavioural testing, individual mice could be traced from the behaviour tests through their corresponding histological outputs. This permitted expansion of the conclusions able to be drawn in this and previous chapters, and direct correlations to be made between inflammatory levels to dendritic spine densities, and the subsequent impact on phenotypic motor function in behavioural assays for separate mice.

Despite these promising findings, this method of assessment required tissue collection and was thus a ‘snap-shot’ in time. Therefore, assessment of synaptic status and glial pruning could occur only once. Whilst tissue was collected at six- and 15-weeks for multiple time-points, time constraints limited analysis. Moreover, the mice from which tissue was collected did not undergo behavioural testing, and thus the same correlations could not be inferred from these mice as those assessed at 20-weeks. Therefore, future studies could

expand upon these findings and utilise the method of *in vivo* imaging, such as the technique of a cranial window (Trachtenberg et al., 2002), to assess dendritic spine plasticity at repeated time-points. This would permit continued monitoring of dendritic spine changes over the disease course, including during and following behavioural testing.

Lastly, as with other assessments of AAV9 gene-based treatment in LSDs, in this study treatment was administered pre-symptomatically. Whilst it is possible to suggest that AAV9-*SGSH* treatment potentially reduced inflammatory-mediated synaptic pruning leading to dendritic spine loss in MPS IIIA, these findings are primarily valuable to early intervention and early diagnosis. Therefore, further investigation is needed to determine the effect of AAV9-*SGSH* on reversing dendritic spine loss when changes and symptoms are established, and thus more readily benefit MPS IIIA children who are diagnosed later in life.

6.4 Conclusion

In summary, this study has shown - for the first time - how AAV9-*SGSH* improves the MPS IIIA phenotype by preserving normal neuronal architecture at the synaptic level within the motor cortex. The study showed that early intervention reduced dendritic spine loss at a pre-symptomatic age, a benefit which persisted to a late-symptomatic age. The study also showed that early intervention prevented (or delayed) the conversion of astrocytes to an A1 phenotype, with reduced overall expression of pro-inflammatory markers. Lastly, it also found that pre-symptomatic treatment of AAV9-*SGSH* reduced the apposition of activated glia to synaptic sites in the motor cortex. Ultimately, these data infer that pre-symptomatic AAV9-*SGSH* treatment to MPS IIIA mice is effective at improving motor function by reducing over-pruning of dendritic spines via restoration of lysosomal function and reductions in neurotoxic glial cells. Based on these findings, future testing of therapeutic function and efficacy could include reversibility effects, with live *in vivo* imaging. Considering the role of the inflammatory mechanism, targeted anti-inflammatories should also be considered in LSDs to supplement genetic therapy.

– CHAPTER 7 –

DISCUSSION AND FUTURE WORK

7.1 Project Significance

Despite extensive investigations into the clinical course of MPS III and evaluation of multiple treatment strategies, disease pathogenesis is presently not well understood, and the precise molecular basis of cognitive impairment and symptom generation is unclear. Symptom generation and progression without significant brain atrophy has suggested the disease may be caused by changes to the functional component of neurons themselves – the synapse. Indeed, recent studies are beginning to show the presence of changes to the composition, structure, and function of the pre- and post-synapse (Keating et al., 2012; Wilkinson et al., 2012; Dwyer et al., 2017; Sambri et al., 2017; de Aragao et al., 2020).

The aim of this study was to explore synaptic morphology and function in MPS III, a paediatric-onset neurodegenerative lysosomal storage disorder. The overarching hypothesis was that changes in synaptic morphology and function underlie neurological decline, and they can be prevented by gene therapy.

This study utilised an MPS IIIA mouse model to determine (i) whether there were changes at the synaptic level on neurons within the motor cortex over time, (ii) whether synaptic abnormalities resulted in abnormal neuronal function, (iii) possible mechanisms contributing to synaptic abnormalities, and (iv) whether they could be prevented by AAV9-*SGSH* gene therapy.

7.2 Outcomes, Limitations and Future Directions

The density and morphology of dendritic spines in the MPS IIIA mouse motor cortex were examined with disease progression from pre- to late-stage symptomatic. This is the first investigation of its type in any mucopolysaccharide disorder model, to the best of our knowledge. The study showed that dendritic spine deficiencies develop from a pre-symptomatic age and persist with disease progression. Therefore, MPS IIIA motor cortical neurons potentially have a reduced excitatory functionality due to reduced excitatory signal output (Arellano et al., 2007). These changes may be contributing to symptom onset and could help explain the neurological decline associated with MPS IIIA without significant neuronal loss. Moreover, our findings suggest that novel biomarkers monitoring synaptic and inflammatory changes may be representative of disease progression and treatment efficacy. Interestingly, a recent study using a radioligand bound to ubiquitously expressed synaptic vesicle glycoprotein 2A in neurons could visualise synaptic density in human patients *in vivo* with positron emission tomography (Cai et al., 2019). This technique has been successfully tested in humans with Alzheimer's and Parkinson's diseases, and epilepsy (Cai et al., 2019), and could potentially be utilised as a prognostic tool for MPS IIIA patients.

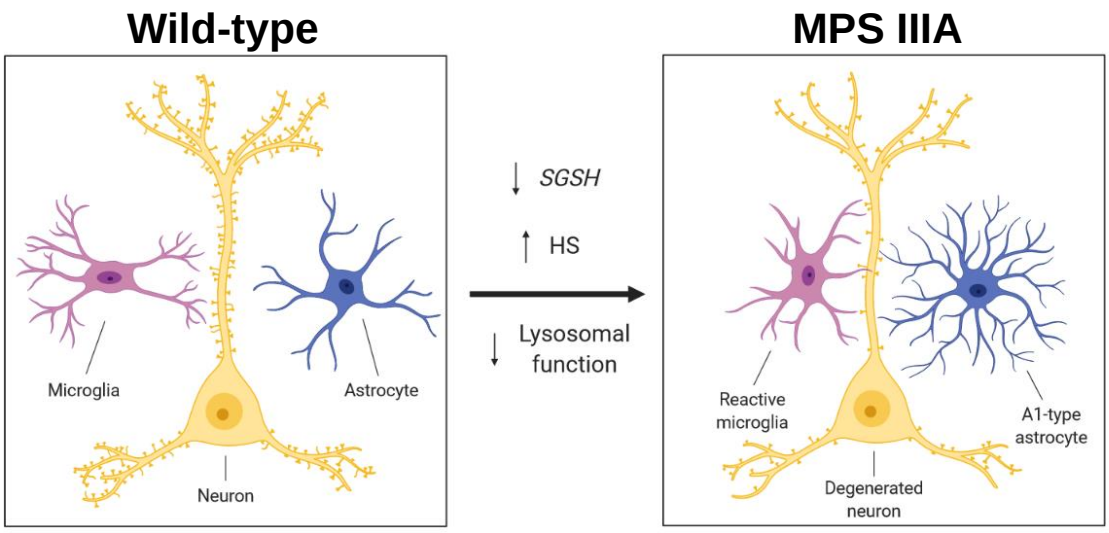
As described, pre-synaptic characteristics have previously been investigated in MPS IIIA mice. Temporally correlating with our observations at five-months of age (late symptomatic), HS accumulation reduced the frequency of synaptic vesicle release in MPS IIIA mouse chromaffin cells (Keating et al., 2012). Moreover, cortical and pyramidal hippocampal neurons of the CA1 region showed synaptic vesicle numbers were reduced from six-months of age in MPS IIIA mice (Sambri et al., 2017). However, this did not translate to changes in synaptic density. More recently, synaptic vesicle transport was

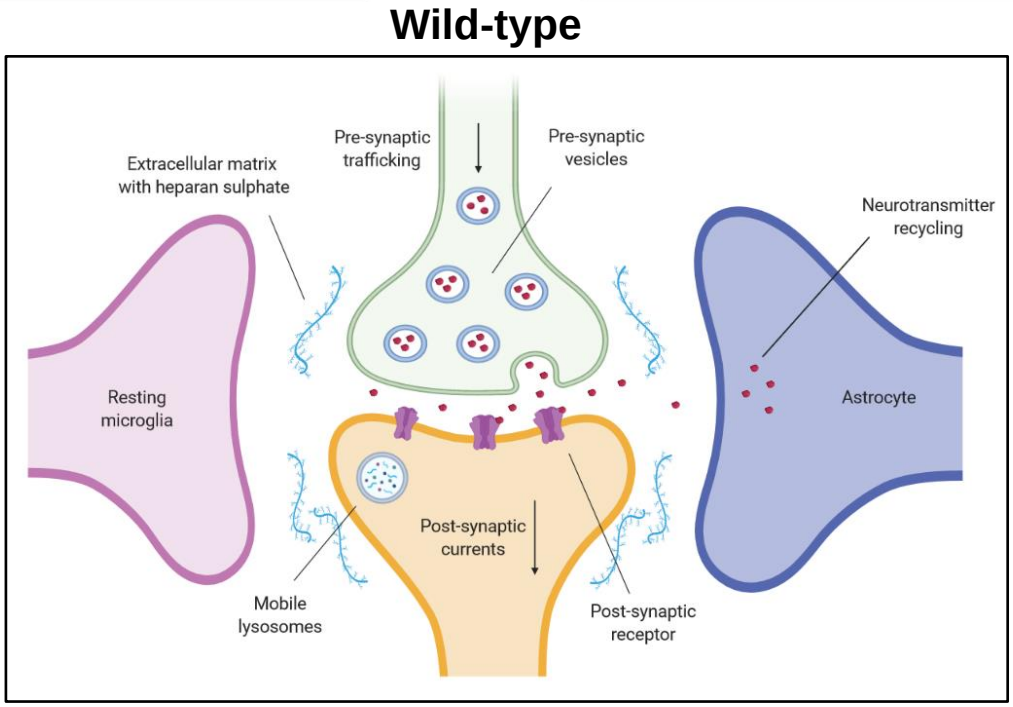
shown to be impaired in MPS IIIC mouse hippocampal neurons, indicative of the impact of lysosomal dysfunction on trafficking to and from the pre- and post-synapse (de Aragao et al., 2020). One novel aspect of the present study was that the investigation focused on the motor cortex of MPS IIIA mice, evaluations of which are currently lacking in the literature despite the presence of motor symptoms in this disorder (Hemsley and Hopwood, 2005; Crawley et al., 2006). Future work should therefore evaluate pre-synaptic functions of neurons synapsing in the motor cortex and expand to other brain regions. This could potentially correlate the role of impaired pre-synaptic transmission with post-synaptic functionality and plasticity, and thus confirm whether reduced signal input, output, or both, are contributing to MPS IIIA neurological symptoms.

The data from studies outlined in Chapter 4 indicated that the post-synaptic changes resulted in abnormal neuronal function in MPS IIIA motor cortical pyramidal neurons in layer 5, with reduced mEPSC activity and kinetics, but no change in action potential kinetics observed from a pre-symptomatic age in neurons exhibiting synaptic loss. The reduction in mEPSC event frequency correlates with the findings of reduced dendritic spine numbers, indicating fewer spines cause fewer post-synaptic events. The reduction in maximum amplitude of the elicited events in MPS IIIA neurons also suggests impaired function of the pre- and/or post-synapse. Lysosomes have been shown to transport synaptic proteins in *in vitro* neuronal models, and lysosomal inhibition reduces movement of lysosomes along dendrites and impairs their recruitment to the spine head (Goo et al., 2017; Padamsey et al., 2017a). These same findings also indicated that trafficking of lysosomes correlates with post-synaptic excitatory AMPARs (Goo et al., 2017), which could be contributing to the reduced mEPSC recordings reported in Goo et al. (2017) and this study. This has been further highlighted in hippocampal neurons from a mouse model of MPS IIIC at eight-weeks of age, wherein abnormal motility of synaptic vesicles was shown to correlate with reduced mEPSC recordings (de Aragao et al., 2020).

When assessing neuronal function, it is important to consider all components of the neuronal synapse. As indicated by Schafer et al. (2013), communication throughout the synapse involves not only the pre- and post-synapse of neurons, but also astrocytes and microglia to create the quad-partite synapse. At excitatory synapses, the primary neurotransmitter, glutamate, is released into the synaptic cleft by the pre-synapse, activates the post-synapse, and leaves the remaining glutamate to be taken-up by the astrocytic component of the synapse to terminate the neurotransmitter signal (Danbolt, 2001; Dong et al., 2018). The glutamate absorbed by healthy astrocytes is converted to glutamine and transported out of the astrocytes back into the pre-synaptic neuron, maintaining the supply of pre-synaptic neurotransmitter and sustaining excitatory communication (Billups et al., 2013; Tani et al., 2014; Marx et al., 2015). The main function of microglia at the synapse is to monitor synaptic connections and to remove unwanted or dysfunctional synapses as mediated by the pro-inflammatory response in coordination with astrocytes (Stevens et al., 2007; Schafer et al., 2012; Gabande-Rodriguez et al., 2020; Klein, 2020). Further development of this quad-partite synaptic model has since included the extracellular matrix, which engulfs synapses and forms net-like structures to provide structural support to what is now termed the 'tetrapartite synapse' (Lepeta et al., 2016).

As discussed, extensive evaluation of the pre-synapse has been reported in models of MPS III, and the findings in Chapter 5 contribute to understanding the role and impact of the post-synapse in MPS IIIA. To that body of research we now add observations of abnormal activity and localisation of microglia and toxic A1 astrocytes to sites of post-synaptic loss in this disorder. Collectively, this helps to build a model of the MPS IIIA 'tetrapartite synapse' and suggests multiple factors could be contributing to symptom onset and disease progression (as depicted in Fig 7.1). Initially, there is reduced pre-synaptic vesicle density and neurotransmitter release in MPS IIIA with immobile lysosomes unable to maintain


Wild-type
MPS IIIA
SGSH
HS
Lysosomal function
Microglia
Astrocyte
Neuron
Reactive microglia
A1-type astrocyte
Degenerated neuron


Wild-type
Extracellular matrix with heparan sulphate
Pre-synaptic trafficking
Pre-synaptic vesicles
Neurotransmitter recycling
Resting microglia
Astrocyte
Post-synaptic currents
Mobile lysosomes
Post-synaptic receptor

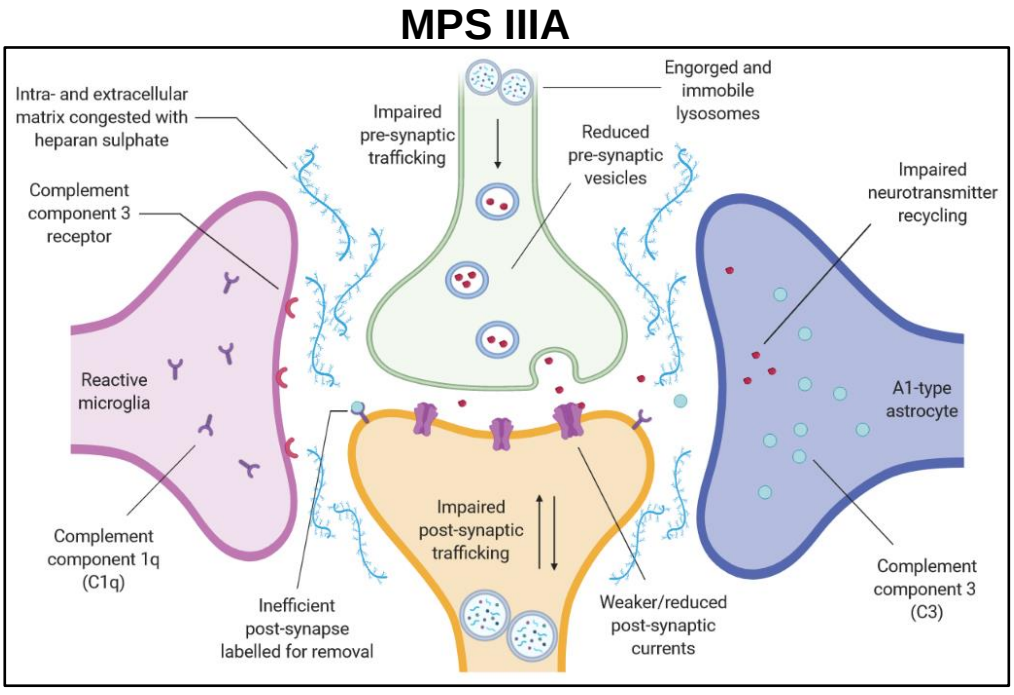

MPS IIIA
Intra- and extracellular matrix congested with heparan sulphate
Engorged and immobile lysosomes
Impaired pre-synaptic trafficking
Reduced pre-synaptic vesicles
Complement component 3 receptor
Impaired neurotransmitter recycling
Reactive microglia
A1-type astrocyte
Impaired post-synaptic trafficking
Complement component 1q (C1q)
Inefficient post-synapse labelled for removal
Weaker/reduced post-synaptic currents
Complement component 3 (C3)

Figure 7.1 – Proposed neurological basis for symptom development in MPS IIIA. The schematic evolved from this study and the existing literature, and proposes the impact of neuropathology on disease pathogenesis in MPS IIIA at the tetrapartite synapse. The multi-factor proposal of substrate accumulation, pre-synaptic dysfunction, and complement-mediated glial activation leads to post-synaptic loss, neuronal dysfunction, and subsequent symptom development. As substrate increases over time due to prolonged lysosomal dysfunction, the process intensifies and exacerbates symptoms. (Created with BioRender.com).

surface receptors; secondly, the increased presence of A1 toxic astrocytes is highly apposed to the synapse in MPS IIIA as a result of the impaired synapse; and, finally, the reactive astrocytes are impaired in their ability to recycle neurotransmitters to the pre-synapse, in addition to an increased level of synaptic pruning by the neighbouring microglia, which ultimately results in reduced post-synaptic currents due to overall reduced transmitter levels and dendritic spines.

The A1-type astrocytes were highly prevalent in the MPS IIIA mouse motor cortex from three-weeks of age; indeed, to our knowledge this was the first assessment of these astrocytes in any LSD. These cells have been associated with higher expression of inflammatory complement components which bind to and identify synapses for removal by microglia (Li and Barres, 2018; Liddelow and Barres, 2017; Li et al., 2019). As illustrated in Figure 7.1, the presence of pro-inflammatory glial cells at the tetrapartite synapse are potential mediators of synaptic plasticity and function, which reduces the efficacy of the pre- and post-synapse. Therefore, findings from this study support existing knowledge about activated glia throughout the MPS IIIA brain by identifying astrocytic phenotypes, and suggest an over-active pruning mechanism at the synaptic level could be contributing to the observed post-synaptic loss via pro-inflammatory marker expression.

Indeed, an enhanced or pathological pruning process has been implicated in other neurodegenerative diseases (Stevens et al., 2007; Liddelow et al., 2017; Sellgren et al., 2019; Hammond et al., 2020). Moreover, microglia have been characterised in neurodegenerative disease progression and shown to induce further neuronal degeneration by phagocytosing neuronal material, including synapses, axons, and dendrites (Vilalta and Brown, 2018; Deczkowska et al., 2018). Interestingly, the proximity of microglia to neurons was recorded in Niemann Pick disease type C prior to cellular loss (Kavetsky et

al., 2019). Additionally, the electron micrographs in that study qualitatively illustrated engulfment of synaptic material within microglial processes and abnormal morphologies of pre-synapses. Moreover, recent evidence suggests that assessments could utilise light sheet fluorescent microscopy on labelled microglia and neurons within *ex vivo* brain slice cultures to provide the capacity to monitor the dynamic microglia-synapse interactions in real-time and over a time course (Weinhard et al., 2018). Therefore, whilst this study examined elevated pro-inflammatory marker expression and proximity of neurotoxic glial cells to sites of post-synaptic loss, further investigation is required, potentially with the methods discussed above to confirm the postulated phagocytic effects of microglia in MPS IIIA.

Alternatively (or additionally), as HSPGs are an important component of the extracellular matrix, the glial cells could be attempting to remove excess HS (Fig. 7.1), which has been implicated in CNS injury and disease (Higginson et al., 2012). Furthermore, abnormal HSPGs in the extracellular matrix around synapses may be dysregulating synaptic development and function, triggering mediation by glial cells (Barros et al., 2011; Qin et al., 2014; Condomitti and de Wit, 2018). Incidentally, matrix metalloproteinases are enzymes which modify the extracellular matrix and, interestingly, have also been reported to affect remodelling of the extracellular matrix and subsequent dendritic spine growth through lysosomal inhibition (Padamsey et al., 2017a).

Furthermore, these findings highlight the importance of a functional lysosome for synaptic structure and function in MPS IIIA, and should be investigated further in future studies, particularly utilising *ex vivo* models, as done in the electrophysiological part of this study. The significant advantage of *ex vivo* brain slices compared with *in vitro* models is that they are more representative of the *in vivo* environment (Cho et al., 2007). *Ex vivo* slices

preserve the architecture of the cellular networks and local synaptic circuitry and provide a more physiologically relevant three-dimensional representation of the brain. This is especially important when considering that multi-cellular populations contribute to the development and progression of symptoms in neurodegenerative diseases (Croft et al., 2019). In addition to electrophysiological experiments, *ex vivo* models should also be considered through use of organotypic brain slice cultures when investigating the molecular mechanisms in neurological conditions, such as visualising synaptic vesicle transport pathways and time-courses of synaptic pruning (Noraberg et al., 2005; Croft et al., 2019).

A secondary finding arising from this study were the observations of differences between females and males found in both the wild-type and MPS IIIA groups, which had not been previously addressed for any brain region in MPS IIIA or any other LSD model. Whilst it remains a preliminary finding as the study was not designed to account for sex of the mice, it is interesting to note the consistent appearance of sex-dependent impacts on the findings throughout this thesis. As discussed in Chapter 3, in combination with environmental factors, sex may have contributed to the statistically non-significant findings for dendritic spine density at 12-weeks of age. Sex-dependent changes in morphology may also elicit an impact on function, as discussed in Chapter 4, where differences between male and female mice could be seen across multiple electrophysiological properties. The effects of gonadal hormones on brain structure and function have in fact been previously investigated throughout both the developing and adult normal mouse and human brains (Luine and Rodriguez, 1994; McEwen and Alves, 1999; Brinton, 2009; Srivastava et al., 2013). Therefore, future studies assessing synaptic properties in animal models of neurological disease and human studies should account for and report sex, and investigate further the role of sex in neurological disease development.

The final component of this study showed that delivering AAV9-*SGSH* gene therapy from birth (pre-symptomatic) prevented/delayed dendritic spine loss in MPS IIIA mice, which persisted through to late-symptomatic disease. This study also showed that early intervention reduced the prevalence of the A1-type reactive astrocyte through to the late-symptomatic stage of 20-weeks, with reduced overall expression of pro-inflammatory markers. Lastly, the study also found that pre-symptomatic treatment with AAV9-*SGSH* reduced the apposition of activated glia to synaptic sites in the motor cortex. Ultimately, these data infer that pre-symptomatic AAV9-*SGSH* treatment is effective at delaying or reducing the severity of neuropathological changes and symptoms in MPS IIIA mice. Potentially, this is the result of reduced over-pruning of post-synaptic dendritic spines via amelioration of lysosomal storage, and reduced neurotoxic glial cells, to at least the late-symptomatic age of 20-weeks.

Yet, studies utilising AAV-based gene therapies still provoke an uncharacterised neuroinflammatory response, which suggests that monitoring of neuroinflammation and/or anti-inflammatory use (in combination with AAV-based gene therapy) is crucial to treatment success and efficacy (Perez et al., 2020). Incidentally, with up-regulation of specific pro-inflammatory markers and suggestive ties to over-pruning of synapses highlighted in this study, anti-inflammatory therapeutics should be particularly investigated for the treatment of mucopolysaccharide and thereby other CNS diseases, including complement-targeted approaches. Indeed, monoclonal antibodies, fusion proteins, and peptidomimetics are some of the latest complement-targeted immunotherapies approved for clinical trial in CNS diseases which have responded poorly to alternative treatments (reviewed in Dalakas et al., 2020).

In fact, early trials in MPS III mice have included anti-inflammatory approaches. Whilst not extensive, tests including aspirin and anakinra have been shown to lower levels of inflammatory cytokines, overall inflammation, oxidative stress, and improve behavioural phenotypes (Arfi et al., 2011; Parker et al., 2020). Targeted anti-inflammatory approaches have also been investigated but not in the LSD field. A gene therapy approach to inhibit C3 at the synapse in mouse models of Alzheimer's disease and multiple sclerosis decreased microglial engulfment of synapses and protected neuronal function (Shi et al., 2017; Werneburg et al., 2020). These data suggest that targeting the complement cascade in MPS IIIA may reduce the impact of over-activated synaptic pruning and potentially reduce cognitive decline. Furthermore, the high abundance of pro-inflammatory markers and reduced synaptic densities in MPS IIIA propose new biomarkers for disease prognosis and treatment efficacy.

In addition to therapeutic strategies, methods for symptom management could potentially be utilised to enhance the treatment effect. Essentially, skill training could improve synaptic plasticity and assist in reducing symptom severity. In relation to motor control, the stabilisation of newly formed dendritic spines in the mouse motor cortex based on sustained motor training has been shown to improve performance on motor skill tests (Clark et al., 2018). Notably, a greater proportion of spines were formed and retained if training extended to 15-days compared with cessation after three-days. Additionally, even in aged wild-type mice, motor skill learning has been shown to improve plasticity in the motor cortex (Tennant et al., 2012). However, training has not been extended to models of neurodegenerative disease. Thus, prolonged training of motor skills in MPS IIIA mice (with or without therapeutic approaches) could potentially reduce the onset or severity of motor skill deficits, and further elucidate the basis of these deficits.

Notably, the mice from which tissues were collected at the earlier time-point of 15-weeks did not undergo components of the behavioural testing, and thus the same correlations could not be inferred as those from the 20-week time-point. Moreover, the behavioural testing occurred within one-day at each time-point, and thus was a measure of motor prowess, and potentially insufficient to affect synaptic plasticity. Therefore, future studies could expand upon these findings and incorporate behavioural skill training to improve synaptic pathology in addition to phenotypic evaluation.

Furthermore, future studies could also utilise the method of *in vivo* imaging to conduct assessments of dendritic spine plasticity at repeated time-points. Utilising two-photon microscopy and a cranial window would permit repeated imaging of the same set of fluorescently-labelled dendritic spines over the time course of disease, in addition to during and after the behavioural testing process (Holtmaat et al., 2005; Nakai et al., 2018). This would overcome the limitations of the 'snap-shot' nature of this study, which does not completely account for the dynamic and plastic nature of dendritic spines. Moreover, this method of assessment would provide the opportunity to assess changes to dendritic spine plasticity in real-time. Potentially, this technique could be combined with therapies and/or symptom management to assess the direct impact on changes to spine plasticity.

As discussed in detail in Chapter 6, a significant limitation to the therapeutic component of this study was the cannibalisation of mice, particularly within the MPS IIIA groups. This severely impacted the power of the behavioural testing and thus limited conclusive assessments of treatment efficacy translating to motor functional testing. Moreover, sample availability was a limiting factor and did not permit electrophysiological assessments on AAV9-*SGSH*-treated mice. Future investigations of AAV9-*SGSH* - and indeed any LSD that assesses the impact on neuronal architecture - should therefore account for an electrophysiological component. This would provide an evaluation of gene therapy on

neuronal functionality at the cellular level as a direct result of altered synaptic properties. Presumptively, as shown in Figure 7.1, if both pre- and post-synaptic integrity is maintained, synaptic function in MPS IIIA would be comparable to wild-type and should be reflected in the electrophysiological data.

In addition, longer-term studies are needed to establish the longevity of the treatment effects reported in this study. Whilst the assessments of treatment efficacy correlated with an age of established symptom onset (Hemsley et al., 2005; Crawley et al., 2006), the continual accumulation of substrate with time exacerbates pathology until end-stage disease. The reported "humane end-point" of disease in MPS IIIA mice is approximately nine-months of age and is at the point where either loss-of-life occurs or symptoms are irreversible (Fu et al., 2016). However, that report showed an increased lifespan and partial correction of symptoms at approximately 17-months of age following treatment with AAV9-*SGSH* in a longevity study. Whilst this would be a desirable time-frame for prolonged testing of treatment efficacy, vehicle or untreated mice would also be required for the same length of time to permit direct comparisons. Maintaining (vehicle-treated) mice up to 17-months may not be ethical given that nine-months has been established as the humane end-point. Therefore, whilst extending the end-point of post-synaptic assessment out from 20-weeks may conclusively show that AAV9-*SGSH* prevents dendritic spine loss in MPS IIIA, ethical considerations must be factored in.

Finally, pre-synaptic delivery of AAV9-*SGSH* appeared to reduce the presumptive inflammatory-mediated synaptic pruning that leads to dendritic spine loss in MPS IIIA. These findings support the need for early diagnosis and early intervention in patients with MPS IIIA. The majority of MPS IIIA patients are currently diagnosed after neurological symptoms are established. Current clinical trials of various therapeutic strategies have so

far failed to reverse, or even slow, disease progression. However, AAV9-*SGSH* treatment in MPS IIIA mice has shown a cessation of disease progression at one- (Fu et al., 2016), two- (Ruzo et al., 2012; Haurigot et al., 2013; Fu et al., 2016), and three-months of age (Fu et al., 2016), yet showed only a partial correction following treatment at six-months (Fu et al., 2016). Unfortunately, mouse and human trials have failed to illustrate a reversal in disease pathology with treatment starting at symptomatic ages. With limited assessment into reversibility via AAV9-*SGSH*, these reports suggest that effective treatment still hinges on early intervention. Therefore, based on these findings, very young patients are most likely to be recruited for trials to see the greatest effects on halting disease progression.

Further investigation is needed to determine the AAV9-*SGSH* effects of halting and reversing dendritic spine loss when changes and symptoms are already established, and thus more readily benefit diagnosed MPS IIIA children. Incidentally, the recent study by de Aragao and colleagues (2020) utilised an AAV9-*HGSNAT* gene therapy on MPS IIIC mice at the age of eight-weeks. They assessed synaptic density through expression of synapsin and PSD95 puncta and reported a slight reduction in average puncta lost six-months post-treatment. The inability to totally prevent puncta loss by providing treatment at this more advanced age further alludes to the importance of early intervention. Moreover, whilst the findings in this study are the first report of AAV9-*SGSH* gene therapy on MPS IIIA neuronal architecture at any delivery time-point, treatment was delivered prior to symptom onset and thereby cannot show a reversal in synaptic loss. Collectively, these data contribute to the establishment of a time-frame or window of treatment that would confer the most benefit MPS IIIA patients. Moreover, the administration of treatment to Day 0 mice corresponds to humans *in utero*. This stresses the importance of newborn screening to permit early diagnosis and administration of

treatment as early as possible to maximise efficacy and provide the greatest opportunity for a higher quality of life.

7.3 Conclusion

In conclusion, the findings collectively reported in this thesis contribute new knowledge to the rapidly expanding literature investigating the underlying basis for symptom development in MPS IIIA. The findings highlight, for the first-time, the age of onset for differences in neuronal architecture and progression with disease, which could not be accurately evaluated from single time-point studies or artificial *in vitro* environments. The study reports the impact of accumulated HS resulting from mutated lysosomal SGSH on the post-synaptic structure and function of layer 5 motor cortical pyramidal neurons prior to symptom onset, with potential influence by complement-mediated inflammation. Furthermore, the study also investigated the impact of a modified in-trial AAV9-*SGSH* gene therapy at the synaptic level, which showed at least a delay in dendritic spine loss, elevated pro-inflammatory markers, and increased glial apposition to neurons in MPS IIIA mice to 20-weeks of age. Together, this thesis contains findings which suggest these measures could provide novel biomarkers to assist disease prognosis and provide a potential target area for therapeutics to delay/prevent neuronal dysfunction in MPS IIIA and other LSDs.

– APPENDICES –

Appendix 1 – Statistical outputs of negative binomial regression models for microglia.

Statistical data generated from outputs for the negative binomial regression models of distance between microglia and neurons at three-weeks (A), six-weeks (B), 12-weeks (C), and 20-weeks of age (D). Group A = wild-type, Group B = MPS IIIA.

A ***Negative binomial model of Frequency versus interaction of Distance (continuous) and Group for Week=3***

Contrast Estimate Results

	Mean			L'Beta					
Label	*Mean Estimate*	*Confidence Limits*		*L'Beta Estimate*	*Standard Error*	*Alpha*	*Confidence Limits*		*Chi-Square*	*Pr > ChiSq*
Slope A	0.8809	0.8664	0.8956	-0.1268	0.0084	0.05	-0.1434	-0.1103	225.53	<.0001
Exp(Slope A)				0.8809	0.0074	0.05	0.8664	0.8956		
Slope B	0.9296	0.9129	0.9465	-0.0731	0.0092	0.05	-0.0911	-0.0550	63.02	<.0001
Exp(Slope B)				0.9296	0.0086	0.05	0.9129	0.9465		
Slope A vs slope B	0.9477	0.9247	0.9711	-0.0538	0.0125	0.05	-0.0782	-0.0293	18.53	<.0001
Exp(Slope A vs slope B)				0.9477	0.0118	0.05	0.9247	0.9711		

B ***Negative binomial model of Frequency versus interaction of Distance (continuous) and Group for Week=6***

Contrast Estimate Results

	Mean			L'Beta					
Label	*Mean Estimate*	*Confidence Limits*		*L'Beta Estimate*	*Standard Error*	*Alpha*	*Confidence Limits*		*Chi-Square*	*Pr > ChiSq*
Slope A	0.6124	0.5848	0.6414	-0.4903	0.0236	0.05	-0.5365	-0.4440	431.73	<.0001
Exp(Slope A)				0.6124	0.0145	0.05	0.5848	0.6414		
Slope B	0.6516	0.6303	0.6736	-0.4284	0.0169	0.05	-0.4616	-0.3952	639.70	<.0001
Exp(Slope B)				0.6516	0.0110	0.05	0.6303	0.6736		
Slope A vs slope B	0.9400	0.8880	0.9949	-0.0619	0.0290	0.05	-0.1188	-0.0051	4.56	0.0327
Exp(Slope A vs slope B)				0.9400	0.0273	0.05	0.8880	0.9949		

C *Negative binomial model of Frequency versus interaction of Distance (continuous) and Group for Week=12*

Contrast Estimate Results

	Mean			*L'Beta*						
Label	*Mean Estimate*	*Confidence Limits*		*L'Beta Estimate*	*Standard Error*	*Alpha*	*Confidence Limits*		*Chi-Square*	*Pr > ChiSq*
Slope A	0.8674	0.8490	0.8861	-0.1423	0.0109	0.05	-0.1636	-0.1209	170.08	<.0001
Exp(Slope A)				0.8674	0.0095	0.05	0.8490	0.8861		
Slope B	0.5588	0.5263	0.5933	-0.5820	0.0306	0.05	-0.6420	-0.5221	362.46	<.0001
Exp(Slope B)				0.5588	0.0171	0.05	0.5263	0.5933		
Slope A vs slope B	1.5523	1.4566	1.6544	0.4398	0.0325	0.05	0.3761	0.5034	183.43	<.0001
Exp(Slope A vs slope B)				1.5523	0.0504	0.05	1.4566	1.6544		

D *Negative binomial model of Frequency versus interaction of Distance (continuous) and Group for Week=20*

Contrast Estimate Results

	Mean			*L'Beta*						
Label	*Mean Estimate*	*Confidence Limits*		*L'Beta Estimate*	*Standard Error*	*Alpha*	*Confidence Limits*		*Chi-Square*	*Pr > ChiSq*
Slope A	0.4571	0.4267	0.4897	-0.7828	0.0352	0.05	-0.8517	-0.7139	495.93	<.0001
Exp(Slope A)				0.4571	0.0161	0.05	0.4267	0.4897		
Slope B	0.4699	0.4422	0.4994	-0.7552	0.0310	0.05	-0.8159	-0.6944	593.48	<.0001
Exp(Slope B)				0.4699	0.0146	0.05	0.4422	0.4994		
Slope A vs slope B	0.9727	0.8878	1.0658	-0.0276	0.0466	0.05	-0.1190	0.0637	0.35	0.5531
Exp(Slope A vs slope B)				0.9727	0.0453	0.05	0.8878	1.0658		

Appendix 2 – Statistical outputs of negative binomial regression models for astrocytes. Statistical data generated from outputs for the negative binomial regression models of distance between astrocytes and neurons at three-weeks (A), six-weeks (B), 12-weeks (C), and 20-weeks of age (D). Group A = wild-type, Group B = MPS IIIA.

A *Negative binomial model of Frequency versus interaction of Distance (continuous) and Group for Week=3*

Contrast Estimate Results

	Mean			*L'Beta*						
Label	*Mean Estimate*	*Confidence Limits*		*L'Beta Estimate*	*Standard Error*	*Alpha*	*Confidence Limits*		*Chi-Square*	*Pr > ChiSq*
Slope A	0.8861	0.8642	0.9086	-0.1209	0.0128	0.05	-0.1459	-0.0959	89.68	<.0001
Exp(Slope A)				0.8861	0.0113	0.05	0.8642	0.9086		
Slope B	0.8927	0.8774	0.9082	-0.1135	0.0088	0.05	-0.1308	-0.0963	166.40	<.0001
Exp(Slope B)				0.8927	0.0079	0.05	0.8774	0.9082		
Slope A vs slope B	0.9926	0.9631	1.0231	-0.0074	0.0154	0.05	-0.0376	0.0228	0.23	0.6317
Exp(Slope A vs slope B)				0.9926	0.0153	0.05	0.9631	1.0231		

B *Negative binomial model of Frequency versus interaction of Distance (continuous) and Group for Week=6*

Contrast Estimate Results

	Mean			*L'Beta*						
Label	*Mean Estimate*	*Confidence Limits*		*L'Beta Estimate*	*Standard Error*	*Alpha*	*Confidence Limits*		*Chi-Square*	*Pr > ChiSq*
Slope A	0.6509	0.6137	0.6903	-0.4294	0.0300	0.05	-0.4883	-0.3706	204.60	<.0001
Exp(Slope A)				0.6509	0.0195	0.05	0.6137	0.6903		
Slope B	0.9354	0.9209	0.9502	-0.0668	0.0080	0.05	-0.0825	-0.0511	69.74	<.0001
Exp(Slope B)				0.9354	0.0075	0.05	0.9209	0.9502		
Slope A vs slope B	0.6958	0.6547	0.7395	-0.3627	0.0311	0.05	-0.4236	-0.3018	136.24	<.0001
Exp(Slope A vs slope B)				0.6958	0.0216	0.05	0.6547	0.7395		

C *Negative binomial model of Frequency versus interaction of Distance (continuous) and Group for Week=12*

Contrast Estimate Results

	Mean			*L'Beta*						
Label	*Mean Estimate*	*Confidence Limits*		*L'Beta Estimate*	*Standard Error*	*Alpha*	*Confidence Limits*		*Chi-Square*	*Pr > ChiSq*
Slope A	0.5726	0.5353	0.6125	-0.5576	0.0344	0.05	-0.6250	-0.4901	262.67	<.0001
Exp(Slope A)				0.5726	0.0197	0.05	0.5353	0.6125		
Slope B	0.6301	0.6019	0.6596	-0.4619	0.0234	0.05	-0.5077	-0.4161	390.89	<.0001
Exp(Slope B)				0.6301	0.0147	0.05	0.6019	0.6596		
Slope A vs slope B	0.9088	0.8376	0.9859	-0.0957	0.0416	0.05	-0.1772	-0.0142	5.29	0.0214
Exp(Slope A vs slope B)				0.9088	0.0378	0.05	0.8376	0.9859		

D *Negative binomial model of Frequency versus interaction of Distance (continuous) and Group for Week=20*

Contrast Estimate Results

	Mean			*L'Beta*						
Label	*Mean Estimate*	*Confidence Limits*		*L'Beta Estimate*	*Standard Error*	*Alpha*	*Confidence Limits*		*Chi-Square*	*Pr > ChiSq*
Slope A	0.9321	0.9150	0.9494	-0.0703	0.0094	0.05	-0.0888	-0.0519	55.79	<.0001
Exp(Slope A)				0.9321	0.0088	0.05	0.9150	0.9494		
Slope B	0.5736	0.5315	0.6191	-0.5558	0.0389	0.05	-0.6321	-0.4795	203.83	<.0001
Exp(Slope B)				0.5736	0.0223	0.05	0.5315	0.6191		
Slope A vs slope B	1.6250	1.5023	1.7577	0.4855	0.0401	0.05	0.4070	0.5640	146.94	<.0001
Exp(Slope A vs slope B)				1.6250	0.0651	0.05	1.5023	1.7577		

Appendix 3 – Statistical outputs of negative binomial regression models for microglia following saline or AAV9-*SGSH* treatment. Statistical data generated from outputs for the negative binomial regression models of distance between microglia and neurons at 20-weeks of age. Group A = wild-type (saline), Group B = MPS IIIA (saline), Group C = MPS IIIA (AAV9).

Contrast Estimate Results

	Mean			*L'Beta*						
Label	*Mean Estimate*	*Confidence Limits*		*L'Beta Estimate*	*Standard Error*	*Alpha*	*Confidence Limits*		*Chi-Square*	*Pr > ChiSq*
Slope A	0.5536	0.5300	0.5784	-0.5913	0.0223	0.05	-0.6349	-0.5476	703.77	<.0001
Exp(Slope A)				0.5536	0.0123	0.05	0.5300	0.5784		
Slope B	0.5692	0.5475	0.5918	-0.5635	0.0198	0.05	-0.6023	-0.5247	809.04	<.0001
Exp(Slope B)				0.5692	0.0113	0.05	0.5475	0.5918		
Slope C	0.6426	0.6188	0.6674	-0.4422	0.0193	0.05	-0.4800	-0.4044	526.21	<.0001
Exp(Slope C)				0.6426	0.0124	0.05	0.6188	0.6674		
Slope A vs slope B	0.9726	0.9174	1.0311	-0.0278	0.0298	0.05	-0.0862	0.0306	0.87	0.3513
Exp(Slope A vs slope B)				0.9726	0.0290	0.05	0.9174	1.0311		
Slope A vs slope C	0.8615	0.8132	0.9127	-0.1491	0.0294	0.05	-0.2068	-0.0913	25.62	<.0001
Exp(Slope A vs slope C)				0.8615	0.0254	0.05	0.8132	0.9127		
Slope B vs slope C	0.8858	0.8392	0.9349	-0.1213	0.0276	0.05	-0.1753	-0.0673	19.37	<.0001
Exp(Slope B vs slope C)				0.8858	0.0244	0.05	0.8392	0.9349		

Appendix 4 – Statistical outputs of negative binomial regression models for astrocytes following saline or AAV9-*SGSH* treatment. Statistical data generated from outputs for the negative binomial regression models of distance between astrocytes and neurons at 20-weeks of age. Shown is the interaction model of Distance (continuous) and Group (A/B/C) for the outcome Frequency (A), and the main effects model for outcome Frequency with predictors Distance and Group (B). Group A = wild-type (saline), Group B = MPS IIIA (saline), Group C = MPS IIIA (AAV9).

A ***Negative binomial model of Astrocyte Frequency versus interaction of Distance (continuous) and Group for Week=20***

Contrast Estimate Results

	Mean			*L'Beta*						
Label	*Mean Estimate*	*Confidence Limits*		*L'Beta Estimate*	*Standard Error*	*Alpha*	*Confidence Limits*		*Chi-Square*	*Pr > ChiSq*
Slope A	0.6450	0.5952	0.6990	-0.4385	0.0410	0.05	-0.5189	-0.3581	114.18	<.0001
Exp(Slope A)				0.6450	0.0265	0.05	0.5952	0.6990		
Slope B	0.6227	0.5819	0.6663	-0.4738	0.0345	0.05	-0.5415	-0.4061	188.12	<.0001
Exp(Slope B)				0.6227	0.0215	0.05	0.5819	0.6663		
Slope C	0.7000	0.6528	0.7506	-0.3567	0.0356	0.05	-0.4264	-0.2869	100.47	<.0001
Exp(Slope C)				0.7000	0.0249	0.05	0.6528	0.7506		
Slope A vs slope B	1.0359	0.9326	1.1507	0.0353	0.0536	0.05	-0.0698	0.1404	0.43	0.5106
Exp(Slope A vs slope B)				1.0359	0.0555	0.05	0.9326	1.1507		
Slope A vs slope C	0.9214	0.8284	1.0249	-0.0818	0.0543	0.05	-0.1883	0.0246	2.27	0.1320
Exp(Slope A vs slope C)				0.9214	0.0500	0.05	0.8284	1.0249		
Slope B vs slope C	0.8895	0.8071	0.9803	-0.1171	0.0496	0.05	-0.2143	-0.0199	5.58	0.0182
Exp(Slope B vs slope C)				0.8895	0.0441	0.05	0.8071	0.9803		

B ***Negative binomial model of Astrocyte Frequency versus Distance (continuous) and Group for Week=20***

Contrast Estimate Results

	Mean			*L'Beta*						
Label	*Mean Estimate*	*Confidence Limits*		*L'Beta Estimate*	*Standard Error*	*Alpha*	*Confidence Limits*		*Chi-Square*	*Pr > ChiSq*
Distance	0.6541	0.6272	0.6821	-0.4245	0.0214	0.05	-0.4665	-0.3826	392.81	<.0001
Exp(Distance)				0.6541	0.0140	0.05	0.6272	0.6821		

Differences of Group Least Squares Means

Group	*Group*	*Estimate*	*Standard Error*	*z Value*	*Pr > |z|*	*Alpha*	*Lower*	*Upper*	*Exponentiated*	*Exponentiated Lower*	*Exponentiated Upper*
A	B	-2.6292	0.2524	-10.42	<.0001	0.05	-3.1239	-2.1344	0.07214	0.04398	0.1183
A	C	-2.2795	0.2765	-8.24	<.0001	0.05	-2.8214	-1.7375	0.1023	0.05952	0.1760
B	C	0.3497	0.2549	1.37	0.1702	0.05	-0.1500	0.8493	1.4186	0.8607	2.3381

Appendix 5 – Identification of individually treated mice. The identification of individual mice and their corresponding symbols categorised by the treatment received. The mice identified underwent behavioural testing at 15- and 20-weeks of age, and histological assessment after euthanasia at 20-weeks.

WT (Saline)		**MPS IIIA (Saline)**		**MPS IIIA (AAV9)**	
Mouse ID	Symbol	Mouse ID	Symbol	Mouse ID	Symbol
663	▲	727	◓	717	◓
664	◭	728	⬒	723	○
665	▼	729	□	741	■
671	●	731	○	742	□
675	▽	747	●	743	●
676	□	748	■	-	-
677	■	-	-	-	-
678	△	-	-	-	-
679	◆	-	-	-	-
681	⬒	-	-	-	-
711	▽	-	-	-	-
712	◓	-	-	-	-
713	○	-	-	-	-

– REFERENCES –

Adrian M, Kusters R, Wierenga CJ, Storm C, Hoogenraad CC, Kapitein LC (2014). Barriers in the brain: resolving dendritic spine morphology and compartmentalization. *Front. Neuroanat. 8*, 142.

Aerts JM, Hollak CE, Boot RG, Groener JE, Maas M. (2006). Substrate reduction therapy of glycosphingolipid storage disorders. *J. Inher. Metab. Dis*. *29*(2-3), 449–456.

Ahrens-Nicklas RC, Tecedor L, Hall AF, Lysenko E, Cohen AS, Davidson BL, Marsh ED. (2019). Neuronal network dysfunction precedes storage and neurodegeneration in a lysosomal storage disorder. *JCI Insight 4*(21), e131961.

Alberts P, Rudge R, Irinopoulou T, Danglot L, Gauthier-Rouvière C, Galli T. (2006). Cdc42 and actin control polarized expression of TI-VAMP vesicles to neuronal growth cones and their fusion with the plasma membrane. *Molec. Biol. Cell. 17*(3), 1194-1203.

Alcami P, Pereda AE. (2019). Beyond plasticity: the dynamic impact of electrical synapses on neural circuits. *Nat. Rev. Neurosci. 20*(5), 253-271.

Alexander BH, Barnes HM, Trimmer E, Davidson AM, Ogola BO, Lindsey SH, Mostany R. (2018). Stable density and dynamics of dendritic spines of cortical neurons across the estrous cycle while expressing differential levels of sensory-evoked plasticity. *Front. Molec. Neurosci. 11*, 83.

Alvarez-Castelao B, Schuman EM. (2015). The regulation of synaptic protein turnover. *J. Biol. Chem*. *290*(48), 28623–28630.

Amorim IS, Mitchell NL, Palmer DN, Sawiak SJ, Mason R, Wishart TM, Gillingwater TH. (2015). Molecular neuropathology of the synapse in sheep with CLN5 Batten disease. *Brain Behav. 5*(11), e00401.

Ampuero E, Dagnino-Subiabre A, Sandoval R, Zepeda-Carreño R, Sandoval S, Viedma A, Aboitiz F, Orrego F, Wyneken U. (2007). Status epilepticus induces region-specific changes in dendritic spines, dendritic length and TrkB protein content of rat brain cortex. *Brain Res. 1150*, 225–238.

Arellano JI, Benavides-Piccione R, Defelipe J, Yuste R. (2007). Ultrastructure of dendritic spines: correlation between synaptic and spine morphologies. *Front. Neurosci. 1*(1), 131–143.

Arfi A, Richard M, Gandolphe C, Bonnefont-Rousselot D, Therond P, Scherman D. (2011). Neuroinflammatory and oxidative stress phenomena in MPS IIIA mouse model: the positive effect of long-term aspirin treatment. *Molec. Genet. Metab. 103*(1), 18-25.

Arnoux I, Audinat E. (2015). Fractalkine signaling and microglia functions in the developing brain. *Neural Plasticity 2015*(2015), 689404. .

Aronovich EL, Hackett PB. (2015). Lysosomal storage disease: gene therapy on both sides of the blood-brain barrier. *Molec. Genet. Metab.114*(2), 83–93.

Aronovich EL, Hyland KA, Hall BC, Bell JB, Olson ER, Rusten MU, Hunter DW, Ellinwood NM, McIvor RS, Hackett PB. (2017). Prolonged expression of secreted enzymes in dogs after liver-directed delivery of Sleeping Beauty transposons: implications for non-viral gene gherapy of systemic disease. *Hum. Gene Ther. 28*(7), 551-564.

Arroyo AI, Camoletto PG, Morando L, Sassoe-Pognetto M, Giustetto M, Van Veldhoven PP, Schuchman EH, Ledesma MD. (2014). Pharmacological reversion of sphingomyelin-induced dendritic spine anomalies in a Niemann Pick disease type A mouse model. *EMBO Molec. Med. 6*(3), 398–413.

Asokan A, Schaffer DV, Samulski RJ. (2012). The AAV vector toolkit: poised at the clinical crossroads. *Molec. Ther. 20*(4), 699-708.

Attar A, Ripoli C, Riccardi E, Maiti P, Li Puma DD, Liu T, Hayes J, Jones MR, Lichti-Kaiser K, Yang F, et al. G. (2012). Protection of primary neurons and mouse brain from Alzheimer's pathology by molecular tweezers. *Brain 135*(Pt 12), 3735–3748.

Ausseil J, Desmaris N, Bigou S, Attali R, Corbineau S, Vitry S, Parent M, Cheillan D, et al. (2008) Early neurodegeneration progresses independently of microglial activation by heparan sulfate in the brain of mucopolysaccharidosis IIIB mice. *PLoS One, 3*(5), e2296.

Avchalumov Y, Kirschstein T, Lukas J, Luo J, Wree A, Rolfs A, Kohling R. (2012). Increased excitability and compromised long-term potentiation in the neocortex of NPC1(-/-) mice. *Brain Res. 1444*, 20-26.

Babu CS, Ramanathan M. (2011). Post-ischemic administration of nimodipine following focal cerebral ischemic-reperfusion injury in rats alleviated excitotoxicity, neurobehavioural alterations and partially the bioenergetics. *Int. J. Dev. Neurosci. 29*(1), 93–105.

Baldwin KT, Eroglu C. (2017). Molecular mechanisms of astrocyte-induced synaptogenesis. *Curr. Opin. Neurobiol. 45*, 113-120.

Ballabio A, Bonifacino JS. (2020). Lysosomes as dynamic regulators of cell and organismal homeostasis. *Nat. Rev. Molec. Cell Biol. 21*(2), 101-118.

Barros CS, Franco SJ, Muller U. (2011). Extracellular matrix: functions in the nervous system. *Cold Spring Harbor Perspect. Biol. 3*(1), a005108.

Bax MC, Colville GA. (1995) Behaviour in mucopolysaccharide disorders. *Arch. Dis. Child. 73*(1), 77-81.

Beard H, Luck AJ, Hassiotis S, King B, Trim PJ, Snel MF, Hopwood JJ, Hemsley KM. (2015). Determination of the role of injection site on the efficacy of intra-CSF enzyme replacement therapy in MPS IIIA mice. *Molecular genetics and metabolism*, *115*(1), 33–40.

Beard H, Hassiotis S, Gai WP, Parkinson-Lawrence E, Hopwood JJ, Hemsley KM. (2017). Axonal dystrophy in the brain of mice with Sanfilippo syndrome. *Exp. Neurol. 295*, 243-255.

Belichenko PV, Brown D, Jeffrey M, Fraser JR. (2000). Dendritic and synaptic alterations of hippocampal pyramidal neurones in scrapie-infected mice. *Neuropath. Appl. Neurobiol. 26*(2), 143–149.

Belichenko PV, Kleschevnikov AM, Salehi A, Epstein CJ, Mobley WC. (2007). Synaptic and cognitive abnormalities in mouse models of Down syndrome: exploring genotype-phenotype relationships. *J. Comp. Neurol. 504*(4), 329–345.

Belichenko NP, Belichenko PV, Kleschevnikov AM, Salehi A, Reeves RH, Mobley WC. (2009). The "Down syndrome critical region" is sufficient in the mouse model to confer behavioral, neurophysiological, and synaptic phenotypes characteristic of Down syndrome. *J. Neurosci. 29*(18), 5938–5948.

Best HL, Neverman NJ, Wicky HE, Mitchell NL, Leitch B, Hughes SM. (2017). Characterisation of early changes in ovine CLN5 and CLN6 Batten disease neural cultures for the rapid screening of therapeutics. *Neurobiol. Dis. 100*, 62-74.

Bevan AK, Duque S, Foust KD, Morales PR, Braun L, Schmelzer L, et al. (2011). Systemic gene delivery in large species for targeting spinal cord, brain, and peripheral tissues for pediatric disorders. *Molec. Ther. 19*(11), 1971-1980.

Bhatt DH, Zhang S, Gan WB. (2009). Dendritic spine dynamics. *Ann. Rev. Physiol. 71*, 261-282.

Bhattacharyya R, Gliddon B, Beccari T, Hopwood JJ, Stanley P. (2001). A novel missense mutation in lysosomal sulfamidase is the basis of MPS IIIA in a spontaneous mouse mutant. *Glycobiology*, *11*(1), 99–103.

Bhaumik M, Muller VJ, Rozaklis T, Johnson L, Dobrenis K, Bhattacharyya R, Wurzelmann S, Finamore P, Hopwood JJ, Walkley SU, Stanley P. (1999). A mouse model for mucopolysaccharidosis type IIIA (Sanfilippo syndrome). *Glycobiology*, *9*(12), 1389–1396.

Bignami A, Eng LF, Dahl D, Uyeda CT. (1972). Localization of the glial fibrillary acidic protein in astrocytes by immunofluorescence. *Brain Res. 43*(2), 429–435.

Billups D, Marx MC, Mela I, Billups B. (2013). Inducible presynaptic glutamine transport supports glutamatergic transmission at the calyx of Held synapse. *J. Neurosci. 33*(44), 17429-17434.

Block ML, Zecca L, Hong JS. (2007). Microglia-mediated neurotoxicity: uncovering the molecular mechanisms. *Nat. Rev. Neurosci. 8*(1), 57-69.

Boche D, Perry VH, Nicoll JA. (2013). Review: activation patterns of microglia and their identification in the human brain. *Neuropathol. Appl. Neurobiol. 39*(1), 3-18.

Bollinger JL, Salinas I, Fender E, Sengelaub DR, Wellman CL. (2019). Gonadal hormones differentially regulate sex-specific stress effects on glia in the medial prefrontal cortex. .*J Neuroendocrinol. 31*(8), e12762.

Bourne J, Harris KM. (2007). Do thin spines learn to be mushroom spines that remember? *Curr. Opin. Neurobiol. 17*(3), 381-386.

Braak E, Braak H. (1997). Alzheimer's disease: transiently developing dendritic changes in pyramidal cells of sector CA1 of the Ammon's horn. *Acta Neuropathol. 93*(4), 323–325.

Brailoiu E, Patel S, Dun NJ. (2003). Modulation of spontaneous transmitter release from the frog neuromuscular junction by interacting intracellular Ca(2+) stores: critical role for nicotinic acid-adenine dinucleotide phosphate (NAADP). *Biochem. J. 373*(Pt 2), 313–318.

Brailsford J. (1929). Chondro-osteo-dystrophy. Roentgenographic and clinical features of a child with dislocation of vertebrae. *Am. J. Surg.* 7:404–410.

Braulke T, Bonifacino JS. (2009). Sorting of lysosomal proteins. *Biochim. Biophys. Acta 1793*(4), 605-614.

Breiden B, Sandhoff K. (2019). Lysosomal glycosphingolipid storage diseases. *Ann. Rev. Biochem. 88*, 461-485.

Brinton RD. (2009). Estrogen-induced plasticity from cells to circuits: predictions for cognitive function. *Trends Pharmacol. Sci. 30*(4), 212-222.

Brodmann K. (1909). *Vergleichende lokalisationslehre der grosshirnrinde in ihren brinzipien dargestellt auf grund des zellenbaues*. Leipzig Verlag von Johann Ambrosius Barth.

Brombacher TM, Nono JK, De Gouveia KS, Makena N, Darby M, Womersley J, Tamgue O, Brombacher F. (2017). IL-13-Mediated regulation of learning and memory. *J. Immunol. 198*(7), 2681–2688.

Buard I, Pfrieger FW. (2014). Relevance of neuronal and glial NPC1 for synaptic input to cerebellar Purkinje cells. *Molec. Cell. Neurosci*. *61*, 65–71.

Burkovetskaya M, Karpuk N, Kielian T. (2017). Age-dependent alterations in neuronal activity in the hippocampus and visual cortex in a mouse model of Juvenile Neuronal Ceroid Lipofuscinosis (CLN3). *Neurobiol. Dis. 100*, 19–29.

Burrows EL, Hannan AJ. (2013). Towards environmental construct validity in animal models of CNS disorders: optimizing translation of preclinical studies. *CNS Neurol. Dis. Drug Targets 12*(5), 587–592.

Buskila Y, Breen PP, Tapson J, van Schaik A, Barton M, Morley JW. (2014). Extending the viability of acute brain slices. *Sci. Rep. 4*, 5309.

Cai Z, Li S, Matuskey D, Nabulsi N, Huang Y. (2019). PET imaging of synaptic density: a new tool for investigation of neuropsychiatric diseases. *Neurosci. Lett. 691,* 44-50.

Cain JT, Likhite S, White KA, Timm DJ, Davis SS, Johnson TB, Dennys-Rivers CN, Rinaldi F, Motti D, et al (2019). Gene therapy corrects brain and behavioral pathologies in CLN6-Batten disease. *Mol. Ther. 27*(10), 1836-1847.

Cameron MA, Kekesi O, Morley JW, Bellot-Saez A, Kueh S, Breen P, van Schaik A, Tapson J, Buskila Y. (2017). Prolonged incubation of acute neuronal tissue for electrophysiology and calcium-imaging. *J. Vis. Exp.* (120). e55396

Canals I, Beneto N, Cozar M, Vilageliu L, Grinberg D. (2015). EXTL2 and EXTL3 inhibition with siRNAs as a promising substrate reduction therapy for Sanfilippo C syndrome. *Sci. Rep. 5*, 13654.

Caporali P, Bruno F, Palladino G, Dragotto J, Petrosini L, Mangia F, Erickson RP, Canterini S, Fiorenza MT. (2016). Developmental delay in motor skill acquisition in Niemann-Pick C1 mice reveals abnormal cerebellar morphogenesis. *Acta Neuropath. Comm. 4*(1), 94.

de Castilhos J, Forti CD, Achaval M, Rasia-Filho AA. (2008). Dendritic spine density of posterodorsal medial amygdala neurons can be affected by gonadectomy and sex steroid manipulations in adult rats: a Golgi study. *Brain Res. 1240,* 73-81**.**

Castro J, Garcia RI, Kwok S, Banerjee A, Petravicz J, Woodson J, Mellios N, Tropea D, Sur M. (2014). Functional recovery with recombinant human IGF1 treatment in a mouse model of Rett Syndrome. *Proc. Natl. Acad. Sci. USA 111*(27), 9941–9946.

Chamoles NA, Blanco M, Gaggioli D. (2001). Fabry disease: enzymatic diagnosis in dried blood spots on filter paper. *Clin. Chim. Acta 308*(1-2), 195–196.

Chapleau CA, Calfa GD, Lane MC, Albertson AJ, Larimore JL, Kudo S, Armstrong DL, Percy AK, Pozzo-Miller L. (2009). Dendritic spine pathologies in hippocampal pyramidal neurons from Rett syndrome brain and after expression of Rett-associated MECP2 mutations. *Neurobiol. Dis. 35*(2), 219–233.

Chapleau CA, Boggio EM, Calfa G, Percy AK, Giustetto M, Pozzo-Miller L. (2012). Hippocampal CA1 pyramidal neurons of Mecp2 mutant mice show a dendritic spine phenotype only in the presymptomatic stage. *Neural Plasticity, 2012*, 976164.

Chen W, Shields J, Huang W, King JA. (2009). Female fear: influence of estrus cycle on behavioral response and neuronal activation. *Behav. Brain Res. 201*(1), 8–13.

Chen Y, Zheng S, Tecedor L, Davidson BL. (2018). Overcoming limitations inherent in sulfamidase to improve mucopolysaccharidosis IIIA gene therapy. *Molec. Ther. 26*(4), 1118-1126.

Chidambaram SB, Rathipriya AG, Bolla SR, Bhat A, Ray B, Mahalakshmi AM, . . . Sakharkar MK. (2019). Dendritic spines: revisiting the physiological role. *Prog. Neuropsychopharmacol. Biol. Psych. 92,* 161-193.

Cho S, Wood A, Bowlby MR. (2007). Brain slices as models for neurodegenerative disease and screening platforms to identify novel therapeutics. *Curr. Neuropharmacol. 5*(1), 19–33.

Choi L, Vernon J, Kopach O, Minett MS, Mills K, Clayton PT, Meert T, Wood JN. (2015). The Fabry disease-associated lipid Lyso-Gb3 enhances voltage-gated calcium currents in sensory neurons and causes pain. *Neurosci. Lett. 594*, 163–168.

Christoffel DJ, Golden SA, Russo SJ. (2011). Structural and synaptic plasticity in stress-related disorders. *Rev. Neurosci*. *22*(5), 535–549.

Chung WS, Clarke LE, Wang GX, Stafford BK, Sher A, Chakraborty C, ... Smith SJ. (2013). Astrocytes mediate synapse elimination through MEGF10 and MERTK pathways. *Nature 504*(7480), 394-400.

Clark TA, Fu M, Dunn AK, Zuo Y, Jones TA. (2018). Preferential stabilization of newly formed dendritic spines in motor cortex during manual skill learning predicts performance gains, but not memory endurance. *Neurobiol. Learn Mem. 152*, 50-60.

Cleary MA, Wraith JE. (1993). Management of mucopolysaccharidosis type III. *Arch. Dis. Child. 69*(3), 403–406.

Colgan LA, Yasuda R. (2014). Plasticity of dendritic spines: subcompartmentalization of signaling. *Ann. Rev. Physiol. 76*, 365–385.

Condomitti G, de Wit J. (2018). Heparan sulfate proteoglycans as emerging players in synaptic specificity. *Front. Molec. Neurosci. 11*, 14.

Cook D, Nuro E, Jones EV, Altimimi HF, Farmer WT, Gandin V, Hanna E, Zong R, Barbon A, Nelson DL, Topisirovic I, Rochford J, Stellwagen D, Béïque JC, Murai KK. (2014). FXR1P limits long-term memory, long-lasting synaptic potentiation, and de novo GluA2 translation. *Cell Rep. 9*(4), 1402–1416.

Coutinho MF, Prata MJ, Alves S. (2012). A shortcut to the lysosome: the mannose-6-phosphate-independent pathway. *Mol. Genet. Metab. 107*(3), 257-266.

Crawley AC, Gliddon BL, Auclair D, Brodie SL, Hirte C, King BM, Fuller M, Hemsley KM, Hopwood JJ. (2006). Characterization of a C57BL/6 congenic mouse strain of mucopolysaccharidosis type IIIA. *Brain Res. 1104*(1), 1-17.

Cressant A, Desmaris N, Verot L, Brejot T, Froissart R, Vanier MT, Maire I, Heard JM. (2004). Improved behavior and neuropathology in the mouse model of Sanfilippo type IIIB disease after adeno-associated virus-mediated gene transfer in the striatum. *J. Neurosci. 24*(45), 10229-10239.

Croft CL, Futch HS, Moore BD, Golde TE. (2019). Organotypic brain slice cultures to model neurodegenerative proteinopathies. *Molec. Neurodeg. 14*(1), 45.

Cruz-Martín A, Crespo M, Portera-Cailliau C. (2010). Delayed stabilization of dendritic spines in fragile X mice. *J. Neurosci. 30*(23), 7793–7803.

Dalakas MC, Alexopoulos H, Spaeth PJ. (2020). Complement in neurological disorders and emerging complement-targeted therapeutics. *Nat. Rev. Neurol.* 1–17. Advance online publication. https://doi.org/10.1038/s41582-020-0400-0

Danbolt NC. (2001). Glutamate uptake. *Prog. Neurobiol. 65*(1), 1–105.

Davidson AM, Mejia-Gomez H, Jacobowitz M, Mostany R. (2020). Dendritic spine density and dynamics of layer 5 pyramidal neurons of the primary motor cortex are elevated with aging. *Cerebral Cortex 30*(2), 767-777.

de Aragão CdB, Bruno L, Bose P, Pan X, Han C, McPherson PS., . . . Pshezhetsky AV. (2020). Early defects in lysosomal storage diseases disrupt excitatory synaptic transmission. doi:10.1101/2020.07.06.186809

Deczkowska A, Keren-Shaul H, Weiner A, Colonna M, Schwartz M, Amit I. (2018). Disease-associated microglia: a universal immune sensor of neurodegeneration. *Cell 173*(5), 1073-1081.

De Duve C. (1957). Les lysosomes: un nouveau groupe de granules cytoplasmiques [The lysosomes: a novel group of cytoplasmic granules]. *J. Physiol. 49*(1), 113-115.

Deisz RA, Meske V, Treiber-Held S, Albert F, Ohm TG. (2005). Pathological cholesterol metabolism fails to modify electrophysiological properties of afflicted neurones in Niemann-Pick disease type C. *Neurosci. 130*(4), 867–873.

de Ruijter J, Valstar MJ, Narajczyk M, Wegrzyn G, Kulik W, Ijlst L, Wagemans, T van der Wal WM, Wijburg FA. (2012). Genistein in Sanfilippo disease: a randomized controlled crossover trial. *Ann. Neurol. 71*(1), 110-120.

Derecki NC, Cardani AN, Yang CH, Quinnies KM, Crihfield A, Lynch KR, Kipnis J. (2010). Regulation of learning and memory by meningeal immunity: a key role for IL-4. *J. Exp. Med. 207*(5), 1067–1080.

Derrick-Roberts A, Jackson MR, Pyragius CE, Byers S. (2017). Substrate deprivation therapy to reduce glycosaminoglycan synthesis improves aspects of neurological and skeletal pathology in MPS I mice. *Diseases 5*(1), 5.

Desnick RJ, Schuchman EH. (2012). Enzyme replacement therapy for lysosomal diseases: lessons from 20 years of experience and remaining challenges. *Ann. Rev. Genomics Hum. Genet. 13*, 307-335.

Deverman BE, Ravina BM, Bankiewicz KS, Paul SM, Sah DWY. (2018). Gene therapy for neurological disorders: progress and prospects. *Nat. Rev. Drug Discov. 17*(9), 641-659.

Dickstein DL, Dickstein DR, Janssen WG, Hof PR, Glaser JR, Rodriguez A, O'Connor N, Angstman P, Tappan SJ. (2016). Automatic dendritic spine quantification from confocal data with neurolucida 360. *Curr. Protocols Neurosci. 77*, 1.27.1–1.27.21.

Dobrunz LE, Stevens CF. (1997). Heterogeneity of release probability, facilitation, and depletion at central synapses. *Neuron 18*(6), 995–1008.

Donati MA, Pasquini E, Spada M, Polo G, Burlina A. (2018). Newborn screening in mucopolysaccharidoses. *Ital. J. Pediatr. 44*(Suppl 2), 126.

Dong W, Todd AC, Broer A, Hulme SR, Broer S, Billups B. (2018). PKC-mediated modulation of astrocyte SNAT3 glutamine transporter function at synapses in situ. *Int. J. Molec. Sci. 19*(4), 924

Dwyer CA, Scudder SL, Lin Y, Dozier LE, Phan D, Allen NJ, Patrick GN, Esko JD. (2017). Neurodevelopmental changes in excitatory synaptic structure and function in the cerebral cortex of Sanfilippo syndrome IIIA mice. *Sci. Rep. 7*, 46576.

Ehlers MD. (2000). Reinsertion or degradation of AMPA receptors determined by activity-dependent endocytic sorting. *Neuron 28*(2), 511–525.

Ellinwood NM, Wang P, Skeen T, Sharp NJH, Cesta M, Decker S, Edwards NJ, Bublot I, Thompson JN, Bush W. et al. (2003). A model of mucopolysaccharidosis IIIB (Sanfilippo syndrome type IIIB): N-acetyl-alpha-D-glucosaminidase deficiency in Schipperke dogs. *J. Inherit. Metab. Dis.* 26, 489-504.

Eroglu C, Barres BA. (2010). Regulation of synaptic connectivity by glia. *Nature 468*(7321), 223–231.

Feldman ML, Dowd C. (1975). Loss of dendritic spines in aging cerebral cortex. *Anatomy Embryol. 148*(3), 279–301.

Feng G, Mellor RH, Bernstein M, Keller-Peck C, Nguyen QT, Wallace M, Nerbonne JM, Lichtman JW, Sanes JR. (2000). Imaging neuronal subsets in transgenic mice expressing multiple spectral variants of GFP. *Neuron 28*(1), 41–51.

Feng D, Zhao WL, Ye YY, Bai XC, Liu RQ, Chang LF, Zhou Q, Sui SF. (2010). Cellular internalization of exosomes occurs through phagocytosis. *Traffic 11*(5), 675-687.

Filiano AJ, Xu Y, Tustison NJ, Marsh RL, Baker W, Smirnov I, Overall CC, Gadani SP, Turner SD, Weng Z, Peerzade SN, Chen H, Lee KS, Scott MM, Beenhakker MP, Litvak V, Kipnis J. (2016). Unexpected role of interferon-γ in regulating neuronal connectivity and social behaviour. *Nature 535*(7612), 425–429.

Filipello F, Morini R, Corradini I, Zerbi V, Canzi A, Michalski B, Erreni M, Markicevic M, Starvaggi-Cucuzza C, et al. (2018). The microglial innate immune receptor TREM2 is required for synapse elimination and normal brain connectivity. *Immunity 48*(5), 979–991.e8.

Fischer A, Carmichael KP, Munnell JF, Jhabvala P, Thompson JN, Matalon R, Jezyk PF, Wang P, Giger U. (1998). Sulfamidase deficiency in a family of Dachshunds: a canine model of mucopolysaccharidosis IIIA (Sanfilippo A). *Ped. Res. 44*(1), 74–82.

Fischer M, Kaech S, Wagner U, Brinkhaus H, Matus A. (2000). Glutamate receptors regulate actin-based plasticity in dendritic spines. *Nature Neurosci. 3*(9), 887–894.

Fraldi A, Hemsley K, Crawley A, Lombardi A, Lau A, Sutherland L, Auricchio A, Ballabio A, Hopwood JJ. (2007). Functional correction of CNS lesions in an MPS-IIIA mouse model by intracerebral AAV-mediated delivery of sulfamidase and SUMF1 genes. *Hum. Molec. Genet. 16*(22), 2693-2702.

Frankfurt M, Gould E, Woolley CS, McEwen BS. (1990). Gonadal steroids modify dendritic spine density in ventromedial hypothalamic neurons: a Golgi study in the adult rat. *Neuroendocrin. 51*(5), 530-535.

Fu H, Cataldi MP, Ware TA, Zaraspe K, Meadows AS, Murrey DA, McCarty DM. (2016). Functional correction of neurological and somatic disorders at later stages of disease in MPS IIIA mice by systemic scAAV9-hSGSH gene delivery. *Mol. Ther. Meth. Clin. Dev. 3*, 16036.

Fu H, Dirosario J, Killedar S, Zaraspe K, McCarty DM. (2011). Correction of neurological disease of mucopolysaccharidosis IIIB in adult mice by rAAV9 trans-blood-brain barrier gene delivery. *Molec. Ther. 19*(6), 1025-1033.

Fu H, Meadows AS, Ware T, Mohney RP, McCarty DM. (2017). Near-complete correction of profound metabolomic impairments corresponding to functional benefit in MPS IIIB mice after IV rAAV9-hNAGLU gene delivery. *Molec. Ther. 25*(3), 792–802.

Gabande-Rodriguez E, Keane L, Capasso M. (2020). Microglial phagocytosis in aging and Alzheimer's disease. *J. Neurosci. Res. 98*(2), 284-298.

Galione A, Morgan AJ, Arredouani A, Davis LC, Rietdorf K, Ruas M, Parrington J. (2010). NAADP as an intracellular messenger regulating lysosomal calcium-release channels. *Biochem. Soc. Trans. 38*(6), 1424–1431.

Galione A. (2015). A primer of NAADP-mediated Ca(2+) signalling: From sea urchin eggs to mammalian cells. *Cell Calcium 58*(1), 27–47.

Garey LJ, Ong WY, Patel TS, Kanani M, Davis A, Mortimer AM, Barnes TR, Hirsch, SR. (1998). Reduced dendritic spine density on cerebral cortical pyramidal neurons in schizophrenia. *J. Neurol. Neurosurg. Psych. 65*(4), 446–453.

Gelb MH. (2018). Newborn screening for lysosomal storage diseases: methodologies, screen positive rates, normalization of datasets, second-tier tests, and post-analysis tools. *Int. J. Neonatal Screen. 4*(3), 23.

Gerfen CR, Economo MN, Chandrashekar J. (2018). Long distance projections of cortical pyramidal neurons. *J. Neurosci. Res. 96*(9), 1467–1475.

Gifford S, Scheie H, Hambrick Jr. G, Barness L. (1962). A newly recognized forme fruste of Hurler's disease (gargoylism). *Am. J. Ophthalmol. 53*, 753–769.

Giger U, Shivaprasad H, Wang P. (1977) Mucopolysaccharidosis type IIIB (Sanfilippo B syndrome) in emus [abstract]. *Vet. Pathol.* 14:473.

Gilkes JA, Bloom MD, Heldermon CD. (2016). Mucopolysaccharidosis IIIB confers enhanced neonatal intracranial transduction by AAV8 but not by 5, 9 or rh10. *Gene Ther. 23*(3), 263–271.

Giugliani R, Federhen A, Michelin-Tirelli K, Riegel M, Burin M. (2017). Relative frequency and estimated minimal frequency of lysosomal storage diseases in Brazil: report from a Reference Laboratory. *Genet. Molec. Biol. 40*(1), 31-39.

Gleitz HF, Liao AY, Cook JR, Rowlston SF, Forte GM, D'Souza Z, O'Leary C, Holley RJ, Bigger BW. (2018). Brain-targeted stem cell gene therapy corrects mucopolysaccharidosis type II via multiple mechanisms. *EMBO Molec. Med. 10*(7), e8730.

Gliddon BL, Hopwood JJ. (2004). Enzyme-replacement therapy from birth delays the development of behavior and learning problems in mucopolysaccharidosis type IIIA mice. *Ped. Res. 56*(1), 65–72.

Gomez-Giro G, Arias-Fuenzalida J, Jarazo J, Zeuschner D, Ali M, Possemis N, Bolognin S, Halder R, Jäger C, et al. (2019). Synapse alterations precede neuronal damage and storage pathology in a human cerebral organoid model of CLN3-juvenile neuronal ceroid lipofuscinosis. *Acta Neuropath. Comm. 7*(1), 222.

Goo MS, Sancho L, Slepak N, Boassa D, Deerinck TJ, Ellisman MH, Bloodgood BL, Patrick GN. (2017). Activity-dependent trafficking of lysosomes in dendrites and dendritic spines. *J. Cell Biol. 216*(8), 2499-2513.

Gould E, Woolley CS, Frankfurt M, McEwen BS. (1990). Gonadal steroids regulate dendritic spine density in hippocampal pyramidal cells in adulthood. *J. Neurosci. 10*(4), 1286-1291.

Graveland GA, Williams RS, DiFiglia, M. (1985). Evidence for degenerative and regenerative changes in neostriatal spiny neurons in Huntington's disease. *Science 227*(4688), 770–773.

Green F, Samaranch L, Zhang HS, Manning-Bog A, Meyer K, Forsayeth J, Bankiewicz KS. (2016). Axonal transport of AAV9 in nonhuman primate brain. *Gene Ther. 23*(6), 520-526.

Grunewald B, Lange MD, Werner C, O'Leary A, Weishaupt A, Popp S, Pearce DA, Wiendl H, Rief A, et al. (2017). Defective synaptic transmission causes disease signs in a mouse model of juvenile neuronal ceroid lipofuscinosis. *Elife, 6*. e28685

Grutzendler J, Kasthuri N, Gan WB. (2002). Long-term dendritic spine stability in the adult cortex. *Nature, 420*(6917), 812–816.

Guidetti P, Charles V, Chen EY, Reddy PH, Kordower JH, Whetsell WO Jr, Schwarcz R, Tagle DA. (2001). Early degenerative changes in transgenic mice expressing mutant huntingtin involve dendritic abnormalities but no impairment of mitochondrial energy production. *Exp. Neurol. 169*(2), 340–350.

Hammond JW, Bellizzi MJ, Ware C, Qiu WQ, Saminathan P, Li H, Luo S, Ma SA, Li Y, Gelbard HA. (2020). Complement-dependent synapse loss and microgliosis in a mouse model of multiple sclerosis. *Brain Behav. Immunol. 87*, 739-750.

Harris KM, Stevens JK. (1989). Dendritic spines of CA 1 pyramidal cells in the rat hippocampus: serial electron microscopy with reference to their biophysical characteristics. *J. Neurosci. 9*(8), 2982–2997.

Haskins ME. (2007). Animal models for mucopolysaccharidosis disorders and their clinical relevance. *Acta Paediatr. 96*(455), 56-62.

Hassiotis S, Beard H, Luck A, Trim PJ, King B, Snel MF, Hopwood JJ, Hemsley KM. (2014a). Disease stage determines the efficacy of treatment of a paediatric neurodegenerative disease. *Eur. J. Neurosci. 39*(12**)**, 2139-2150.

Hassiotis S, Jolly RD, Hemsley KM. (2014b). Development of cerebellar pathology in the canine model of mucopolysaccharidosis type IIIA (MPS IIIA). *Molec. Genet. Metab. 113*(4), 283-293.

Haurigot V, Marco S, Ribera A, Garcia M, Ruzo A, Villacampa P, Ayuso E, Anor S, et al. (2013). Whole body correction of mucopolysaccharidosis IIIA by intracerebrospinal fluid gene therapy. *J. Clin. Invest. 123*(8), 3254-3271.

Hayashi-Takagi A. (2017). Synapse pathology and translational applications for schizophrenia. *Neurosci. Res. 114*, 3–8.

Heldermon CD, Hennig AK, Ohlemiller KK, Ogilvie JM, Herzog ED, Breidenbach A, Vogler C, et al. (2007). Development of sensory, motor and behavioral deficits in the murine model of Sanfilippo syndrome type B. *PLoS One, 2*(8), e772.

Hemsley KM, Hopwood JJ. (2005). Development of motor deficits in a murine model of mucopolysaccharidosis type IIIA (MPS-IIIA). *Behav. Brain Res. 158*(2), 191-199.

Hemsley KM, King B, Hopwood JJ. (2007). Injection of recombinant human sulfamidase into the CSF via the cerebellomedullary cistern in MPS IIIA mice. *Molec. Genet. Metab. 90*(3), 313-328.

Hemsley KM, Beard H, King BM, Hopwood JJ. (2008). Effect of high dose, repeated intra-cerebrospinal fluid injection of sulphamidase on neuropathology in mucopolysaccharidosis type IIIA mice. *Genes, brain, and behavior*, *7*(7), 740–753.

Hemsley KM, Luck AJ, Crawley AC, Hassiotis S, Beard H, King B, Rozek T, Rozaklis T, Fuller M, Hopwood JJ. (2009). Examination of intravenous and intra-CSF protein delivery for treatment of neurological disease. *Eur. J. Neurosci. 29*(6), 1197-1214.

Hendricks AG, Perlson E, Ross JL, Schroeder HW 3rd, Tokito M, Holzbaur EL. (2010). Motor coordination via a tug-of-war mechanism drives bidirectional vesicle transport. *Curr. Biol. 20*(8), 697-702.

Heppner FL, Ransohoff RM, Becher B. (2015). Immune attack: the role of inflammation in Alzheimer disease. *Nat. Rev Neurosci. 16*(6), 358–372.

Hering H, Sheng M. (2001). Dendritic spines: structure, dynamics and regulation. *Nat. Rev. Neurosci. 2*(12), 880–888.

Hers HG. (1963) alpha-Glucosidase deficiency in generalized glycogen storage disease (Pompe's disease). *Biochem. J.* 86(1):11-16.

Hess DC, Abe T, Hill WD, Studdard AM, Carothers J, Masuya M, Fleming PA, Drake CJ, Ogawa M. (2004). Hematopoietic origin of microglial and perivascular cells in brain. *Exp. Neurol. 186*(2), 134–144.

Heuser JE, Reese TS. (1973). Evidence for recycling of synaptic vesicle membrane during transmitter release at the frog neuromuscular junction. *J. Cell Biol. 57*(2), 315–344.

Higashi Y, Murayama S, Pentchev PG, Suzuki K. (1993). Cerebellar degeneration in the Niemann-Pick type C mouse. *Acta Neuropath. 85*(2), 175–184.

Higginson JR, Thompson SM, Santos-Silva A, Guimond SE, Turnbull JE, Barnett SC. (2012). Differential sulfation remodelling of heparan sulfate by extracellular 6-O-sulfatases regulates fibroblast growth factor-induced boundary formation by glial cells: implications for glial cell transplantation. *J. Neurosci. 32*(45), 15902-15912.

Hocquemiller M, Hemsley KM, Douglass ML, Tamang SJ, Neumann D, King BM, Beard H, Trim PJ, et al. (2019). AAVrh10 vector corrects disease pathology in MPS IIIA ,ice and achieves widespread distribution of SGSH in large animal brains. *Molec. Ther. Meth. Clin. Dev. 17*, 174–187.

Hofer SB, Mrsic-Flogel TD, Bonhoeffer T, Hübener M. (2009). Experience leaves a lasting structural trace in cortical circuits. *Nature 457*(7227), 313–317.

Holley RJ, Ellison SM, Fil D, O'Leary C, McDermott J, Senthivel N, Langford-Smith A, Wilkinson FL, et al. (2018). Macrophage enzyme and reduced inflammation drive brain correction of mucopolysaccharidosis IIIB by stem cell gene therapy. *Brain 141*(1), 99–116.

Holtmaat AJ, Trachtenberg JT, Wilbrecht L, Shepherd GM, Zhang X, Knott GW, Svoboda K. (2005). Transient and persistent dendritic spines in the neocortex in vivo. *Neuron 45*(2), 279-291

Honkura N, Matsuzaki M, Noguchi J, Ellis-Davies GC, Kasai H. (2008). The subspine organization of actin fibers regulates the structure and plasticity of dendritic spines. *Neuron 57*(5), 719-729.

Hooper AW, Igdoura SA. (2016). Bi-phasic gliosis drives neuropathology in a Sandhoff disease mouse model. *J. Neuroimmunol. 299,* 19–27.

Hooper AWM, Alamilla JF, Venier RE, Gillespie DC, Igdoura SA. (2017). Neuronal pentraxin 1 depletion delays neurodegeneration and extends life in Sandhoff disease mice. *Hum. Molec. Genet. 26*(4), 661-673.

Hopperton KE, Mohammad D, Trepanier MO, Giuliano V, Bazinet RP. (2018). Markers of microglia in post-mortem brain samples from patients with Alzheimer's disease: a systematic review. *Molec. Psych. 23*(2), 177-198.

Hudry E, Vandenberghe LH. (2019). Therapeutic AAV gene transfer to the nervous system: a clinical reality. *Neuron 101*(5), 839-862.

Hughes DA, Nicholls K, Shankar SP, Sunder-Plassmann G, Koeller D, Nedd K. Vockley G, Hamazaki T, et al. (2017). Oral pharmacological chaperone migalastat compared with enzyme replacement therapy in Fabry disease: 18-month results from the randomised phase III ATTRACT study. *J. Med. Genet. 54*(4), 288–296.

Hunter C. (1917). A rare disease in two brothers. *Proc. Royal Soc. Med. 10,* 104–116.

Hurler G. (1920). Über einen typ multiple abartungen, vorwiegend am skelettsystem.*Z. Kinderheilk* 24, 220–234

Hutsler JJ, Zhang H. (2010). Increased dendritic spine densities on cortical projection neurons in autism spectrum disorders. *Brain Res. 1309,* 83–94.

Jacobsen JS, Wu CC, Redwine JM, Comery TA, Arias R, Bowlby M, Martone R, et al. (2006). Early-onset behavioral and synaptic deficits in a mouse model of Alzheimer's disease. *Proc. Natl. Acad. Sci. USA 103*(13), 5161–5166.

Jelks KB, Wylie R, Floyd CL, McAllister AK, Wise P. (2007). Estradiol targets synaptic proteins to induce glutamatergic synapse formation in cultured hippocampal neurons: critical role of estrogen receptor-alpha. *J. Neurosci. 27*(26), 6903-6913.

Jennings LJ, Xu QW, Firth TA, Nelson MT, Mawe, GM. (1999). Cholesterol inhibits spontaneous action potentials and calcium currents in guinea pig gallbladder smooth muscle. *Am. J. Phys. 277*(5), G1017–G1026.

Jia R, Guardia CM, Pu J, Chen Y, Bonifacino JS. (2017). BORC coordinates encounter and fusion of lysosomes with autophagosomes. *Autophagy, 13*(10), 1648-1663.

Johnson DE, Ostrowski P, Jaumouille V, Grinstein S. (2016). The position of lysosomes within the cell determines their luminal pH. *J. Cell Biol. 212*(6), 677-692.

Jolly RD, Allan FJ, Collett MG, Rozaklis T, Muller VJ, Hopwood JJ. (2000). Mucopolysaccharidosis IIIA (Sanfilippo syndrome) in a New Zealand Huntaway dog with ataxia. *NZ Vet. J. 48*(5), 144–148.

Jones SA, Breen C, Heap F, Rust S, de Ruijter J, Tump E, Marchal JP, Pan L, Qiu Y, et al. (2016). A phase 1/2 study of intrathecal heparan-N-sulfatase in patients with mucopolysaccharidosis IIIA. *Molec. Genet. Metab. 118*(3), 198-205.

Joshi AU, Minhas PS, Liddelow SA, Haileselassie B, Andreasson KI, Dorn GW 2nd, Mochly-Rosen D. (2019). Fragmented mitochondria released from microglia trigger A1 astrocytic response and propagate inflammatory neurodegeneration. *Nat. Neurosci, 22*(10), 1635-1648.

Jung S, Jeong H, Yu SW. (2020). Autophagy as a decisive process for cell death. *Exp. Molec. Med. 52*(6), 921-930.

Kalaivani P, Ganesh M, Sathiya S, Ranju V, Gayathiri V, Saravana Babu C. (2014). Alteration in bioenergetic regulators, SirT1 and Parp1 expression precedes oxidative stress in rats subjected to transient cerebral focal ischemia: molecular and histopathologic evidences. *J. Stroke Cerebrovasc. Dis. 23*(10), 2753–2766.

Kalkan Ucar S, Ozbaran B, Demiral N, Yuncu Z, Erermis S, Coker M. (2010). Clinical overview of children with mucopolysaccharidosis type III A and effect of Risperidone treatment on children and their mothers psychological status. *Brain Dev. 32*(2), 156–161.

Kan SH, Aoyagi-Scharber M, Le SQ, Vincelette J, Ohmi K, Bullens S, Wendt DJ, Christianson TM, et al. (2014). Delivery of an enzyme-IGFII fusion protein to the mouse brain is therapeutic for mucopolysaccharidosis type IIIB. *Proc. Natl. Acad. Sci. USA 111*(41), 14870–14875.

Kang MG, Guo Y, Huganir RL. (2009). AMPA receptor and GEF-H1/Lfc complex regulates dendritic spine development through RhoA signaling cascade. *Proc. Natl Acad. Sci. USA 106*(9), 3549–3554.

Karageorgos L, Hill B, Bawden MJ, Hopwood JJ. (2007). Bovine mucopolysaccharidosis type IIIB. *J. Inherit. Metab. Dis.* 30, 358-364.

Karten B, Campenot RB, Vance DE, Vance JE. (2006). The Niemann-Pick C1 protein in recycling endosomes of presynaptic nerve terminals. *J. Lipid Res. 47*(3), 504–514.

Kasai H, Fukuda M, Watanabe S, Hayashi-Takagi A, Noguchi J. (2010). Structural dynamics of dendritic spines in memory and cognition. *Trends Neurosci. 33*(3), 121–129.

Kato A, Hojo Y, Higo S, Komatsuzaki Y, Murakami G, Yoshino H, Uebayashi M, Kawato S. (2013). Female hippocampal estrogens have a significant correlation with cyclic fluctuation of hippocampal spines. *Front. Neural Circuits 7*, 149.

Kavetsky L, Green KK, Boyle BR, Yousufzai FAK, Padron ZM, Melli SE, Kuhnel VL, et al. (2019). Increased interactions and engulfment of dendrites by microglia precede Purkinje cell degeneration in a mouse model of Niemann Pick Type-C. *Sci. Rep. 9*(1), 14722.

Keating DJ, Winter MA, Hemsley KM, Mackenzie KD, Teo EH, Hopwood JJ, Brooks DA, Parkinson-Lawrence EJ. (2012). Exocytosis is impaired in mucopolysaccharidosis IIIA mouse chromaffin cells. *Neurosci. 227*, 110–118.

Kharazia VN, Weinberg RJ. (1997). Tangential synaptic distribution of NMDA and AMPA receptors in rat neocortex. *Neurosci. Lett. 238*(1-2), 41–44.

Kielar C, Wishart TM, Palmer A, Dihanich S, Wong AM, Macauley SL, Chan C-H, et al. (2009). Molecular correlates of axonal and synaptic pathology in mouse models of Batten disease. *Hum. Molec. Genet. 18*(21), 4066-4080.

Kilinc D. (2018). The emerging role of mechanics in synapse formation and plasticity. *Front. Cell Neurosci. 12*, 483.

King B, Hassiotis S, Rozaklis T, Beard H, Trim PJ, Snel MF, Hopwood JJ, Hemsley KM. (2016). Low-dose, continuous enzyme replacement therapy ameliorates brain pathology in the neurodegenerative lysosomal disorder mucopolysaccharidosis type IIIA. *J. Neurochem. 137*(3), 409-422.

Kjellén L, Lindahl U. (1991). Proteoglycans: structures and interactions. *Ann. Rev. Biochem. 60*, 443–475.

Klein RS. (2020). On complement, memory, and microglia. *New Engl. J. Med. 382*(21), 2056–2058.

Koster KP, Francesconi W, Berton F, Alahmadi S, Srinivas R, Yoshii A. (2019). Developmental NMDA receptor dysregulation in the infantile neuronal ceroid lipofuscinosis mouse model. *Elife 8*, e40316.

Kowalewski B, Lamanna WC, Lawrence R, Damme M, Stroobants S, Padva M, Kalus I, et al. (2012). Arylsulfatase G inactivation causes loss of heparan sulfate 3-O-sulfatase activity and mucopolysaccharidosis in mice. *Proc. Natl. Acad. Sci USA 109*(26), 10310-10315.

Kresse H, Neufeld EF. (1972). The Sanfilippo A corrective factor. Purification and mode of action. *J. Biol. Chem. 247*(7), 2164–2170.

Kuramoto E, Furuta T, Nakamura KC, Unzai T, Hioki H, Kaneko T. (2009). Two types of thalamocortical projections from the motor thalamic nuclei of the rat: a single neuron-tracing study using viral vectors. *Cerebral Cortex 19*(9), 2065–2077.

Kuramoto E, Ohno S, Furuta T, Unzai T, Tanaka YR, Hioki H, Kaneko T. (2015). Ventral medial nucleus neurons send thalamocortical afferents more widely and more preferentially to layer 1 than neurons of the ventral anterior-ventral lateral nuclear complex in the rat. *Cerebral Cortex 25*(1), 221–235.

Lacagnina MJ, Rivera PD, Bilbo SD. (2017). Glial and neuroimmune mechanisms as critical modulators of drug use and abuse. *Neuropsychopharmacol. 42*(1), 156–177.

Lan YL, Zhao J, Li S. (2015). Update on the neuroprotective effect of estrogen receptor alpha against Alzheimer's disease. *J. Alzheimer's Dis. 43*(4), 1137–1148.

Landi S, Putignano E, Boggio EM, Giustetto M, Pizzorusso T, Ratto GM. (2011). The short-time structural plasticity of dendritic spines is altered in a model of Rett syndrome. *Sci. Rep.* ***1,*** 45.

Langford-Smith A, Wilkinson FL, Langford-Smith KJ, Holley RJ, Sergijenko A, Howe SJ, Bennett WR, et al. (2012). Hematopoietic stem cell and gene therapy corrects primary neuropathology and behavior in mucopolysaccharidosis IIIA mice. *Molec. Ther. 20*(8), 1610-1621.

LaPlante JM, Sun M, Falardeau J, Dai D, Brown EM, Slaugenhaupt SA, Vassilev PM. (2006). Lysosomal exocytosis is impaired in mucolipidosis type IV. *Molec. Genet. Metab. 89*(4), 339–348.

Larson TA. (2018). Sex steroids, adult neurogenesis, and inflammation in CNS homeostasis, degeneration, and repair. *Front. Endocrinol. 9*, 205.

Lau AA, Crawley AC, Hopwood JJ, Hemsley KM. (2008). Open field locomotor activity and anxiety-related behaviors in mucopolysaccharidosis type IIIA mice. *Behav. Brain Res. 191*(1), 130-136.

Lau AA, Hannouche H, Rozaklis T, Hassiotis S, Hopwood JJ, Hemsley, KM. (2010). Allogeneic stem cell transplantation does not improve neurological deficits in mucopolysaccharidosis type IIIA mice. *Exp. Neurol. 225*(2), 445-454.

Lau AA, King BM, Thorsen CL, Hassiotis S, Beard H, Trim PJ, Whyte LS, Tamang SJ, et al. (2017). A novel conditional Sgsh knockout mouse model recapitulates phenotypic and neuropathic deficits of Sanfilippo syndrome. *J. Inherit. Metab. Dis. 40*(5), 715-724.

Lazzarino DA, Gabel CA. (1989). Mannose processing is an important determinant in the assembly of phosphorylated high mannose-type oligosaccharides. *J. Biol. Chem. 264*(9), 5015–5023.

LealAF, Espejo-Mojica AJ, Sanchez OF, Ramirez CM, Reyes LH, Cruz JC, Almeciga-Diaz CJ. (2020). Lysosomal storage diseases: current therapies and future alternatives. *J. Molec. Med. 98*(7), 931-946.

Lee B, Kamitani T. (2011). Improved immunodetection of endogenous α-synuclein oligomeric intermediates via the lysosomal degradation pathway. *J. Neurosci.* 24, 1888-1896.

Lehrman EK, Wilton DK, Litvina EY, Welsh CA, Chang ST, Frouin A, Walker AJ, Heller MD, et al. (2018). CD47 protects synapses from excess microglia-mediated pruning during development. *Neuron, 100*(1), 120-134 e126.

Lendvai B, Stern EA, Chen B, Svoboda K. (2000). Experience-dependent plasticity of dendritic spines in the developing rat barrel cortex in vivo. *Nature, 404*(6780), 876–881.

Lepeta K, Lourenco MV, Schweitzer BC, Martino Adami PV, Banerjee P, Catuara-Solarz S, et al. (2016). Synaptopathies: synaptic dysfunction in neurological disorders - A review from students to students. *J. Neurochem. 138*(6), 785-805.

Li HH, Yu WH, Rozengurt N, Zhao HZ, Lyons KM, Anagnostaras S, Fanselow MS, Suzuki K, Vanier MT, Neufeld EF. (1999). Mouse model of Sanfilippo syndrome type B produced by targeted disruption of the gene encoding alpha-N-acetylglucosaminidase. *Proc. Natl. Acad. Sci. USA 96*(25), 14505–14510.

Li HH, Zhao HZ, Neufeld EF, Cai Y, Gomez-Pinilla F. (2002). Attenuated plasticity in neurons and astrocytes in the mouse model of Sanfilippo syndrome type B. *J. Neurosci. Res. 69*(1), 30-38.

Li Q, Barres BA. (2018). Microglia and macrophages in brain homeostasis and disease. *Nat. Rev. Immunol. 18*(4), 225-242.

Li Y, Scott CR, Chamoles NA, Ghavami A, Pinto BM, Turecek F, Gelb MH. (2004). Direct multiplex assay of lysosomal enzymes in dried blood spots for newborn screening. *Clin. Chem. 50*(10), 1785-1796. d

Li X, Qin L, Li Y, Yu H, Zhang Z, Tao C, Liu Y, Xue Y, Zhang X, et al. (2019). Presynaptic endosomal cathepsin D regulates the biogenesis of GABAergic synaptic vesicles. *Cell Res, 28*(4), 1015–1028.e5.

Liddelow SA, Barres BA. (2017). Reactive astrocytes: production, function, and therapeutic potential. *Immunity 46*(6), 957-967.

Liddelow SA, Guttenplan KA, Clarke LE, Bennett FC, Bohlen CJ, Schirmer L, Bennett ML, et al. (2017). Neurotoxic reactive astrocytes are induced by activated microglia. *Nature 541*(7638), 481-487.

Lin B, Kramar EA, Bi X, Brucher FA, Gall CM, Lynch G. (2005). Theta stimulation polymerizes actin in dendritic spines of hippocampus. *J. Neurosci. 25*(8), 2062-2069.

Lin HY, Chuang CK, Lee CL, Tu R-Y, Lo YT, Chiu PC, Niu D-M, Fang Y-Y, Chen T-L, et al. (2018). Mucopolysaccharidosis III in Taiwan: natural history, clinical and molecular characteristics of 28 patients diagnosed during a 21-year period. *Am. J. Med. Genet. 176*(9), 1799-1809.

Lindsay SL, McCanney GA, Willison AG, Barnett SC. (2020). Multi-target approaches to CNS repair: olfactory mucosa-derived cells and heparan sulfates. *Nat. Rev. Neurol. 16*(4), 229-240.

Linnartz B, Kopatz J, Tenner AJ, Neumann H. (2012). Sialic acid on the neuronal glycocalyx prevents complement C1 binding and complement receptor-3-mediated removal by microglia. *J. Neurosci. 32*(3), 946-952.

Lischka FW, Gomez G, Yee KK, Dankulich-Nagrudny L, Lo L, Haskins ME, Rawson NE. (2008). Altered olfactory epithelial structure and function in feline models of mucopolysaccharidoses I and VI. *J. Comp. Neurol. 511*(3), 360–372.

Lopez ME, Klein AD, Scott MP. (2012). Complement is dispensable for neurodegeneration in Niemann-Pick disease type C. *J. Neuroinflamm. 9,* 216.

Luine V, Rodriguez M. (1994) Effects of estradiol on radial arm maze performance of young and aged rats. *Behav. Neural. Biol*. 62(3):230-6.

Lundbaek JA, Birn P, Girshman J, Hansen AJ, Andersen OS. (1996). Membrane stiffness and channel function. *Biochem. 35*(12), 3825–3830.

Maday S, Twelvetrees AE, Moughamian AJ, Holzbaur EL. (2014). Axonal transport: cargo-specific mechanisms of motility and regulation. *Neuron 84*(2), 292-309.

Mahon LV, Lomax M, Grant S, Cross E, Hare DJ, Wraith JE, Jones S, Bigger B, Langford-Smith K, Canal M. (2014). Assessment of sleep in children with mucopolysaccharidosis type III. *PLoS One 9*(2), e84128.

Marco S, Pujol A, Roca C, Motas S, Ribera A, Garcia M, Molas M, Villacampa P, Melia CS, et al. (2016). Progressive neurologic and somatic disease in a novel mouse model of human mucopolysaccharidosis type IIIC. *Dis. Model Mech. 9*(9), 999-1013.

Morimoto K, Nakajima K. (2019). Role of the Immune System in the Development of the Central Nervous System. *Frontiers in neuroscience, 13,* 916.

Marino G, Kroemer G. (2013). Mechanisms of apoptotic phosphatidylserine exposure. *Cell Res. 23*(11), 1247-1248.

Markham JA, Juraska JM. (2002). Aging and sex influence the anatomy of the rat anterior cingulate cortex. *Neurobiol. Aging 23*(4), 579–588.

Maroteaux P, Leveque B, Marie J, Lamy, M. (1963). Une nouvelle dysostose avec elimination urinaire de chondroitine-sulfate B. *Presse Med.* 71: 1849.

Martin SJ, Reutelingsperger CP, McGahon AJ, Rader JA, van Schie RC, LaFace DM, Green DR. (1995). Early redistribution of plasma membrane phosphatidylserine is a general feature of apoptosis regardless of the initiating stimulus: inhibition by overexpression of Bcl-2 and Abl. *J. Exp. Med. 182*(5), 1545–1556.

Martinez FO, Gordon S. (2014). The M1 and M2 paradigm of macrophage activation: time for reassessment. *F1000Prime Rep. 6,* 13.

Martins C, Hůlková H, Dridi L, Dormoy-Raclet V, Grigoryeva L, Choi Y, Langford-Smith A, Wilkinson FL, et al. (2015). Neuroinflammation, mitochondrial defects and neurodegeneration in mucopolysaccharidosis III type C mouse model. *Brain 138*(Pt 2), 336–355.

Marx MC, Billups D, Billups B. (2015). Maintaining the presynaptic glutamate supply for excitatory neurotransmission. *J. Neurosci. Res. 93*(7), 1031-1044.

Matos L, Canals I, Dridi L, Choi Y, Prata MJ, Jordan P, Vilageliu L. (2014). Therapeutic strategies based on modified U1 snRNAs and chaperones for Sanfilippo C splicing mutations. *Orphanet J. Rare Dis. 9*, 180.

Matsuzaki M, Ellis-Davies GC, Nemoto T, Miyashita Y, Iino M, Kasai H. (2001). Dendritic spine geometry is critical for AMPA receptor expression in hippocampal CA1 pyramidal neurons. *Nat. Neurosci. 4*(11), 1086-1092.

McCarthy MM, Nugent BM, Lenz KM. (2017). Neuroimmunology and neuroepigenetics in the establishment of sex differences in the brain. *Nat. Rev. Neurosci. 18*(8), 471-484.

McCarthy MM, Wright CL. (2017). Convergence of sex differences and the neuroimmune system in autism spectrum disorder. *Biol. Psych. 81*(5), 402-410.

McEwan DG, Popovic D, Gubas A, Terawaki S, Suzuki H, Stadel D, Dikic I. (2015). PLEKHM1 regulates autophagosome-lysosome fusion through HOPS complex and LC3/GABARAP proteins. *Molec. Cell 57*(1), 39-54.

McEwen BS, Alves SE. (1999). Estrogen actions in the central nervous system. *Endocrine Rev. 20*(3), 279-307.

McGlynn R, Dobrenis K, Walkley SU. (2004). Differential subcellular localization of cholesterol, gangliosides, and glycosaminoglycans in murine models of mucopolysaccharide storage disorders. *J. Comp. Neurol. 480*(4), 415-426.

McGuinness L, Bardo SJ, Emptage NJ. (2007). The lysosome or lysosome-related organelle may serve as a Ca2+ store in the boutons of hippocampal pyramidal cells. *Neuropharmacol., 52*(1), 126–135.

McKinney RA, Lüthi A, Bandtlow CE, Gähwiler BH, Thompson SM. (1999). Selective glutamate receptor antagonists can induce or prevent axonal sprouting in rat hippocampal slice cultures. *Proc. Natl. Acad. Sci. USA 96*(20), 11631–11636.

Meikle PJ, Hopwood JJ, Clague AE, Carey, WF. (1999) Prevalence of lysosomal storage disorders. *JAMA, 281(3)* 249-254.

Mellman I, Fuchs R, Helenius A (1986) Acidification of the endocytic and exocytic pathways. *Ann. Rev. Biochem. 55*, 663-700

Meyer A, Kossow K, Gal A, Muhlhausen C, Ullrich K, Braulke T, Muschol N. (2007). Scoring evaluation of the natural course of mucopolysaccharidosis type IIIA (Sanfilippo syndrome type A). *Pediatrics, 120*(5), e1255-1261.

Milatovic D, Montine TJ, Zaja-Milatovic S, Madison JL, Bowman AB, Aschner M. (2010). Morphometric analysis in neurodegenerative disorders. *Curr. Prot. Toxicol. Chapter 12*, 1–12.16.

Miller T, Goude MC, McDevitt TC, Temenoff JS. (2014). Molecular engineering of glycosaminoglycan chemistry for biomolecule delivery. *Acta Biomaterialia*, *10*(4), 1705–1719.

Miller JJ, Aoki K, Moehring F, Murphy CA, O'Hara CL, Tiemeyer M, Stucky CL, Dahms NM. (2018). Neuropathic pain in a Fabry disease rat model. *JCI Insight 3*(6), e99171.

Millington DS, Kodo N, Norwood DL, Roe CR. (1990) Tandem mass spectrometry: a new method for acylcarnitine profiling with potential for neonatal screening for inborn errors of metabolism. *J. Inherit. Metab. Dis. 13(3,)* 321-324.

Morelli AE, Larregina AT, Shufesky WJ, Sullivan ML, Stolz DB, Papworth GD, Thomson AW. (2004). Endocytosis, intracellular sorting, and processing of exosomes by dendritic cells. *Blood 104*(10), 3257-3266.

Morimoto K, Nakajima K. (2019). Role of the immune system in the development of the central nervous system. *Front. Neurosci. 13*, 916.

Morquio L. (1929). Sur une forme de dystrophie osseuse familiale. *Pediat. Paris.* 27: 145-152

Moughamian AJ, Holzbaur EL. (2012). Dynactin is required for transport initiation from the distal axon. *Neuron 74*(2), 331-343.

Motas S, Haurigot V, Garcia M, Marco S, Ribera A, Roca C, Sanchez X, Sanchez V, Molas M, et al. (2016). CNS-directed gene therapy for the treatment of neurologic and somatic mucopolysaccharidosis type II (Hunter syndrome). *JCI Insight 1*(9), e86696.

Muenzer J. (2011) Overview of the mucopolysaccharidoses. *Rheumatology 50(5)*, 4-12

Muschol NM, Pape D, Kossow K, Ullrich K, Arash-Kaps L, Hennermann JB, Stucker R, Breyer SR. (2019). Growth charts for patients with Sanfilippo syndrome (Mucopolysaccharidosis type III). *Orphanet J. Rare Dis. 14*(1), 93.

Nagree MS, Scalia S, McKillop WM, Medin JA. (2019). An update on gene therapy for lysosomal storage disorders. *Expert Opin. Biol. Ther. 19*(7), 655-670.

Nakai N, Takumi T, Nakai J, Sato M. (2018). Common defects of spine dynamics and circuit function in neurodevelopmental disorders: a systematic review of findings from in vivo optical imaging of mouse models. *Front. Neurosci. 12*, 412.

Namer B, Ørstavik K, Schmidt R, Mair N, Kleggetveit IP, Zeidler M, Martha T, Jorum, E, Schmelz M, Kalpachidou T, Kress M, Langeslag M. (2017). Changes in ionic conductance signature of nociceptive neurons underlying Fabry disease phenotype. *Front. Neurol. 8*, 335.

Naso MF, Tomkowicz B, Perry WL 3rd, Strohl WR. (2017). Adeno-associated virus (AAV) as a vector for gene therapy. *BioDrugs 31*(4), 317-334.

Natowicz M, Short M, Wang Y. (1996). Clinical and biochemical manifestations of hyaluronidase deficiency. *New Engl. J. Med. 335(14),* 1029–1033

Neufeld EF. (1989). The Metabolic Basis of Inherited Disease II. 6 edn, *McGraw-Hill*, New York.

Neufeld EF, Muenzer J. (2001). The mucopolysaccharidoses. In: *The Metabolic and Molecular Bases of Inherited Disease*. *McGraw-Hill*, New York.

Nevian T, Sakmann B. (2004). Single spine Ca2+ signals evoked by coincident EPSPs and backpropagating action potentials in spiny stellate cells of layer 4 in the juvenile rat somatosensory barrel cortex. *J. Neurosci. 24*(7), 1689–1699.

Nicholson K, MacLusky NJ, Leranth C. (2020). Synaptic effects of estrogen. *Vitam. Horm. 114*, 167-210.

Nishimura M, Owens J, Swann JW. (2008). Effects of chronic network hyperexcitability on the growth of hippocampal dendrites. *Neurobiol. Dis.* ***29*****(2)**, 267–277.

Nishiyama J. (2019). Plasticity of dendritic spines: molecular function and dysfunction in neurodevelopmental disorders. *Psych. Clin. Neurosci. 73*(9), 541–550.

Nithianantharajah J, Hannan AJ. (2006). Enriched environments, experience-dependent plasticity and disorders of the nervous system. *Nat. Rev. Neurosci. 7*(9), 697-709.

Nithianantharajah J, Hannan AJ. (2013). Dysregulation of synaptic proteins, dendritic spine abnormalities and pathological plasticity of synapses as experience-dependent mediators of cognitive and psychiatric symptoms in Huntington's disease. *Neuroscience*, ***251***, 66-74.

Noguchi J, Matsuzaki M, Ellis-Davies GC, Kasai H. (2005). Spine-neck geometry determines NMDA receptor-dependent Ca2+ signaling in dendrites. *Neuron 46*(4), 609-622.

Noraberg J, Poulsen FR, Blaabjerg M, Kristensen BW, Bonde C, Montero M, Meyer M, Gramsbergen JB, Zimmer J. (2005). Organotypic hippocampal slice cultures for studies of brain damage, neuroprotection and neurorepair. *Curr. Drug Targets. CNS Neurol. Dis. 4*(4), 435–452.

Norris GT, Kipnis J. (2019). Immune cells and CNS physiology: microglia and beyond. *J. Exp. Med. 216*(1), 60-70.

Nur BG, Nur H, Mihci E. (2017). Bone mineral density in patients with mucopolysaccharidosis type III. *J. Bone Miner. Metab. 35*(3), 338-343.

Nusser Z, Hájos N, Somogyi P, Mody I. (1998). Increased number of synaptic GABA(A) receptors underlies potentiation at hippocampal inhibitory synapses. *Nature 395*(6698), 172–177.

Ohmi K, Greenberg DS, Rajavel KS, Ryazantsev S, Li HH, Neufeld EF. (2003). Activated microglia in cortex of mouse models of mucopolysaccharidoses I and IIIB. *Proc. Natl. Acad. Sci. USA 100*(4), 1902–1907.

Ohno S, Kuramoto E, Furuta T, Hioki H, Tanaka YR, Fujiyama F, Sonomura T, Uemura M, Sugiyama K, Kaneko T. (2012). A morphological analysis of thalamocortical axon fibers of rat posterior thalamic nuclei: a single neuron tracing study with viral vectors. *Cerebral Cortex 22*(12), 2840–2857.

Okamoto K, Nagai T, Miyawaki A, Hayashi Y. (2004). Rapid and persistent modulation of actin dynamics regulates postsynaptic reorganization underlying bidirectional plasticity. *Nat. Neurosci. 7*(10), 1104-1112.

Ozcan AS. (2017). Filopodia: a rapid structural plasticity substrate for fast learning. *Front. Synaptic Neurosci. 9*, 12.

Padamsey Z, McGuinness L, Bardo SJ, Reinhart M, Tong R, Hedegaard A, Hart ML, Emptage NJ. (2017a). Activity-dependent exocytosis of lysosomes regulates the structural plasticity of dendritic spines. *Neuron 93*(1), 132-146.

Padamsey Z, McGuinness L, Emptage NJ. (2017b). Inhibition of lysosomal Ca(2+) signalling disrupts dendritic spine structure and impairs wound healing in neurons. *Commun. Integr. Biol. 10*(5-6), e1344802.

Papale AE, Hooks BM. (2018). Circuit changes in motor cortex during motor skill learning. *Neuroscience 368*, 283–297.

Para C, Bose P, Pshezhetsky AV. (2020). Neuropathophysiology of lysosomal storage diseases: synaptic dysfunction as a starting point for disease progression. *J. Clin. Med. 9*(3), 616.

Parker H, Ellison SM, Holley RJ, O'Leary C, Liao A, Asadi J, Glover E, Ghosh A, Jones S, et al. (2020). Haematopoietic stem cell gene therapy with IL-1Ra rescues cognitive loss in mucopolysaccharidosis IIIA. *EMBO Molec. Med. 12*(3), e11185.

Parton RG, Simons K, Dotti CG. (1992). Axonal and dendritic endocytic pathways in cultured neurons. *J. Cell Biol. 119*(1), 123–137.

Parzych KR, Klionsky DJ. (2014). An overview of autophagy: morphology, mechanism, and regulation. *Antioxi.d Redox. Signal. 20*(3), 460-473.

Paxinos G, Franklin K. (2004). The mouse brain in stereotaxic coordinates, compact. 3rd Edition, *Academic Press*, Sydney.

Peng S, Xu J, Pelkey KA, Chandra G, Zhang Z, Bagh MB, Yuan X, Wu L-G, McBain CJ, Mukherjee AB. (2015). Suppression of agrin-22 production and synaptic dysfunction in Cln1 (-/-) mice. *Ann. Clin. Transl. Neurol. 2*(12), 1085-1104.

Perez BA, Shutterly A, Chan YK, Byrne BJ, Corti M. (2020). Management of neuroinflammatory responses to AAV-mediated gene therapies for neurodegenerative diseases. *Brain Sci. 10*(2), 119

Peters A, Kaiserman-Abramof IR. (1970). The small pyramidal neuron of the rat cerebral cortex. The perikaryon, dendrites and spines. *Am. J. Anat. 127*(4), 321–355.

Pfrieger FW, Barres BA. (1997). Synaptic efficacy enhanced by glial cells in vitro. *Science 277*(5332), 1684–1687.

Phillips M, Pozzo-Miller L. (2015). Dendritic spine dysgenesis in autism related disorders. *Neurosci. Lett. 601*, 30–40.

Platt FM, d'Azzo A, Davidson BL, Neufeld EF, Tifft CJ. (2018). Lysosomal storage diseases. *Nat. Rev. Dis. Primers, 4*(1), 27.

Poe MD, Chagnon SL, Escolar ML. (2014). Early treatment is associated with improved cognition in Hurler syndrome. *Ann. Neurol. 76*(5), 747–753.

van Praag H, Kempermann G, Gage FH. (2000). Neural consequences of environmental enrichment. *Nat. Rev. Neurosci. 1*(3), 191–198.

Prange-Kiel J, Jarry H, Schoen M, Kohlmann P, Lohse C, Zhou L, Rune GM. (2008). Gonadotropin-releasing hormone regulates spine density via its regulatory role in hippocampal estrogen synthesis. *J. Cell Biol. 180*(2), 417–426.

Presta I, Vismara M, Novellino F, Donato A, Zaffino P, Scali E, Pirrone KC, Spadea MF, Malara N, Donato G. (2018). Innate immunity cells and the neurovascular unit. *Int. J. Molec. Sci. 19*(12), 3856

Protopopescu X, Butler T, Pan H, Root J, Altemus M, Polanecsky M, McEwen B, Silbersweig D, Stern E. (2008). Hippocampal structural changes across the menstrual cycle. *Hippocampus 18*(10), 985-988.

Pshezhetsky AV. (2015). Crosstalk between 2 organelles: lysosomal storage of heparan sulfate causes mitochondrial defects and neuronal death in mucopolysaccharidosis III type C. *Rare Dis. 3*(1), e1049793.

Purpura DP, Suzuki K. (1976). Distortion of neuronal geometry and formation of aberrant synapses in neuronal storage disease. *Brain Res. 116*(1), 1–21.

Qin J, Liang J, Ding M. (2014). Perlecan antagonizes collagen IV and ADAMTS9/GON-1 in restricting the growth of presynaptic boutons. *J. Neurosci. 34*(31), 10311-10324.

Rabenstein M, Peter F, Joost S, Trilck M, Rolfs A, Frech MJ. (2017). Decreased calcium flux in Niemann-Pick type C1 patient-specific iPSC-derived neurons due to higher amount of calcium-impermeable AMPA receptors. *Molec. Cell Neurosci. 83*, 27–36.

Rabenstein M, Murr N, Hermann A, Rolfs A, Frech MJ. (2019). Alteration of GABAergic input precedes neurodegeneration of cerebellar Purkinje cells of NPC1-deficient mice. *Int. J. Molec. Sci. 20*(24), 6288.

Ramón y Cajal S. (1888). Estructura de los centros nerviosos de las aves. *Rev. Trim. Histol. Norm. Pat. 1,* 1-10.

Ranjan A, Mallick BN. (2010). A modified method for consistent and reliable Golgi-cox staining in significantly reduced time. *Front. Neurol. 1*, 157.

Rasia-Filho AA, Haas D, De Oliveira AP, De Castilhos J, Frey R, Stein D, Lazzari VM, Back GN, et al. (2012). Morphological and functional features of the sex steroid-responsive posterodorsal medial amygdala of adult rats. *Mini Rev. Med. Chem. 12*(11), 1090-1106.

Raymond GV, Bauman ML, Kemper TL. (1996). Hippocampus in autism: a Golgi analysis. *Acta Neuropath. 91*(1), 117–119.

Rizzoli SO, Betz WJ. (2005). Synaptic vesicle pools. *Nat. Rev. Neurosci. 6*(1), 57–69.

Roca C, Motas S, Marco S, Ribera A, Sanchez V, Sanchez X, Bertolin J, Leon X, Perez J, et al. (2017). Disease correction by AAV-mediated gene therapy in a new mouse model of mucopolysaccharidosis type IIID. *Hum. Molec. Genet. 26*(8), 1535-1551.

Rouach N, Avignone E, Même W, Koulakoff A, Venance L, Blomstrand F, Giaume C. (2002). Gap junctions and connexin expression in the normal and pathological central nervous system. *Biol. Cell 94*(7-8), 457–475.

Ruijter GJ, Valstar MJ, van de Kamp JM, van der Helm RM, Durand S, van Diggelen OP, Wevers RA, et al. (2008). Clinical and genetic spectrum of Sanfilippo type C (MPS IIIC) disease in The Netherlands. *Molec. Genet. Metab. 93*(2), 104-111.

Ruzo A, Marco S, Garcia M, Villacampa P, Ribera A, Ayuso E, Maggioni L, Mingozzi F, Haurigot V, Bosch F. (2012). Correction of pathological accumulation of glycosaminoglycans in central nervous system and peripheral tissues of MPSIIIA mice through systemic AAV9 gene transfer. *Hum. Gene Ther. 23*(12), 1237-1246.

Ryu J, Liu L, Wong TP, Wu DC, Burette A, Weinberg R, Wang YT, Sheng M. (2006). A critical role for myosin IIb in dendritic spine morphology and synaptic function. *Neuron 49*(2), 175-182.

Sambri I, D'Alessio R, Ezhova Y, Giuliano T, Sorrentino NC, Cacace V, De Risi M, Cataldi M, Annunziato L, De Leonibus E, Fraldi A. (2017). Lysosomal dysfunction disrupts presynaptic maintenance and restoration of presynaptic function prevents neurodegeneration in lysosomal storage diseases. *EMBO Molec. Med. 9*(1), 112–132.

Sands MS, Davidson BL. (2006). Gene therapy for lysosomal storage diseases. *Molec. Ther. 13*(5), 839-849.

Sanfilippo S, Podosin R, Langer L, Good, R. (1963). Mental retardation associated with acid mucopolysaccharidurıa (heparitin sulfate type) *J. Ped.* 63:837–838

Savas PS, Hemsley KM, Hopwood JJ. (2004). Intracerebral injection of sulfamidase delays neuropathology in murine MPS-IIIA. *Molec. Genet. Metab. 82*(4), 273-285.

Schafer DP, Lehrman EK, Kautzman AG, Koyama R, Mardinly AR, Yamasaki R, Ransohoff FM, Greenberg ME, Barres BA, Stevens B. (2012). Microglia sculpt postnatal neural circuits in an activity and complement-dependent manner. *Neuron 74*(4), 691-705.

Schafer DP, Lehrman EK, Stevens B. (2013). The "quad-partite" synapse: microglia-synapse interactions in the developing and mature CNS. *Glia 61*(1), 24-36.

Schaefer L. (2014). Proteoglycans, key regulators of cell-matrix dynamics. *Matrix Biol. 35*, 1–2.

Schielen P, Kemper EA, Gelb MH. (2017). Newborn screening for lysosomal storage diseases: a concise review of the literature on screening methods, therapeutic possibilities and regional programs. *Int. J. Neonatal Screen. 3*(2), 6.

Schikorski T, Stevens CF. (1999). Quantitative fine-structural analysis of olfactory cortical synapses. *Proc. Natl. Acad. Sci. USA 96*(7), 4107–4112.

Schindelin J, Arganda-Carreras I, Frise E, Kaynig V, Longair M, Pietzsch T, Preibisch S, Rueden C, Saalfeld S, Schmid B, Tinevez JY, White DJ, Hartenstein V, Eliceiri K, Tomancak P, Cardona A. (2012). Fiji: an open-source platform for biological-image analysis. *Nat. Meth. 9*(7), 676–682.

Schmidt R, Von Figura K, Paschke E, Kresse H. (1977). Sanfilippo's disease type A: sulfamidase activity in peripheral leukocytes of normal, heterozygous and homozygous individuals. *Clin. Chim. Acta 80*(1), 7–15.

Schwarz LA, Hall BJ, Patrick GN. (2010). Activity-dependent ubiquitination of GluA1 mediates a distinct AMPA receptor endocytosis and sorting pathway. *J. Neurosci. 30*(49), 16718–16729.

Scott HS, Blanch L, Guo XH, Freeman C, Orsborn A, Baker E, Sutherland GR, Morris CP, Hopwood JJ. (1995). Cloning of the sulphamidase gene and identification of mutations in Sanfilippo A syndrome. *Nat. Genet. 11*(4), 465–467.

Sellgren CM, Gracias J, Watmuff B, Biag JD, Thanos JM, Whittredge PB, Fu T, Worringer K, et al. (2019). Increased synapse elimination by microglia in schizophrenia patient-derived models of synaptic pruning. *Nat. Neurosci. 22*(3), 374-385.

Serrano-Pozo A, Frosch MP, Masliah E, Hyman BT. (2011). Neuropathological alterations in Alzheimer disease. *Cold Spring Harbor Perspect. Med. 1*(1), a006189.

Shapiro E, Ahmed A, Whitley C, Delaney K. (2018). Observing the advanced disease course in mucopolysaccharidosis, type IIIA; a case series. *Molec. Genet. Metab. 123*(2), 123-126.

Shapiro EG, Nestrasil I, Delaney KA, Rudser K, Kovac V, Nair N, Richard 3rd CW, Haslett P, Whitley CB. (2016a). A prospective natural history study of mucopolysaccharidosis type IIIA. *J. Pediatr. 170*, 278-287 e271-274.

Shapiro E, King K, Ahmed A, Rudser K, Rumsey R, Yund B, Delaney K, Nestrasil I, Whitley C, Potegal M. (2016b). The neurobehavioral phenotype in mucopolysaccharidosis type IIIB: an exploratory study. *Molec. Genet. Metab. Rep. 6*, 41-47.

Sharma J, di Ronza A, Lotfi P, Sardiello M. (2018). Lysosomes and brain health. *Annu. Rev. Neurosci. 41*, 255-276.

Shepherd GM. (2013). Corticostriatal connectivity and its role in disease. *Nat. Rev. Neurosci. 14*(4), 278–291.

Shi Q, Chowdhury S, Ma R, Le KX, Hong S, Caldarone BJ, Stevens B, Lemere CA. (2017). Complement C3 deficiency protects against neurodegeneration in aged plaque-rich APP/PS1 mice. *Sci. Transl. Med. 9*(392), eaaf6295.

Shors TJ, Chua C, Falduto J. (2001). Sex differences and opposite effects of stress on dendritic spine density in the male versus female hippocampus. *J. Neurosci. 21*(16), 6292–6297.

Shoubridge AP. (2013). The complement cascade in the developing MPS IIIA brain. Honours Thesis. *University of Adelaide, School of Medicine.*

Siegel DA, Walkley SU. (1994). Growth of ectopic dendrites on cortical pyramidal neurons in neuronal storage diseases correlates with abnormal accumulation of GM2 ganglioside. *J. Neurochem. 62*(5), 1852–1862.

Sisková Z, Page A, O'Connor V, Perry VH. (2009). Degenerating synaptic boutons in prion disease: microglia activation without synaptic stripping. *Am. J. Path. 175*(4), 1610–1621.

Sly W, Quinton B, McAlister W, Rimoin D. (1973). Beta glucuronidase deficiency: report of clinical, radiologic, and biochemical features of a new mucopolysaccharidosis. *J. Pediatr.* 82:249–57

Smith PK, Krohn RI, Hermanson GT, Mallia AK, Gartner FH, Provenzano MD, Fujimoto EK, Goeke NM, Olson BJ, Klenk DC. (1985). Measurement of protein using bicinchoninic acid. *Anal. Biochem. 150*(1), 76–85.

Spires TL, Meyer-Luehmann M, Stern EA, McLean PJ, Skoch J, Nguyen PT, Bacskai BJ, Hyman BT. (2005). Dendritic spine abnormalities in amyloid precursor protein transgenic mice demonstrated by gene transfer and intravital multiphoton microscopy. *J. Neurosci. 25*(31), 7278–7287.

Srivastava DP, Woolfrey KM, Penzes P. (2013) Insights into rapid modulation of neuroplasticity by brain estrogens. *Pharmacol. Rev.* 65(4), 1318-1350.

Stephens B, Mueller AJ, Shering AF, Hood SH, Taggart P, Arbuthnott GW, Bell JE, Kilford L, Kingsbury AE, Daniel SE, Ingham CA. (2005). Evidence of a breakdown of corticostriatal connections in Parkinson's disease. *Neuroscience 132*(3), 741–754.

Stephenson JR, Wang X, Perfitt TL, Parrish WP, Shonesy BC, Marks CR, Mortlock DP, Nakagawa T, Sutcliffe JS, Colbran RJ. (2017). A novel human *CAMK2A* mutation disrupts dendritic morphology and synaptic transmission, and causes ASD-related behaviors. *J. Neurosci. 37*(8), 2216–2233.

Stephenson J, Nutma E, van der Valk P, Amor S. (2018). Inflammation in CNS neurodegenerative diseases. *Immunology 154*(2), 204-219.

Stevens B, Allen NJ, Vazquez LE, Howell GR, Christopherson KS, Nouri N, Micheva KD, Mehalow AK, et al. (2007). The classical complement cascade mediates CNS synapse elimination. *Cell 131*(6), 1164-1178.

Stroobants S, Damme M, Van der Jeugd A, Vermaercke B, Andersson C, Fogh J, Saftig P, Blanz J, D'Hooge R. (2017). Long-term enzyme replacement therapy improves neurocognitive functioning and hippocampal synaptic plasticity in immune-tolerant alpha-mannosidosis mice. *Neurobiol. Dis. 106*, 255-268.

Sudhof TC. (2012). The presynaptic active zone. *Neuron 75*(1), 11-25.

Sun CL, Su LD, Li Q, Wang XX, Shen Y. (2011). Cerebellar long-term depression is deficient in Niemann-Pick type C disease mice. *Cerebellum 10*(1), 88-95.

Sun Y, Florer J, Mayhew CN, Jia Z, Zhao Z, Xu K, Ran H, Liou B, Zhang W, Setchell KD, Gu J, Grabowski GA. (2015). Properties of neurons derived from induced pluripotent stem cells of Gaucher disease type 2 patient fibroblasts: potential role in neuropathology. *PloS One 10*(3), e0118771.

Suzuki K. (1978). Enzymic diagnosis of sphingolipidoses. *Meth. Enzymol*. 50, 456-488.

Sweet RA, Henteleff RA, Zhang W, Sampson AR, Lewis DA. (2009). Reduced dendritic spine density in auditory cortex of subjects with schizophrenia. *Neuropsychopharmacol. 34*(2), 374–389.

Takashima S, Becker LE, Chan FW, Augustin R. (1985). Golgi and computer morphometric analysis of cortical dendrites in metabolic storage disease. *Exp. Neurol. 88*(3), 652–672.

Tang G, Gudsnuk K, Kuo SH, Cotrina ML, Rosoklija G, Sosunov A, Sonders MS, Kanter E, Castagna C, et al. (2014). Loss of mTOR-dependent macroautophagy causes autistic-like synaptic pruning deficits. *Neuron 83*(5), 1131–1143.

Tani H, Dulla CG, Farzampour Z, Taylor-Weiner A, Huguenard JR, Reimer RJ. (2014). A local glutamate-glutamine cycle sustains synaptic excitatory transmitter release. *Neuron 81*(4), 888-900.

Tardieu M, Zérah M, Husson B, de Bournonville S, Deiva K, Adamsbaum C, Vincent F, Hocquemiller M, et al. (2014). Intracerebral administration of adeno-associated viral vector serotype rh.10 carrying human SGSH and SUMF1 cDNAs in children with mucopolysaccharidosis type IIIA disease: results of a phase I/II trial. *Hum. Gene Ther. 25*(6), 506–516.

Tardieu M, Zérah M, Gougeon M-L, Ausseil J, de Bournonville S, Husson B, Zafeiriou D, Parenti G, et al. (2017). Intracerebral gene therapy in children with mucopolysaccharidosis type IIIB syndrome: an uncontrolled phase 1/2 clinical trial. *Lancet Neurol. 16*(9), 712-720.

Teichberg S, Holtzman E, Crain SM, Peterson ER. (1975). Circulation and turnover of synaptic vesicle membrane in cultured fetal mammalian spinal cord neurons. *J. Cell Biol. 67*(1), 215–230.

Teixeira CA, Miranda CO, Sousa VF, Santos TE, Malheiro AR, Solomon M, Maegawa GH, Brites P, Sousa MM. (2014). Early axonal loss accompanied by impaired endocytosis, abnormal axonal transport, and decreased microtubule stability occur in the model of Krabbe's disease. *Neurobiol. Dis. 66*, 92–103.

Tennant KA, Adkins DL, Scalco MD, Donlan NA, Asay AL, Thomas N, Kleim JA, Jones TA. (2012). Skill learning induced plasticity of motor cortical representations is time and age-dependent. *Neurobiol. Learn. Mem. 98*(3), 291-302.

Thompson JN, Jones MZ, Dawson G, Hu¡man PS (1992) N-Acetylglucosamine 6-sulphatase deficiency in a Nubian goat: a model of San¢lippo syndrome type D (mucopolysaccharidosis IIID). *J. Inherit Metab. Dis. 15*, 760-768

Tjia M, Yu X, Jammu LS, Lu J, Zuo Y. (2017). Pyramidal meurons in different cortical layers exhibit distinct dynamics and plasticity of apical dendritic spines. *Front. Neural Circuits 11*, 43.

Tordo J, O'Leary C, Antunes A, Palomar N, Aldrin-Kirk P, Basche M, Bennett A, D'Souza, Z, Gleitz, H, et al. (2018). A novel adeno-associated virus capsid with enhanced neurotropism corrects a lysosomal transmembrane enzyme deficiency. *Brain 141*(7), 2014–2031.

Trachtenberg JT, Chen BE, Knott GW, Feng G, Sanes JR, Welker E, Svoboda K. (2002). Long-term in vivo imaging of experience-dependent synaptic plasticity in adult cortex. *Nature 420*(6917), 788–794.

Trim PJ, Hopwood JJ, Snel MF. (2015). Butanolysis derivatization: improved sensitivity in LC-MS/MS quantitation of heparan sulfate in urine from mucopolysaccharidosis patients. *Anal. Chem., 87*(18), 9243–9250.

Trivedi PC, Bartlett JJ, Pulinilkunnil T. (2020). Lysosomal biology and function: modern view of cellular debris bin. *Cells 9*(5). doi:10.3390/cells9051131

Truman LA, Ford CA, Pasikowska M, Pound JD, Wilkinson SJ, Dumitriu IE, Melville L, Melrose LA, et al. (2008). CX3CL1/fractalkine is released from apoptotic lymphocytes to stimulate macrophage chemotaxis. *Blood 112*(13), 5026-5036.

Truxal KV, Fu H, McCarty DM, McNally KA, Kunkler KL, Zumberge NA, Martin L, Aylward SC, et al. (2016). A prospective one-year natural history study of mucopolysaccharidosis types IIIA and IIIB: implications for clinical trial design. *Molec. Genet. Metab. 119*(3), 239-248.

Valstar MJ, Ruijter GJ, van Diggelen OP, Poorthuis BJ, Wijburg FA. (2008). Sanfilippo syndrome: a mini-review. *J. Inherit. Metab. Dis. 31*(2), 240-252.

Valstar MJ, Marchal JP, Grootenhuis M, Colland V, Wijburg FA. (2011). Cognitive development in patients with mucopolysaccharidosis type III (Sanfilippo syndrome). *Orphanet J. Rare Dis. 6,* 43.

van Meel E, Klumperman J. (2008). Imaging and imagination: understanding the endo-lysosomal system. *Histochem. Cell Biol. 129*(3), 253-266.

Vegeto E, Bonincontro C, Pollio G, Sala A, Viappiani S, Nardi F, Brusadelli A, Viviani B, Ciana P, Maggi A. (2001). Estrogen prevents the lipopolysaccharide-induced inflammatory response in microglia. *J. Neurosci. 21*(6), 1809–1818.

Vilalta A, Brown GC. (2018). Neurophagy, the phagocytosis of live neurons and synapses by glia, contributes to brain development and disease. *FEBS J. 285*(19), 3566-3575.

Villalba RM, Smith Y. (2013). Differential striatal spine pathology in Parkinson's disease and cocaine addiction: a key role of dopamine? *Neuroscience, 251,* 2–20.

Villani,GR, Gargiulo N, Faraonio R, Castaldo S, Gonzalez YRE, Di Natale P. (2007). Cytokines, neurotrophins, and oxidative stress in brain disease from mucopolysaccharidosis IIIB. *J. Neurosci. Res. 85*(3), 612-622.

Vitry S, Ausseil J, Hocquemiller M, Bigou S, Dos Santos Coura R, Heard JM. (2009). Enhanced degradation of synaptophysin by the proteasome in mucopolysaccharidosis type IIIB. *Molec. Cell Neurosci. 41*(1), 8-18.

Voikar V, Vasar E, Rauvala H. (2004). Behavioral alterations induced by repeated testing in C57BL/6J and 129S2/Sv mice: implications for phenotyping screens. *Genes Brain Behav. 3*(1), 27-38.

Wagner VF, Northrup H. (2019). Mucopolysaccharidosis type III. In, M. P. Adam (Eds.) et. al., *GeneReviews*®. University of Washington, Seattle.

Wang G, Cheng Y, Gong M, Liang B, Zhang M, Chen Y, Zhang C, Yuan X, Xu J. (2013). Systematic correlation between spine plasticity and the anxiety/depression-like phenotype induced by corticosterone in mice. *Neurorep. 24*(12), 682–687.

Walkley SU, Blakemore WF, Purpura DP. (1981). Alterations in neuron morphology in feline mannosidosis. A Golgi study. *Acta Neuropath. 53*(1), 75–79.

Walkley SU, Baker HJ. (1984). Sphingomyelin lipidosis in a cat: Golgi studies. *Acta Neuropath. 65*(2), 138–144.

Walkley SU. (1987). Further studies on ectopic dendrite growth and other geometrical distortions of neurons in feline GM1 gangliosidosis. *Neuroscience 21*(2), 313–331.

Walkley SU, Haskins ME, Shull RM. (1988). Alterations in neuron morphology in mucopolysaccharidosis type I. A Golgi study. *Acta Neuropath. 75*(6), 611–620.

Walkley SU. (2004). Secondary accumulation of gangliosides in lysosomal storage disorders. *Seminars Cell Dev. Biol. 15*(4), 433–444.

Walkley SU, Suzuki K. (2004). Consequences of NPC1 and NPC2 loss of function in mammalian neurons. *Biochim. Biophys. Acta 1685*(1-3), 48–62.

Weber B, Blanch L, Clements PR, Scott HS, Hopwood JJ. (1996). Cloning and expression of the gene involved in Sanfilippo B syndrome (mucopolysaccharidosis III B). *Hum. Molec. Genet. 5*(6), 771–777.

Weiler N, Wood L, Yu J, Solla SA, Shepherd GM. (2008). Top-down laminar organization of the excitatory network in motor cortex. *Nat. Neurosci. 11*(3), 360–366.

Weinhard L, di Bartolomei G, Bolasco G, Machado P, Schieber NL, Neniskyte U, Exiga M, Vadisiute A, et al. (2018). Microglia remodel synapses by presynaptic trogocytosis and spine head filopodia induction. *Nat. Commun. 9*(1), 1228.

Werneburg S, Jung J, Kunjamma RB, Ha SK, Luciano NJ, Willis CM, Gao G, Biscola NP, Havton LF, et al. (2020). Targeted complement inhibition at synapses prevents microglial synaptic engulfment and synapse loss in demyelinating disease. *Immunity 52*(1), 167-182 e167.

Whitley CB, Cleary M, Eugen Mengel K, Harmatz P, Shapiro E, Nestrasil I, Haslett P, Whiteman D, Alexanderian D. (2018). Observational prospective natural history of patients with Sanfilippo syndrome type B. *J. Pediatr. 197*, 198-206 e192.

Wilhelm CM, Truxal KV, McBride KL, Kovalchin JP, Flanigan KM. (2018). Natural history of echocardiographic abnormalities in mucopolysaccharidosis III. *Molec. Genet. Metab. 124*(2), 131-134.

Wilkinson FL, Holley RJ, Langford-Smith KJ, Badrinath S, Liao A, Langford-Smith A, Cooper JD, et al. (2012). Neuropathology in mouse models of mucopolysaccharidosis type I, IIIA and IIIB. *PLoS One 7*(4), e35787.

Winner LK, Beard H, Hassiotis S, Lau AA, Luck AJ, Hopwood JJ, Hemsley KM. (2016). A preclinical study evaluating AAVrh10-based gene therapy for Sanfilippo syndrome. *Hum. Gene Ther. 27*(5), 363-375.

Woolley CS, Gould E, Frankfurt M, McEwen BS. (1990). Naturally occurring fluctuation in dendritic spine density on adult hippocampal pyramidal neurons. *J. Neurosci. 10*(12), 4035–4039.

Woolley CS, McEwen BS. (1992). Estradiol mediates fluctuation in hippocampal synapse density during the estrous cycle in the adult rat. *J. Neurosci. 12*(7), 2549–2554.

Xie Y, Hayden MR, Xu B. (2010). BDNF overexpression in the forebrain rescues Huntington's disease phenotypes in YAC128 mice. *J. Neurosci. 30*(44), 14708–14718.

Xu D, Arnold K, Liu J. (2018). Using structurally defined oligosaccharides to understand the interactions between proteins and heparan sulfate. *Curr. Opin. Struct. Biol. 50*, 155–161.

Xu S, Zhou S, Xia D, Xia J, Chen G, Duan S, Luo J. (2010). Defects of synaptic vesicle turnover at excitatory and inhibitory synapses in Niemann-Pick C1-deficient neurons. *Neuroscience 167*(3), 608-620.

Yanamadala V, Friedlander RM. (2010). Complement in neuroprotection and neurodegeneration. *Trends Molec. Med. 16*(2), 69–76.

Yang G, Gan WB. (2012). Sleep contributes to dendritic spine formation and elimination in the developing mouse somatosensory cortex. *Dev. Neurobiol. 72*(11), 1391–1398.

Yang G, Lai CS, Cichon J, Ma L, Li W, Gan WB. (2014). Sleep promotes branch-specific formation of dendritic spines after learning. *Science 344*(6188), 1173–1178.

Yang Q, Zhao X, Xing Y, Jiang C, Jiang K, Xu P, Liu W, Ren J, Huang L. (2018). A model of mucopolysaccharidosis type IIIB in pigs. *Biol. Open*, *7*(10), bio.035386.

Yasojima K, Schwab C, McGeer EG, McGeer PL. (1999). Up-regulated production and activation of the complement system in Alzheimer's disease brain. *Am. J. Path. 154*(3), 927–936.

Yue WW, Mackinnon S, Bezerra GA. (2019). Substrate reduction therapy for inborn errors of metabolism. *Emerg. Topics Life Sci. 3*(1), 63–73.

Yuste R, Denk W. (1995). Dendritic spines as basic functional units of neuronal integration. *Nature*, *375*(6533), 682–68**4.**

Yuste R. (2011). Dendritic spines and distributed circuits. *Neuron 71*(5), 772-781**.**

Zaja-Milatovic S, Milatovic D, Schantz AM, Zhang J, Montine KS, Samii A, Deutch AY, Montine TJ. (2005). Dendritic degeneration in neostriatal medium spiny neurons in Parkinson disease. *Neurology 64*(3), 545–547.

Zamanian JL, Xu L, Foo LC, Nouri N, Zhou L, Giffard RG, Barres BA. (2012). Genomic analysis of reactive astrogliosis. *J. Neurosci. 32*(18), 6391-6410

Zempel H, Thies E, Mandelkow E, Mandelkow EM. (2010). Abeta oligomers cause localized Ca(2+) elevation, missorting of endogenous Tau into dendrites, Tau phosphorylation, and destruction of microtubules and spines. *J. Neurosci. 30*(36), 11938–11950.

Zeng LH, Xu L, Rensing NR, Sinatra PM, Rothman SM, Wong M. (2007). Kainate seizures cause acute dendritic injury and actin depolymerization in vivo. *J. Neurosci. 27*(43), 11604–11613.

Zhang JM, Wang HK, Ye CQ, Ge W, Chen Y, Jiang ZL, Wu CP, Poo MM, Duan S. (2003). ATP released by astrocytes mediates glutamatergic activity-dependent heterosynaptic suppression. *Neuron 40*(5), 971–982.

Zhang L, Rossi A, Lange L, Meumann N, Koitzsch U, Christie K, Nesbit MA, Moore CBT, Hacker UT, et al. (2019). Capsid engineering overcomes barriers toward adeno-associated virus vector-mediated transduction of endothelial cells. *Hum. Gene Ther. 30*(10), 1284-1296.

Zhou SY, Xu SJ, Yan YG, Yu HM, Ling SC, Luo JH. (2011). Decreased purinergic inhibition of synaptic activity in a mouse model of Niemann-Pick disease type C. *Hippocampus 21*(2), 212-219.

Zhu H, Wang T, John Lye R, French BA, Annex BH. (2018). Neuraminidase-mediated desialylation augments AAV9-mediated gene expression in skeletal muscle. *J. Gene Med. 20*(9), e3049.

Zincarelli C, Soltys S, Rengo G, Rabinowitz JE. (2008). Analysis of AAV serotypes 1-9 mediated gene expression and tropism in mice after systemic injection. *Molec. Ther. 16*(6), 1073-1080.

Zuo Y, Lin A, Chang P, Gan WB. (2005). Development of long-term dendritic spine stability in diverse regions of cerebral cortex. *Neuron 46*(2), 181–189.